N°d'ordre : 526

Centre de Recherche Astrophysique De Lyon
École Doctorale de Physique et Astrophysique de Lyon

THÈSE

en vue d'obtenir le grade de

Docteur de l'École Normale Supérieure de Lyon - Université de Lyon

Spécialité : *Physique*

Présentée et soutenue publiquement le 21/09/2009 par

Benoît Commerçon

Sujet :

Formation d'étoiles : étude de l'effondrement des coeurs prestellaires

Directeurs de thèse : Mrs. Gilles Chabrier et Edouard Audit

Après avis de :

M.	Philippe André	
M.	Ian Bonnell	

Devant la commission d'examen composée de :

M.	Philippe André	Rapporteur
M.	Edouard Audit	Directeur de thèse
M.	Ian Bonnell	Rapporteur
M.	Gilles Chabrier	Directeur de thèse
M.	Thierry Forveille	Président
M.	Patrick Hennebelle	Membre invité

Remerciements

Comment ne pas commencer ce manuscrit sans remercier ma "dream team" pour avoir rendu possible cette aventure. Par ordre alphabétique : commençons par Edouard! Edouard... merci de t'être tant investi durant ces 3 années... Malgré tes diverses sollicitations, tu as toujours su prendre le temps de t'assurer que tout allait bien, à tous les niveaux. Ton expertise, ton sens critique à toute épreuve et ta gentillesse m'ont permis de passer trois années très riches en enseignement et très agréables au SAp. Ensuite Gilles! Merci de m'avoir accueilli et si bien intégré dans ton équipe. J'espère t'avoir rendu toute la confiance que tu m'as accordée. A ton contact, j'ai appris en permanence. De plus, tu as toujours pris le temps de répondre à mes interrogations. Enfin Patrick! Nous nous sommes connus à la fin de mon master et je ne t'ai pas lâché! Toi non plus! Un grand merci pour tes sollicitations permanentes et tes encouragements qui m'ont permis de toujours avancer. Ton impressionnant dynamisme scientifique m'a beaucoup servi et j'espère en avoir acquis un peu à ton contact. Envers vous trois, je suis infiniment reconnaissant pour ces trois années, ponctuées par quelques grands moments que seul un trinôme de chefs peut offrir!

En second, je tiens à remercier sincèrement Romain Teyssier, sans qui l'aventure n'aurait jamais commencé un soir de grand froid de décembre depuis une cabine téléphonique de la Merangasse à Graz... Tu m'as permis d'entrer dans ce milieu et m'as fourni toutes les clés pour bien démarrer et réussir. Mention spéciale pour ton implication "sous-marine" dans cette thèse. Merci à Jean-Pierre Chièze de m'avoir accueilli au sein de son laboratoire au SAp et pour avoir toujours gardé un oeil sur mon travail. Pierre-Olivier Lagage et Michel Perrault puis Maryvonne Gerin pour leurs accueils respectifs au SAp et au LRA.

Je tiens à remercier les membres de mon jury pour leur présence et leur disponibilité : le président, Thierry Forveille et les rapporteurs Philippe André et Ian Bonnell.

Viennent ensuite toutes les personnes que j'ai pu croiser et avec lesquelles j'ai interagi tout au long de ces trois années. Merci à Sébastien Fromang pour ses conseils toujours avisés et son agréable compagnie. Merci à tous les voisins de l'aile ouest : Benjamin l'ami motard, Neil l'anglais, Franck et ses cheveux longs, Thomas, dompteur de reptiles open source et enfin l'ancien-nouveau Matthias. Mention spéciale à la team A&A, aux thésards made in CEA et assimilés : Julien, malgré son amour de l'OL, Sandrine, Laurène, Fabio, Vince, Alain, Guillaume, Teuteuillon, Arnaud, Henri, Ivan, Ana, Anais, mon pendant observationnel Anaelle, Timéa, Benjamin, Marie, Laurie, Nicolas, Pierrick, Jules, Jérôme, Astrid, Johanne, etc.... Petite pensée envers les sympathiques Lyonnais : Albéric, Maxime le grand, mon compagnon de galère Guillaume et sa Florence, Jérémy, José, Gégé, Christophe que je peux enfin tutoyer, Jeff, Cédric, Isa, Rolf, Nathaniel, Laure, etc... Merci enfin aux membres du LRA : Ludo, Christophe, Emmanuel, Javier, François, Edith, Jean-François, Benjamin et le futur martyr de Patrick, Marc. Merci enfin à tous ceux que j'ai pu croiser au SAp, au LRA et au CRAL que j'ai pu oublier dans cette liste exhaustive.

Comment ne pas avoir une chaleureuse pensée pour mes coboureaux : Quang et Damien qui ont eu le privilège de me supporter lors de ma dernière année, et les amis : Clément pour sa bonne humeur contagieuse et Yohan malgré son goût vestimentaire douteux, merci les gars!

Merci à tous les relecteurs et correcteurs de ce manuscrit : Amandine, Gilles, Patrick,

Edouard, Clément, Neil, Damien et Quang.

Un petit coucou aux compères insaiens : les colocs Papy et Denis pour m'avoir supporté pendant les deux premières années, avant qu'Amandine ne me reprenne en main, Greg, Mat G., Mat V., Charly, Brendan, Keken, Nico, JC, etc... Petite pensée pour mes amis de toujours du Mâconnais : Cyril, Olivier, Guillaume, Marchio, Coco, Henri-Luc et tous les autres.

Finissons par la grande famille. Merci à mes parents, ma petite soeur, mes grand-parents, arrière-grand parents, oncles, tantes, beaux parents et cousins qui m'ont vu grandir ou vieillir pour les plus jeunes. Merci à tous pour tous les beaux moments que nous avons passés, que nous passons et que nous passerons ensemble. Merci à la belle famille nivernaise pour les séjours ressourçants.

Merci enfin à Amandine. Ton amour, ton soutien et ta confiance sont mes moteurs. Une nouvelle étape nous attend, que nous allons vivre à fond tous les deux, je suis impatient!

Résumé

La compréhension des processus conduisant à la formation des étoiles est l'un des enjeux majeurs de l'astrophysique contemporaine. Au sein des nuages conduisant à la formation d'étoiles, les conditions de température, pression, etc... sont telles qu'il est impossible de les reproduire par l'expérience. C'est pourquoi la simulation numérique reste le seul moyen d'étudier les phénomènes physiques intervenant dans le processus de formation des étoiles et ainsi de vérifier la théorie. Ma thèse est axée autour des méthodes numériques utilisées dans le contexte de la formation d'étoiles, phénomène multi-échelles et hautement non-linéaire, nécessitant l'utilisation d'outils bien adaptés.

Dans cette thèse autour de l'étude des premières phases de l'effondrement de coeurs denses préstellaires, mon travail s'est divisé en 4 parties liées. Dans une première étude, j'ai utilisé un code lagrangien 1D à symétrie sphérique (Audit et al. 2002) pour comparer plusieurs modèles traitant plus ou moins précisément le transfert radiatif et l'interaction matière-rayonnement. Cette comparaison est basée sur des calculs simples d'effondrement gravitationnel conduisant à la formation du premier coeur de Larson. J'ai aussi tiré bénéfice de ce premier travail pour étudier les propriétés du choc d'accrétion sur le premier coeur de Larson. Nous avons développé un modèle semi-analytique permettant de reproduire les propriétés de saut au choc en partant d'hypothèses bien connues. Ayant validé les méthodes utilisées précédemment, nous avons retenu l'approche de diffusion à flux limité que j'ai ensuite intégrée avec les équations de l'hydrodynamique radiative dans le code AMR RAMSES (Teyssier 2002). Après validation des schémas implémentés, nous avons utilisé RAMSES pour réaliser des effondrements multidimensionnels avec champ magnétique et transfert radiatif. Nous avons ainsi réalisé les premières simulations combinant les effets du champ magnétique et du transfert radiatif aux petites échelles avec une grande précision. Nos résultats montrent que le transfert radiatif à un impact significatif sur la fragmentation au cours de l'effondrement des coeurs denses préstellaires. Enfin, j'ai réalisé une comparaison du code RAMSES (approche eulérienne) et du code SPH DRAGON (Goodwin 2004, approche lagrangienne). Nous avons étudié l'impact de la résolution numérique sur la conservation du moment angulaire et la fragmentation. Nous avons montré qu'en utilisant des critères de résolution forts et bien supérieurs aux critères usuels de la littérature, les deux outils convergent et semblent donc bien adaptés à la formation d'étoiles.

Abstract

One of the priorities of contemporary astrophysics remains to understand the mechanisms which lead to star formation. In the dense cores where star formation occurs, temperature, pressure, etc... are such that it is impossible to reproduce them in the laboratory. Numerical calculations remain the only mean to study physical phenomena that are involved in the star formation process. The focus of this thesis has been on the numerical methods that are used in the star formation context to describe highly non-linear and multi-scale phenomena. In particular, I have concentrated my work on the first stages of the prestellar dense cores collapse.

This work is divided in 4 linked part. In a first study, I use a 1D Lagrangean code in spherical symmetry (Audit et al. 2002) to compare three models that incorporate radiative transfer and matter-radiation interactions. This comparison was based on simple gravitational collapse calculations which lead to the first Larson core formation. It was found that the Flux Limited Diffusion model is appropriate for star formation calculations. I also took benefit from this first work to study the properties of the accretion shock on the first Larson core. We developed a semi-analytic model based on well-known assumptions, which reproduces the jump properties at the shock. The second study consisted in implementing the Flux Limited Diffusion model with the radiation-hydrodynamics equations in the RAMSES code (Teyssier 2002). After a first step of numerical tests that validate the scheme, we used RAMSES to perform the first multidimensional collapse calculations that combine magnetic field and radiative transfer effects at small scales with a high numerical resolution. Our results show that the radiative transfer has a significant impact on the fragmentation in the collapse of prestellar dense cores. I also present a comparison we made between the RAMSES code (Eulerian approach) and the SPH code DRAGON (Goodwin 2004, Langrangean approach). We studied the effect of the numerical resolution on the angular momentum conservation and on the fragmentation. We show that the two methods converge, provided that we use high numerical resolution criteria, which are much greater than the usual criteria found in the literature. The two methods then seem to be adapted to the study of tar formation.

Contents

List of Figures

List of Tables

Chapter 1

Our current understanding of low mass star formation

Contents

The most exciting phrase to hear in science, the one that heralds new discoveries, is not 'Eureka!' (I found it!) but 'That's funny ...' Isaac Asimov (1920 - 1992)

In this first chapter, we briefly review our knowledge of the low mass star formation process. We first present the famous low mass star evolutionary sequence, defined from the theoretical and observational points of view. In a second part, we recall what observations tell us about star formation regions. Then, we review the theoretical work that has been done in the field. In the third part, basic concepts, useful for the following chapters, are introduced. In this chapter, we focus on the collapse of prestellar cores and do not address the issue of their formation processes. Eventually, I introduce the different parts of this work.

1.1 Introduction

Stars are the main source of luminous matter in the universe. By transforming gas into star, star formation is a dominant process in the interstellar cycle. During its life, a star burns its hydrogen and forms most of the heavy elements that make the world around us. When a star dies, it can explode as a supernova that will trigger star formation in compressed surrounding regions. Star formation can also determine the evolution and the structure of galaxies. Consequently, it is of prime importance in astrophysics to understand how stars form. Although star formation is a very common process, we do not completely understand it. We know that three solar masses of molecular gas per year are transformed into stars in the Galaxy. It is also established that stars form from the gravitational collapse of molecular dense cores, essentially composed of H_2 and He. Observations of dynamical star forming regions remain challenging, since most of the star forming regions in our Galaxy are opaque to optical radiation and quite far away ($\sim$ 100 pc). At this distance, the astronomical unit (AU), the Sun-Earth distance, cannot be resolved by present day telescopes... During the past twenty years, significant progress and breakthroughs have yet been done in the observational field, thanks to the development of observing techniques in the submillimeter and in the millimeter wavelengths.

Low mass stars (M$<$ 8M$_\odot$) form in a short time compared to their Kelvin-Helmholtz time, $t_{\rm KH} = GM^2/RL$ (L is the luminosity of the star), which is the time for a star to radiate its gravitational energy. The limit between low and high mass stars remains arbitrary (McKee and Ostriker 2007). Low mass protostars have their luminosity dominated by accretion and form from dense cores that have masses close to the thermal Jeans mass. Dense cores are formed by the fragmentation of big molecular clouds. These fragments are initially near equipartition between thermal, magnetic and turbulent pressures (Mouschovias 1991). Their evolution is governed by various mechanisms such as turbulence dissipation (Audit and Hennebelle 2005; Ballesteros-Paredes et al. 2007; Nakano 1998), ambipolar diffusion (e.g. Basu et al. 2009; Shu et al. 1987) or outside impulse (Bonnell et al. 1997; Hennebelle et al. 2003).

1.2 The low mass star evolutionary sequence

1.2.1 An overview and definitions

The low mass star formation process can be divided into three steps (André et al. 2000) and involves a series of different stages:

- the *prestellar phase* during which the gravitationally-bound dense core condenses isothermally, the energy increases because of gravitational compression and is radiated away by dust (Larson 1969): this is the *first collapse phase*. The density profile in the core becomes steeper and tends to a profile $\rho \propto r^{-2}$ independently of initial conditions (e.g. Foster and Chevalier 1993). The infalling gas is in a supersonic free-fall regime. When the density increases, the gas becomes optically thick. The radiation is trapped and the gas begins to heat up adiabatically. This occurs at a typical density $\rho_{\rm ad} \sim 10^{-13}$ g cm^{-3}. The central region reaches an hydrostatic equilibrium state. The first core, named the *first Larson core* is born. Its typical radius is $R_{\rm fc} \sim 5$ AU and its initial mass is $M_{\rm fc} \sim 0.01$ M$_\odot$. Because of gravitational contraction, the core temperature grows up and once it reaches 2000 K, the endothermic dissociation of H_2 triggers a *second collapse phase*, of polytropic index $\gamma_{\rm eff} \sim 1.1$ (Masunaga and Inutsuka 2000b). The infall velocity becomes very large ($>$ 20 km s^{-1})and the first core is quickly engulfed, within a few 10^3 yr. When the central density reaches the stellar density of $\rho_\star \sim 1$ g cm^{-3}, a new protostellar object of radius $R \sim 3-5$ R$_\odot$ forms in the center, the *second Larson core*.

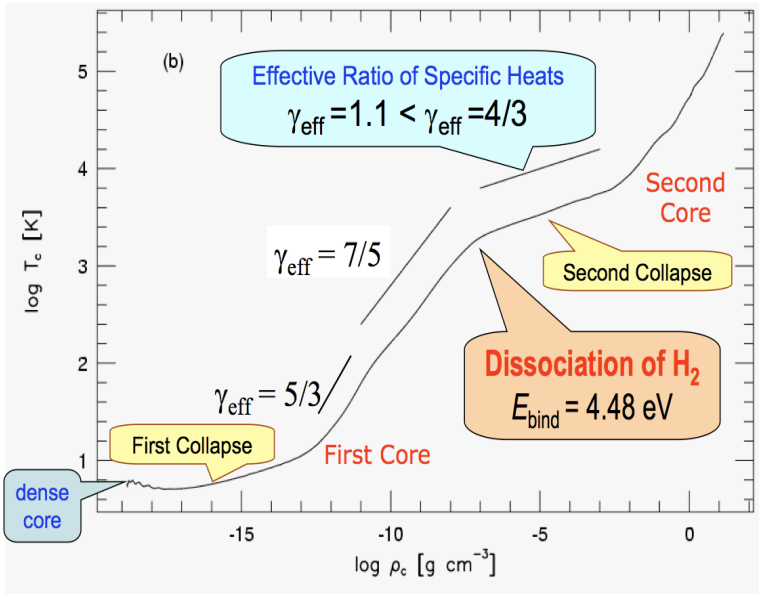

Figure 1.1: Evolution of the central temperature as a function of the central density for a collapsing dense core. Taken from André et al. (2008), and based on Masunaga and Inutsuka (2000b) results.

- the *protostellar phase*: this is the main accretion phase. The hydrostatic protostellar object builds up its mass by accretion from a surrounding infalling envelope. During this phase, the accretion is time dependent. Angular momentum conservation leads to the formation of an accretion disk. Through the accretion shock, potential energy of the accreted material is radiated away. The estimate of the amount of energy radiated away is of prime interest since it determines the entropy level of the protostellar object. It is admitted that protostars radiate the accretion luminosity $L_{\rm acc} = GM\dot{M}_{\rm acc}/R_\star$. A rarefaction wave propagates from the center to the envelope at the speed of sound. The density profile varies as $\rho \propto r^{-1.5}$ and the radial velocity as $v \propto r^{-0.5}$ (Shu 1977). Observations of this accretion phase show material bipolar outflows and jets along the rotational axis (Bachiller 1996). A contemporary challenge is to reproduce this observed outflow velocities with multidimensional magneto-hydrodynamics numerical calculations (Banerjee and Pudritz 2006; Hennebelle and Fromang 2008; Machida et al. 2007; Mellon and Li 2009).

- the *pre-main sequence phase*: the protostar has almost its final mass and starts to burn deuterium at T$\sim 10^6$ K. The protostar appears on its *birth-line* (Stahler 1988) and can be observed in the optical, even though the concept of birth-line is probably inappropriate (Baraffe et al. 2009). The protostar contracts in a quasi-static way in a Kelvin-Helmotz time (10^7 yr) and the temperature continues to increase until hydrogen fusion starts at 10^7 K. A star is born and has reached the main sequence. For instance, the Sun is at the middle of its life on the main sequence. The modeling of this step is only accessible by steady state calculations (e.g. Chabrier and Baraffe 2000).

Figure 1.1 shows the central temperature evolution obtained by Masunaga and Inutsuka (2000b), using a 1D spherical code, which integrates radiation hydrodynamics equations. This corresponds to the prestellar phase described above. The cloud remains isothermal during the first collapse phase. Once the compression rate exceeds the radiative cooling rate, the central temperature increases above the equilibrium initial temperature $\sim$ 10 K. The temperature increases with the density first with a slope that corresponds to an adiabatic index (or ratio of

specific heats) $\gamma = 5/3$. At low temperature, H_2 is at its ground state, since its rotational degrees of freedom are not excited. When the temperature exceeds 100 K, the rotational degrees of freedom are excited and $\gamma = 7/5$. We show in part 1.5.2 that the critical value for gravitational instability to proceed is $\gamma_{\rm crit} = 4/3$. The adiabatic gas is thus supported by the thermal pressure against self-gravity. This defines the first core. When the temperature exceeds $\sim$ 2000 K, the dissociation of H_2 starts and acts as an efficient coolant of the gas. The binding energy of H_2 is about 4.48 eV, which is much larger than the thermal energy per hydrogen molecule in this temperature regime. The adiabatic index becomes $\gamma \sim 1.1 < \gamma_{\rm crit}$ and the second collapse phase proceeds. Eventually, the central density reaches a stellar value $\rho_\star \sim 1$ g cm^{-3} and a hydrostatic protostellar object is formed in the center.

1.2.2 The empirical evolutionary sequence

Originally, Young Stellar Objects (YSO) were classified into three categories, according to the logarithmic slope $\alpha_{\rm IR} = d\log(\lambda F_\lambda)/d\log(\lambda)$ of the observed Spectral Energy Distributions (SEDs) in the near and mid-infrared. Going backward in time, we find Class III ($\alpha_{\rm IR} < -1.5$), Class II ($-1.5 < \alpha_{\rm IR} < 0$) and Class I ($\alpha_{\rm IR} > 0$) sources. The Class II and III correspond to Pre Main Sequence (PMS) stars ("Weak-line" and "Classical" T Tauri stars, respectively), surrounded by a circumstellar disk. The Class I sources are the youngest YSO detected and are interpreted as relatively evolved protostars, surrounded by both a disk and a circumstellar envelope ($M_\star < M_{\rm env}$).

The recent progress in the infrared and millimeter techniques in the past two decades have made possible a better understanding of low mass dense cores, prior to Class I stage. It is related to compact condensations that are invisible at $\lambda < 25\mu$m. Three broad categories of cores can now be distinguished within nearby molecular clouds and may represent an empirical evolutionary sequence (André 2002; André et al. 2000): starless cores, prestellar cores and "Class 0" protostellar cores. Starless cores are concentrations of molecular gas, which do not show evidence of infall. They are observed in tracers such as $C^{18}O$, NH_3 or dust extinction. Prestellar cores are denser and self-gravitating, without embedded YSOs ($M_\star = 0$). They are observed in sub-millimeter dust continuum and tracers such as NH_3 or N_2H^+ and exhibit evidence of infall motions. All the starless cores do not evolve to prestellar cores. Prestellar cores are characterized by large density contrasts over the local background medium (factor 5-10). Class 0 objects have been introduced in André et al. (1993) and are well distinguished from other stages thanks to observational properties, such as collimated CO outflows. They are young accreting protostars observed in the first stages after the second core formation. Most of the mass of the system remains in the envelope, in opposition with YSOs ($M_\star \ll M_{\rm env}$).

This empirical evolutionary sequence is summarized in figure 1.2, where $T_{\rm bol}$ is the bolometric temperature, defined as the temperature of a blackbody, whose spectrum has the same mean frequency as the observed spectrum.

1.3 Observational properties of individual low mass prestellar cores

1.3.1 Density and thermal structures

The density structure is estimated through the analysis of dust emission or absorption, mapping of the optically thin (sub)millimeter dust continuum emission and mapping of dust absorption against infrared emission. Under the assumption of spatially uniform dust temperature and emissivity properties, the radial density profile of isolated prestellar cores is found to be flatter than $\rho(r) \propto r^{-1}$ in their inner region ($r \leq R_{flat} \sim 2500 - 5000$ AU) and approaches a profile

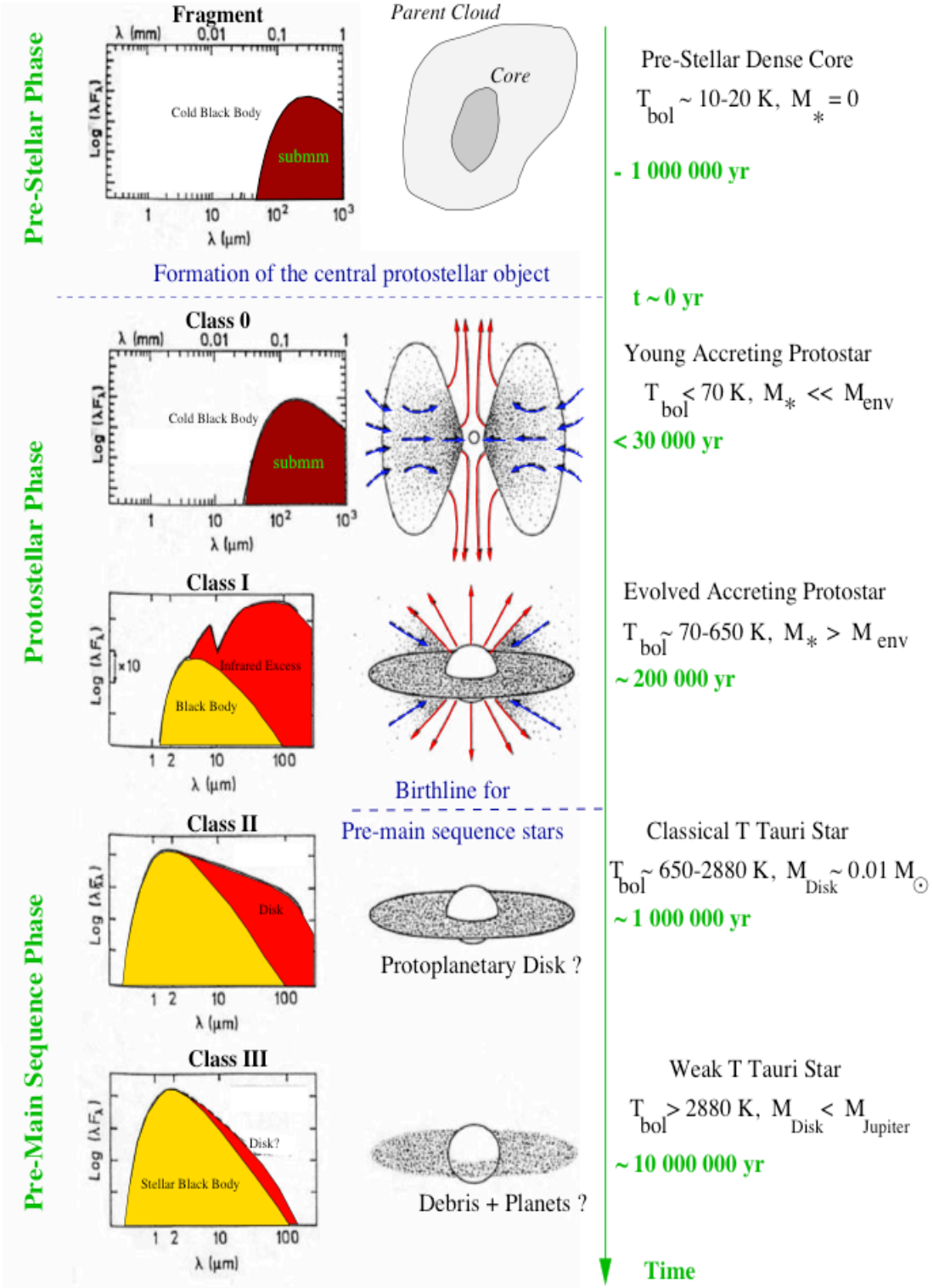

Figure 1.2: Empirical evolutionary sequence for the formation of a single star from a prestellar cloud core to a Class III YSO. Taken from André (2002).

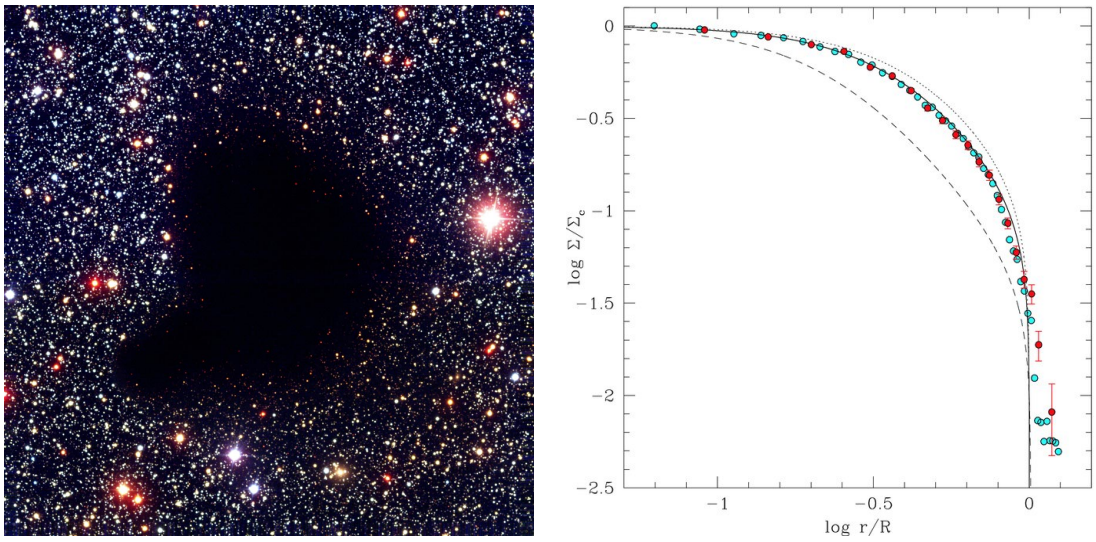

Figure 1.3: *Left:* color composite of visible-light images of the famous dark cloud Barnard 68. *Right:* radial surface density structure of Barnard 68. The dotted, solid, and dashed lines show theoretical Bonnor-Ebert spheres with $\xi_{\max}$ =6, 7, and 10, respectively. Red points with error bars show the observed structure of Barnard 68 as determined from near-IR dust extinction measurements (e.g. Alves et al. 2001). The cyan points show results of numerical simulations. Taken from Burkert and Alves (2009).

$\rho(r) \propto r^{-2}$ beyond R_{flat} (André et al. 1996; Ward-Thompson et al. 1999). The typical central density [1] is $10^5 - 10^6$ cm^{-3} . The truncated isothermal Bonnor-Ebert sphere (Bonnor 1956; Ebert 1955) provides a good fit to the data (e.g. Alves et al. 2001, see figure 1.3).

The thermal structure of prestellar cores is regulated by the interplay between various heating and cooling processes. At high densities in the inner part of the cores ($> 10^5$ cm^{-3}), the gas and dust have to be coupled thermally via collisions (e.g. Goldsmith 2001). In the outer parts of the cores, the dust and gas temperature are not expected to be the same. The dust temperature in cores ($8-12$ K) is colder than the temperature in the clouds, $\sim 15-20$ K (e.g. Ward-Thompson et al. 2002). The gas temperature is estimated from the level of excitation of molecules such as CO or NH_3. The estimated gas temperature is 10-20 K (Evans 1999).

1.3.2 Kinematic structure

Dense cores have low internal velocities. During the Class 0 phase, subsonic velocities persist in the outer parts of the core (Belloche et al. 2002). The gas motions inside the core ($r < 2000$ AU) are at best transsonic, with Mach numbers ≤ 2 (e.g. André et al. 2007). Belloche et al. (2002) propose that the inner envelope is in the process of decoupling from the ambient cloud (outer part) and corresponds to the effective mass reservoir (~ 0.5 M$_\odot$) from which the central star is being built. Dense cores are yet rotating. Goodman et al. (1993) found that cores typically have a rotational energy to gravitational energy ratio $\beta \sim 0.02$. The corresponding values of the specific angular momentum are four orders of magnitude larger than the actual specific angular momentum of the solar system: this is the well-known angular momentum issue in star formation. A significant amount of angular momentum has to be extracted during the star formation process. Goodman et al. (1993) also found that β is roughly constant along a

[1] Density n in units cm^{-3} gives the number of particle per cubic centimeter. $n = \rho/\mu m_{\rm H}$, where $\mu = 2.375$ is the typical mean molecular weight for the molecular gas, with molecular hydrogen, helium and heavy elements mass fractions $X = 0.7$, $Y = 0.28$ and $Z = 0.02$.

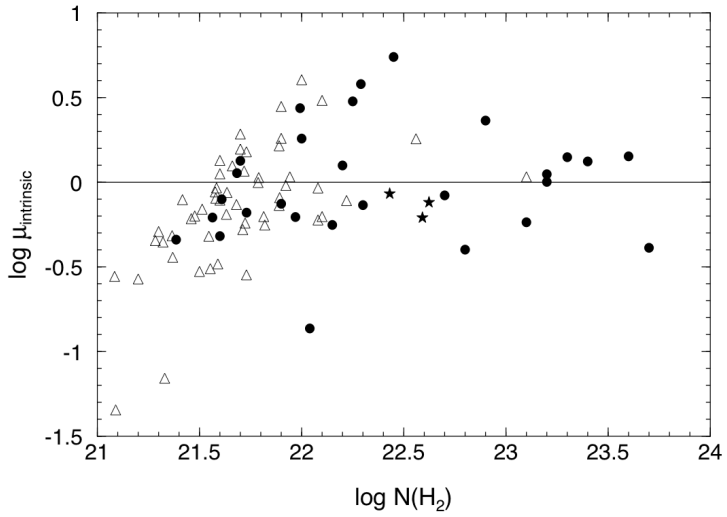

Figure 1.4: Plot of observed mass-to-flux ratios as a function of the column density. Taken from Heiles and Crutcher (2005).

cylindrical radius (solid body rotation).

1.3.3 Magnetic field structure

The magnetic field is present in the interstellar medium on all scales. Magnetic field is observed using two techniques: measurement of the Zeeman effect and maps of linearly polarized dust emission at submillimeter wavelengths. Magnetic fields measurements are then expressed in terms of mass-to-flux ratio (the core mass divided by the magnetic flux) over critical mass-to-flux ratio μ, at which the core is supported against self-gravity by the magnetic field. In supercritical cores, this ratio exceeds 1 and the collapse can proceed. Figure 1.4 shows observed mass-to-flux ratios corrected for projections effects, normalized by the critical mass-to-flux ratio, as a function of the column density (Heiles and Crutcher 2005). Values in all cloud cores are scattered around the critical mass-to-flux ratio, suggesting that cores are close to be magnetically supported. This could imply that magnetic field is a dominant process for the formation of the prestellar cores, and also for isolated star formation. However, these results remain quite controversial in the community.

1.4 Theory

Recent reviews on the theoretical work done on star formation are compiled in Larson (2003), Klein et al. (2007), McKee and Ostriker (2007), Larson (2007), André et al. (2008) and Klessen et al. (2009). In this section, I briefly review some of the theoretical works that have helped to built my background knowledge in the isolated low mass star formation field. Some interesting studies are unavoidably missing in this non-exhaustive list.

1.4.1 Pioneer studies

Pioneer studies on star formation have been done by Larson (1969), Penston (1969) or Shu (1977), which define two limiting cases for the gravitational collapse of an isothermal sphere. In the Larson-Pentson solution, the cloud has initially a uniform density and the collapse proceeds with a r^{-2} profile. The mass accretion rate onto the star is large and the collapse is highly

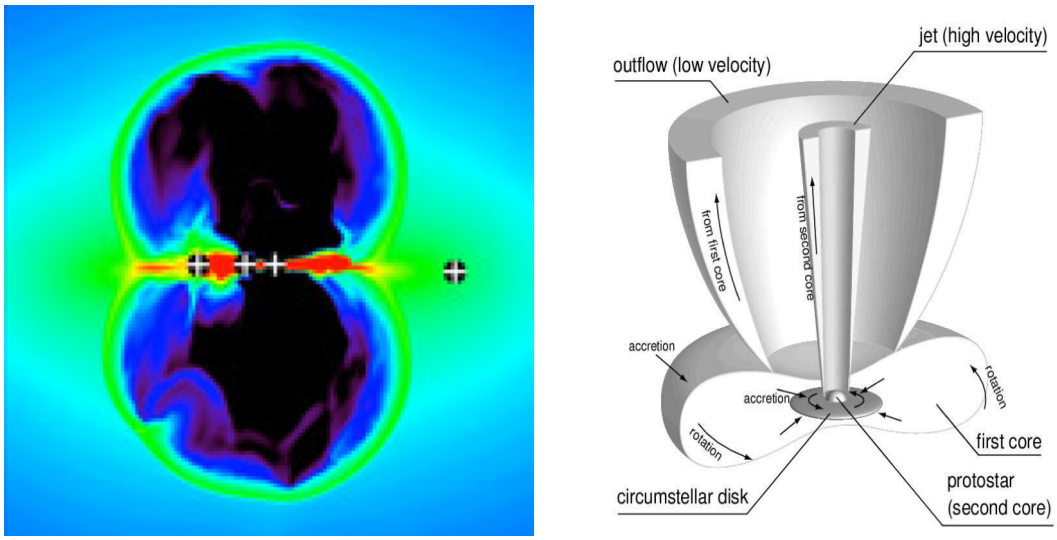

Figure 1.5: *Left:* Radiation-hydrodynamics calculations of massive stars formation, where the radiative pressure exceeds the gravitational force. The star drives gas outward around the polar axis, inflating radiation filled bubbles both above and below the accretion disk. (Krumholz et al. 2009). *Right:* Schematic picture proposed by Machida et al. (2008a) for the jet and outflow driven from the protostar and the first core. Taken from Machida et al. (2008a).

dynamic. In the opposite case, the Shu solution assumes that the evolution of the r^{-2} profile is quasi-static, so that the infall motions are negligible at the moment of protostar formation. Initial conditions are given by the singular isothermal sphere (SIS) configuration, which is the most unstable hydrostatic equilibrium (Chieze 1987). The collapse proceeds from the center outwards at the sound speed (expansion wave): this is the inside-out collapse. The mass accretion rate is constant in time and slow. One finds a more general discussion of the family of self-similar solutions in Whitworth and Summers (1985).

The first multidimensional calculations with rotation have been performed by Larson (1972), Black and Bodenheimer (1975) or Tscharnuter (1975). These isothermal calculations suffer from insufficient numerical resolution. However, these studies showed that even with rotation, isothermal collapse produces a central density singularity. They suggested that the earliest stages of star formation occur in qualitatively the same way even with rotation and magnetic field, provided that these effects do not prevent the initial collapse.

1.4.2 Contemporary trend

A key question posed by observations and not yet answered, is the formation process of binary and multiple systems. Bodenheimer et al. (2000) retain five possible mechanisms: capture, fission, prompt initial fragmentation, disk fragmentation and fragmentation during the protostellar collapse phase. These two last scenarii are the main topic of this work. Fragmentation during protostellar collapse can produce binaries with a wide range of periods. To tackle this issue, a wide variety of idealized initial conditions has been employed. The most famous is the sphere in uniform rotation with a $m = 2$ density perturbation with 10-50% amplitude (Boss and Bodenheimer 1979). After many studies treating the isothermal phase of the collapse (e.g. Bonnell et al. 1991; Truelove et al. 1997), the transition to the optically thick regime has been approximated by a barotropic EOS (Bonnell 1994; Klein 1999), which consists of a change in the EOS from isothermal to adiabatic at a critical density $\sim \rho_{\rm ad} = 1 \times 10^{-13}$ g cm^{-3} (Tohline 1982). Miyama (1992) studied the fragmentation of rotating cores and derived some criteria for

the fragmentation as a function of the polytropic index. Today, it seems established that fragmentation within a collapsing cloud is not expected to occur in the isothermal phase. Tsuribe and Inutsuka (1999) develop a semi-analytic model that supports this result.

Another key issue is the question of how stars acquire their final mass. Over the past several years, two dominant models have emerged: the Direct Gravitational Collapse and the Competitive Accretion. The Direct Gravitational collapse theory suggests that star forming turbulent clouds fragment into cores that eventually collapse to make individual stars or small multiple systems (Hennebelle and Chabrier 2008, 2009; Padoan and Nordlund 2004). In contrast, the Competitive Accretion theory suggests that at birth, all stars are much smaller than the typical stellar mass and the final stellar mass is determined by the subsequent accretion of unbound gas from the clump (Bate and Bonnell 2005; Bonnell et al. 1998; Klessen et al. 1998). The debate on the validity of the two scenarii remains open.

1.4.3 Up to date computational star formation: a brief state of the art

Numerical calculations are nowadays the most widely used tools for the theoretical study of star formation. Thanks to the permanent increase of the computing power, models integrate a lot of physical processes, such as magnetic field and radiative transfer. Stamatellos et al. (2007), Attwood et al. (2009) use an hybrid method that integrates a simple model for the radiative transfer in Smoothed Particle Hydrodynamics (SPH) calculations. Attwood et al. (2009) show that an accurate description of the cooling and heating processes allows more fragmentation in the absence of radiative feedback from protostars. Price and Bate (2007) present an original method that integrates ideal magneto-hydrodynamics (MHD) equations in their SPH code and find that the extra support due to magnetic field reduces the tendency of molecular cloud cores to fragment. Whitehouse and Bate (2006) present the results of calculations studying the collapse of molecular cloud cores performed using a SPH code with radiative transfer in the flux-limited diffusion approximation. Price and Bate (2009) combine these two methods and perform the first star cluster formation calculations with both radiative feedback and magnetic field. They find that radiative transfer and magnetic field significantly reduce the fragmentation process. Radiative transfer acts more at small scales (up to 5000 AU), whereas magnetic field inhibits fragmentation at larger scales. Using a nested grid code, Machida et al. (2007, 2008a) perform calculations modeling MHD equations with resistivity terms (ambipolar diffusion and Ohmic dissipation), without radiative transfer, the thermal behaviour of the gas being modeled with a barotropic EOS. They find that two distinct flows are driven by the first and second core (see right panel of figure 1.5). They propose that the low-velocity flow from the first core corresponds to observed molecular outflow, while the high-velocity flow from the protostar corresponds to observed optical jets. Machida et al. (2008b) explore the parameters space and derive some criteria for the fragmentation of the first or second cores according to the initial rotation of the core and to the strength of the magnetic field. Hennebelle and Fromang (2008) use the AMR code RAMSES (Teyssier 2002), that integrates the ideal MHD equations and a barotropic EOS, and find that the outflow emerging from the first core can be launched independently from the high velocity jet launching. In a companion paper focused on fragmentation, Hennebelle and Teyssier (2008) find that magnetic field, taken at observational values, inhibits the fragmentation of the first core. Banerjee and Pudritz (2006) use the FLASH code with ideal MHD and a cooling/heating function for the radiative transfer and study the collapse of rotating, magnetized Bonnor-Ebert spheres. They find that a large scale outflow is driven by toroidal magnetic pressure, whereas the jet is powered by magnetocentrifugal force. Eventually, Krumholz et al. (2007b, 2009); Offner et al. (2009) use the ORION code, which integrates the radiation hydrodynamics equations with the flux limited diffusion approximation, to study the importance of the radiative feedback from protostars in massive and low mass star formation

calculations. They find that radiative feedback has a great impact in the two cases. For massive star formation, Krumholz et al. (2007b, 2009) find that the gravitational and Rayleigh-Taylor instabilities channel gas onto the star system through nonaxisymmetric disks and filaments that self-shield against radiation while allowing radiation to escape through optically thin bubbles. They show that the radiation pressure does not limit stellar masses, but the instabilities that allow accretion to continue lead to small multiple systems. Offner et al. (2009) demonstrate that radiative feedback has a profound effect on accretion, multiplicity, and mass by reducing the number of stars formed and the total rate at which gas turns into stars. Let us conclude by pointing out that at present time, no grid based method integrates both magnetic field and radiative transfer...

1.5 Gravitational collapse of dense core - Fundamentals

In this section, we derive the fundamental notions commonly used in the star formation field.

1.5.1 Virial theorem

The Virial theorem describes the equilibrium state of self-gravitating structure in the Universe. Consider the simple case of self-gravitating material, without magnetic field and external pressure. For a particle with mass m, position $\mathbf{r}$ and bound to a force $\mathbf{F}$, the Fundamental Principle of Dynamics (Newton's second law) reads

$$m\frac{d^2\mathbf{r}}{dt^2} = \mathbf{F}. \tag{1.1}$$

By multiplying by $\mathbf{r}$, (1.1) becomes:

$$m\frac{d}{dt}\left(\mathbf{r}\cdot\frac{d\mathbf{r}}{dt}\right) = m\left(\frac{d\mathbf{r}}{dt}\right)^2 + \mathbf{F}.\mathbf{r}. \tag{1.2}$$

The quantity $\mathbf{F}.\mathbf{r}$ is called *Virial*. Let us now consider a system of particles with mass m, their inertial momentum I is

$$I = \sum m\mathbf{r}^2,$$

whose second time derivative gives

$$\frac{1}{2}\ddot{I} = \sum m\left(\frac{d\mathbf{r}}{dt}\right)^2 + \sum \mathbf{F}.\mathbf{r}. \tag{1.3}$$

The system's kinetic energy is

$$\mathcal{T} = \frac{1}{2}\sum m\left(\frac{d\mathbf{r}}{dt}\right)^2. \tag{1.4}$$

For a material driven by macroscopic motions, $\mathcal{T}$ is the sum of thermal energy and macroscopic kinetic energy.

The quantity $\sum \mathbf{F}.\mathbf{r}$ in equation (1.3) is the gravitational potential energy Ω of the system. In our simple case, only gravitational force plays a role, thus:

$$\Omega = -\sum_j m_j\mathbf{r}_j\sum_k \frac{Gm_k\left(\mathbf{r}_j-\mathbf{r}_k\right)}{|\mathbf{r}_j-\mathbf{r}_k|^3} - \sum_{j<k}\frac{Gm_jm_k}{|\mathbf{r}_j-\mathbf{r}_k|}, \tag{1.5}$$

for an isolated material or spherical symmetry. Then, according to equation (1.3), the system's dynamic follows

$$\frac{1}{2}\ddot{I} = 2\mathcal{T} + \Omega, \tag{1.6}$$

which means that at equilibrium

$$2\mathcal{T} + \Omega = 0. \tag{1.7}$$

This simple relation expresses the fact that in our simple model, thermal support, i.e. particle motions, balances collapse due to gravitational interaction. It is worth to derive relations giving potential and thermal energies of a uniform density sphere of ideal gas, with mass M, radius R and temperature T

$$\mathcal{T}_{therm} = \frac{3}{2}\frac{MkT}{\mu m_H}, \tag{1.8}$$

and

$$\Omega = -\frac{3}{5}\frac{GM^2}{R}. \tag{1.9}$$

Note also that equation (1.7) gives an instability criterion for an isolated, uniform density and isothermal sphere

$$M > M_{\rm crit} = \left(\frac{1}{\mu m_H}\right)^2 \left(\frac{5}{2}\frac{kT}{G}\right)^{3/2} \left(\frac{4}{3}\pi n\right)^{-1/2}, \tag{1.10}$$

where mass M has been expressed as a function of R and density $n = \rho/\mu m_H$. A cloud is unstable if its mass exceeds the critical mass $M_{\rm crit}$.

1.5.2 Jeans mass and length

Another fundamental point of gravitational collapse theory is the concept of *Jeans length* and by extent of *Jeans mass* due to gravitational instability (Jeans 1902). The Jean length is estimated using a simple linear analysis of the gravitational stability of an infinite and uniform medium. This medium is isothermal, and we do not consider magnetic field and macroscopic motions. For this system, the Euler equations, including source terms due to gravity, are

- Mass conservation

$$\frac{\partial \rho}{\partial t} + \nabla\left(\rho \mathbf{u}\right) = 0 \tag{1.11}$$

- Momentum conservation, with Φ the gravitational potential

$$\frac{\partial \rho \mathbf{u}}{\partial t} + \nabla\left(\rho \mathbf{u} \otimes \mathbf{u} + P\mathbb{I}\right) = -\rho \nabla \Phi \tag{1.12}$$

- Total energy conservation ($E = e + \rho\frac{u^2}{2}$)

$$\frac{\partial E}{\partial t} + \nabla\left[\mathbf{u}\left(E + P + \rho\Phi\right)\right] = -\rho \mathbf{u} \nabla \Phi \tag{1.13}$$

To solve this system, let us introduce the Poisson equation that links the density field to the gravitational field

$$\Delta\Phi = 4\pi\rho G. \tag{1.14}$$

Consider a perturbative development, using index 0 for equilibrium quantities and index 1 for the perturbed quantities. The initial conditions are such that the velocity is zero ($\mathbf{u}_0 = 0$).

$$\left\{\begin{array}{rcl} \mathbf{u} & = & \mathbf{u}_1 \\ \rho & = & \rho_0 + \rho_1 \\ \Phi & = & \Phi_0 + \Phi_1 \end{array}\right. \tag{1.15}$$

We now linearize the Euler system of equations and with the isothermal speed of sound $c_s^2 = P/\rho = kT/\mu m_H$, we have

$$\frac{\partial \mathbf{u}_1}{\partial t} = -\nabla\Phi_1 - \frac{c_s^2}{\rho_0}\nabla\rho_1 \tag{1.16}$$

$$\frac{\partial \rho_1}{\partial t} = -\rho_0 (\nabla \cdot \mathbf{u}_1) \tag{1.17}$$

$$\nabla^2\Phi_1 = 4\pi G\rho_1. \tag{1.18}$$

The divergence of equation (1.16), the temporal derivative of equation (1.17) and the combination of the three previous equations

$$\frac{\partial^2\rho_1}{\partial t^2} = \rho_0\nabla^2\Phi_1 + c_s^2\nabla^2\rho_1. \tag{1.19}$$

Assuming a sinusoidal perturbation of the density field, $\rho_1 = Ke^{i(kx+\omega t)}$, we have the dispersion relation

$$\omega^2 = k^2c_s^2 - 4\pi G\rho_0, \tag{1.20}$$

that links the pulsation ω to the wave number $k = 2\pi/\lambda$. The unstable modes are for $\omega^2 < 0$, then

$$k < k_{\rm J} = \left(\frac{4\pi G\rho_0}{c_s^2}\right)^{1/2}. \tag{1.21}$$

We can then define the Jeans length $\lambda_{\rm J} = 2\pi/k$

$$\lambda_{\rm J} = c_s\left(\frac{\pi}{G\rho_0}\right)^{1/2}, \tag{1.22}$$

and the Jeans mass $M_{\rm J}$

$$M_{\rm J} = \frac{4\pi}{3}\lambda_{\rm J}^3\rho_0. \tag{1.23}$$

The Jeans mass represents the largest mass that is gravitationally stable, and though it is based on some simple assumptions, it is similar to the value obtained with the Virial theorem (1.10). For a uniform temperature, when the density increases, the Jeans mass decreases. A piece of material can thus collapse as long as it remains cold enough to undergo gravitational collapse via the Jeans instability.

It is also interesting to perform the same analysis for a polytropic gas $P \propto \rho^\gamma$. Then, the Jeans mass depends on the value of the polytropic coefficient γ

$$M_{\rm J} \propto \rho^{3/2\gamma-2}. \tag{1.24}$$

We note that there exists a critical value $\gamma_{\rm crit} = 4/3$, above which the gas is thermally supported against self-gravity. When $\gamma > 4/3$, the Jeans mass increases with the density and the cloud stabilizes.

1.5.3 Free-fall time

The third theoretical point is the characteristic collapse time: the free-fall time $t_{\rm ff}$. Let us still consider the simple model of a spherical cloud, with a uniform initial density ρ_0, without magnetic field and rotation (Spitzer 1978). The momentum equation for a shell of radius r and initial radius a reads

$$\frac{d^2r}{dt^2} = -\frac{GM(a)}{r^2} = -\frac{4\pi G\rho_0 a^3}{3r^2}, \tag{1.25}$$

where $M(a)$ is the constant mass contained within the radius a, which does not depend on r. When multiplying equation (1.25) by dr/dt, we have

$$\frac{dr}{dt}\frac{d^2r}{dt^2} = -\frac{4\pi G\rho_0 a^3}{3}\frac{1}{r^2}\frac{dr}{dt}. \tag{1.26}$$

Eventually, the square root of the integral of equation (1.26) reads

$$\frac{1}{a}\frac{dr}{dt} = -\left[\frac{8\pi G\rho_0 a^3}{3}\left(\frac{a}{r}-1\right)\right]^{1/2} \tag{1.27}$$

With $r/a = cos^2\beta$, we have

$$\beta + \frac{1}{2}sin2\beta = t\left(\frac{8\pi G\rho_0 a^3}{3}\right)^{1/2} \tag{1.28}$$

Assuming that β is the same for each shell ta time t and that all the shells reach the center at the same time (when $\beta = \pi/2$), we get the free-fall time $t_{\rm ff}$

$$t_{\rm ff} = \left(\frac{3\pi}{32G\rho_0}\right)^{1/2} \tag{1.29}$$

1.5.4 Effect of rotation and angular momentum conservation

The last fundamental notion that I wish to point out is the conservation of the angular momentum. Let us consider a spherical and non-magnetized cloud of radius R_0, in solid body rotation about the z-axis. Since no external force acts on the cloud, no torque is applied to the cloud and the angular momentum must be conserved. In our model, only the gravity and the thermal pressure forces act and they are both oriented in the radial direction. In this part, we use the cylindrical coordinate system (r, θ, z).
The angular momentum is defined as

$$\mathbf{J} = Rv_\theta = \omega R^2, \tag{1.30}$$

where v_θ is the azimuthal velocity and ω the angular velocity. The angular momentum conservation implies that, at all time

$$\omega(t)R(t)^2 = \omega_0 R_0^2 \tag{1.31}$$

In the collapse process, rotation tends to contrast the gravity. In the equatorial plane, the centrifugal force $Mr\omega^2$ varies with $1/r^3$, whereas the gravitational force GM^2/r^2 varies with $1/r^2$. These two forces compensate in the equatorial plane at a given radius. The cloud cannot contract itself anymore in the equatorial plane. The cloud evolves to a disk of mass $M_{\rm disk}$ of typical radius $R_{\rm disk}$ ($\sim$ 100 AU) given by

$$R_{\rm disk}v_\theta\left(R_{\rm disk}\right) = \left(GM_{\rm disk}R_{\rm disk}\right)^{1/2} = \omega_0 R_0^2. \tag{1.32}$$

1.6 This work

In this manuscript, I present the work I have completed during this thesis. This theoretical work presents numerical developments and results applied to the star formation issue. I focus on the low mass star formation process, studying the collapse and the fragmentation of isolated 1 $M_\odot$ prestellar cores. We tackle the first collapse phase and the first core formation and fragmentation issues, but we do not study the second collapse phase. As I mentioned below, no grid based

code benefits from models that integrate both radiative transfer and magnetic field, in the star formation framework. The development of a numerical tool for the radiation-hydrodynamics in the RAMSES code is the main task I have been working on. In parallel, I have compared three different models for radiative transfer that are used in star formation calculations. A second parallel study has been to compare RAMSES with the SPH code DRAGON from the Cardiff University Star Formation group.

This manuscript is organized as follows

- In chapter 2, I first introduce basic notions and definitions of radiative transfer. Then, I present two moment models, the M1 and the FLD models, that are based on the moments of the radiative transfer equation. Eventually, the coupling between radiation and hydrodynamics is presented and I derive the equations of radiation-hydrodynamics (RHD) in the comoving frame.

- In chapter 3, we use a 1D Lagrangean spherical code to perform collapse calculations of a 1 $M_\odot$ dense core and to compare the FLD and the M1 models in the context of star formation. We show that the FLD approximation gives correct results compared to the more accurate M1 model. We derive the first Larson core properties and compare these RHD results with calculations using a barotropic EOS and with previous studies. In a second stage, we study the properties of the accretion shock on the first core and derive a semi-analytical model for radiative shocks. We combine this semi-analytic model to the well-known self-similar solutions of protostellar collapse to retrieve the jump conditions at the accretion shock.

- Chapter 4 summarizes the numerical developments I have done to integrate the FLD in the RAMSES code for star formation calculations. First, I recall the main features of the RAMSES code. In a second part, I present the RHD solver we have developed for RAMSES. This solver uses a time-splitting scheme, combining the usual explicit scheme for the hydrodynamics and an implicit scheme for the radiative transfer. Then, usual compulsory tests to validate our developments are presented. Eventually, I present the first multidimensional RHD calculations we have done to validate our method for protostellar collapse calculations.

- In chapter 5, a comparison between RAMSES and the SPH DRAGON code is presented. We look at the impact of the numerical resolution and of various numerical tricks on protostellar collapse calculations. Assuming simple initial conditions, we study the angular momentum conservation in each code. Then we study the fragmentation process for three test cases. We derive numerical resolution criteria that are required to get a convergence between these two methods.

- In chapter 6, we present original radiation-magneto-hydrodynamics collapse calculations using the RAMSES code. We first study the influence of the radiative transfer on the fragmentation and compare results with those obtained with a barotropic EOS. Then, magnetic field is added under the ideal MHD approximation. We perform collapse calculations of strongly and weakly magnetized dense cores and look at the influence of the radiative transfer. Then, we introduce sink particles that model accretion and radiation of protostars and study the impact of the radiative feedback from these protostars on our results.

- Eventually, I summarize and recall the main results of this work. I also give some future applications and prospects that will follow this work.

Chapter 2
Radiative transfer

Contents

Radiative transfer plays a fundamental role in contemporary astrophysics, but it is not straightforward to incorporate it to dynamical calculations. In most numerical studies of gas dynamics, simple assumptions are often made in order to overcome the difficulty to model the coupling between radiation and matter. The radiative transfer is crudely reproduced in most numerical studies of protostellar collapse thanks to a barotropic equation of state. In this chapter, the basics of radiative transfer and radiation hydrodynamics are introduced. After a description of the radiative transfer equation, we derive the moment equations appropriate for modeling the radiative transfer. In the last part, the coupling between radiative transfer and hydrodynamics is presented.

2.1 Radiative transfer

2.1.1 Definitions

The *specific intensity* I is the fundamental concept in astrophysical radiation transport and provides a complete description of the radiation field. The specific intensity $I(\mathbf{x}, t; \mathbf{n}, \nu)$ is a function of space (3 spatial coordinates and 2 angles coordinates), radiation frequency and time. Spatial coordinates $\mathbf{x}$ specify the location of the intensity measurement and angle coordinates the direction of radiation propagation defined by $\mathbf{n}$. The intensity is expressed in power unit, i.e. in cgs units: erg cm^{-2} s^{-1} Hz^{-1} sr^{-1}. From a microscopic point of view, the radiation field is composed of massless, extreme-relativistic particles, the photons.

Radiation energy density

The spectral energy density E_ν at frequency ν is defined as the number density of photons at that frequency, integrated over all solid angles, times their energy $h\nu$. It corresponds to the specific intensity integrated over all directions for the radiation, weighted by $d\Omega$, i.e. the total radiation energy density E_ν per bandwidth in the spectrum

$$E_\nu = \frac{1}{c} \int_{4\pi} I_\nu d\Omega. \tag{2.1}$$

The total radiation energy density is

$$E_\mathrm{r} = E_\mathrm{r}(\mathbf{x}, t) = \int_0^\infty E(\mathbf{x}, t; \nu) d\nu, \tag{2.2}$$

whose dimensions are erg cm^{-3}. The radiation energy corresponds to the zeroth angular moment of the specific intensity.

Radiation flux

The first moment of the intensity is the radiation flux $\mathbf{F}_\nu = \mathbf{F}(\mathbf{x}, t; \nu)$. It defines a vector, such that $\mathbf{F}_\nu . d\mathbf{S}$ gives the net rate of spectral radiation energy flow across $d\mathbf{S}$

$$\mathbf{F}_\nu = \int_{4\pi} \mathbf{n} I_\nu d\Omega, \tag{2.3}$$

where $\mathbf{n}$ is a unit vector that defines the direction of propagation. The total radiation flux is

$$\mathbf{F}_\mathrm{r} = \mathbf{F}_\mathrm{r}(\mathbf{x}, t) = \int_0^\infty \mathbf{F}(\mathbf{x}, t; \nu) d\nu. \tag{2.4}$$

Note that the ratio of $\mathbf{F}_\nu$ to E_ν is the "fluid velocity" of the radiation. It is then evident that it cannot be larger than the speed of light c.

Radiation pressure tensor

The second angular moment of the intensity is the radiation pressure tensor $\mathbb{P}$ or P^{ij}. It defines the net rate of transport, per unit area of a surface oriented perpendicular to the j^th coordinate axis, of the i^th component of momentum

$$\mathbb{P}_\nu = \mathbb{P}(\mathbf{x}, t; \nu) = \frac{1}{c} \int_{4\pi} \mathbf{n}\mathbf{n} I_\nu d\Omega. \tag{2.5}$$

$\mathbb{P}_\nu$ is symmetric and has dimensions of dyne cm^{-2} Hz^{-1}. From equation (2.5), we see that

$$\mathrm{Tr}(\mathbb{P})_\nu = E_\nu. \tag{2.6}$$

It is also useful to define the dimensionless ratio χ_ν that determines the Eddington tensor $\mathbb{D}$

$$\mathbb{D}(\chi_\nu) = \mathbb{P}(\mathbf{x}, t; \nu) / E(\mathbf{x}, t; \nu), \tag{2.7}$$

which is known as the variable Eddington factor and gives a measure of the anisotropy of the radiation field. χ_ν ranges from 1/3 in optically thick medium to 1 in the transport regime.

The Eddington tensor must be defined by a closure relation for the system of moments of the radiation transfer equation, like, for example, the ideal gas relation for material particles.

Deep inside an opaque material all directions look the same, the radiation field is said to be isotropic. The pressure tensor becomes a diagonal tensor, diagonal elements should be all the same and off-diagonal elements vanish. The pressure tensor is therefore

$$\mathbb{P}_\nu = P_\nu \mathbb{I}, \tag{2.8}$$

then, the trace is

$$\mathrm{Tr}(\mathbb{P}_\nu) = 3P_\nu. \tag{2.9}$$

Thus we get

$$\mathbb{P}_\nu = \frac{1}{3} E_\nu \mathbb{I}, \tag{2.10}$$

that is the Eddington approximation. This relation corresponds to a relation between the pressure and the energy density of an ideal gas with heat capacity ratio $\gamma = 4/3$. Radiation is then a $\gamma = 4/3$ ideal gas when photons mean free paths are short enough that transport effects are small and that an equilibrium distribution is obtained.

Last, the total radiation pressure is

$$\mathrm{P_r} = \mathrm{P_r}(\mathbf{x}, t) = \int_0^\infty \mathbb{P}(\mathbf{x}, t; \nu) d\nu. \tag{2.11}$$

2.1.2 The radiative transfer equation

Absorption, emission and scattering

We consider how matter and radiation interact via absorption, emission and scattering processes.

First, when a beam of radiation passes through a material, energy is removed from the beam because of the material's opacity. This loss is described by the extinction coefficient $\chi(\mathbf{x}, t; \mathbf{n}, \nu)$, defined by Mihalas and Mihalas (1984) such that "an element of material of length dl and cross section dS, oriented normal to a beam of radiation having specific intensity $I(\mathbf{x}, t; \mathbf{n}, \nu)$ propagating along $\mathbf{n}$ into solid angle $d\omega$ in frequency band $d\nu$, removes an amount of energy

$$\delta E = \chi(\mathbf{x}, t; \mathbf{n}, \nu) I(\mathbf{x}, t; \mathbf{n}, \nu)\, dl\, dS\, d\omega\, d\nu\, dt, \tag{2.12}$$

from the beam in a time interval dt". χ_ν is expressed in cm^{-1} and the quantity $\lambda_\nu = 1/\chi_\nu$ is the *mean free path* of photons of frequency ν in the material.

The *emission coefficient* $\eta(\mathbf{x}, t; \mathbf{n}, \nu)$ is defined such that an element of material of length dl and cross section dS, emits an amount of energy in the direction $\mathbf{n}$ into the solid angle $d\omega$ in the frequency band $d\nu$

$$\delta E = \eta(\mathbf{x}, t; \mathbf{n}, \nu)\, dl\, dS\, d\omega\, d\nu\, dt. \tag{2.13}$$

The dimensions of η are erg $\mathrm{cm}^{-3}\mathrm{s}^{-1}\mathrm{Hz}^{-1}\mathrm{sr}^{-1}$.

Last, it is important to distinguish between *true* or *thermal* absorption-emission processes and the process of *scattering* (see Mihalas and Mihalas 1984). It is thus convenient to define a thermal absorption coefficient $\kappa(\mathbf{x}, t; \mathbf{n}, \nu)$ and a scattering coefficient $\sigma(\mathbf{x}, t; \mathbf{n}, \nu)$. The extinction coefficient becomes

$$\chi(\mathbf{x}, t; \mathbf{n}, \nu) = \kappa(\mathbf{x}, t; \mathbf{n}, \nu) + \sigma(\mathbf{x}, t; \mathbf{n}, \nu). \tag{2.14}$$

Similarly, we can break the total emissivity into a thermal and a scattering components

$$\eta(\mathbf{x}, t; \mathbf{n}, \nu) = \eta_{\mathrm{th}}(\mathbf{x}, t; \mathbf{n}, \nu) + \eta_{\mathrm{s}}(\mathbf{x}, t.\mathbf{n}, \nu). \tag{2.15}$$

Note that in this work, scattering will be neglected.

Transport equation

In the absence of absorption-emission and scattering processes, the specific intensity along a beam of radiation does not change. Consider now the radiation energy balance of an element of a radiative beam passing through material of length dl and cross section dS fixed in the laboratory frame. The change in a time Δt in energy of the radiation field at position $\mathbf{x}$ and time t, contained in a frequency interval $d\nu$ traveling into the solid angle $d\omega$ along a direction $\mathbf{n}$ normal to dS as it passes through the element of material must equal the difference between the amount of energy created by emission from the material and the amount absorbed

$$\begin{aligned}[I(\mathbf{x}+\,\mathbf{dl}, t+\Delta t; \mathbf{n}, \nu) \;-\; I(\mathbf{x}, t; \mathbf{n}, \nu)]\; dS\, d\omega\, d\nu\, dt \\ = \;[\eta(\mathbf{x}, t; \mathbf{n}, \nu) - \chi(\mathbf{x}, t; \mathbf{n}, \nu) I(\mathbf{x}, t; \mathbf{n}, \nu)]\; dl\, dS\, d\omega\, d\nu\, dt. \end{aligned} \tag{2.16}$$

Next, we perform a Taylor expansion of I around the point $\mathbf{x}$ and time t

$$I(\mathbf{x} + \Delta\mathbf{x}, t + \Delta t; \mathbf{n}, \nu) = I(\mathbf{x}, t; \mathbf{n}, \nu) + \left[\frac{1}{c}\frac{\partial I}{\partial t} + \frac{\partial I}{\partial l}\right] dl. \tag{2.17}$$

Note that we have $dt = dl/c$ and $\partial/\partial l = \mathbf{n} \cdot \nabla$. We obtain the radiative transfer equation

$$\left[\frac{1}{c}\frac{\partial}{\partial t} + \mathbf{n} \cdot \nabla\right] I(\mathbf{x}, t; \mathbf{n}, \nu) = \eta(\mathbf{x}, t; \mathbf{n}, \nu) - \chi(\mathbf{x}, t; \mathbf{n}, \nu) I(\mathbf{x}, t; \mathbf{n}, \nu). \tag{2.18}$$

The radiative transfer equation naturally has two asymptotic behaviors depending on the opacities. The *diffusion limit* is obtained at high opacity, when matter and radiation are highly coupled and where the photon mean free path is shorter than all typical length of the system. On the contrary, the *transport limit* is reached at low opacity, when photons do no interact with the matter. The photons mean free path is larger than the typical system scale.

Thermal radiation

Assuming thermodynamic equilibrium, the radiation field is described by an isotropic distribution function that depends only on the temperature. This *thermal radiation* is described by the *Planck function* $B_\nu(T) = 4\pi/cE^*(\nu, T)$ that gives the isotropic specific intensity

$$B_\nu(T) = \frac{2h\nu^3}{c^2}(e^{h\nu/kT} - 1)^{-1}, \tag{2.19}$$

where h is the Planck constant, k the Boltzmann constant and c the speed of light in vacuum. This is the so-called *blackbody radiation.*

The integrated energy density for thermal radiation is

$$E^*(T) = \int_0^\infty E^*(\nu, T) d\nu = a_\mathrm{R} T^4, \tag{2.20}$$

where $a_\mathrm{R} = 8\pi^5 k^4/15c^3h^3$. This is known as *Stefan's law.* The frequency integrated Planck function is $B(T) = (a_\mathrm{R}c/4\pi)T^4 = \sigma_\mathrm{R}/\pi T^4$, where $\sigma_\mathrm{R} = a_\mathrm{R}c/4$ is the Stefan-Boltzmann constant. Assuming thermodynamic equilibrium, the thermal emission coefficient becomes

$$\eta_\mathrm{th}(\mathbf{x}, t; \mathbf{n}, \nu) = \kappa(\mathbf{x}, t; \mathbf{n}, \nu) B(\mathbf{x}, t; \mathbf{n}, \nu). \tag{2.21}$$

2.1.3 Optical depth

The concept of optical depth is a well-loved concept in astrophysics. The usual notation of the optical depth is τ. If $\mathbf{x}$ and $\mathbf{x}'$ are two points in the medium separated by $l = |\mathbf{x}' - \mathbf{x}|$, the optical depth between them is

$$\tau_\nu(\mathbf{x}, \mathbf{x}') = \int_0^l \chi(\mathbf{x} + \mathbf{n}s; \mathbf{n}, \nu) ds, \tag{2.22}$$

where ds is a path-length increment, and $\mathbf{n}$ is a unit vector along the straight line ($\mathbf{x}$,$\mathbf{x}'$). Since χ_ν^{-1} is the mean free path of a photon of frequency ν, the optical depth is equal to the number of photon mean free paths between $\mathbf{x}$ and $\mathbf{x}'$. The total optical depth is

$$\tau = \int_0^l \chi ds. \tag{2.23}$$

An optical depth $\tau << 1$ defines optically the thin regions, whereas $\tau >> 1$ defines the optically thick regions. For static spherical media, the optical depth is measured inward along a radius vector.

2.2 Moment Models

2.2.1 Moment equations

The radiative transfer equation has to be integrated over 6 dimensions at each time step. This process is too computationally demanding for multidimensional numerical analysis. Angular moments of the transfer equation can thus be both physically important and mathematically useful in providing a large reduction of the computational cost. However, each evolution equation of a moment of the transfer equation involves the next higher order moment of the intensity. Consequently, as for the kinetic theory of gases, the system must be closed by using an *ad hoc* relation that gives the highest moment as a function of the lower order moments. For radiation transport, the closure theory is usually limited to the two first moments of the transfer equation. To obtain the zeroth-order moment equation, we integrate equation (2.18) over all directions

$$\frac{\partial E_\nu}{\partial t} + \nabla \cdot \mathbf{F}_\nu = \oint_{4\pi} [\eta(\mathbf{x}, t; \mathbf{n}, \nu) - \chi(\mathbf{x}, t; \mathbf{n}, \nu) I(\mathbf{x}, t; \mathbf{n}, \nu)] d\Omega. \tag{2.24}$$

Assuming that emission coefficient is isotropic, we have

$$\frac{\partial E_\nu}{\partial t} + \nabla \cdot \mathbf{F}_\nu = 4\pi\eta_\nu - \chi_\nu c E_\nu, \tag{2.25}$$

where $\eta_\nu = \eta(\mathbf{x}, t; \nu)$ and $\chi_\nu = \chi(\mathbf{x}, t; \nu)$. Similarly, we get the first-order moment equation

$$\frac{1}{c}\frac{\partial \mathbf{F}_\nu}{\partial t} + c\nabla \cdot \mathbb{P}_\nu = -\chi_\nu \mathbf{F}_\nu. \tag{2.26}$$

Assuming local thermodynamic equilibrium and that diffusion is always isotropic, we have (Gonzáles 2006)

$$\frac{\partial E_\nu}{\partial t} + \nabla \cdot \mathbf{F}_\nu = \kappa_\nu (4\pi B_\nu - c E_\nu), \tag{2.27}$$

and

$$\frac{1}{c}\frac{\partial \mathbf{F}_\nu}{\partial t} + c\nabla \cdot \mathbb{P}_\nu = -\kappa_\nu \mathbf{F}_\nu. \tag{2.28}$$

In this work, we consider only the simplified case of *grey material*, where all frequency dependent quantities are integrated over frequency. As a matter of fact, we cannot use a frequency dependent model for our purpose because of the CPU limitation. In the particular case of grey material, source terms of equations (2.27) and (2.28) becomes

$$\int_0^\infty \kappa_\nu (4\pi B_\nu - cE_\nu) d\nu = c(\kappa_{\mathrm{P}} a_{\mathrm{R}} T^4 - \kappa_{\mathrm{E}} E_{\mathrm{r}}), \tag{2.29}$$

and

$$\int_0^\infty \kappa_\nu \mathbf{F}_{\mathrm{r}} d\nu = \kappa_{\mathrm{F}} \mathbf{F}_{\mathrm{r}}, \tag{2.30}$$

where T is the gas temperature and κ_{P}, κ_{E} and κ_{P} are the Planck-, energy- and flux-mean of absorption coefficient κ_ν, defined by

$$\kappa_{\mathrm{P}} = \frac{\int_0^\infty \kappa_\nu B_\nu d\nu}{\int_0^\infty B_\nu d\nu}, \tag{2.31}$$

$$\kappa_{\mathrm{E}} = \frac{\int_0^\infty \kappa_\nu E_{\mathrm{r},\nu} d\nu}{\int_0^\infty E_{\mathrm{r},\nu} d\nu}, \tag{2.32}$$

$$\kappa_{\mathrm{F}} = \frac{\int_0^\infty \kappa_\nu \mathbf{F}_{\mathrm{r},\nu} d\nu}{\int_0^\infty \mathbf{F}_{\mathrm{r},\nu} d\nu}. \tag{2.33}$$

Note that these are linear means that favor high absorption bands in the spectra. In practice, we assume that radiation and matter have the spectrum of a blackbody, so that $E_\nu = B_\nu(T)$. We thus have

$$\kappa_{\mathrm{E}} = \kappa_{\mathrm{P}}. \tag{2.34}$$

κ_{P} is a good representative of the opacity to be used in the radiation energy equation. On the other hand, if κ_{P} is used in the first moment equations, it does not yield the correct flux in the diffusion limit. This is the main problem of using mean opacity for which we must find a proper way to compute mean opacity. Last, $c^{-1}\kappa_{\mathrm{F}}\mathbf{F}_{\mathrm{r}}$ is the radiation force per unit volume on the material.

As mentioned earlier, we need a closure relation to solve the moments equation system, and this relation is of prime importance. Many possible choices for the closure relation exist. In the following, we present two models based on more or less accurate closure relations, that we will use in this work.

2.2.2 The Flux Limited Diffusion approximation

The diffusion approximation is by far the most approximate and used moment model of radiation transport. The diffusion limit is valid when the photon mean free path is small compared with other length scales in the system. On the contrary, the approximation is no longer accurate in the transport regime. In the diffusion limit, photons diffuse through the material in a random walk. Readers can find a more accurate derivation of the diffusion limit in Mihalas and Mihalas (1984), §80.

In the diffusion limit, we suppose that $\partial_t \mathbf{F} = 0$ (stationary) . This is a valid assumption since the time required for photons to diffuse over a distance l, $\Delta t \sim l^2/\lambda_\nu c$, is very high. Equation (2.28) becomes

$$c\nabla \cdot \mathbb{P}_\nu = -\kappa_\nu \mathbf{F}_\nu. \tag{2.35}$$

Since the radiation pressure is isotropic in the diffusion limit, we have $\mathbb{P}_\mathrm{r} = E_\mathrm{r}/3\mathbb{I}$ (Eddington approximation). Then, the equation on the radiative flux simply reduces to

$$\mathbf{F}_\nu = -\frac{c}{3\kappa_\nu}\nabla E_\nu. \tag{2.36}$$

The radiative flux is expressed directly as a function of the radiative energy and is proportional and colinear to the radiative energy gradient. Integrating (2.36) over frequency, we find

$$\mathbf{F}_\mathrm{r} = \int_0^\infty \mathbf{F}_\nu, \tag{2.37}$$

$$= -\int_0^\infty \frac{c}{3\kappa_\nu}\nabla B(\nu,T)d\nu, \tag{2.38}$$

$$= -\frac{c}{3\kappa_\mathrm{R}}\int_0^\infty \nabla B(\nu,T)d\nu, \tag{2.39}$$

$$= -\frac{c}{3\kappa_\mathrm{R}}\nabla E_\mathrm{r}, \tag{2.40}$$

where κ_R is the *Rosseland mean opacity*, defined by

$$\frac{1}{\kappa_\mathrm{R}} = \frac{\int_0^\infty \kappa_\nu^{-1}\frac{\partial B_\nu(T)}{\partial T}d\nu}{\int_0^\infty \frac{\partial B_\nu(T)}{\partial T}d\nu}. \tag{2.41}$$

This is a harmonic mean, that gives greatest weight to the most transparent regions of the spectrum.

Equation (2.40) has no constraining upper limit, but for optically thin flows, the effective propagation speed of the radiation must be limited to c ($\mathrm{F} \leq cE_\mathrm{r}$). We thus have to limit the propagation speed of the radiation by means of a flux limiter. Equation (2.40) is then expressed as

$$\mathbf{F}_\nu = -\frac{c\lambda}{\kappa_\nu}\nabla E_\nu, \tag{2.42}$$

where $\lambda = \lambda(R)$ is the flux limiter. Levermore (1984) showed that the flux limiter λ and the Eddington factor χ are implicitly linked through

$$\chi = \lambda + \lambda^2 R^2, \tag{2.43}$$

with $R = |\nabla E_\mathrm{r}|/(\kappa_\mathrm{R}E_\mathrm{r})$. As $0 \leq \chi \leq 1$, we thus have the property

$$\lambda + \lambda^2 R^2 \leq 1. \tag{2.44}$$

We can now link the χ factor and the flux limiter for various underlying photon distributions. In this study, we will retain two flux limiters which reproduce the two limiting cases (see figure 2.1). The first one has been derived by Minerbo (1978), assuming intensity as a piecewise linear function of solid angle

$$\lambda = \begin{cases} 2/(3+\sqrt{9+12R^2}) & \text{if} \quad 0 \leq R \leq 3/2, \\ (1+R+\sqrt{1+2R})^{-1} & \text{if} \quad 3/2 < R \leq \infty. \end{cases} \tag{2.45}$$

Levermore and Pomraning (1981), using a Chapman-Enskog approach, obtained the flux limiter

$$\lambda = (1/R)[\coth R - 1/R]. \tag{2.46}$$

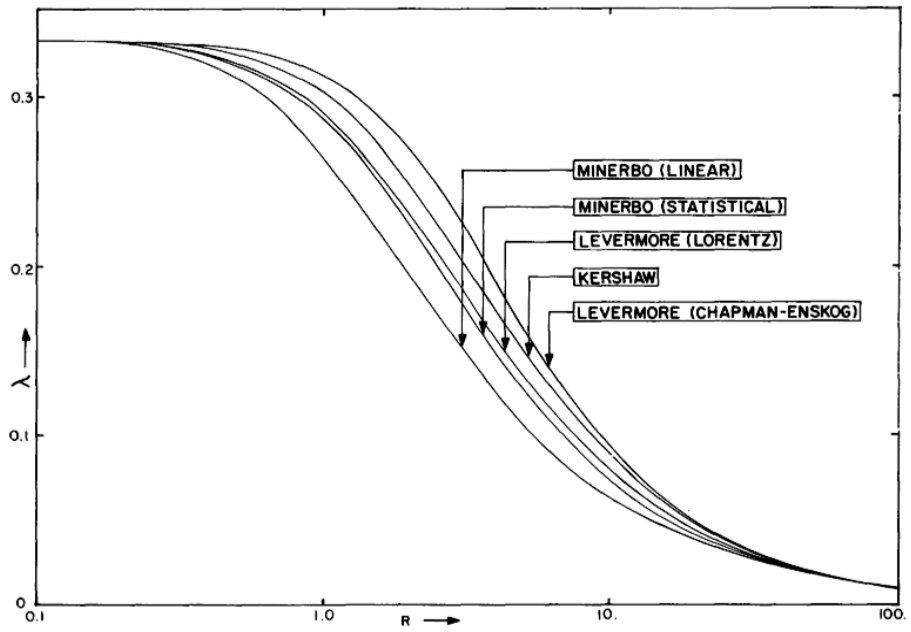

Figure 2.1: Run of flux limiter λ as a function of R for various photon distribution model. Taken from Levermore (1984).

In both cases, the flux limiter has the property that $\lambda \to 1/3$ in optically thick regions and $\lambda \to 1/R$ in optically thin regions. We recover the proper value for diffusion in optically thick regime, $\mathrm{F} = -c/(3\kappa_\mathrm{R})\nabla E_\mathrm{r}$, and the flux is limited to cE_r in the optically thin regime. We now obtain a unique diffusion equation on the radiative energy

$$\frac{\partial E_\mathrm{r}}{\partial t} - \nabla \cdot \left(\frac{c\lambda}{\kappa_\mathrm{R}} \nabla E_\mathrm{r} \right) = \kappa_\mathrm{P}(4\pi B - cE_\mathrm{r}). \tag{2.47}$$

2.2.3 M1 model

In the M1 model, the radiation is described by the grey moment system of the first two moments of the radiative transfer equation (radiative energy and flux) using a closure relation introduced by Dubroca and Feugeas (1999). Based on a minimum entropy principle, this method is able to account for large anisotropy of the radiation as well as for the correct diffusion limit. The main advantage of the M1 system is that the underlying photon distribution function is not isotropic, but has a preferential direction of propagation. The associated Eddington factor is then a non constant function of the reduced flux $\mathbf{f} = \frac{\mathbf{F}_\mathrm{r}}{cE_\mathrm{r}}$, resulting in a nonlinear hyperbolic system for radiation. This also allows to explicitly get rid off the *ad-hoc* limitation of the flux in the transport regime. However, Levermore (1984) showed that the closure relation of M1-type moment models can be reduced to a flux limited diffusion model.

Let us consider the evolution equations of the zeroth and first moments of the specific intensity in the laboratory frame

$$\left\{ \begin{array}{lcl} \partial_t E_\mathrm{r} + \nabla \cdot \mathbf{F}_\mathrm{r} & = & \kappa_\mathrm{P}(4\pi B - cE_\mathrm{r}) \\ \partial_t \mathbf{F}_\mathrm{r} + c^2 \nabla \cdot \mathbb{P}_\mathrm{r} & = & -\kappa_\mathrm{R} c \mathbf{F}_\mathrm{r} \end{array} \right. , \tag{2.48}$$

where κ_R and κ_P are the Rosseland and Planck mean opacities. Note that we use the Rosseland mean instead of κ_F in the first moment equation in order to yield the diffusion limit. As a

closure relation, the radiative pressure is often expressed as $\mathbb{P}_\mathrm{r} = \mathbb{D}E_\mathrm{r}$ where $\mathbb{D}$ is the Eddington tensor. Assuming that the direction of the radiative flux is an axis of symmetry of the local specific intensity, the Eddington tensor is given by (Levermore 1984)

$$\mathbb{D} = \frac{1-\chi}{2}\mathbb{I} + \frac{3\chi-1}{2}\mathbf{n}\otimes\mathbf{n}, \tag{2.49}$$

where χ is the Eddington factor, $\mathbb{I}$ the identity matrix and $\mathbf{n} = \frac{\mathbf{f}}{f}$ a unit vector aligned with the radiative flux. The Eddington factor χ is then obtained either by applying a Lorentz transform to an isotropic photon distribution (Levermore 1984) or by minimizing the radiative entropy (Dubroca and Feugeas 1999). In both cases, the Eddington factor is found to be

$$\chi = \frac{3+4f^2}{5+2\sqrt{4-3f^2}}. \tag{2.50}$$

It is then trivial to recover the two asymptotic regimes of radiative transfer. When $f \to 0$, $\chi = 1/3$ and $\mathbb{P}_\mathrm{r} = 1/3E_\mathrm{r}\mathbb{I}$ which corresponds to the diffusion limit with an isotropic radiative pressure. On the other hand, if $f = 1$, $\chi = 1$ and $\mathbb{P}_\mathrm{r} = \mathbf{n}\otimes\mathbf{n}E_\mathrm{r}$, which corresponds to the free-streaming limit. Moreover, in between these two limits, the closure relation ensures that energy remains positive and that the flux is limited ($\mathbf{F}_\mathrm{r} < cE_\mathrm{r}$).

2.3 Coupling with hydrodynamics

2.3.1 Which frame?

The next step consists of coupling the radiative equations to the hydrodynamic equations. The coupling is not straightforward, since we must take into account *Doppler shifts* or *aberration* effects due to fluid velocity. In the previous equations, sink terms describing matter/radiation interactions are estimated in the *comoving* frame, moving with the fluid, in which material properties are isotropic. On the other hand, radiative quantities are estimated in the *laboratory* frame. We must then choose between these two frames to write the proper equations of radiation hydrodynamics. In the laboratory frame, the left hand side terms are unchanged, but source terms become complex since we must take into account Doppler shifts and aberrations if velocity gradients are present in the flow, which is virtually always the case in astrophysics (Mihalas and Auer 2001). On the contrary, in the comoving frame, source terms are unchanged and additional terms appear on the right hand side (e.g. Lowrie et al. 2001).

In this work, we chose the *comoving frame* picture since it is only in this frame that opacities have the values specified by atomic physics. For instance, when the photorecombination process results in the emission of photons, the emission will be isotropic only in the comoving frame.

In order to write the radiative transfer equation in different frames, we must determine the Lorentz transformation properties of specific intensity, opacity, emissivity and photon directions and energies. Photons being relativistic particles, we have to deal with relativistic kinematics. We consider the position four-vector $(x^\mu) = (t, \mathbf{r})$, where index μ runs from 0 to 3, with the 0 value designating the time component and 1, 2 and 3 designating the space components. If a particle moves from $(t, \mathbf{r})$ to $(t + dt, \mathbf{r} + d\mathbf{r})$ in the (relative) time dt, then the amount of proper time elapsed in its own frame is

$$ds^2 = dt^2 - \frac{d\mathbf{r}^2}{c^2}. \tag{2.51}$$

Then, the particle's four-velocity is

$$\left(\frac{dx^\mu}{ds}\right) = \frac{dt}{ds}(1, \mathbf{r}) = (\gamma, \gamma\mathbf{v}), \tag{2.52}$$

where $\gamma = 1/\sqrt{1-(v/c)^2}$ is the Lorentz factor. The particle's four-momentum is

$$(p^\mu) = \left(m\frac{dx^\mu}{ds}\right) = (m\gamma, m\gamma\mathbf{v}) = \frac{h\nu}{c^2}(1, \mathbf{n}c), \tag{2.53}$$

where m is the rest mass of particles defined by $m\gamma = h\nu/c^2$ and $\mathbf{n}$ the direction of propagation.

We now consider the Lorentz transformation from one set of coordinates $(x^\mu_{(0)})$ to the (x^μ) set, such that a point with fixed $\mathbf{r}_0$ is moving with the velocity $\mathbf{u}$ in the $(\mathbf{r}, t)$ coordinates

$$x^\mu = A^\mu_\lambda x^\lambda_{(0)}, \tag{2.54}$$

where

$$A^\mu_\lambda = \begin{pmatrix} \gamma & \gamma\mathbf{u}^{\mathrm{T}}/c^2 \\ \gamma\mathbf{u} & \mathbb{I} + (\gamma-1)\mathbf{u}\mathbf{u}^{\mathrm{T}}/u^2 \end{pmatrix}. \tag{2.55}$$

Note that the 3×3 matrix in the lower right-hand corner is arranged to leave unchanged a vector perpendicular to $\mathbf{u}$ and to multiply by γ one that is parallel to $\mathbf{u}$.

The Lorentz transformation leaves the proper time ds unchanged in the transformation, so the four-velocity and four-momentum transformations are the same as for the coordinates

$$\frac{dx^\mu}{ds} = A^\mu_\lambda \frac{x^\lambda_{(0)}}{ds}, \tag{2.56}$$

and

$$(p^\mu) = A^\mu_\lambda p^\lambda_{(0)}. \tag{2.57}$$

We can now apply this transformation to a photon and get the Doppler shift and aberration relations

$$\nu = \nu_0\gamma\left(1 + \frac{\mathbf{n}_{(0)}\cdot\mathbf{u}}{c}\right), \tag{2.58}$$

$$\mathbf{r} = \frac{\gamma\mathbf{u}/c + \mathbf{n}_{(0)} + (\gamma-1)(\mathbf{n}_{(0)}\cdot\mathbf{u}\mathbf{u})/u^2}{\gamma(1+\mathbf{n}_{(0)}\cdot\mathbf{u})/c}. \tag{2.59}$$

We now seek an expression for the *radiation stress energy tensor* $\mathbb{T}$, the spacetime generalization of the radiation stress tensor $\mathbb{P}_{\mathrm{r}}$. This tensor is defined by

$$\mathbb{T}^{\lambda\mu} = \int \frac{d^3\mathbf{p}}{E} p\lambda^\lambda p^\mu \mathcal{I}, \tag{2.60}$$

where $\mathcal{I} = I_\nu/(2h\nu^3/c^2)$ is the Lorentz invariant intensity that corresponds to the number of photons per mode (see Castor 2004) and $d^3\mathbf{p} = \frac{h^3\nu^2}{c^3}d\nu d\Omega$, the quantity $d^3\mathbf{p}/E$ being also a Lorentz invariant. We have

$$\mathbb{T}^{\lambda\mu} = \frac{h^3}{2c^4}\begin{pmatrix} E_{\mathrm{r}} & \mathbf{F}_{\mathrm{r}}^{\mathrm{T}} \\ \mathbf{F}_{\mathrm{r}} & c^2\mathbb{P}_{\mathrm{r}} \end{pmatrix}. \tag{2.61}$$

We can then use the Lorentz transformation matrix A to obtain $\mathbb{T}$ components in the laboratory frame from those in the comoving frame, by multiplying it by one factor A from the left and one from the right. At first order $\mathcal{O}(u/c)$ we get

$$E_{\mathrm{r}} = E_{\mathrm{r},0} + 2/c^2\mathbf{u}\cdot\mathbf{F}_{\mathrm{r},0}, \tag{2.62}$$

$$\mathbf{F}_{\mathrm{r}} = \mathbf{F}_{\mathrm{r},0} + \mathbf{u}E_{\mathrm{r},0} + \mathbf{u}\cdot\mathbb{P}_{\mathrm{r},0}, \tag{2.63}$$

$$\mathbb{P}_{\mathrm{r}} = \mathbb{P}_{\mathrm{r},0} + 1/c^2(\mathbf{u}\mathbf{F}^{\mathrm{T}}_{\mathrm{r},0} + \mathbf{F}^{\mathrm{T}}_{\mathrm{r},0}\mathbf{u}). \tag{2.64}$$

We can now rewrite moment equations with radiative quantities estimated in the comoving frame, retaining only $\mathcal{O}(u/c)$ terms and terms of important relative size (Mihalas and Mihalas 1984)

$$\left\{\begin{array}{rcrcrcl} \partial_t E_{\rm r} & + & \nabla\cdot[\mathbf{u}E_{\rm r}] & + & \nabla\cdot\mathbf{F}_{\rm r} & + & \mathbb{P}_{\rm r}:\nabla\mathbf{u} = \kappa_{\rm P}(a_{\rm R}T^4 - E_{\rm r}) \\ \partial_t \mathbf{F}_{\rm r} & + & \nabla\cdot[\mathbf{u}\mathbf{F}_{\rm r}] & + & c^2\nabla\cdot\mathbb{P}_{\rm r} & + & (\mathbf{F}_{\rm r}\cdot\nabla)\mathbf{u} = -\kappa_{\rm F}c\mathbf{F}_{\rm r}. \end{array}\right. \tag{2.65}$$

The terms $\nabla\cdot[\mathbf{u}E_{\rm r}]$ and $\nabla\cdot[\mathbf{u}\mathbf{F}_{\rm r}]$ correspond to the advection of radiative energy and radiative flux and the term $\mathbb{P}_{\rm r}:\nabla\mathbf{u}$ corresponds to the work done by radiative pressure. Note that in this work, we do not take into account additional terms that are necessary for the set of equations to be accurate at $\mathcal{O}(v/c)$ in optically thin regions with high gradients.

2.3.2 Radiation Hydrodynamics equations in the comoving frame

We consider the equations governing the evolution of an inviscid, radiating fluid, with source terms due to gravity

$$\left\{\begin{array}{rcrcl} \partial_t\rho & + & \nabla[\rho\mathbf{u}] & = & 0 \\ \partial_t\rho\mathbf{u} & + & \nabla[\rho\mathbf{u}\otimes\mathbf{u} + P\mathbb{I}] & = & -\rho\nabla\Phi + \kappa_{\rm R}\mathbf{F}_{\rm r}/c \\ \partial_t E & + & \nabla[\mathbf{u}(E+P)] & = & -\rho\mathbf{u}\cdot\nabla\Phi + \kappa_{\rm R}\mathbf{F}_{\rm r}/c\cdot\mathbf{u} - \kappa_{\rm P}(4\pi B - cE_{\rm r}) \\ \partial_t E_{\rm r} & + & \nabla[\mathbf{u}E_{\rm r}] & = & -\nabla\cdot\mathbf{F}_{\rm r} - \mathbb{P}_{\rm r}:\nabla\mathbf{u} + \kappa_{\rm P}(4\pi B - cE_{\rm r}) \\ \partial_t\mathbf{F}_{\rm r} & + & \nabla[\mathbf{u}\mathbf{F}_{\rm r}] & = & -c^2\nabla\cdot\mathbb{P}_{\rm r} - (\mathbf{F}_{\rm r}\cdot\nabla)\,\mathbf{u} - \kappa_{\rm R}c\mathbf{F}_{\rm r}. \end{array}\right. \tag{2.66}$$

where ρ is the material density, $\mathbf{u}$ is the velocity, P the isotropic thermal pressure, Φ the gravitational potential and E the fluid total energy $E = \rho\varepsilon + 1/2\rho u^2$. We see that the term $\kappa_{\rm R}\mathbf{F}_{\rm r}/c$ acts as a radiative force on the material. The material energy lost by emission is transfered into radiation and radiative energy lost by material absorption is given to the material.

To close this system, we need two closure relations: one for the gas and one for the radiation. In this work, we will only consider a ideal gas closure relation for the material: $P = (\gamma-1)e = \rho k_{\rm B}T/\mu m_{\rm H}$ where γ is the specific heats ratio and $e = \rho c_v T$ is the gas internal energy. For the radiation, we will use either the FLD relation or the M1 closure relation.

The particular case of the Flux Limited Diffusion approximation

The radiative flux is replaced by the gradient of radiative energy times the flux limiter. Radiation hydrodynamics equations in that case simply read

$$\left\{\begin{array}{rcrcl} \partial_t\rho & + & \nabla[\rho\mathbf{u}] & = & 0 \\ \partial_t\rho\mathbf{u} & + & \nabla[\rho\mathbf{u}\otimes\mathbf{u} + P\mathbb{I}] & = & -\rho\nabla\Phi + \lambda\nabla E_{\rm r} \\ \partial_t E & + & \nabla[\mathbf{u}(E+P)] & = & -\rho\mathbf{u}\cdot\nabla\Phi + \lambda\nabla E_{\rm r}\cdot\mathbf{u} - \kappa_{\rm P}(4\pi B - cE_{\rm r}) \\ \partial_t E_{\rm r} & + & \nabla[\mathbf{u}E_{\rm r}] & = & -\mathbb{P}_{\rm r}:\nabla\mathbf{u} + \nabla\cdot\left(\frac{c\lambda}{\kappa_{\rm R}}\nabla E_{\rm r}\right) + \kappa_{\rm P}(4\pi B - cE_{\rm r}). \end{array}\right. \tag{2.67}$$

In the next chapters, we first compare the FLD and the M1 models by applying them into a 1D code with spherical symmetry for protostellar collapse calculations. We will then implement the FLD in a 3D AMR code (RAMSES, Teyssier 2002). We abandoned the M1 model in this multidimensional study for technical reasons, since it introduces two additional equations as well as a non trivial matrix system to invert. We find that the FLD is a good compromise between accuracy and CPU time saving for 3D collapse calculations.

A few words on the mixed frame RHD

Castor (1972) demonstrated that in the comoving frame, an additional advective flux of the radiation enthalpy is not taken into account. In the dynamic diffusion regime, where $\tau >> 1$ and $(v/c)\tau >> 1$, this radiative flux can dominate the diffusion flux, emission or absorption. Krumholz et al. (2007b) proposed a method based on the mixed framed radiation hydrodynamics equations, that was first derived in Mihalas and Klein (1982). In the mixed frame, radiation quantities are written in the inertial lab frame, but fluid quantities and opacities are evaluated in the non-inertial frame moving with the fluid. When radiation quantities are evaluated in the comoving frame, there is a lack in the energy conservation in the radiation-gas energy exchange. This has a non negligible effect in the dynamic diffusion limit. An estimate of the error induced by the comoving frame formalism has to be done in a future work. However, in the low mass star framework, we do not expect to encounter dynamic diffusion situation such as photon bubbles.

Chapter 3
Spherical collapse with radiative transfer

Contents

In this Chapter, we study the influence of the model for radiative transfer on protostellar collapse. Radiation hydrodynamics play here an important role, for instance evacuating the compressional energy to enable isothermal collapse to occur in the free-fall phase. Radiation transfer will also have a dramatic impact on the accretion shock, where the kinetic energy of the free-falling gas is either converted into internal energy in the static adiabatic core or radiated away. The radiative loss has also an important effect and sets the entropy profile of the objects in formation. Using a 1D spherical code, we compare results of calculations done with grey Flux Limited Diffusion, grey M1 model and a barotropic EOS. 1D calculations in spherical geometry

remains the best way to introduce easily more physics into collapse models of dense core, which is not the case in multidimensional calculations. Subsequently, we can have a first guess on whether the effect of the introduced physical processes is important or not. Therefore, we use the 1D tool as a preliminary step, prior to multidimensional studies, to check if the assumptions are reasonable. In the two first sections, we present the opacity models for Rosseland and Planck means and the numerical method we use. In section 3.3, we reproduce results obtained by Masunaga et al. (1998) and derive first Larson core properties. We look at typical properties of collapse, accretion, entropy level of this first core. Then, we focus on the accretion shock in section 3.4. We perform a detailed analysis of the energy balance through the shock and extract some typical value for the emergent luminosity. In the last section, we present an original semi-analytic method that retrieves (and confirms) our numerical results. This study is based on basic assumptions on the flow, combining known auto-similar solutions for the collapse and basic assumptions for radiative shocks.

3.1 Introduction

3.1.1 Previous work

Famous and reference calculations are compiled in the two companion papers Masunaga et al. (1998), that we refer as MMI , and Masunaga and Inutsuka (2000b). In the first study, they focus on the first core formation and its properties using a frequency dependent RHD model, while the second core formation is studied in the second paper. Indeed, no breakthrough or original study has been published in 1D calculations framework since their study.

Let us give a few words about Masunaga et al. numerical techniques. They use a 1D spherical code in the Lagrangean frame, with a higher initial resolution in the region where the accretion shock on the first core will take place. Moment equations of radiation in the comoving frame are solved, following Stone et al. (1992) who dropped the terms of $\mathcal{O}(v/c)$ in all physical regimes, in order to account for all dynamical effects. Moment equations system is closed using a Variable Eddington Tensor Factor (VETF) that retains frequency dependence, whereas grey opacities are used for the coupling of matter and radiation and the work of radiative pressure.

Their initial cores have uniform density and temperature, and a radius adjusted so that the cloud core should be slightly more massive that the Jeans mass. Initial masses range from 0.1 $\mathrm{M}_\odot$ to 3 $\mathrm{M}_\odot$. They find that whatever the initial cloud mass is, the first core radius $R_{\rm fc}$ is almost constant, ~ 5 AU, and the first core mass is $M_{\rm fc} \sim 0.05\ \mathrm{M}_\odot$. $R_{\rm fc}$ is defined as the point where the gas pressure is balanced by the ram pressure of the infalling envelope. Approximating the first core as a polytropic sphere in equilibrium (Lane-Emden equation), they derive the analytical description of $R_{\rm fc}$

$$R_{\rm fc} = 5.3\ \mathrm{AU} \left(\frac{\rho_{\rm c}}{10^{-9}\ \mathrm{g\,cm^{-3}}}\right)^{-1/6} \left(\frac{T_{\rm init}}{10\,\mathrm{K}}\right)^{1/2} \left(\frac{\rho_{\rm ad}}{10^{-13}\ \mathrm{g\,cm^{-3}}}\right)^{-1/3}, \tag{3.1}$$

where $\rho_{\rm ad}$ is the critical density at which the core becomes adiabatic (see §3.2.2), $\rho_{\rm c}$ the central density and $T_{\rm init}$ the initial core temperature.

They also derived an analytic expression for the accretion luminosity. The accretion luminosity is usually expressed as

$$L_{\rm fc}^{\rm acc} = \frac{G M_{\rm fc} \dot{M}}{R_{\rm fc}}, \tag{3.2}$$

where $\dot{M}$ is the mass accretion rate and $M_{\rm fc}$ the mass of the accreting object. To derive an analytic estimate of the accretion luminosity, they define $M_{\rm fc}$ as the mass of an equilibrium

polytropic sphere and the accretion rate is generally defined as (e.g. Stahler et al. 1980)

$$\dot{M} = \alpha \frac{c_{s0}^3}{G}, \tag{3.3}$$

where α is a dimensionless coefficient and c_{s0} the isothermal sound speed. α is estimated assuming that a non-magnetic, non-rotating cloud, whose initial state corresponds approximately to thermal support against self-gravity, will have comparable free-fall time ($t_{\rm ff} \sim R_c^{3/2}/(GM_c)^{1/2}$) and sound-crossing time ($t_{\rm sc} \sim R_c/c_{s0}$). Then the mass accretion rate must have the order of magnitude $\dot{M} \sim M_c/t_{\rm ff}$. Shu (1977) found $\alpha = 0.975$ for the expansion-wave solution, whereas $\alpha \sim 50$ for the Larson-Penston solution. They obtain

$$L_{\rm fc}^{\rm acc} = 0.07\ {\rm L}_\odot \left(\frac{\alpha}{10}\right) \left(\frac{\rho_{\rm c}}{10^{-9}\ {\rm g\,cm^{-3}}}\right)^{-1/6} \left(\frac{T_{\rm init}}{10\,{\rm K}}\right)^{1/2} \left(\frac{\rho_{\rm ad}}{10^{-13}\ {\rm g\,cm^{-3}}}\right)^{-1/3}. \tag{3.4}$$

Both analytical estimates are weakly dependent on the initial temperature and on the opacity.

Eventually, MMI present Spectral Energy Distributions (SEDs), whose shape does not reflect the central thermal evolution of collapsing cloud cores throughout the first collapse, because the envelope is opaque. Their luminosity increases up to ~ 0.1 L$_\odot$ at the end of the first collapse. They conclude that dense cloud cores with luminosity higher than 0.1 L$\odot$ possibly have young protostars inside the opaque envelopes.

3.1.2 Numerical method

We use a 1D full Lagrangean version of the code developed by Edouard Audit and Jean-Pierre Chièze (see for a more advanced version Audit et al. 2002) that integrates the equations of grey radiation hydrodynamics under three different assumptions (in increasing complexity order): barotropic equation of state, Flux Limited Diffusion approximation and M1 model. RHD equations are integrated in their non-conservative form using finite volumes and a standard artificial viscosity scheme. For this work, we had to implement the barotropic EOS and the FLD modules. Note that some conventional tests have been performed to validate our implementations of the FLD model but they are not presented in this manuscript. Examples of tests are presented in the next chapter.

Space is discretized into computational zones centered on points r_i according to a logarithmic distribution, grid interfaces being located at $r_{i+1/2}$. In spherical geometry, the volume of a zone is given by $\Delta V_i = \frac{4}{3}\pi(r_{i+1/2}^3 - r_{i-1/2}^3)$. Scalar quantities like density, pressure or energy are estimated in r_i and within ΔV_i. On the contrary, vectors velocity and fluxes are estimated in a staggered mesh, i.e. in $r_{i+1/2}$ and supposed to be constant in $\Delta V_{i+1/2} = \frac{4}{3}\pi(r_{i+1}^3 - r_i^3)$.

For instance, in Lagrangean framework, conservation of mass is integrated as follows

$$\frac{dM}{dt} = \frac{1}{dt}\int \rho dV = \frac{\rho_i^{n+1}\Delta V_i^{n+1} - \rho_i^n \Delta V_i^n}{\Delta t} = 0, \tag{3.5}$$

with volume's variations that are given by

$$\Delta V_i^{n+1} = \frac{4\pi}{3}\left[(r_{i+1/2}^{n+1})^3 - (r_{i-1/2}^{n+1})^3\right]. \tag{3.6}$$

Equation of momentum with source term due to gravity reads

$$\frac{1}{dt}\int \rho v dV = \frac{u_{i+1/2}^{n+1} - u_{i+1/2}^n}{\Delta t}\Delta m_i^{n+1} = [(P_{i+1} + Q_{i+1}) - (P_i + Q_i)]dS_{i+1/2}^{n+1} - \frac{G dm_{i+1/2} M_{i+1/2}}{(r_{i+1/2}^{n+1})^2}, \tag{3.7}$$

with $M_j = \int_0^{r_j^n} \rho dV$, $dm_{j+1/2} = M_{j+1} - M_j$ and $dS_j^{n+1} = 4\pi(r_j^{n/1})^2$. P_i and Q_i stand for the gas pressure and the artificial viscosity tenors. RHD equations are thus discretized and integrated using a fully implicit scheme, unconditionally stable. This enables us to monitor fluid flow and radiative energy exchanges with time step much greater than those given by the CFL condition. According to the model used, various numbers N of equations have to be integrated: 2 for the barotropic case (conservation of mass and momentum), 4 for the FLD (two additional equations on gas and radiative energies) and 5 for the M1 model (an additional equation for the radiative flux). It results a system of N nonlinear equations that can be put in the form

$$F = F(X^{n+1}) = 0, \tag{3.8}$$

with X^{n+1} a vector that contains all RHD variables at time t^{n+1}. System (3.8) is solved using an iterative Raphson-Newton solver, built as follows. First an initial guess of X_0^{n+1} is made using X^n. Then iterations k start assuming that system (3.8) can be rewritten as

$$F(X_k^{n+1}) = F(X_{k-1}^{n+1} + \Delta X_k) = F\left(X_{k-1}^{n+1}\right) + \left(\frac{\partial F}{\partial X}\right)_{X_{k-1}^{n+1}} \Delta X_k = 0, \tag{3.9}$$

with increment ΔX_k given by

$$\Delta X_k = -\left(\frac{\partial F}{\partial t}\right)^{-1}_{X_{k-1}^{n+1}} F(X_{k-1}^{n+1}) \tag{3.10}$$

System (3.10) involves at each iteration a matrix inversion performed using common LU decompositions. Eventually, X_k^{n+1} is simply

$$X_k^{n+1} = X_{k-1}^{n+1} + \Delta X_k. \tag{3.11}$$

Iterations continues until convergence, i.e. $||\Delta X_k||/||X_k^{n+1}|| < \varepsilon$. We use $\varepsilon = 1 \times 10^{-4}$ in our calculations. The maximum number of iterations per time step is set to 50 and in case of non-convergence after 50 iterations, the integration time step is re-estimated in order to reduce RHS variables variations. The implicit time step is computed in order to limit variations of positive quantities to a factor less than 5%.

3.1.3 Initial and boundary conditions

We use the standard model of Masunaga et al. (1998), i.e. a uniform density sphere of mass 1 $M_\odot$, temperature 10 K ($c_{s0} = 0.187$ km s^{-1}) and radius $R = 10^4$ AU. That initial setup corresponds to a ratio α of thermal to gravitational energies of $\alpha \sim 0.97$ (see definition 5.1) and to a free-fall time $t_{ff} \sim 1.77 \times 10^5$ yr. Boundary conditions are very simple: for hydrodynamics, we impose a constant thermal pressure equals to the initial pressure (other quantities are free) and for the radiation field, we impose a vanishing gradient on radiative temperature. Calculations have been performed using a Lagrangean grid containing 4500 cells.

3.2 Assumptions for the radiation field

3.2.1 General assumptions

The first approximation we make is the grey radiation field assumption, i.e. we consider only one group of photons, integrated over all frequencies. The grey approximation is valid when temperature varies spatially on a scale much larger than a mean free path of thermal photon. This is the case in the first stage of the protostellar evolution, except in the close region around the accretion shock.

The second assumption concerns the coupling with hydrodynamics. We write the RHD equations in the comoving frame, which introduces some non-conservative coupling terms. Mixed framed formulation is only effective in the dynamic diffusion limit ($\lambda_{\rm p}/L << 1, v/c \sim 1$) that we will not encounter in our study.

3.2.2 The barotropic equation of state

According to previous studies using accurate model for the radiation field (e.g. Masunaga et al. 1998), it is well established that the molecular gas follows two thermal regimes during the first collapse. At low density, the gas is able to radiate freely and to couple with the dust. This is the isothermal regime, the Jeans mass decreases with the density. Then, when the gas becomes denser, typically $\rho > \rho_c \sim 1 \times 10^{-13}$ g cm^{-3}, the radiation is trapped within the gas that begins to heat in an adiabatic way. The Jeans mass then increases with the density until the gas becomes hot enough to dissociate H_2 and to start the second collapse.

This thermal behavior can be recovered using a barotropic equation of state that reproduces the isothermal and adiabatic regimes as a function of the density. We use the following barotropic equation of state

$$\frac{P}{\rho} = c_{\rm s}^2 = c_{s0}^2 \left[1 + \left(\frac{\rho}{\rho_{\rm ad}} \right)^{2/3} \right], \tag{3.12}$$

where $\rho_{\rm ad}$ is the critical density at which the gas becomes adiabatic. This critical density is obtained by more accurate calculations and depends on the opacities and the composition and the geometry of the molecular gas. At low densities, $\rho \ll \rho_{\rm ad}$, $c_{\rm s} \sim c_{s0} = 0.19$ km s^{-1}, the molecular gas is able to radiate freely by thermally coupling to the dust and remains isothermal at 10 K. At high densities $\rho > \rho_{\rm ad}$, we assume that the cooling due to radiative transfer is trapped by the dust opacity. Therefore, $P \propto \rho^{5/3}$ which corresponds to an adiabatic, monoatomic gas with adiabatic exponent $\gamma = 5/3$. Molecular hydrogen behaves like a monoatomic gas until the temperature reaches several hundred Kelvin. This is because the rotational degrees of freedom are not excited at lower temperatures, and hence $\gamma = 5/3$ is the appropriate adiabatic exponent (Masunaga and Inutsuka 2000a; Whitworth and Clarke 1997).

The barotropic EOS therefore stands for a closure relation of our system, replacing the equation of energy in the Euler system. We then have only to solve the system

$$\left\{ \begin{array}{lcl} \partial_t \rho + \nabla \left[\rho \mathbf{u} \right] & = & 0 \\ \partial_t \rho \mathbf{u} + \nabla \left[\rho \mathbf{u} \otimes \mathbf{u} + P \mathbb{I} \right] & = & -\rho \nabla \Phi. \end{array} \right. \tag{3.13}$$

3.2.3 The opacities

For the M1 model and the FLD approximation, we use the set of opacities given by Semenov et al. (2003) for low temperature (< 1000 K) and Ferguson et al. (2005) for high temperature (> 1000 K), that we compute as a function of the gas temperature and density. For each cell, we perform a bilinear interpolation on the mixed opacities table. In figure 3.2, the table for the Rosseland opacity is plotted as a function of the temperature and the density. Note that for low temperature (< 200 K), the opacity does not depend on the density, and all dust components are present. The first step in the table at T$\sim$ 165K results from ice evaporation. Below 1500 K, opacities are dominated by grain (silicate, iron, troilite, etc..). Between 1500 K and 10 000K, the molecules dominate. At higher temperature, atoms and then Thomson scattering dominates. In Semenov et al. (2003), the dependence of the evaporation temperatures of ice, silicates and iron on gas density are taken into account. In this work, we use spherical composite aggregate

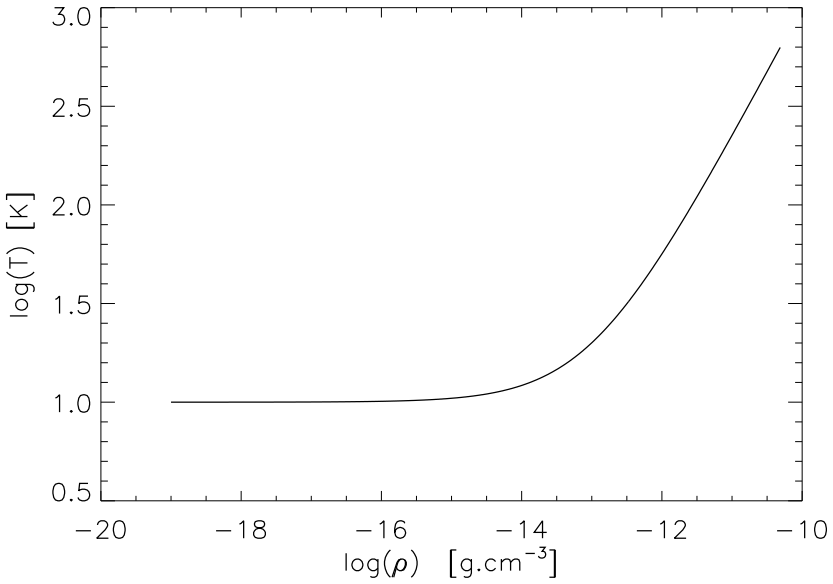

Figure 3.1: Temperature given by the barotropic equation of state as a function of the density. Isothermal and adiabatic regimes are reproduced around the critical density $\rho_{\rm ad}$.

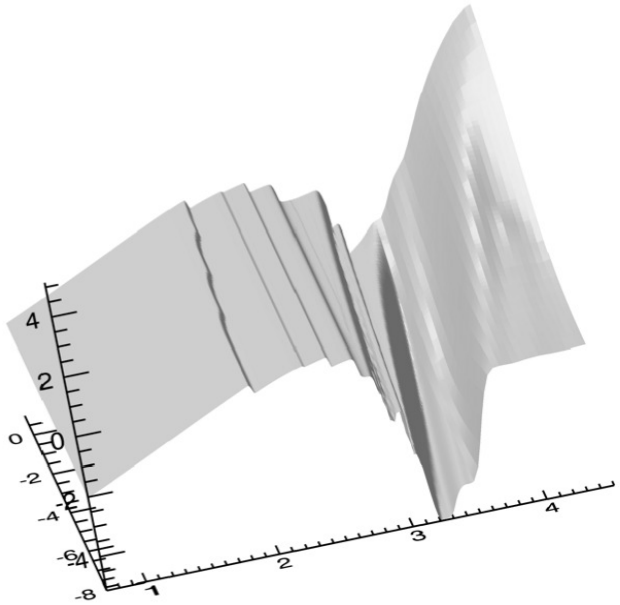

Figure 3.2: Rosseland opacity made of a mix of Semenov et al. (2003) model at low temperature and Ferguson et al. (2005) model at high temperature. Rosseland opacity is plotted as a function of temperature (x-axis) and $R = \rho/(T_6^3)$, with $T_6 = T/10^6$, (y-axis) using logarithm scales.

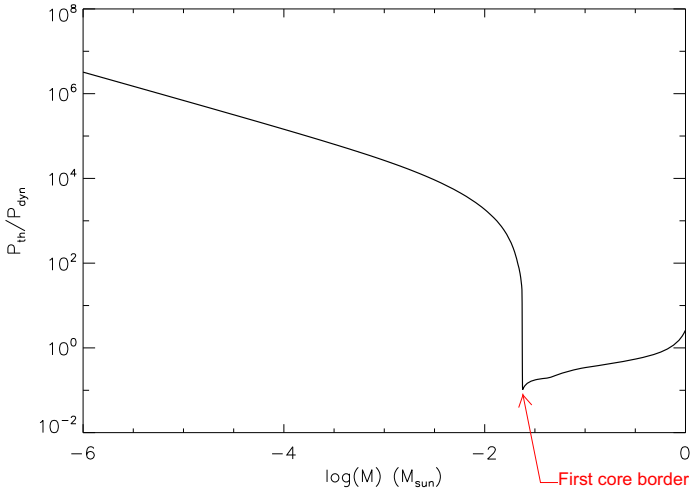

Figure 3.3: Ratio between thermal and dynamic pressure ($\rho u^2/2$) as a function of the integrated mass for M1 calculations. The first core radius is defined where $P_{\rm th}/P_{\rm dyn} = 1$.

particles for the grain structure and topology and a normal iron content in the silicates, Fe/(Fe + Mg)=0.3.

3.3 Results

As we mentioned before, all calculations presented here have been performed with 4500 cells, distributed according to a logarithmic scale in our initial setup. These mass and spatial resolution will appear to be sufficient to resolve the accretion shock structure. Calculations with the barotropic equation of state have been performed using a critical density of $\rho_{\rm ad} = 3.7 \times 10^{-13}$ g cm^{-3}, according to the intersection of extrapolated lines of the isotherm and adiabat in the log(ρ)-log(T) plane, made on RHD calculations results using M1 model.

3.3.1 Results at the center

Table 3.1 gives results of barotropic EOS (Baro), M1 and FLD calculations, when the central density reads $\rho_c = 1 \times 10^{-10}$ g cm^{-3}. Note that for all calculations, dynamical times are very close to ~ 0.189 Myr ~ 1.07 t$_{\rm ff}$. We define the first core radius as the radius at which dynamical pressure $\rho u^2/2$ overtakes thermal pressure (i.e. position of the accretion shock). Figure 3.3 shows the ratio between the two pressures as a function of the mass and two parts are clearly distinguished: the pressure supported core at radius smaller than $R_{\rm fc}$ and a free-falling gas at larger radius than $R_{\rm fc}$. Accretion luminosity is estimated at the first core border, according to equation (3.2). We evaluate the mass accretion rate $\dot{M}$ and the accretion parameter α at $R_{\rm fc}$ (α should not be mixed up with the ratio of initial thermal energy to gravitational energy). The central temperature $T_{\rm c}$ and entropy $S_{\rm c}$ are given, as well as the first core border temperature $T_{\rm fc}$. We compute the entropy assuming a perfect gas with an adiabatic coefficient $\gamma = 5/3$

$$S = \frac{k}{\mu m_{\rm H}(\gamma - 1)} \ln\left(\frac{P}{\rho^\gamma}\right). \tag{3.14}$$

From table 3.1, first core radii and mass are very similar and agree with MMI results. The results from M1 or FLD are also very similar with each other. The central temperature with

Model	$R_{\rm fc}$ (AU)	$M_{\rm fc}$ ($M_\odot$)	$\dot{M}$ ($M_\odot$/yr)	$L_{\rm acc}$ ($L_\odot$)	$T_{\rm c}$ (K)	$T_{\rm fc}$ (K)	$S_{\rm c}$ (erg K^{-1} g^{-1})	α
Baro	5.5	2.33×10^{-2}	2.7×10^{-5}	0.017	551	21	2.03×10^{9}	17
FLD	6.9	2.31×10^{-2}	2.95×10^{-5}	0.015	411	69	2.02×10^{9}	19
M1	6.8	2.31×10^{-2}	2.8×10^{-5}	0.013	419	70	2.02×10^{9}	18

Table 3.1: Summary of first core properties for $\rho_c = 1 \times 10^{-10}$ g cm^{-3}.

FLD is slightly higher ($\sim 2\%$) than the one in the M1 calculations, which could be the first proof of the known fact that diffusion approximation tends to cool more. In comparison with the barotropic EOS, the central entropy for M1 and FLD models is also lower, and this difference increases with time. Indeed energy is radiated away when using a radiative transfer equation, while this is not the case with the barotropic EOS. This leads to a lower entropy level of the first core. The temperature of the border of the first core is higher in the M1 and FLD cases, since photons escaping the accretion shock are flowing backwards and heat up the infalling material. However, the mass accretion rate, the mass, the radius and the α accretion parameter of the first core are in good agreement for all the models we use. α values indicate that our solution is between the expansion wave solution and the Larson-Pentson solution.

Figure 3.4 shows the evolution of the central temperature, central entropy, heating and cooling rates and central optical depth as a function of the central density. From figure 3.4(a), it is worth noticing the perfect two-thermal behavior of the gas (i.e. isothermal-adiabatic). The critical density at which the gas begins to heat up in both M1 and FLD calculations is the same. The difference that we see with the barotropic case comes from our choice for the barotropic EOS and for the critical density. Now, having the results that converge with both grey FLD and M1, we could determine a barotropic EOS that would perfectly fit with our opacity set. For FLD and M1, we find a slope of $\gamma_{\rm eff} - 1 \sim 0.61 < 2/3$ at high density, when temperature increases linearly with density. This means that the first core is not fully adiabatic, but there is a heat loss, which enables a significant cooling.

In figure 3.4(b), the central entropy is plotted as a function of the central density. At high density, we recover the adiabatic regime and M1 and FLD calculations settle at the same entropy level in the center, that is lower than the one reached by the barotropic model. In the barotropic case, entropy is determined by the EOS. The value of the "adiabat" at which the gas settles is

$$S \propto \ln\left(\frac{P}{\rho^\gamma}\right) ==> S \propto \ln\left[\rho^{-2/3} c_{s0}^2 \left(1 + \left(\frac{\rho}{\rho_{\rm ad}}\right)^{2/3}\right)\right] \propto \ln\left(\frac{c_{s0}^2}{\rho_{\rm ad}^{2/3}} + \frac{c_{s0}^2}{\rho^{2/3}}\right). \tag{3.15}$$

Hence, at high density, $S \rightarrow \ln(c_{s0}^2/\rho_{\rm ad})$. The limiting value for the entropy is then $\sim 2.03 \times 10^9$ erg K^{-1} g^{-1} for the barotropic EOS, which is higher than the value obtained with FLD and M1. Moreover, as slope index in figure 3.4(a) does not equal precisely to $\gamma = 5/3$, the gas tends to cool down and to decrease the entropy at a rate $\sim 10^{-3,-4}$ erg K^{-1} g^{-1} s^{-1}. This is one of the immediate consequences of dealing with accurate radiative transfer: the accretion shock becomes a real radiative shock and radiation is transported outward in the core.

We now consider the physical processes that determine the thermal evolution from isothermal to adiabatic regime, i.e. the evolution of the heating, cooling, diffusion and compression rates as a function of the central density. The heating and cooling rates are given by the coupling term in the energy equation, i.e $\kappa_{\rm P}\rho(a_{\rm R}T^4 - E_{\rm r})$, thus, let $\Lambda_{\rm cool} = \kappa_{\rm P}\rho a_{\rm R}T^4$ be the cooling rate

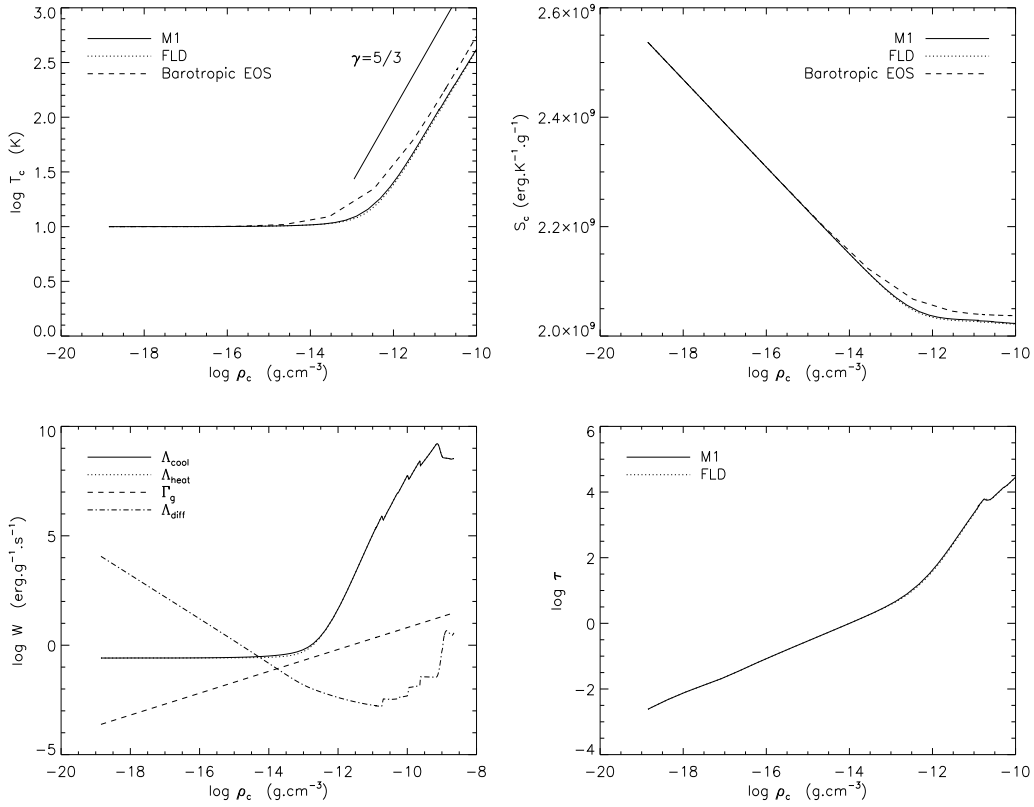

Figure 3.4: (a) *Top-left*: Evolution of the central temperature as a function of the central density. (b) *Top-right*: Evolution of the central entropy as a function of the central density. (c) *Bottom-left*: Runs of the cooling, heating, compressional heating and diffusion rates at the center with the central density for the diffusion case. (d) *Bottom-right*: Evolution of the central optical depth as a function of the central density for the diffusion calculations.

and $\Lambda_{\rm heat} = \kappa_{\rm P}\rho E_{\rm r}$ the heating rate. The compressional heating rate is given by

$$\Gamma_{\rm g} = \frac{P}{\rho}\nabla\cdot\mathbf{u} = -P\frac{d}{dt}\left(\frac{1}{\rho}\right). \tag{3.16}$$

Let us assume that the central density evolves with a dynamical time $\sim 1/\sqrt{4\pi G\rho}$ so that d/dt can be replaced by $C_1(4\pi G\rho^3)^{1/2}(d/d\rho)$ (Larson 1969). Hence

$$\Gamma_{\rm g} = C_1\sqrt{4\pi G\rho}c_{s0}^2 \sim 3.04\rho_{\rm c}^{0.5}(\frac{T_{\rm init}}{10\ {\rm K}}), \tag{3.17}$$

where c_{s0} is the isothermal sound speed at initial temperature and C_1 a constant close to unity ($C_1 = 1.5$ for the Larson-Penston solution). The diffusion rate is given by the ratio $\Lambda_{\rm diff} = (E_{\rm r}/\rho)\tau_{\rm diff}$, with the diffusion time estimated in the optically thick regime as

$$\tau_{\rm diff} = \frac{l^2}{\frac{c}{3\kappa_{\rm R}\rho}}. \tag{3.18}$$

With this definition, the diffusion time is underestimated in optically thin regions. Assuming that the characteristic length l is the local Jeans length, the diffusion rate reads

$$\Lambda_{\rm diff} = \frac{Gck_{\rm B}}{3\gamma\pi\mu m_{\rm H}}\frac{E_{\rm r,c}}{\kappa_{\rm R,c}\rho_{\rm c}T_{\rm c}} \sim 3.6\times10^{-6}E_{\rm r,c}\kappa_{\rm R}^{-1}\rho_{\rm c}^{-1}T_{\rm c}^{-1}. \tag{3.19}$$

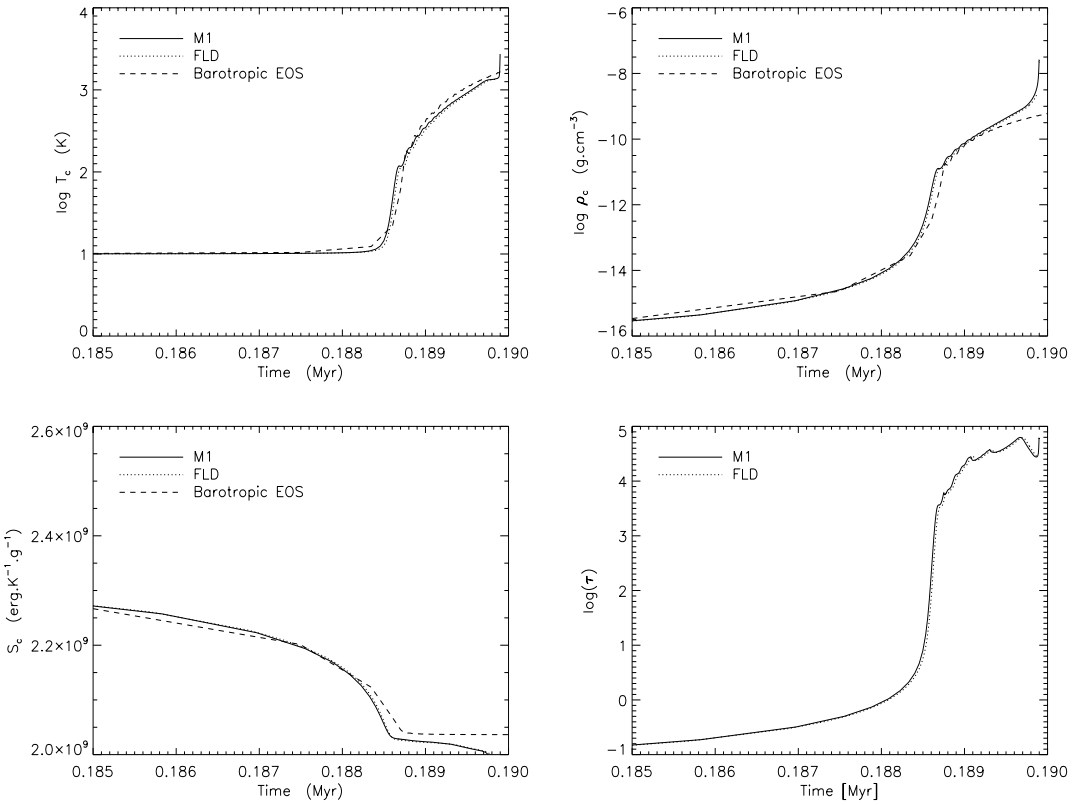

Figure 3.5: Run of central temperature, density, entropy and optical depth with time. FLD and M1 results are in good agreement.

Let us have a look at the condition that violates isothermality in our calculations. We will have a "cross-look" to figures 3.4(c) and (d), which show the evolution of the various rates and of the optical depth at the center as a function of the central density. When the gas begins to collapse, the diffusion time is less than any other cooling or heating times. However, the gas is optically thin (see figure 3.4(d)), thus radiation can escape freely. Moreover, the heating and cooling rates are shorter than the dynamical one (free-fall time), matter and radiation are coupled and the gas remains isothermal. This is the free-fall collapse phase. At higher density ($\rho_c \sim 1 \times 10^{-14}$ g cm^{-3}), the gas begins to heat a little, which corresponds to the turn to the optically thick regime. When the compressional heating rate overtakes the diffusion rate ($\rho_c \sim 3 \times 10^{-14}$ g cm^{-3}), radiation is trapped and the gas enters the adiabatic phase: the first core is born! From this short analysis, it turns out that when the diffusion time equals the compressional heating time, the isothermality is broken. This result is in good agreement with Masunaga and Inutsuka (1999) for low mass star formation, when internal energy of material dominates the radiation energy density. The condition $\tau \sim 1$ does not terminate the isothermal evolution.

Figure 3.5 shows the central temperature, density, entropy and optical depth profiles as a function of time. Variations of all variables are quite similar for temperature lower than T$\sim$ 100 K. At 100 K, we find the first discontinuity in the opacity tables, due to ice destruction. The density can play here a role in the opacity estimate, in the sense that the discontinuity moves to higher temperature when the density increases. However, these differences are really subsidiary. From figure 3.5(c), we clearly see that entropy level remains constant with the barotropic model, whereas the first core keeps up cooling to reach lower entropy level with M1 and FLD. This

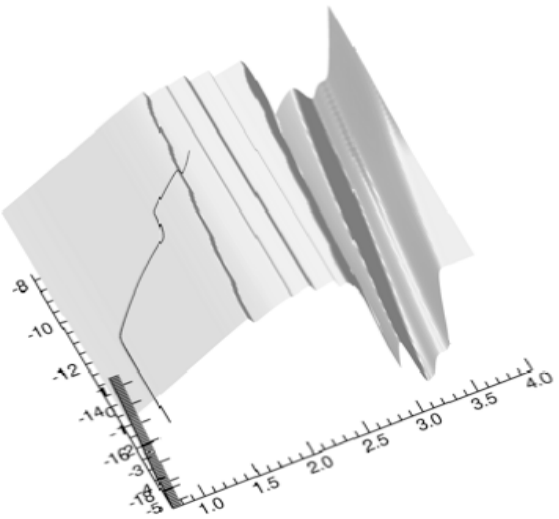

Figure 3.6: Rosseland opacity run as a function of temperature and density for FLD calculations at a given time using Semenov et al. (2003) table.

result is of prime interest, since the entropy level of a low mass protostar determines its pre-main sequence evolution. In figure 3.5(d), we see that the first core quickly becomes optically thick once it begins to heat up. Optical depth at the center is so high that observations are not able to catch the central evolution of the cores at this stage of evolution.

3.3.2 Profile within the prestellar core

First, the run of the Rosseland opacity value using the FLD model, as a function of temperature (x-axis) and density (y-axis) using logarithmic scales, is shown in figure 3.6. We can see the density jump at the accretion shock. In that region, opacity does not depend on the density. At higher density, we reach the first discontinuity in the table due to ice evaporation at ~ 100 K.

In figure 3.7, we plot the profiles of density, gas temperature, velocity, entropy, optical depth, luminosity, radiative flux and integrated mass as a function of the radius, at central density $\rho_c = 1 \times 10^{-10}$ g cm^{-3} for calculations with M1, FLD and the barotropic EOS. As mentioned before, the first core radius is smaller with the barotropic model, whereas both M1 and FLD profiles are similar. For the latter models, we find only small differences around $\tau \sim 1$, i.e. the transition between optically thick and thin regimes. Since the M1 model naturally retrieves diffusion and transport regimes and the FLD model is built in order to respect those two regimes, it is well-founded that we get similar results when either transport or diffusion are well established. Although the accretion shock is located in that transition region, small differences do not affect first core properties. The entropy jump at the accretion shock is much higher with M1 and FLD. We also see from the temperature and entropy profiles that the barotropic EOS cannot deal accurately with the transition from isothermal to adiabatic regime. The radiative precursor in front of the shock is not reproduced with the barotropic EOS, material being immediately isothermal after the shock, whereas it is heated up by photons escaping from the shock in FLD and M1 models. As a consequence, the temperature is higher in the core in the barotropic case. Differences in the behavior of the radiative flux at small radius comes from the differences in temperature between M1 and FLD model. Eventually, we see that the emergent luminosity is the same for both models. The luminosity jump is coherent with the accretion luminosity computed from equation (3.2), i.e. 0.014 $L_\odot$.

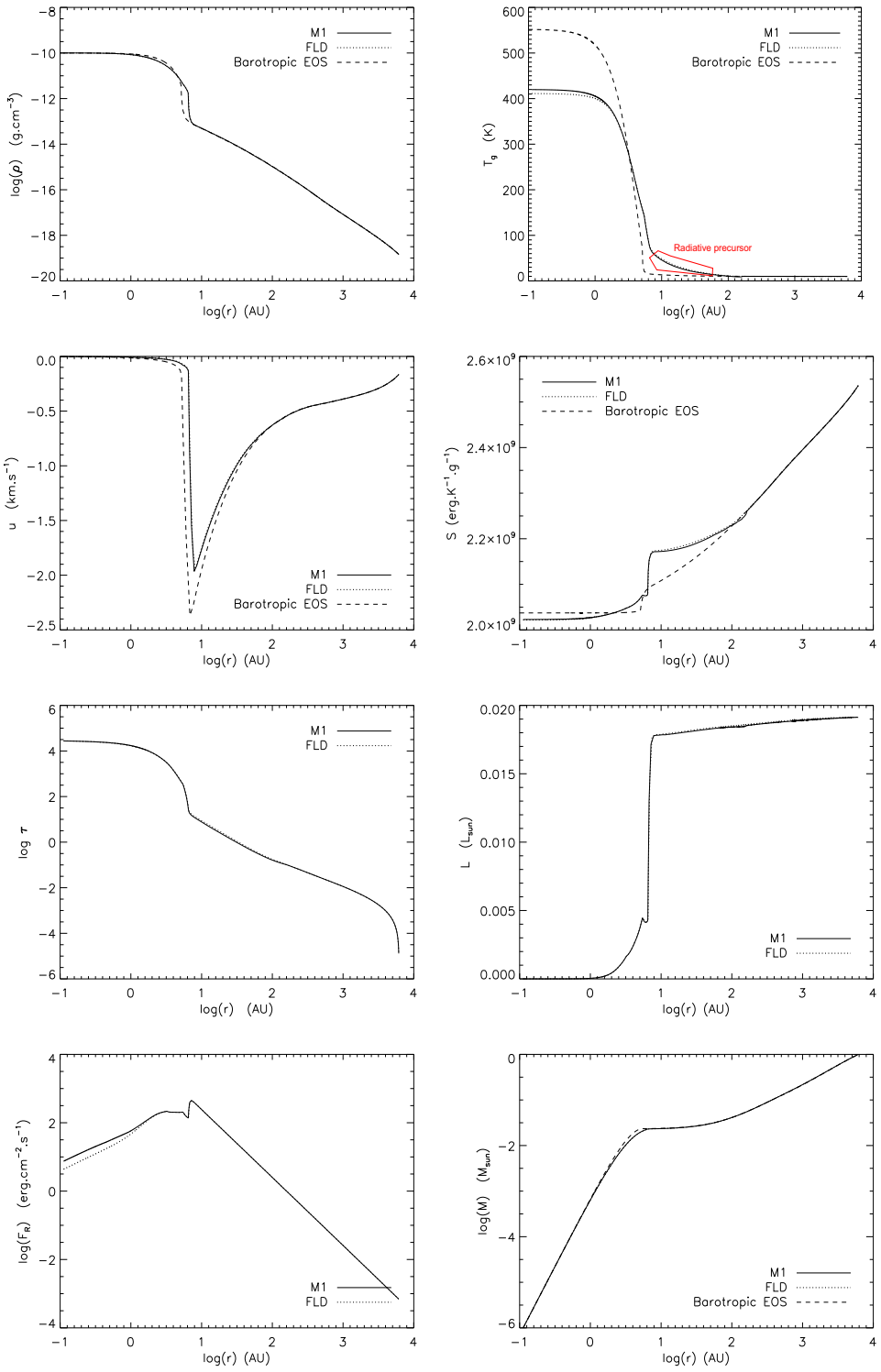

Figure 3.7: Profiles at $\rho_c = 1 \times 10^{-10}$ g cm^{-3} as a function of the radius, for M1, FLD and Barotropic models. The figures depicts (*a*) density, (*b*) gas temperature, (*c*) entropy, (*d*) velocity, (*e*) optical depth, (*f*) luminosity, (*g*) radiative flux and (*h*) integrated mass.

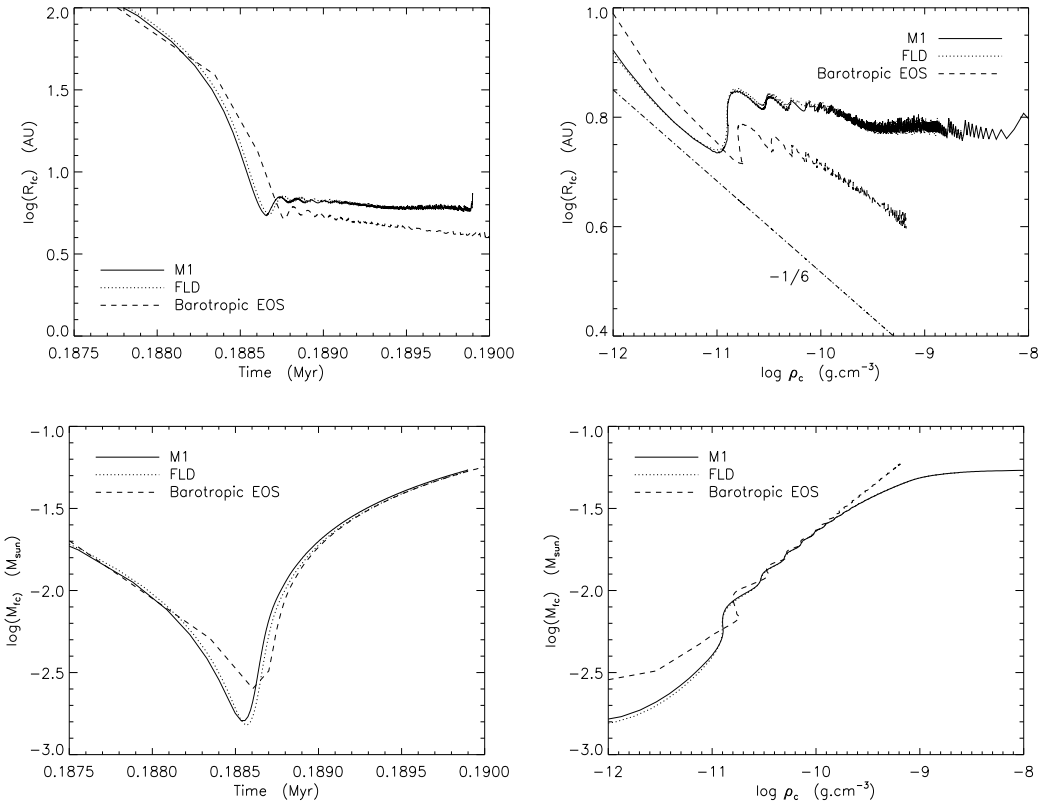

Figure 3.8: First core radius (*top*) and mass (*bottom*) evolutions as a function of time (*left*) and central density (*right*).

3.3.3 First core properties evolution

In this part, we focus on first core properties evolution as a function of time. We recall that the first core border is defined as the radius at which the thermal pressure equals the dynamical pressure. In figure 3.8 we show first core mass, $M_{\rm fc}$, and radius, $R_{\rm fc}$, evolutions as a function of time and of the central density $\rho_{\rm c}$. Note that the first core is formed at time $t \sim 0.1886$ Myr and when $\rho_{\rm c}$ exceeds 10^{-11} g cm^{-3}. The first core radius decreases faster with the barotropic EOS than with M1 and FLD. If we look at the dependence of $R_{\rm fc}$ upon central density, we note that $R_{\rm fc}$ has a weaker slope with M1 and FLD than in the barotropic case, whose slope is closer to analytic predictions of MMI (equation (3.1)). Since the first core is not isentropic and cools down with M1 and FLD, a larger radius is needed to get the thermal support to balance with its own gravity. The first core initial mass depends on the model but it reaches the same value ~ 0.1 M$_\odot$ for all models. We also notice that typical oscillations of the first core decreases at later times.

Figure 3.9 shows the evolution of the luminosity computed from radiation flux ($L = 4\pi r^2 \mathbf{F}_{\rm r}$), the accretion luminosity, the optical depth and the α parameter as a function of the central density. From the luminosity profiles, we note that the luminosity is first dominated by the accretion luminosity ($\rho_{\rm c} < 10^{-9}$ g cm^{-3}). Then, the luminosity increases because of the first core higher temperature. The dependence of the accretion luminosity upon the central density is quite in good agreement with MMI prediction, that gives a 2/3 slope in the log-log plane (see equation 3.4).

The accretion shock is always located in the optically thick region with $\tau > 20$. Finally, we

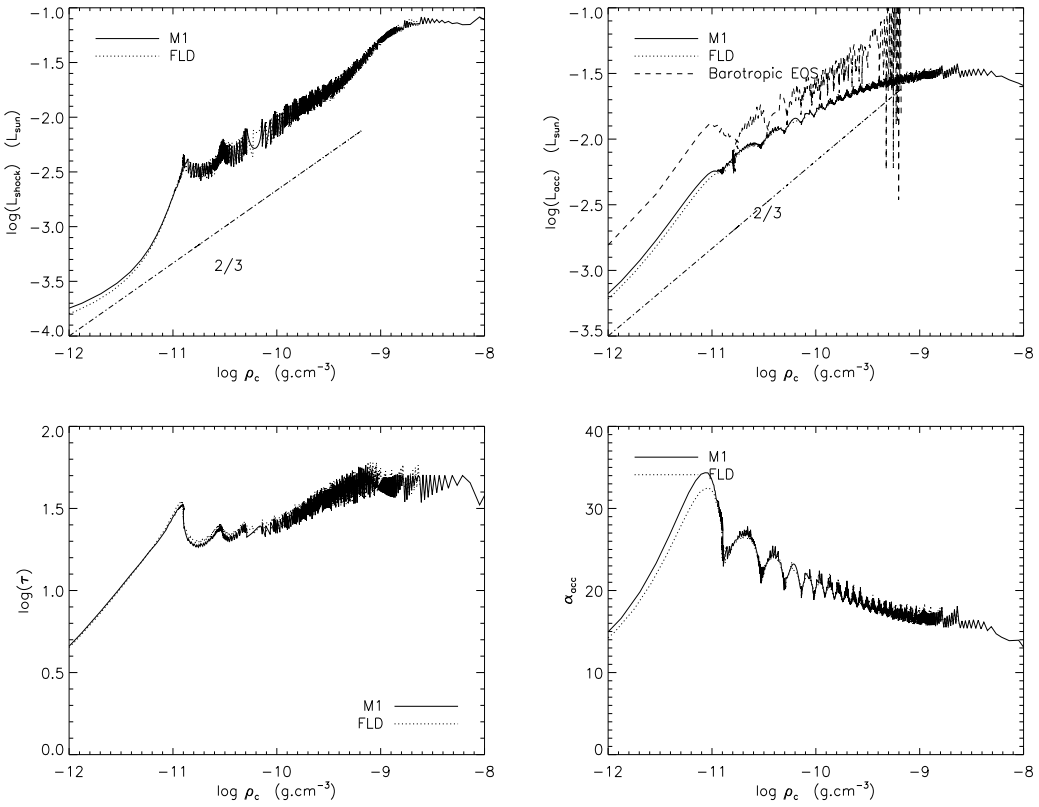

Figure 3.9: *Top*: First core radiative and accretion luminosity evolutions as a function of time and central density. *Bottom*: Optical depth and parameter of accretion α evolutions at the accretion shock as a function of the central density.

find that α values computed from equation (3.3) are decreasing with time and central density, but remains much higher than the value of Shu solution, which is approximately 0.975.

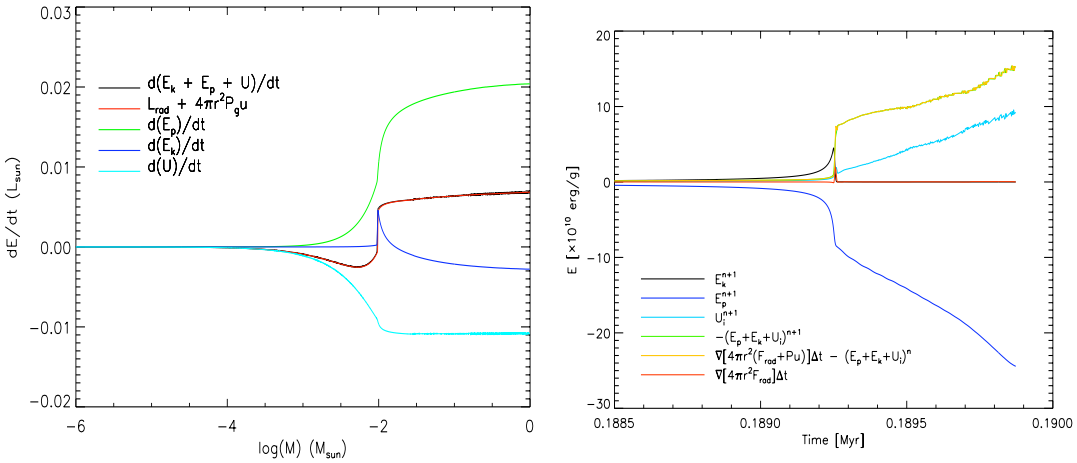

Figure 3.10: (a) - Left: Energy balance at t=0.1888 Myr integrated as a function of the mass. The accretion shock at 10^{-2} $M_\odot$ shows a spike in luminosity as well as strong variation of the kinetic energy. (b) - Right: Energy balance as a function of the time for a piece of fluid that is shocked during the collapse.

3.4 Energy Balance

3.4.1 Basic equations

In this section, we study in detail the energy balance in our calculations. This step is essential to get a first guess of the amount of kinetic energy transferred to the central object (here the first core) through the radiative shock. In the next section, we will tackle the radiative shock issue with some first basic ideas. Let us write the first law of thermodynamics for the radiating fluid (Mihalas and Mihalas 1984)

$$\frac{D}{Dt}\left(e+\frac{E_\mathrm{r}}{\rho}\right)+P\frac{D}{Dt}\left(\frac{1}{\rho}\right)+\left[P_\mathrm{r}\frac{D}{Dt}\left(\frac{1}{\rho}\right)-(3P_\mathrm{r}-E_\mathrm{r})\frac{v}{\rho r}\right]=\varepsilon-\frac{\partial}{\partial M_r}(4\pi r^2F_\mathrm{r}) \tag{3.20}$$

which states that the rate of change of the total energy density in a fluid element plus the rate of work done by the total pressure in the fluid element equals the rate of thermonuclear energy input into the element minus the rate of radiant energy loss by transport. Now, consider the mechanical energy equation for a fluid element

$$\rho\frac{D\frac{1}{2}v^2}{Dt}=-\frac{GM_rv\rho}{r^2}-v\frac{\partial P}{\partial r}+\left(\frac{v}{c}\kappa_\mathrm{R}F_\mathrm{r}\right) \tag{3.21}$$

where $\left(\frac{v}{c}\kappa_\mathrm{R}F_\mathrm{r}\right)$ is the radiative force evaluated in the comoving frame and P is the gas pressure. We can then obtain a total energy equation which includes variations of kinetic, internal, radiative and potential energies. First note that we have: $-(GM_rv)/r^2=D/Dt(GM_r/r)$. Then, after a few substitutions (see §96 in Mihalas and Mihalas 1984) and ignoring second order terms, we get the total energy equation

$$\frac{D}{Dt}\left(e+\frac{E_\mathrm{r}}{\rho}+\frac{1}{2}v^2-\frac{GM_r}{r}\right)+\frac{\partial}{\partial M_r}\left[4\pi r^2[v(P+P_\mathrm{r})+F_\mathrm{r}]\right]=\varepsilon \tag{3.22}$$

This defines the total energy equation of an inviscid fluid whose internal energy density is the sum of the gas and radiation energy densities, and whose pressure equals the sum of the gas and radiation pressure. Note that in our case, we do not take into account thermonuclear processes

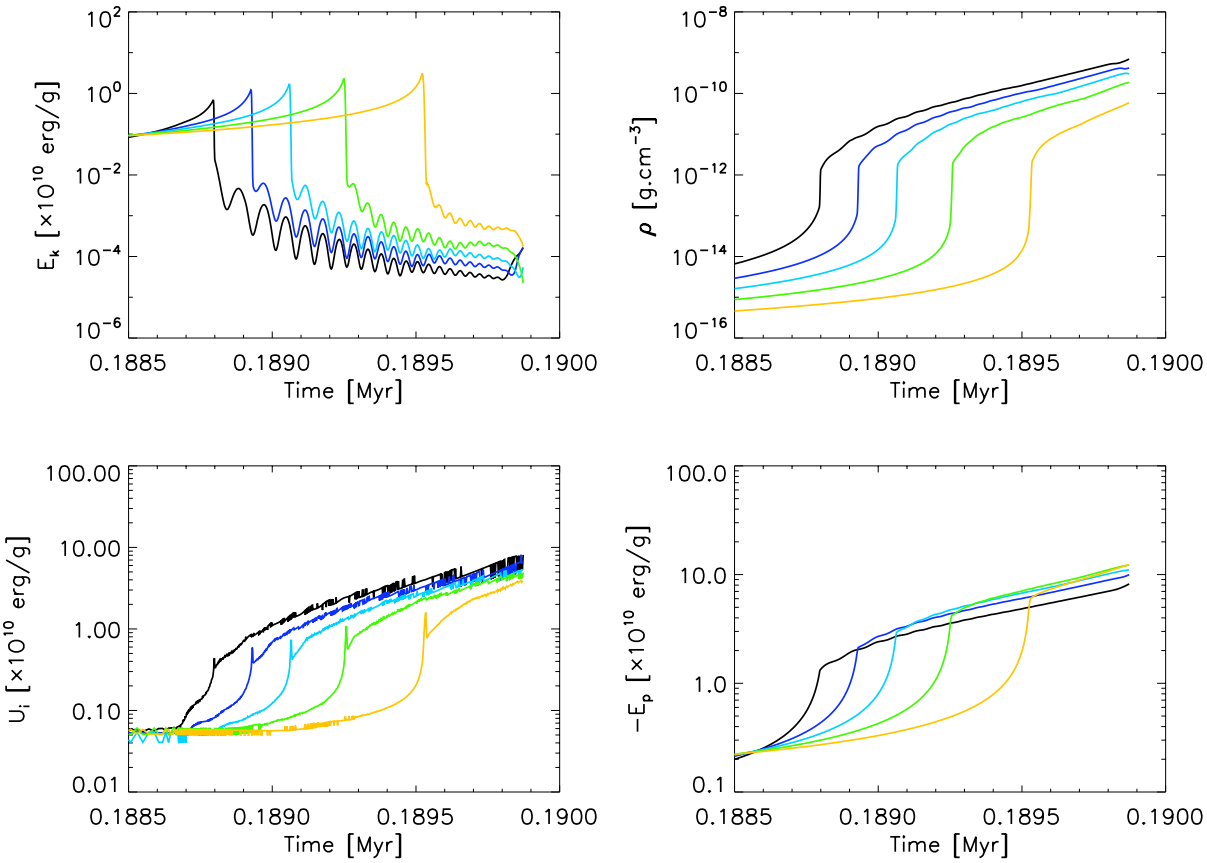

Figure 3.11: Time evolution profiles of the kinetic energy (upper left), density (upper right), internal energy (bottom left) and potential energy (bottom right) for five sets of Lagrangean particles. The accretion shock is revealed in the density profile, when it increases by more than two orders of magnitude. It is also obvious from kinetic energy profile, where all the kinetic energy is removed after the shock.

as for instance deuterium burning, the RHS of equation 3.22 is then equal to zero. Therefore, we will be able to identify the energy exchange through the accretion shock. In the next paragraph, we will study this energy conservation with either an integration in time at a given mass or in space at a given time.

3.4.2 Through the shock?

We plot in figure 3.10(a) the evolution of the mass-integrated energies as a function of the mass at a given times tep according to equation (3.22) for the calculations using the FLD approximation. Radiative energy density has been neglected. Terms $d\mathrm{E_k}$, $d\mathrm{E_p}$ and $d\mathrm{U}$ gives the variations of kinetic, potential and internal energies with time. The integration is performed as follows

$$\int_0^r \left(\frac{dE_\mathrm{k} + dE_\mathrm{p} + dU}{dt} \right) dm = 4\pi r^2 (\mathbf{F}_\mathrm{r} + Pu). \tag{3.23}$$

The luminosity increases discontinuously through the accretion shock, and remains almost constant in the outer envelope, which is optically thin. Note that variations of internal energy

are smooth through the shock, because of photons that escape from the shock to heat the outer gas at the postshock temperature (see figure 3.7). We have a supercritical shock, i.e. the pre- and postshock temperatures are equal. Moreover, if we compare the luminosity and kinetic energy jumps at the accretion shock, we note that they are equal, i.e. all the infalling kinetic energy is radiated away at the accretion shock. This confirms the supercritical nature of the shock. The inner gas is at rest, its kinetic energy equals zero. In figure 3.10(b), we perform the same energy balance, but as a function of the time for a given piece of fluid. Let us explain: we follow a fixed number of Lagrangean cells (typically 5) and compute its various energies at each timestep. Cells are chosen for passing through the accretion shock once the first core has been formed. From figure 3.10(b), we can easily see that most luminosity is produced only in the accretion shock, the first core temperature being too low to have a dominant effective luminosity.

In figure 3.11, we plot energies evolutions as a function of the time for different cells passing through the accretion shock. Potential energy remains continuous through the shock, whereas both kinetic and internal energies are affected by the jump through the shock. All the kinetic energy is removed at the shock, whereas internal energy shows a spike, typical of radiative shocks. Around this spike, the pre and post-shock internal energy are equal. The variations of density through the shock are also plotted in order to have an idea of the density jump across the shock, close to an increase of more than one order of magnitude.

3.4.3 Results for a 0.01 $M_\odot$ cloud collapse

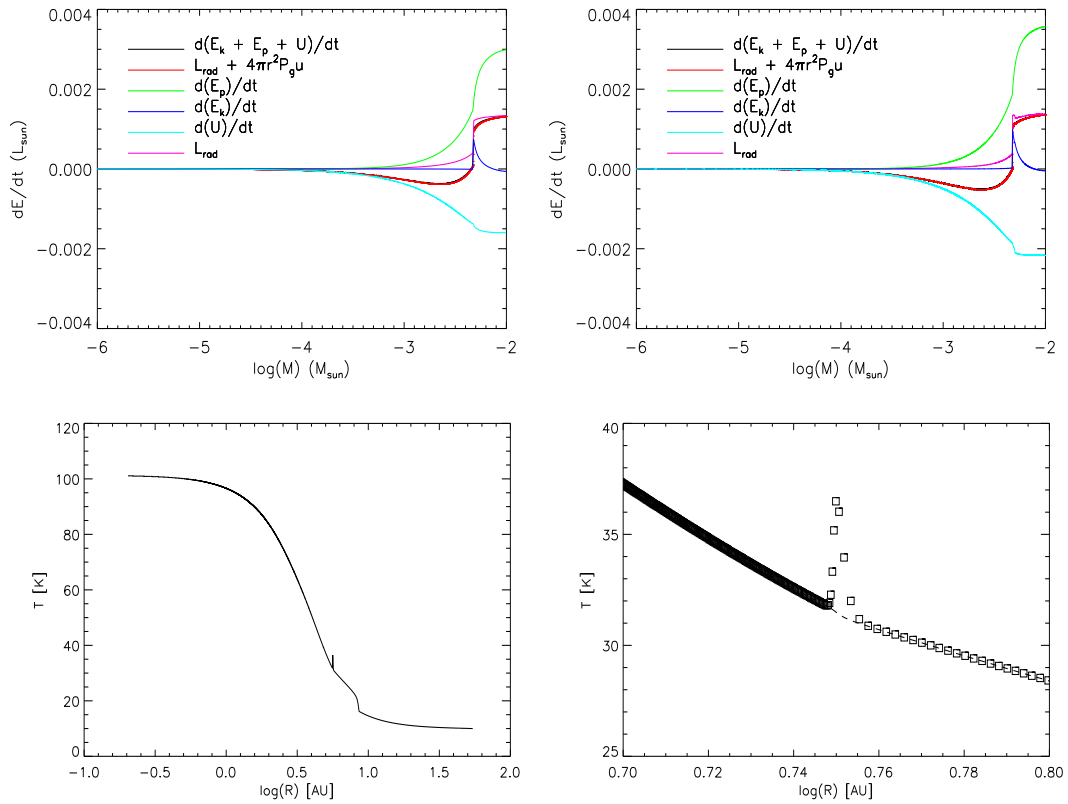

Figure 3.12: *Top:* Energy balance for calculations of the collapse of a 0.01 $M_\odot$ dense core, using 4500 cells (*left*) and 18000 cells (*right*), at the same time $t = 1.19 t_{\rm ff}$. *Bottom:* Gas temperature profile as a function of the radius showing Zel'dovich spike in the high resolution calculations.

In this part, we present results obtained for the collapse of a 0.01 $M_\odot$ dense core, using the same ratio between thermal and gravitational energies as in the 1 $M_\odot$ case. We completed two calculations, one with a resolution of 4500 cells and a high resolution one with 18000 cells. The high resolution enables us to resolve the Zel'dovich spike in the downstream flow immediately behind the accretion shock front (see Chapter VII in Zel'Dovich and Raizer 1967). The material within the spike cools down by radiating into the upstream material and the spike's length is about a photon mean free path.

Figure 3.12 shows the energy balance for the two calculations (top plots) and the temperature profile as a function of the radius (bottom). The high resolution enables us to describe Zel'dovich spike, but its amplitude is not as high as predicted by Zel'Dovich and Raizer (1967) since the resolution remains still too low. The top panels show that resolving the spike does not affect the emerging luminosity. Although luminosity is higher at the accretion shock with a high resolution, there is no difference at the first core border since upstream material is optically thick to radiation produced at the shock. Moreover, kinetic energy and luminosity jumps at the accretion shock remain equal in the two calculations. The differences in potential and internal energies variations come from differences in the path of integration in mass and time steps in the two calculations. For our study of the accretion shock at the first core, even if the temperature spike is not described, this makes no difference. However, this becomes more dramatic at the second core accretion shock, which can imply strong gradients in opacity. At the second core border temperature and density ranges, grains are destroyed and the shock can be subcritical with different pre- and postshock temperatures. This is the famous opacity gap, for instance described in Stahler et al. (1980). This result is of prime importance, since in the next part of this work, we run multi dimensional calculations of dense core collapse, where it is even more difficult to resolve the temperature spike at the accretion shock.

3.5 Radiative shock - A semi-analytic model

3.5.1 A qualitative picture of radiative shocks

In this section, we will focus on the main properties of radiative shocks that involve both radiation and hydrodynamics. When material is sufficiently hot or rarefied, the shocked gas emits enough radiation to penetrate upstream and preheat the material in front of the shock: this is the *radiative precursor* that has a length much greater than the photon mean free path. According to the shock's strength, radiative shocks fall into two groups: the *subcritical* and *supercritical* shocks. In fact, radiation transport may completely disperse the shock, producing a continuous transition between the upstream and downstream materials. Moreover, radiative flux and energy density across the shock must always be continuous in order to avoid infinite flux or absorption/emission. Most of the early qualitative work on radiative shocks has been done in Zel'Dovich and Raizer (1967) and Mihalas and Mihalas (1984), where readers can refer to find basic equations of the front structure, radiative precursor extension, etc...

Subcritical shock

Consider a weak shock in a cold material of temperature T_1; radiation has negligible influence on the energy balance. We thus obtain the usual jump relation of an adiabatic shock in an ideal fluid. As the strength of the shock increases, the postshock temperature T_2 will rise, producing a radiative flux of order σT_2^4 that increases very rapidly. This flux penetrates the upstream material and preheats it to a temperature T_- immediately ahead of the shock front that is proportional to the incident flux. T_- increases rapidly with the shock strength and eventually equals T_2. A shock with $T_- < T_2$ is called a *subcritical shock*. Because material entering the

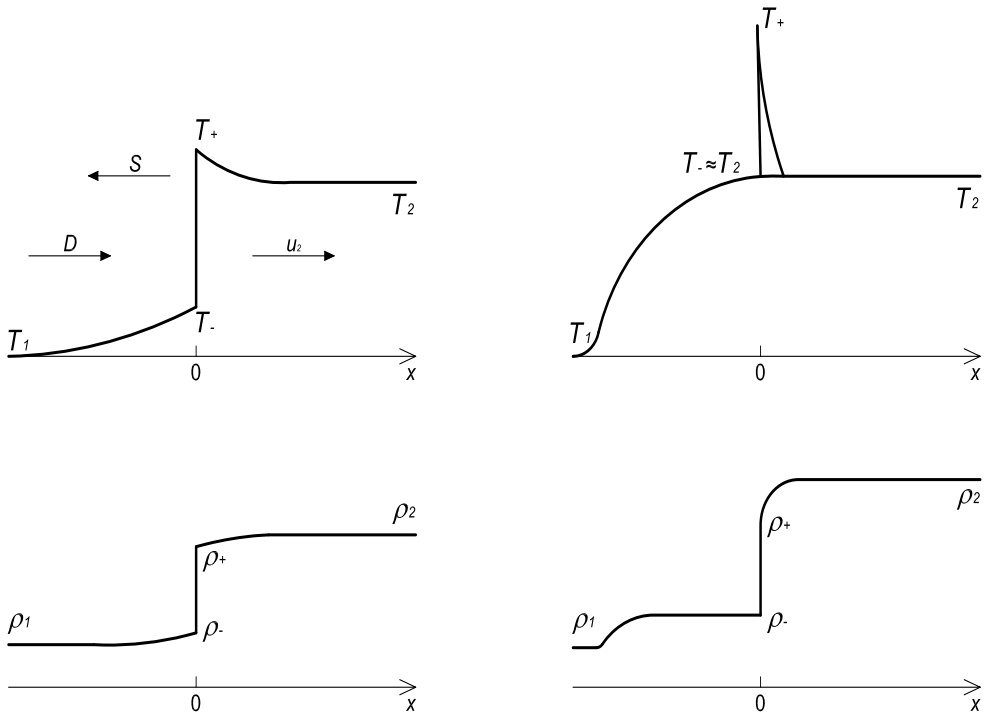

Figure 3.13: Temperature and density profiles in a subcritical shock (*left*) and a supercritical shock (*right*). Adapted from Zel'Dovich and Raizer (1967).

shock is preheated, the postshock temperature T_+ overshoots its final equilibrium value T_2. The overshoot decays downstream as the material cools down by emitting photons that penetrate across the shock.

Mihalas and Mihalas (1984) found an approximate solution for the radiative precursor in an optically thick gas which shows that the flux, radiation energy density, gas temperature, pressure and density all decrease upstream as $\exp(-3^{1/2}\tau)$, where τ is the optical depth measured from the shock front. As $T_\mathrm{r} \propto E_\mathrm{r}^{1/4}$, this means that radiative temperature decreases more slowly than gas temperature, radiation and matter being then out of equilibrium in the precursor. Moreover, at any position in front of the shock, radiative flux flowing upstream just equals material internal energy flux flowing downstream. All radiation energy goes is converted to heat the gas.

Supercritical shock

In the case where the strength of the shock increases, preheating will become so great that the preshock temperature will equal the postshock equilibrium temperature T_2. The shock velocity at which postshock and preshock temperatures are equal defines the critical shock. At higher shock velocities, T_- cannot exceeds T_2, the excess in energy forces the radiative precursor further into the upstream region with a temperature close to T_2. In fact, a Marshack wave is driven into the preshock material by a kind of radiating wall, the shock, at temperature T_2. Pre- and postshock temperatures are equal, thus the supercritical shock is isothermal. Radiation and matter are still out of equilibrium in a part of the precursor, but come to equilibrium when

temperature approaches T_2. The upstream kinetic energy is radiated at the shock. The spike just behind the front shock becomes less than a photon mean free path, its length decreasing as the strength of the shock increases. The maximum temperature can be estimated as $T_+ \sim (3-\gamma)T_2$.

In the next part, we show that, in some cases, the post and preshock quantities in an optically thick or thin medium can be estimated using a semi-analytic model.

3.5.2 Jump relations for a radiating material

Consider the jump relations (Rankine Hugoniot) for a radiating flow (see Mihalas and Mihalas 1984). Following the conservation of mass, momentum and energy, we have

$$\rho_1 u_1 = \rho_2 u_2 \equiv \dot{m}, \tag{3.24}$$

$$\rho_1 u_1^2 + P_1 + P_{\rm r1} = \rho_2 u_2^2 + P_2 + P_{\rm r2}, \tag{3.25}$$

$$\dot{m}\left(h_1 + \rho_1 u_1^2\right) + F_{\rm r1} + u_1\left(E_{\rm r1} + P_{\rm r1}\right) = \dot{m}\left(h_2 + \rho_2 u_2^2\right) + F_{\rm r2} + u_2\left(E_{\rm r2} + P_{\rm r2}\right), \tag{3.26}$$

where subscripts "1" and "2" denote respectively upstream and downstream states, all radiation quantities being estimated in the comoving frame. h corresponds to the gas enthalpy density ($h = e + P/\rho$) and $\dot{m}$ is the mass flux through the shock. Comparing with the hydrodynamical case, pressure is replaced by the total pressure $P + P_{\rm r}$ and enthalpy density by the total enthalpy density $e + (P + P_{\rm r} + E_{\rm r})/\rho$. Radiation energy and radiation pressure are important only at high temperatures or low densities, whereas radiation transport (flux) plays a fundamental role in all radiative shocks.

Contrary to the hydrodynamical case, system of equations (3.24), (3.25) and (3.26) can not be solved explicitly We need to make some assumptions on both upstream and downstream materials. In what follows, we distinguish two cases: opaque material and optically thin upstream material.

Radiative shock in a optically thick medium

At a sufficient large distance from the front, matter and radiation are in equilibrium and both downstream and upstream materials are opaque ($F_{\rm r1} = F_{\rm r2} = 0$). Any radiation crossing the front from the hot downstream material into the cool upstream material will be reabsorbed in the radiative precursor into which it penetrates by diffusion. Outside this diffusion layer, flux vanishes and we have

$$\dot{m}\left(h_1 + \rho_1 u_1^2\right) + u_1\left(E_{\rm r1} + P_{\rm r1}\right) = \dot{m}\left(h_2 + \rho_2 u_2^2\right) + u_2\left(E_{\rm r2} + P_{\rm r2}\right). \tag{3.27}$$

Since matter and radiation are in equilibrium and material is opaque, we have $E_{\rm r} = 3P_{\rm r} = a_{\rm R}T^4$. Defining the compression ratio $r = \rho_2/\rho_1 = u_1/u_2$, we can rewrite equations (3.25) and (3.26) in the nondimensional form

$$\gamma \mathcal{M}_1^2 \left(\frac{r-1}{r}\right) = (\Pi - 1) + \alpha_1 \left(\left(\frac{\Pi}{r}\right)^4 - 1\right), \tag{3.28}$$

and

$$\frac{\gamma}{2}\mathcal{M}_1^2 \left(\frac{r^2-1}{r^2}\right) = \frac{\gamma}{\gamma-1}\left(\frac{\Pi}{r} - 1\right) + 4\alpha_1 \left(\frac{\Pi^4}{r^5} - 1\right), \tag{3.29}$$

where $\Pi = P_2/P_1$, $\alpha_1 = (1/3)a_{\rm R}T_1^4/P_1$, $\mathcal{M}_1$ is the hydrodynamic Mach number, $\mathcal{M}_1 = u_1/c_{s1} = u_1/(\gamma P_1/\rho_1)^{1/2}$ and γ is the gas ratio of specific heats. Coupled equations (3.28) and (3.29) are solved numerically to get variations of Π and r as function of $\mathcal{M}_1$ and α_1.

Figure 3.14 shows the run of the compression ratio r with hydrodynamic Mach number and with α_1. We see the importance of radiative quantities that enhance the compression ratio

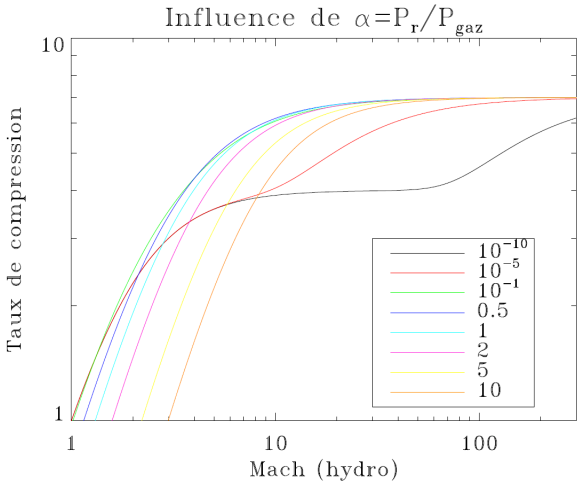

Figure 3.14: Compression ratio r as a function of the upstream Mach number for a radiative shock in an opaque material. Taken from Gonzáles (2006).

from $r = 4$ for a pure hydrodynamic shock with $\gamma = 5/3$ to $r = 7$ corresponding to the limiting compression ratio for a gas with $\gamma = 4/3$, i.e pure radiation, a gas made of photons. The stronger the shock, the stronger the radiative effects, even for a ratio of radiative pressure to gas pressure of 10^{-10}. When the upstream radiative pressure increases, the shock becomes immediately radiative since radiative pressure grows as T^4, whereas the gas pressure grows linearly with the temperature. Mihalas and Mihalas (1984) show that for a strong radiating shock, since the compression ratio is fixed, temperature ratio grows only as $\mathcal{M}_1^{1/2}$, whereas it rises as $\mathcal{M}_1^2$ in a non-radiating shock. Note that when $P_r/P < 10^{-5}$, the nonradiating fluid approximation is valid for upstream Mach number $\mathcal{M}_1 < 10$.

Radiative shock with an optically thin upstream material at low Mach number

Suppose now that the shock is propagating in optically thin material. Moreover, in low mass star formation context, we can neglect the radiative energy and pressure in front of internal gas energy for the first core accretion shock. We have

$$\rho_1 u_1 = \rho_2 u_2 \equiv \dot{m}, \tag{3.30}$$

$$\rho_1 u_1^2 + P_1 = \rho_2 u_2^2 + P_2, \tag{3.31}$$

$$\dot{m}\left(h_1 + \rho_1 u_1^2\right) = \dot{m}\left(h_2 + \rho_2 u_2^2\right) + \Delta F_r, \tag{3.32}$$

where $\Delta F_r = F_{r2} - F_{r1}$. We consider the case of non zero net flux $|F_2 - F_1|$ across the shock. This is typically our case, where, although the postshock material is opaque ($\tau > 1$), the radiation originating from this hot region can flow freely across the shock front and escape to infinity upstream (see luminosity profiles). In this case, as in the non radiative case, we can derive jump relations from the conservation equations (3.24), (3.25) and (3.26)

$$\frac{\rho_2}{\rho_1} = \frac{\left[(\gamma+1)P_2 + (\gamma-1)P_1\right] u_2 + 2(\gamma-1)\Delta F}{\left[(\gamma+1)P_1 + (\gamma-1)P_2\right] u_2} \tag{3.33}$$

and

$$\frac{T_2}{T_1} = \left(\frac{P_2}{P_1}\right) \frac{\left[(\gamma+1)P_1 + (\gamma-1)P_2\right] u_1 - 2(\gamma-1)\Delta F}{\left[(\gamma+1)P_2 + (\gamma-1)P_1\right] u_1}. \tag{3.34}$$

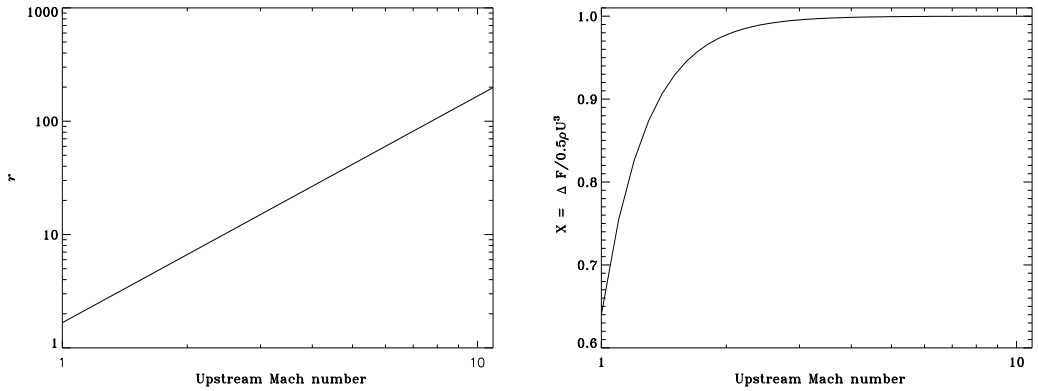

Figure 3.15: Run of compression ratio r and amount of kinetic energy radiated away X with the upstream Mach number for a supercritical shock.

These two relations show that the radiative energy transport (i.e. radiative flux) across a shock can significantly alter the density, temperature and velocity profiles. Both upstream and downstream materials will be altered over distances depending on the opacity of the material. As we mentioned before, the structure of a radiative shock is as follow: the upstream material is preheated by a radiation precursor, and the downstream material is cooled by radiative losses.

As for the previous opaque case and contrary to the case of a non radiating fluid, the conservation relations cannot give analytically downstream quantities once upstream conditions are set. The radiative flux has to be known and the result depends on the upstream flow. The simplest case to study is a supercritical shock, where $T_1 = T_2$ and then $h_1 = h_2$. Using the same adimensional parameters as for the opaque case, we have

$$\gamma \mathcal{M}_1^2 \left(\frac{r-1}{r} \right) = \Pi - 1, \tag{3.35}$$

and

$$\frac{\gamma}{2} \mathcal{M}_1^2 \left(\frac{r^2-1}{r^2} \right) = \frac{\gamma}{\gamma - 1} \left(\frac{\Pi}{r} - 1 \right) + \frac{\Delta F}{P_1 u_1}. \tag{3.36}$$

Note that since the shock is isothermal, $r = \Pi$ and thus

$$\Pi = \gamma \mathcal{M}_1^2. \tag{3.37}$$

Eventually, radiative flux jump normalized with the upstream kinetic energy is

$$X = \frac{\Delta F_\mathrm{r}}{0.5 \rho_1 u_1^3} = \frac{\gamma^2 \mathcal{M}_1^4 - 1}{\gamma^2 \mathcal{M}_1^4}. \tag{3.38}$$

Figure 3.15 shows the run of adimensional ratio r and X with the upstream Mach number for a supercritical shock. We see that compression ratio does not saturate, which is contrary to the case of an opaque material. From equations (3.33) and (3.34) it is evident that a non-zero flux across the front, with $F_{\mathrm{r}2} > F_{\mathrm{r}1}$, increases the density jump, whereas it decreases the temperature jump. To get an isothermal shock at low Mach number $M < 2$, downstream velocity is not negligible since all upstream kinetic energy is not radiated away. In protostellar collapse calculations, Mach number at the accretion shock is ~ 3, almost all the kinetic energy is radiated away.

Including radiative terms in equations (3.31) and (3.32) does not affect the dependency of compression ratio on the upstream Mach number. The dependence of the amount of kinetic energy radiated away is stronger

$$X = \frac{\Delta F_{\rm r}}{0.5\rho_1 u_1^3} = \frac{\gamma^2 \mathcal{M}_1^4 - 1}{\gamma^2 \mathcal{M}_1^4}(1 + 4\alpha_1). \tag{3.39}$$

The same analysis cannot be carried out for a subcritical shock with an optically thin upstream media, since no constraint enables us to close system of equations (3.31) and (3.32). We must have a prescription on the radiation flux or luminosity in the upstream material to close the system.

3.5.3 Super- or sub-critical?

The purpose of these calculations is to estimate the regime of the shock. The radiative precursor in front of the shock will not have the same influence in the sub- or supercritical cases. The simplest case would be to have a supercritical case, when the preshock gas ahead of the discontinuity is heated up to the postshock temperature. According to equation (3.25), it is easy to show that the compression work balances the change in kinetic energy. Then, equation of energy when the gas is neither compressed nor slowed down, reads

$$-F = u_1 \rho_1 \varepsilon(T_1, \rho_1), \tag{3.40}$$

with $\varepsilon = \frac{1}{\gamma - 1}\frac{k_{\rm B}T}{\mu m_{\rm H}}$. If we evaluate the flux just at the discontinuity, we find the maximum preheating temperature T$_-$

$$|F| \sim \sigma T_1^4 = u_1 \rho_1 \varepsilon(T_-, \rho_1). \tag{3.41}$$

In a gas with constant specific heats, the preheating increases with increasing wave strength ($u_1 \sim \sqrt{T_1}$ and $T_- \sim T_1^{3.5}$). We can now determine the critical temperature $T_{\rm cr}$ at which T_- will equal T_1

$$\sigma T_{\rm cr}^4 = u_1 \rho_1 \varepsilon(T_{\rm cr}), \tag{3.42}$$

thus,

$$T_{\rm cr} = \left(\frac{u_1 \rho_1 k_{\rm B}}{(\gamma - 1)\mu m_{\rm H} \sigma}\right)^{1/3}. \tag{3.43}$$

We apply this criterion to upstream quantities estimated in figure 3.7, where we read: $\rho_1 = 1.3 \times 10^{-13}$ g cm^{-3}, $u_1 = 1.07 \times 10^5$cm s^{-1} and $T_1 \sim 60$ K. The corresponding critical temperature is $T_{\rm cr} \sim 23$ K. This validates our first guess that the accretion shock on the first core is supercritical.

3.5.4 Estimate of the preshock temperature

In this part, we simply estimate the preshock temperature as function of the upstream quantities and the nature of the shock.

Supercritical shock with an optically thin or thick upstream medium

This is the simplest case and does not depend on whether the upstream material is optically thin or thick. Once upstream density is known, velocity and temperature are set, the full system is known. When the upstream gas is not compressed and for a strong shock ($M > 2$ so that $X \sim 1$), it is easy to get the shock temperature $T_{\rm s} = T_1 = T_2$ since all the upstream kinetic energy is radiated away

$$T_{\rm s} = \left(\frac{0.5\rho_1 u_1^3}{\sigma}\right)^{1/4}. \tag{3.44}$$

Subcritical shock with an optically thick upstream medium

In this case, the shock temperature is fixed by the upstream velocity. Mihalas and Mihalas (1984) show that the equilibrium postshock temperature is

$$T_2 = \frac{2(\gamma-1)u_1^2}{\mathcal{R}(\gamma+1)^2}, \tag{3.45}$$

with $\mathcal{R} = k/\mu m_{\rm H}$. The preshock temperature T_- is estimated as

$$\frac{\dot{m}\mathcal{R}T_-}{\gamma-1} = 2\sigma T_2^4\sqrt{3}, \tag{3.46}$$

which indicates that at any position in front of the shock, all radiative energy passing that position is absorbed and heats the gas.

3.5.5 Protostellar application

We have developed a semi-analytical solver that can be applied to the accretion radiative shock on the first core and that cover three cases: the case of sub- or supercritical shocks in an optically thick medium and the case of a supercritical shock in an optically thin medium. In order to get a model for the protostellar collapse, we have to estimate the density, velocity and temperature in the preshock region in the context of the first core formation. We can easily get the density (and velocity) from self-similar solutions of Larson-Penston and Shu. The tricky part comes form the estimate of the temperature before the shock. However, as we mentioned just above, the preshock temperature is determined by the upstream velocity. If we assume that the shock is supercritical and that the upstream material is optically thin, it is then easy to get this temperature and to recover all fluid variables. Omukai (2007) proposes an alternative model that fully describes the first core characteristics but that does not use jump relations for a radiating fluid. In this part, we only consider the characteristics at the first core border.

We approximate the upstream velocity by the free-fall velocity

$$u_{1,\rm ff} = \sqrt{\frac{2GM_{\rm fc}}{R_{\rm fc}}}. \tag{3.47}$$

According to our numerical results, we find that the upstream material is not in free-fall. As a matter of fact, gas has been compressed before the shock and then heated up. The loss of incident kinetic energy compared with free-fall solution equals the rise in temperature in front of the shock. We find that the effective velocity is $u_1 \sim u_{1,\rm ff}/2$.

The preshock density is given assuming a profile $\propto r^{-2}$ in the free-falling envelope

$$\rho_1 = \frac{c_s^2}{2\pi G}R_{\rm fc}^{-2}, \tag{3.48}$$

where $c_s = (\gamma P/\rho)^{0.5}$ is the sound speed. Eventually, the temperature is given assuming a supercritical shock, i.e. all the upstream kinetic energy is radiated away. Moreover, our calculations using FLD or M1 models shows that $\mathcal{M}_1 \sim 2$ and from figure 3.15 , wee see that $X \sim 1$. Therefore, the shock temperature reads (c.f. equation 3.44)

$$\sigma T_2^4 = \frac{\rho_2 u_{1,\rm ff}^3}{2}. \tag{3.49}$$

To get the correct energy balance, the velocity $u_{1,\rm ff}$ must be the velocity given by the free-fall velocity. However, if we take the velocity given by numerical calculations, we must take into

account the heating of the gas due to compression. In that case, our results show that upstream flow speed is less than half of the free-fall velocity, implying that more than half of the kinetic energy has been converted into internal energy before the accretion shock at the first core and thus the velocity departs from free-fall velocity.

If equations (3.47), (3.48) and (3.49) are applied according to the first core properties given in table 3.1, i.e. $M_{\rm fc} = 2.3 \times 10^{-2}$ $M_\odot$ and $R_{\rm fc} \sim 7$ AU, we get: $\rho_1 = 7.6 \times 10^{-14}$ g cm^{-3},$u_1 = 1.2 \times 10^5$ cm s^{-1} and $T_1 = 56$ K. We check these preshock quantities according to the data given in figure 3.7 and in table 3.1. We thus have: $\rho = 1 \times 10^{-13}$ g cm^{-3}, $u_1 = 1.45 \times 10^5$ cm s^{-1} and $T_1 = 60$ K. All these numerical values are in good agreement with our analytic estimates. Eventually, using equation (3.38) since we assume a supercritical shock, we get $X \sim 0.99$, $\rho = 1 \times 10^{-12}$ g cm^{-3},$u_2 = 1.45 \times 10^4$ cm s^{-1} $<< u_1$. These results are similar to the plotted values in figure 3.7.

3.6 Summary and perspectives

In this chapter, we get various valuable results, that will help us for the next part of this work. Our findings and the limitations and prospects of this study are summarized below:

1. We investigated the properties of the first collapse and of the first core. Our results are in good agreement with Masunaga et al. (1998), even though they use a more accurate scheme for radiative transfer. We find that the first core has a typical radius of ~ 7 AU and a mass $\sim 10^{-2}$ $M_\odot$. However, the first core has a short living time, its properties have to be investigated in calculations which integrates the physics of the second collapse (H_2 dissociation). This work is under progress.

2. We demonstrate that a barotropic EOS cannot reproduce the correct jump conditions at the accretion shock, since the latter is isothermal. Moreover, the first core entropy obtained in barotropic EOS is too high, since the model does not allow for the cooling of the first core. This can have a dramatic influence on the fragmentation process.

3. We focus on the accretion shock properties. We show that the accretion shock on the first core is supercritical and that its properties can easily be retrieved by a simple grey model. We develop a very simple analytical model for supercritical shocks with an optically thin medium, that reproduces the jump conditions of our numerical experiments. We show that the compression ratio in such kind of shocks can become very high. Using a frequency dependent model could give slightly different results, since for instance, strong shocks on protostars are known to be optically thick for hard photons, while optically thin for UV radiation (e.g. Stahler et al. 1980).

4. We show that Flux Limited Diffusion is appropriate to study star formation. FLD can be safely used for multi-dimensional calculations of the star formation process. It gives very similar results as the M1 model. However, our 1D spherical geometry code cannot account for multi dimensional effects like the anisotropy of the radiation field. Moreover, we have not taken into account the effects of rotation and magnetic field. This issue will be addressed in the next chapters.

In the subsequent part of this work, we will present the RHD solver that we designed using the FLD in a multidimensional code. Then, in the last chapter, we will see the influence of accurate radiative transfer on fragmentation with calculations integrating rotational, magnetic and radiative effects.

Chapter 4

The AMR code RAMSES and its extension to Radiation HydroDynamics

Contents

In this chapter, we first introduce the **A**daptive **M**esh **R**efinement (AMR) code RAMSES (Teyssier 2002). In modern numerical astrophysics, two different methods are widely used: grid based methods, for an *Eulerian* approach of hydrodynamical flows, and particle based codes, such as **S**moothed **P**articles **H**ydrodynamics (SPH), for a *Lagrangean* approach. We will focus primarily on the first approach that is used in all this work. A comparison between

RAMSES and a SPH code is presented in the next chapter in the star formation framework. Basic features of RAMSES are first introduced. In a second part, I present the solver that we developed to integrate Radiation Hydrodynamics (RHD) in RAMSES. We uses the equations of radiation-hydrodynamics in the comoving frame, to include effects of radiative pressure. We modified the usual hydrodynamical solver of RAMSES and designed it for RHD flows. In a third part, our method is tested against various conventional problems for validation purposes. FInally, we performed first RHD 3 dimensional collapse calculations and investigated the effect of the flux limiter and subcycling.

4.1 The RAMSES code

The Adaptive Mesh Refinement method is one of the most promising numerical methods to solve the fluid equations in very large simulation grids. This technique was first introduced in Berger and Oliger (1984). Originally, the AMR method was an Eulerian hydrodynamical scheme, with a hierarchy of nested grids covering high resolution regions of the flow. This first AMR structure, called "patch-based AMR", consists of computational-grid building blocks as rectangular patches of various sizes. An alternative method was proposed, the "tree-based" AMR (Khokolov 1998), where the parent cells are refined into children cells on a cell-by-cell basis. These adaptive mesh structures are coupled with grid-based, fluid-dynamics schemes handling high-resolution shock capturing. Nowadays, high order Godunov methods appear to be amongst the best schemes to capture discontinuities within only a few cells (e.g. Fromang et al. 2006; Matsumoto and Hanawa 2003; Teyssier 2002; Ziegler 2005).

4.1.1 The Eulerian approach and properties of conservation laws

The Eulerian frame is the appropriate frame for grid based codes. In Eulerian hydrodynamics, the mesh is fixed and gas density, velocity and internal energy are primary variables. Eulerian methods fall into two groups: finite difference methods (e.g. the ZEUS code, Hayes et al. 2006; Stone and Norman 1992) and finite volume methods (e.g. the RAMSES code, Teyssier 2002). In the first group, flow variables are conceived as being samples at certain points in space and time. Partial derivatives are then computed from these sampled values and follow Euler equations. In the finite volume approach, flow variables correspond to average values over a finite volume - the cell - and obey the conservation laws in the integral form. Their evolution is determined by calculating the flux of every conserved quantity across each cell interface.

For an inviscid, compressible flow, the Euler equations read, in their conservative form

$$\frac{\partial \rho}{\partial t} + \nabla \cdot [\rho \mathbf{u}] = 0, \tag{4.1}$$

$$\frac{\partial \rho \mathbf{u}}{\partial t} + \nabla \left[\rho \mathbf{u} \otimes \mathbf{u} + P \mathbb{I}\right] = 0, \tag{4.2}$$

$$\frac{\partial \mathrm{E}}{\partial t} + \nabla \left[\mathbf{u} \left(\mathrm{E} + P\right)\right] = 0, \tag{4.3}$$

where ρ is the density, $\mathbf{u}$ the velocity, P the gas pressure ($\mathbb{I}$ is the identity matrix), and $\mathrm{E} = 1/2\rho\mathbf{u}^2 + \rho\varepsilon$ the total energy density. The system of equations is closed with the perfect gas equation of state $P/\rho = k_\mathrm{B}T/\mu m_\mathrm{H} = (\gamma - 1)\varepsilon$. Each equation expresses a conservation law: mass conservation for equation (4.1), momentum conservation for equation (4.2) and total energy conservation for equation (4.3). Note that source terms can be added to take into account gain or loss of mass, momentum or energy. A common source's term in astrophysics is due to

gravitational field. Equations (4.1), (4.2) and (4.3) can be written in the general conservative form

$$\frac{\partial \mathbb{U}}{\partial t} + \nabla.\mathbb{F}(\mathbb{U}) = 0, \tag{4.4}$$

where the vector $\mathbb{U} = (\rho, \rho\mathbf{u}, E)$ contains conservative variables, and the flux vector $\mathbb{F}(\mathbb{U}) = (\rho\mathbf{u}, \rho\mathbf{u} \otimes \mathbf{u} + P\mathbb{I}, \mathbf{u}\,(\mathrm{E} + P))$ is a linear function of $\mathbb{U}$. Integrating equation (4.4) over space and time gives

$$\int_{x_1}^{x_2}\int_{t_1}^{t_2} (\partial_t \mathbb{U} + \nabla.\mathbb{F}) dx dt = 0, \tag{4.5}$$

$$\int_{x_1}^{x_2} (\mathbb{U}(t_2) - \mathbb{U}(t_1)) dx + \int_{t_1}^{t_2} (\mathbb{F}(x_1) - \mathbb{F}(x_2)) dt = 0. \tag{4.6}$$

From equations (4.5) and (4.6), it is evident that the system (4.4) obeys a conservation law. For all $t \in [t_1, t_2]$, the magnitude of $\mathbb{U}$ is a function of the incoming and outgoing flux $\mathbb{F}$ in x_1 and x_2. In addition, the system (4.4) forms a hyperbolic system of equations, i.e. the Jacobian matrix $\nabla_{\mathbb{U}}\mathbb{F}(\mathbb{U})$ is diagonalizable (see Toro 1999, def. 2.1.5). Equation (4.4) can then be written in its quasi-linear form

$$\frac{\partial \mathbb{U}}{\partial t} + \nabla_{\mathbb{U}}\mathbb{F}(\mathbb{U})\nabla_x \mathbb{U} = 0. \tag{4.7}$$

Then, let us assume that hyperbolicity properties are conserved after variable transformation. It is easier to find spectral properties of the Jacobian matrix $\nabla_{\mathbb{U}}\mathbb{F}(\mathbb{U})$. A useful transformation in hydrodynamics is to rewrite (4.4) using primitive variables $\mathbb{V} = (\rho, \mathbf{u}, P)^T$. System (4.4) can then be recast as

$$\frac{\partial \mathbb{V}}{\partial t} + \mathbb{B}(\mathbb{V})\nabla_x \mathbb{U} = 0, \tag{4.8}$$

with matrix $\mathbb{B}(\mathbb{V})$ similar to $\nabla_{\mathbb{U}}\mathbb{F}(\mathbb{U})$ (i.e. it has the same spectral properties). Note that the primitive form of Euler equations should only be used to simplify the calculations of eigenvalues. Euler equations have to be integrated in their conservative form to get the correct wave propagation speed (see the classical Burgers equation integration issue in textbooks). The conservative form is always used in conservative codes like RAMSES, except in the case where negative temperatures are found in supersonic flows. The primitive form is only used in this case to the get the correct temperature and pressure fields.

From equation (4.6), it is obvious that a value of the flux has to be known at the cell interfaces in x_1 and x_2. Therefore a value of $\mathbb{U}$ components is needed at the interface, which leads to the famous Godunov method (Godunov 1959). In order to estimate fluxes at the cells interfaces, let us imagine that $\mathbb{U}$ is uniform over each cell (piecewise constant - finite volume approach). At the interfaces, there is a discontinuity between two regions of constant fluid properties, which is known as a *Riemann problem*. The temporal evolution of $\mathbb{U}$ at the interface is the solution to a classical Riemann problem. Such a solution involves three waves: a rarefaction wave, a contact discontinuity and a shock wave (c.f. figure 4.1).

In the first order Godunov formalism, the system of conservation laws is discretized as follows

$$\frac{\mathbb{U}_i^{n+1} - \mathbb{U}_i^n}{\Delta t} + \frac{\mathbb{F}_{i+1/2}^{n+1/2} - \mathbb{F}_{i-1/2}^{n+1/2}}{\Delta x} = 0, \tag{4.9}$$

where $\mathbb{F}_{i+1/2}^{n+1/2}$ and $\mathbb{F}_{i-1/2}^{n+1/2}$ are the Godunov fluxes evaluated at cell interfaces, given by

$$\mathbb{F}_{i+1/2}^{n+1/2} = \mathbb{F}^*(\mathbb{U}_i^n, \mathbb{U}_{i-1}^n), \tag{4.10}$$

where $\mathbb{F}^*(\mathbb{U}_i^n, \mathbb{U}_{i-1}^n)$ is the solution to the inter-cell Riemann problem. Solutions to the Riemann problem can be exact. However, finding the exact solution is computationally expensive since it involves Raphson-Newton iterations and complex non-linear functions (see Toro 1999). Approximate Riemann solvers are therefore commonly used and fall into two groups

- Linear solvers like the Roe solver, where the Jacobian matrix is linearized and all the eigenvalues are known.
- Lax-Friedrich, HLL or HLLC solvers. The Lax-Friedrich solver involves two waves propagating in opposite directions with the highest wave propagation speed. The HLL (Harten-Lax-van Leer) solver approximates the true Riemann fan by two waves and an intermediate state. The HLLC solver adds a third wave for the contact (entropy) wave.

Details on approximate Riemann solvers can be found in Toro (1999). First order Godunov are unfortunately very diffusive. Since van Leer (1979), second order Godunov methods have been widely developed. RAMSES uses among others, the second order (in both time and space), predictor-corrector scheme MUSCL, which we present in the next section.

4.1.2 The MUSCL predictor-corrector scheme

The method using the MUSCL scheme have been introduced to achieve higher order of accuracy. MUSCL stands for Monotone Upstream-centered Scheme for Conservation Laws. The main difference with first order methods is that it uses a piecewise linear approximation of the solution within a cell. This introduces a length scale, and the Riemann solution is not self-similar any more. The flux function is approximated using a *predictor-corrector* scheme

$$\mathbb{F}_{i+1/2}^{n+1/2} = \frac{1}{\Delta t} \int_{t^n}^{t^{n+1}} \mathbb{F}_{i+1/2} dt \approx \mathbb{F}\left(\mathbb{U}_{i+1/2}^*\left(\frac{\Delta t}{2}\right)\right). \tag{4.11}$$

The corrected Riemann solver has now predicted states as initial data

$$\mathbb{U}_{i+1/2}^* = \mathcal{RP}[\mathbb{U}_{i+1/2,L}^{n+1/2}, \mathbb{U}_{i+1/2,R}^{n+1/2}]. \tag{4.12}$$

The predicted states are computed using a Taylor expansion in space and time that introduces slope estimates. In practice, the central finite difference approximation is used for the slope in the linear interpolation

$$\left(\frac{\partial \mathbb{U}}{\partial x}\right) = \frac{\Delta \mathbb{U}}{\Delta x} = \frac{\mathbb{U}_{i+1} - \mathbb{U}_{i-1}}{\Delta x}. \tag{4.13}$$

However, using a central finite difference approximation for the slope does not preserve monotonicity: local extrema are created when predicted states at interfaces are estimated. The slope of the linear interpolation within each cells has to be limited. For that purpose, Harten (1983) introduced the Total Variation of the numerical solution

$$TV^n = \sum_i^n |\mathbb{U}_{i+1} - \mathbb{U}_i|. \tag{4.14}$$

Following this idea, a Total Variation Diminishing (TVD) scheme is monotonicity preserving if

$$TV^{n+1} \leq TV^n. \tag{4.15}$$

Various TVD slope limiters are implemented in RAMSES, such as *minmod*, *moncen*, *superbee* and *ultrabee*. Figure 4.3 illustrates *minmod* and *moncen* limiters. Riemann solvers have now

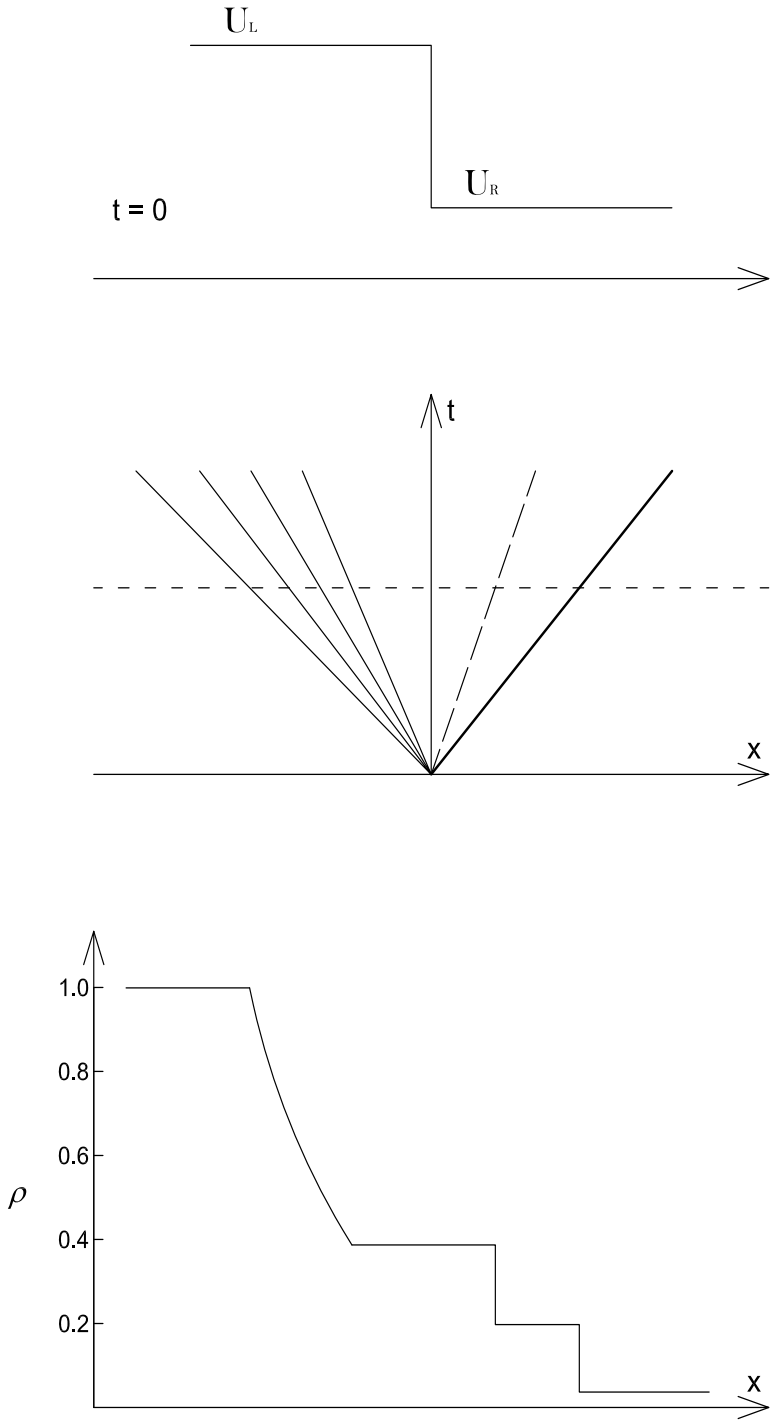

Figure 4.1: *Top:* Illustration of the initial data for the Riemann problem. At the initial time, the data consists of two constant states on the left and right cells, separated by a discontinuity at the cell interface (diaphragm). *Middle:* Solution of the Riemann problem for a shock tube made of 3 waves: expansion, contact discontinuity and shock waves. *Bottom:* corresponding density profile that reproduces the resulting 4 states.

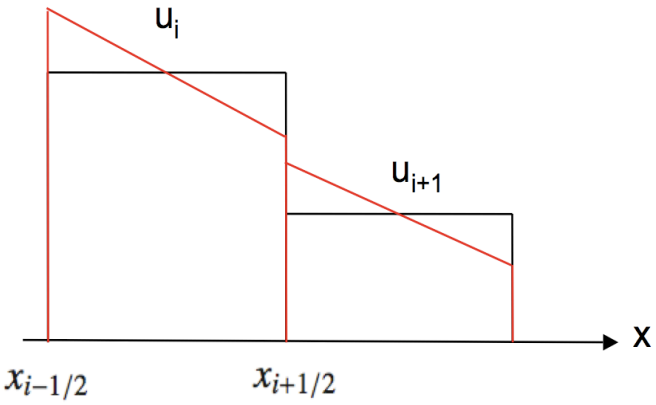

Figure 4.2: Piecewise linear approximation within cells (red) compared to piecewise constant approximation (black) of first order Godunov method. Taken from Romain Teyssier lecture.

initial predicted states that preserve monotonicity. Once intermediate states are computed by the Riemann solver, the conservative update given by equation (4.9) is performed to get $\mathbb{U}_i^{n+1}$. To deal with multi-dimensional grid, RAMSES uses directional splitting. A MUSCL predictor-corrector step is done in each direction independently and a conservative update is performed using mono-directional fluxes.

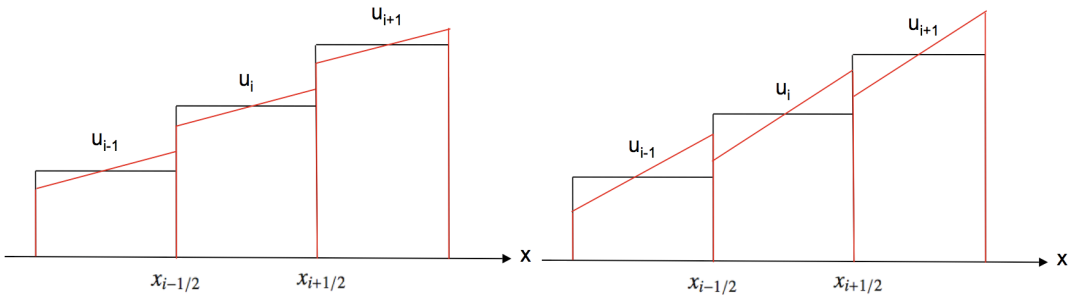

Figure 4.3: Illustration of the *minmod* (left) and *moncen* (right) slope limiters applied to a piecewise constant function. Slope limiter *minmod* ensures that $\mathbb{U}_{i+1/2,L} \leq \mathbb{U}_{i+1/2,R}$ and *mocen* ensures that $\mathbb{U}_{i-1} \leq \mathbb{U}_{i+1/2,L} \leq \mathbb{U}_{i+1}$. Taken from Romain Teyssier lecture.

CFL condition on the time step

The second order Godunov scheme is based on an explicit discretization of the Euler equations. In order to get a stable scheme, the time step Δt has to be limited by the so-called CFL condition (Courant et al. 1928). This condition states that informations cannot propagate over more than one cell in a single time step Δt

$$\Delta t \leq C_{\mathrm{CFL}} \frac{\Delta x}{c_s + u}, \tag{4.16}$$

where $C_{\mathrm{CFL}} < 1$ is the CFL number, c_s the sound speed and u the fluid velocity. This condition on the time step ensures convergence and stability for any explicit scheme solving hyperbolic systems.

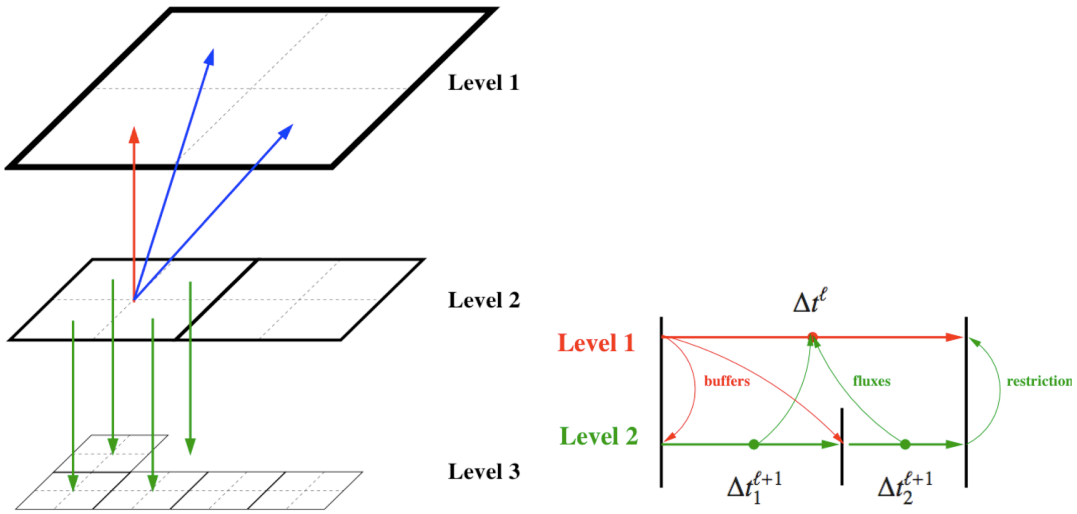

Figure 4.4: *Left*: Octal structure in a 2D grid. Each oct at level ℓ points to its parent cell at coarser level $\ell - 1$, to the $2 \times dim$ neighboring parent cells at level $\ell - 1$ and to the 2^{dim} child octs at level $\ell + 1$. *Right:* Adaptive time step scheme for the hydrodynamical solver. Taken from Romain Teyssier lecture.

4.1.3 Adaptive Mesh Refinement

AMR methods appear to be particularly suitable for calculations of structure formation. Thanks to the versatility of the refinement criteria (hydrodynamical variables gradients, Jeans mass, etc...), AMR codes are adapted to a wide range of astrophysical phenomena. The main interest of AMR is to refine the grid in the regions of interest, that are only a small fraction of the full simulation box. The filling factor of refined cells should not exceed 30%; otherwise, a uniform grid is found to be more adapted (faster and more accurate).

RAMSES data structure is organized in a "Fully Threaded Tree" (FTT) (Khokolov 1998). The Cartesian mesh is refined on a cell by cell basis. Basic elements of the grid are *octs*, i.e. group of 2^{dim} sibling cells for a *dim*-dimensional problem. Each oct belongs to a given level of refinement ℓ, the coarse grid being the base of the structure ($\ell = 0$). When a cell is flagged for refinement at level ℓ, it produces a child oct on level $\ell + 1$. Then, if a cell has no children, it is called a *leaf* cell. Otherwise, a cell is flagged as a *split* cell and no hydrodynamics calculations will be performed upon it.

Time integration can be performed for each level independently using an adaptive time step scheme. Each level evolves with its own time step, determined by the level's CFL condition. Consequently, when level $\ell = 0$ is advanced in time using one coarse time step, level $\ell = 1$ is advanced in time using two time steps and level $\ell = 4$ using eight time steps, etc... (see right panel of figure 4.4). Every level dependent time step obeys the synchronization law

$$\Delta t^\ell = \Delta t_1^{\ell+1} + \Delta t_2^{\ell+1}. \tag{4.17}$$

For hydrodynamics update, the coarse level $\ell = 0$ is frozen during fine level iterations, and fluxes are then time-averaged at coarse-fine boundaries.

Refinement criterion in star formation calculations

Our refinement criterion is based on the Jeans length resolution which is fundamental to monitor accurately the gravitational collapse. We impose a minimum number of points N_J per Jeans

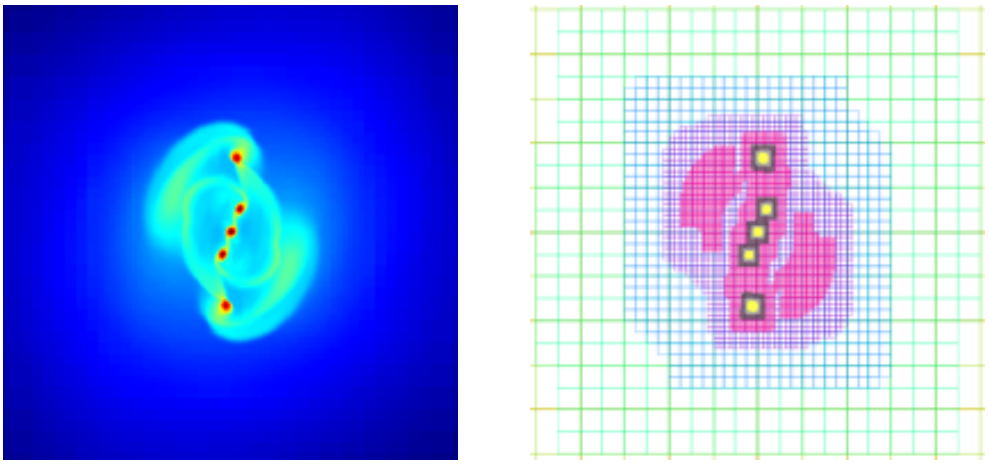

Figure 4.5: *Left plot:* Density map in the equatorial plane for a collapse calculation with fragmentation. *Right plot:* Corresponding AMR grid, the refinement criterion is based on the local Jeans length.

length $\lambda_{\rm J}$. The cell size must be smaller than a constant fraction of the local Jeans length. The dimension of cells belonging to the ℓ_i refinement level is $L_{\rm box}/2^{\ell_i}$, where $L_{\rm box}$ is the physical length of the simulation box. The mesh is locally refined in order to satisfy the local Jeans criterion

$$\frac{L_{\rm box}}{2^{\ell_i}} < \frac{\lambda_{\rm J}}{N_{\rm J}}. \tag{4.18}$$

Truelove et al. (1997) defined a minimum resolution condition for the validity of grid-based simulations aimed at modeling the collapse of a molecular cloud core, namely $N_{\rm J} > 4$. This condition ensures that the collapse and the fragmentation is of physical rather than numerical origin.

Solving the Poisson equation and N-body dynamics

In RAMSES, the Poisson equation for gravity is solved using an efficient Multigrid Solver (Guillet, *in prep*). The method uses enforced boundary capturing in order to overcome the multigrid "small islands" problem, when coarser levels are solving a different problem than finer grids. The efficiency is also improved by problem dependent automatic choices and by combination with a classical Conjugate Gradient algorithm.

RAMSES also integrates a N-body dynamics solver, accounting for collisionless material such as dark matter, stars or sink particles moving with the flow. For our purpose, we will only use sink particles which enables us to save CPU time by modeling accretion on a compact object (Krumholz et al. 2004). The number of sink particles will never be high in our calculations. In a cosmological framework, stars or dark matter particle numbers are very large ($> 10^6$). It is time consuming to compute the time evolution for each individual particle. The N-body solver used in RAMSES is very similar to the one developed in the ART code by Kravtsov et al. (1997). Collisionless particle evolution is described by the Vlasov-Poisson equation which is integrated with a Particle-Mesh scheme using Cloud In Cell interpolations. For more details, we refer the reader to Teyssier (2002).

4.1.4 Magneto-HydroDynamics

Magnetic fields also play an important role in astrophysics. RAMSES integrates original and efficient algorithms for solving the equations of **M**agneto**H**ydro**D**ynamics (MHD) (Fromang et al. 2006; Teyssier et al. 2006). Introducing a magnetic field in the material changes the classical Euler equations. In the non-relativistic limit, the induction equation, derived from Maxwell equations, reads

$$\frac{\partial \mathbf{B}}{\partial t} = \nabla \times (\mathbf{u} \times \mathbf{B}) + \eta \nabla^2 \mathbf{B}, \tag{4.19}$$

where $\eta = 1/(\mu_0 \sigma)$ is the magnetic diffusivity. This equation states that a local change in the magnetic field in a material arises from fluid motions and diffusion. The magnetic Reynolds number R_m is the ratio of the advective to the diffusive terms

$$R_m = \frac{||\nabla \times (\mathbf{u} \times \mathbf{B})||}{||\eta \nabla^2 \mathbf{B}||} \sim \frac{v_0 l_0}{\eta}, \tag{4.20}$$

where v_0 and l_0 are the typical velocity and length scale of the plasma. In most astrophysical cases, the advective term dominates ($R_m >> 1$), and the field lines are frozen into the plasma (Alfvén 1943) with typical a time-scale, $tc = l_0/v_0$. This corresponds to the *ideal* MHD approximation. It applies for a material with infinite conductivity σ. In this case, the induction equation simply reads

$$\frac{\partial \mathbf{B}}{\partial t} = \nabla \times (\mathbf{u} \times \mathbf{B}). \tag{4.21}$$

In cases where the magnetic energy is comparable to thermal or kinetic energies, the pressure on material due to the magnetic field line strength (magnetic pressure) cannot be neglected. The material feels the Lorentz force

$$\mathbf{j} \times \mathbf{B} = (\mathbf{B}.\nabla)\mathbf{B} - \nabla \frac{\mathbf{B}.\mathbf{B}}{2}. \tag{4.22}$$

The first term on the RHS of equation (4.22) represents a force due to magnetic tension, parallel to **B**, which results from the curvature of the magnetic field lines. The second term on the RHS of equation (4.22) is a scalar magnetic pressure force.

Hence, the usual MHD equations, written in conservative form, are

$$\frac{\partial \rho}{\partial t} + \nabla \cdot [\rho \mathbf{u}] = 0, \tag{4.23}$$

$$\frac{\partial \rho \mathbf{u}}{\partial t} + \nabla \left[\rho \mathbf{u} \otimes \mathbf{u} - \mathbf{B} \otimes \mathbf{B} + P_{tot} \mathbb{I}\right] = 0, \tag{4.24}$$

$$\frac{\partial \mathrm{E}}{\partial t} + \nabla . \left[\mathbf{u} \left(\mathrm{E} + P_{tot}\right) - \mathbf{B}(\mathbf{B}.\mathbf{u})\right] = 0, \tag{4.25}$$

$$\frac{\partial \mathbf{B}}{\partial t} = \nabla \times (\mathbf{u} \times \mathbf{B}) \tag{4.26}$$

where P_{tot} is the total pressure, sum of the thermal and magnetic pressures

$$P_{tot} = P + \frac{\mathbf{B}.\mathbf{B}}{2}, \tag{4.27}$$

and E the total fluid energy per unit volume

$$E = \rho(\varepsilon + \frac{\mathbf{u}.\mathbf{u}}{2}) + \frac{\mathbf{B}.\mathbf{B}}{2}. \tag{4.28}$$

This system of equations is closed by the perfect gas equation of state $P/\rho = (\gamma - 1)\varepsilon$. An additional constraint comes from the fact that the divergence of the magnetic field has to vanish everywhere at all times

$$\nabla.\mathbf{B} = 0. \tag{4.29}$$

To ensure that this solenoidal constraint is fulfilled to machine roundoff precision, RAMSES uses the Constraint Transport scheme (Evans and Hawley 1988; Teyssier et al. 2006). It consists in writing the induction equation (4.21) in its integral form

$$\frac{\partial \Phi}{\partial t} = \frac{\partial}{\partial t} \int \int \mathbf{B}.\mathrm{d}\mathbf{S} = \oint \mathbf{E}.\mathrm{d}\mathbf{l}, \tag{4.30}$$

where $\mathbf{E}$ is the electrical field vector defined by $\mathbf{E} = \mathbf{u} \times \mathbf{B}$. This approach requires the magnetic field components to lie on the cell faces, i.e. on a *staggered mesh*. Magnetic field components are surface-averaged over the cell face

$$\mathbf{B}_{x,i-1/2,j,k} = \frac{1}{\Delta y \Delta z} \int_{y_{j-1/2}}^{y_{j+1/2}} \int_{z_{k-1/2}}^{z_{k+1/2}} \mathbf{B}_x(x_{i-1/2}, y', z') dy' dz' \tag{4.31}$$

Then, the induction equation can be written in conservative form by an integration in space and time that gives for component $\mathbf{B}_{x,i-1/2,j,k}$

$$\frac{\mathbf{B}^{n+1}_{x,i-1/2,j,k} - \mathbf{B}^{n}_{x,i-1/2,j,k}}{\Delta t} - \frac{\mathbf{E}^{n+1/2}_{z,i-1/2,j+1/2,k} - \mathbf{E}^{n+1/2}_{z,i-1/2,j-1/2,k}}{\Delta y} + \frac{\mathbf{E}^{n+1/2}_{y,i-1/2,j,k+1/2} - \mathbf{E}^{n+1/2}_{y,i-1/2,j,k-1/2}}{\Delta z} = 0. \tag{4.32}$$

As for the Euler system, the numerical evaluation of the time- and edge-averaged electromotive force (EMF) $\mathbf{E}^{n+1/2}_{y,i-1/2,j,k+1/2}$ proceeds in a predictor step followed by a corrector step using the MUSCL scheme (Teyssier et al. 2006). This scheme implies resolution of 2D Riemann problems, that are difficult to summarize briefly. We refer readers to Teyssier et al. (2006) and Fromang et al. (2006) for a complete description of the scheme.

Last but not least, the usual 1D Riemann problem is modified by the presence of the magnetic field. MHD systems remain hyperbolic, but they now have seven eigenvalues. The solution of the Riemann problem thus comprises of seven waves

- 2 Alfvén waves (transverse mode) of speed,
- 2 slow magneto-acoustic waves (coupling between Lorentz force and thermal pressure, $\mathbf{B}$ and ρ are anti-correlated),
- 2 fast magneto-acoustic waves (coupling between Lorentz force and thermal pressure, $\mathbf{B}$ and ρ are correlated),
- 1 entropy wave (contact discontinuity).

Various MHD Riemann solvers are implemented in RAMSES. As for the hydrodynamics solver, the simplest one remains the Lax-Friedrich solver which uses 2 waves, given by the propagation speed of the fastest wave and its opposite. Lax-Friedrich remains a very diffusive solver but is robust. There is also an HLL solver, which retains only the two fastest waves (e.g. the two fast magneto- acoustic waves) and then assumes that the gas is uniform between the two states. The best approximate solver is the HLLD solver, that retains five waves (Miyoshi and Kusano 2005), the two fast magneto-acoustic waves, two Alfvén waves and the entropy wave. Thus, four intermediate states have to be computed. A linear Roe solver which retains all seven waves is also implemented in RAMSES. The Roe solver encounters severe difficulties in some cases, in presence of strong density gradients. This is due to the linearization which is a poor approximation for highly non linear discontinuities encountered in stiff problems.

4.2 A multidimensional Radiation Hydrodynamics solver for RAMSES

Another mandatory physical process to account for is the radiative transfer. Implementing radiative transfer in RAMSES has been the major parts of this thesis. We chose to use the well-known Flux Limited Diffusion (FLD) approximation for implementation within RAMSES. The FLD is easier to implement in an AMR code, since it involves only one additional equation on the radiative energy. Implementation of the M1 model, although more accurate for radiative transfer, is not straightforward in AMR codes and it implies large matrix inversions, which is hard to handle on AMR grids. The main features of RAMSES have been presented in the previous section, as well as the FLD approximation in 2.2.2. Note here that I present the implementations in the hydrodynamics case. Extension to MHD flows has been done and is trivial, since there is no coupling between magnetic and radiative terms.

4.2.1 The conservative Radiation Hydrodynamics scheme

Let us rewrite the grey Radiation Hydrodynamics (RHD) equations within the comoving frame

$$\left\{\begin{array}{lcl} \partial_t \rho + \nabla\left[\rho\mathbf{u}\right] & = & 0 \\ \partial_t \rho\mathbf{u} + \nabla\left[\rho\mathbf{u}\otimes\mathbf{u} + P\mathbb{I}\right] & = & -\rho\nabla\Phi - \lambda\nabla E_{\rm r} \\ \partial_t E_{\rm T} + \nabla\left[\mathbf{u}\left(E_{\rm T}+P_{\rm T}\right)\right] & = & -\rho\mathbf{u}\cdot\nabla\Phi - \mathbb{P}_{\rm r}\nabla:\mathbf{u} - \lambda\mathbf{u}\nabla E_{\rm r} + \nabla\cdot\left(\frac{c\lambda}{\rho\kappa_{\rm R}}\nabla E_{\rm r}\right) \\ \partial_t E_{\rm r} + \nabla\left[\mathbf{u}E_{\rm r}\right] + \mathbb{P}_{\rm r}\nabla:\mathbf{u} & = & \nabla\cdot\left(\frac{c\lambda}{\rho\kappa_{\rm R}}\nabla E_{\rm r}\right) + \kappa_{\rm P}\rho(4\pi B - cE_{\rm r}) \end{array}\right. \tag{4.33}$$

Note that we rewrite the opacity $\kappa_{\rm i}$ as $\kappa_{\rm i}\rho$. $\kappa_{\rm i}$ has now dimensions cm^2 g^{-1}.

The basic idea is to build a solver for a radiative fluid, with an additional pressure due to the radiation field: the radiative pressure. Following the Euler equations in their conservative form, the new conservative quantities are: density ρ, momentum $\rho\mathbf{u}$, total energy $E_{\rm T}$ of the fluid (gas + photon) per unit volume, i.e. $\rho\varepsilon + \rho u^2/2 + E_{\rm r}$ where $E_{\rm r}$ is the radiative energy. The total pressure $P_{\rm T}$ equals $P + P_{\rm r}$. Primitive hydrodynamical variables do not change for the fluid, but we add a fourth equation for the radiative energy. Our solver is built on the combination of four equations, closed by the perfect gas relation.

In order to simply integrate these equations in RAMSES and to minimize the number of changes with the pure hydrodynamical version, we need to find the correct strategy. For example, it is not easy to have access at any time to the flux limiter within a single cell. To compute it, access to neighboring cells is needed, etc... For simplicity, we decompose each term where the flux limiter λ appears as follows: $\lambda = 1/3 + (\lambda - 1/3)$. We thus distinguish an isotropic part (Eddington approximation, $\mathbb{P}_{\rm r} = 1/3E_{\rm r}$) and a correction one. The computation of predicted states and fluxes in the MUSCL scheme will then be done under the Eddington approximation which will then be corrected in an additional corrective step. The RHD equations can be rewritten as

$$\left\{\begin{array}{lcl} \partial_t \rho + \nabla\left[\rho\mathbf{u}\right] & = & 0 \\ \partial_t \rho\mathbf{u} + \nabla\left[\rho\mathbf{u}\otimes\mathbf{u} + (P+1/3E_{\rm r})\mathbb{I}\right] & = & -\rho\nabla\Phi - (\lambda-1/3)\nabla E_{\rm r} \\ \partial_t E_{\rm T} + \nabla\left[\mathbf{u}\left(E_{\rm T}+P+1/3E_{\rm r}\right)\right] & = & -\rho\mathbf{u}\cdot\nabla\Phi - (\lambda-1/3)(\mathbf{u}\nabla E_{\rm r} + E_{\rm r}\nabla:\mathbf{u}) + \nabla\cdot\left(\frac{c\lambda}{\rho\kappa_{\rm R}}\nabla E_{\rm r}\right) \\ \partial_t E_{\rm r} + \nabla\left[\mathbf{u}E_{\rm r}\right] & = & -\mathbb{P}_{\rm r}\nabla:\mathbf{u} + \kappa_{\rm P}\rho(4\pi B - cE_{\rm r}) + \nabla\cdot\left(\frac{c\lambda}{\rho\kappa_{\rm R}}\nabla E_{\rm r}\right) \end{array}\right. \tag{4.34}$$

The left hand side of this set of equations is the new hyperbolic system $\partial_t\mathbb{U} + \nabla\mathbb{F}(\mathbb{U}) = 0$. The

hyperbolic system, as well as corrective terms are integrated in time with an explicit scheme. On the other hand, the diffusion term $\nabla \cdot \left(\frac{c\lambda}{\rho\kappa_{\rm R}}\nabla E_{\rm r}\right)$ and the coupling term $\kappa_{\rm P}\rho(4\pi B - cE_{\rm r})$ must be integrated implicitly, since they involve processes of very short time scales compared to the explicit CFL condition.

The hyperbolic system reads

$$\mathbb{U} = \begin{bmatrix} \rho \\ \rho\mathbf{u} \\ E_{\rm T} \\ E_{\rm r} \end{bmatrix} \quad , \quad \mathbb{F}(\mathbb{U}) = \begin{bmatrix} \rho\mathbf{u} \\ \rho\mathbf{u}\otimes\mathbf{u} + (P + 1/3E_{\rm r})\mathbb{I} \\ \mathbf{u}\left(E_{\rm T} + P + 1/3E_{\rm r}\right) \\ \mathbf{u}E_{\rm r} \end{bmatrix} . \tag{4.35}$$

Consider the variable transformation $\mathbb{U} = \Theta(\mathbb{V})$, system (4.35) can be written with primitive variables $\mathbb{V} = (\rho,\, u,\, P,\, E_{\rm r})$ (for a 1D case in what follows). As we pointed out in the previous section, the hyperbolicity property is invariant by variable transformation. Regular solutions of our system therefore satisfy

$$\partial_t\Theta(\mathbb{V}) + \frac{\partial\mathbb{F}}{\partial\mathbb{U}}\nabla\Theta(\mathbb{V}) = 0, \tag{4.36}$$

where $\frac{\partial\mathbb{F}}{\partial\mathbb{U}}$ is the Jacobian matrix of $\mathbb{F}(\mathbb{U})$, which is diagonalisable and admit real and distinguishable eigenvalues. Equation (4.36) can also be written as

$$D\Theta(\mathbb{V})\partial_t\mathbb{V} + \frac{\partial\mathbb{F}}{\partial\mathbb{U}}D\Theta(\mathbb{V})\nabla\mathbb{V} = 0, \tag{4.37}$$

with $D\Theta(\mathbb{V})$ assumed to be invertible. $\mathbb{V}$ eventually satisfies:

$$\partial_t\mathbb{V} + \mathbb{B}(\mathbb{V})\nabla\mathbb{V} = 0. \tag{4.38}$$

Since $\mathbb{B}(\mathbb{V})$ and $\frac{\partial\mathbb{F}}{\partial\mathbb{U}}$ are similar, both have the same spectral properties. The system of primitive variables reads

$$\left\{\begin{array}{lllllllllll} \partial_t\rho & + & u\partial_x\rho & + & \rho\partial_x u & + & 0 & + & 0 & = & 0 \\ \partial_t u & + & 0 & + & u\partial_x u & + & \frac{1}{\rho}\partial_x P & + & \frac{1}{3\rho}\partial_x E_{\rm r} & = & 0 \\ \partial_t P & + & 0 & + & \gamma P\partial_x u & + & u\partial_x P & + & 0 & = & 0 \\ \partial_t E_{\rm r} & + & 0 & + & \frac{4E_{\rm r}}{3}\partial_x u & + & 0 & + & u\partial_x E_{\rm r} & = & 0 \end{array}\right. \tag{4.39}$$

This system is used in the predictor step of the MUSCL temporal integration. Hence, to predict states, we consider the worst case, where the radiative pressure is the greatest ($1/3E_{\rm r}$). For the conservative update (corrector step) we consider the LHS of system (4.34).

The Jacobian matrix $\mathbb{B}(\mathbb{V})$ of system is

$$\mathbb{B}(\mathbb{V}) = \begin{pmatrix} u & \rho & 0 & 0 \\ 0 & u & \frac{1}{\rho} & \frac{1}{3\rho} \\ 0 & \gamma P & u & 0 \\ 0 & \frac{4E_{\rm r}}{3} & 0 & u \end{pmatrix} . \tag{4.40}$$

The associated eigenvalues corresponding to the 3 waves are

$$\lambda_i = \left\{\begin{array}{l} u - \sqrt{\frac{\gamma P}{\rho} + \frac{4E_{\rm r}}{9\rho}} \\ u \\ u + \sqrt{\frac{\gamma P}{\rho} + \frac{4E_{\rm r}}{9\rho}} \end{array}\right. . \tag{4.41}$$

Note that radiative pressure enlarges the span of solutions, since wave speeds are larger. Once again, with the Eddington approximation, we build the system in the case where the radiative pressure would be the greatest. Hence solution waves propagate at a speed that is within the wave extrema.

The next step consists in correcting errors due to the Eddington approximation by integrating source terms f_{ne}

$$f_{ne} = \begin{pmatrix} 0 \\ -(\lambda - 1/3)\nabla E_{\rm r} \\ -(\lambda - 1/3)(\mathbf{u}\nabla E_{\rm r} + E_{\rm r}\nabla : \mathbf{u}) \\ \mathbb{P}_{\rm r}\nabla : \mathbf{u} \end{pmatrix}. \tag{4.42}$$

A drawback comes from the fact that computing the flux limiter λ involves an additional storage of $\nabla E_{\rm r}$.

4.2.2 The implicit radiative scheme

The most demanding step in our time-splitting scheme is to deal with diffusion and coupling terms. This update has to be done with an **implicit** scheme, since time scales involved are much shorter than those of pure hydrodynamical processes. Two coupled equations are integrated in such a way

$$\left\{ \begin{array}{lcl} \partial_t \rho\varepsilon & = & -\kappa_{\rm P}\rho{\rm c}(a_{\rm R}T^4 - E_{\rm r}) \\ \partial_t E_{\rm r} - \nabla\frac{{\rm c}\lambda}{\kappa_{\rm R}\rho}\nabla E_{\rm r} & = & +\kappa_{\rm P}\rho{\rm c}(a_{\rm R}T^4 - E_{\rm r}) \end{array} \right. , \tag{4.43}$$

which give the implicit scheme on an uniform grid[1]

$$\left\{ \begin{array}{lcl} \frac{C_v T^{n+1} - C_v T^n}{\Delta t} & = & -\kappa_{\rm P}^n \rho^n {\rm c}(a_{\rm R}(T^{n+1})^4 - E_{\rm r}^{n+1}) \\ \frac{E_{\rm r}^{n+1} - E_{\rm r}^n}{\Delta t} - \nabla\frac{{\rm c}\lambda^n}{\kappa_{\rm R}^n\rho^n}\nabla E_{\rm r}^{n+1} & = & +\kappa_{\rm P}^n \rho^n {\rm c}(a_{\rm R}(T^{n+1})^4 - E_{\rm r}^{n+1}) \end{array} \right. , \tag{4.44}$$

where $\rho\varepsilon = C_v T$. The nonlinear term $(T^{n+1})^4$ makes this scheme hard to invert. On the other hand, it is much easier to solve implicitly a linear system. Assuming that changes of temperature are small within a time step, we can write

$$(T^{n+1})^4 = (T^n)^4 \left(1 + \frac{(T^{n+1} - T^n)}{T^n}\right)^4 \approx 4(T^n)^3 T^{n+1} - 3(T^n)^4. \tag{4.45}$$

Eventually, with (4.44a) we obtain T_i^{n+1} as a function of T_i^n and $E_{{\rm r},i}^{n+1}$. Then T_i^{n+1} can be directly injected in the radiative energy equation (4.44b), and $E_{{\rm r},i}^{n+1}$ is finally expressed as a function of $E_{{\rm r},i+1}^{n+1}$, $E_{{\rm r},i-1}^{n+1}$, $E_{{\rm r},i}^n$ and T_i^n. The implicit scheme for the radiative energy in a cell of volume V_i in the $x-$direction becomes

$$\begin{aligned} (E_{r,i}^{n+1} - E_{r,i}^n)V_i - c\Delta t \left(\frac{\lambda}{\kappa_{\rm R}\rho}\right)_{i+1/2} S_{i+1/2}\frac{E_{r,i+1}^{n+1} - E_{r,i}^{n+1}}{\Delta x_{i+1/2}} + c\Delta t \left(\frac{\lambda}{\kappa_{\rm R}\rho}\right)_{i-1/2} S_{i-1/2}\frac{E_{r,i}^{n+1} - E_{r,i-1}^{n+1}}{\Delta x_{i-1/2}} \\ = c\Delta t \kappa_{{\rm P},i}^n \rho_i^n \left(4a_{\rm R}(T_i^n)^3 T_i^{n+1} - 3a_{\rm R}(T_i^n)^4 - E_{r,i}^{n+1}\right) V_i, \end{aligned} \tag{4.46}$$

[1]Index n and $n+1$ are used for variables before and after the implicit update. Exit of the explicit hydrodynamics scheme supplies variables with index n. It does not match the variables at time t^n and t^{n+1}.

Therefore, with

$$C_{i+1/2} = c\Delta t \left(\frac{\lambda}{\kappa_{\mathrm{R}}\rho}\right)_{i+1/2} \frac{S_{i+1/2}}{\Delta x_{i+1/2}}, \tag{4.47}$$

and

$$\omega_i = c\Delta t \kappa^n_{\mathrm{P},i}, \tag{4.48}$$

we have

$$-C_{i-1/2}E^{n+1}_{r,i-1} + \left[V_i + \omega_i \rho^n_i \left(1 - \frac{4\omega_i a_{\mathrm{R}}(T^n_i)^3}{C_v + 4\omega_i a_{\mathrm{R}}(T^n_i)^3}\right) V_i + C_{i-1/2} + C_{i+1/2}\right] E^{n+1}_{r,i} - C_{i+1/2}E^{n+1}_{r,i+1}$$
$$= \frac{\omega_i a_{\mathrm{R}}(T^n_i)^3}{C_v + 4\omega_i a_{\mathrm{R}}(T^n_i)^3} C_v T^n_i V_i + E^n_{r,i} V_i. \tag{4.49}$$

The gas temperature within a cell is simply given by

$$T^{n+1}_i = \frac{3a_{\mathrm{R}}\kappa^n_{\mathrm{P},i}c\Delta t\,(T^n_i)^4 + C_v T^n_i + \kappa^n_{\mathrm{P},i}c\Delta t E^{n+1}_{r,i}}{C_v + 4a_{\mathrm{R}}\kappa^n_{\mathrm{P},i}c\Delta t\,(T^n_i)^3}. \tag{4.50}$$

Note that we compute the Planck and Rosseland opacities and the flux limiter with a gas temperature value given before the implicit update (with index n), in order to preserve linearity of the solver.

4.2.3 Implicit scheme integration

Conjugate Gradient algorithm

Equation (4.49) is solved on a full grid, made of N cells. It results in a system of N linear equations, that can be written as a linear system of equations

$$Ax = b \tag{4.51}$$

where x is a vector containing radiative energy values. The Conjugate Gradients (CG) method is one of the most popular non-stationary iterative method for solving large systems of linear equations $Ax = b$. CG method can be used if the matrix A to be inverted is square, symmetric and positive-definite (which is our case!). The CG is memory-efficient (no matrix storage) and runs quickly with sparse matrices. For a $N \times N$ matrix, the CG converges in less than N iterations. Basically, CG method is a steepest gradient descent method in which descent directions are updated at each iteration. The method proceeds by generating vector sequences of iterates $x^{(i)}$ (i.e., successive approximation of the solution), residuals $r^{(i)}$ corresponding to the iterates, and searches directions used in updating the iterates and residuals. Although the length of these sequences can become large, only a small number of vectors needs to be stored. In every iteration, the CG method involves one matrix-vector product, three vector updates and three dot products that are performed in order to compute update scalars defined to make the sequences satisfy certain orthogonality conditions. Another advantage is that the CG method can be run easily on parallel machines.

The iterates $x^{(i)}$ are updated in each iteration by a multiple (α_i) of the search direction vector $p^{(i)}$

$$x^{(i+1)} = x^{(i)} + \alpha_i p^{(i)}. \tag{4.52}$$

Correspondingly, the residual vectors $r^{(i)} = b - Ax^{(i)}$ must satisfy the recurrence

$$r^{(i+1)} = r^{(i)} - \alpha_i q^{(i)} \quad \text{where} \quad q^{(i)} = Ap^{(i)}. \tag{4.53}$$

The choice $\alpha = \alpha_i = r^{(i)^T} r^{(i)} / p^{(i)^T} A p^{(i)}$ minimizes $r^{(i+1)^T} A^{-1} r^{(i+1)}$ over all possible choices for α in equation (4.53). Search directions are updated using the residuals

$$p^{(i+1)} = r^{(i+1)} + \beta_i p^{(i)}, \tag{4.54}$$

where the choice $\beta_i = r^{(i+1)^T} r^{(i+1)} / r^{(i)^T} r^{(i)}$ ensures that $p^{(i)}$ and $Ap^{(i-1)}$ are orthogonal.

In order to improve convergence of CG or even to insure convergence in case of an ill-conditioned matrix A, we use a preconditioning matrix M which approximates A. M is also assumed to be symmetric and positive definite. In practice, the only requirement for M is that it is inexpensive to solve linear systems, $Mx = b$. This is because the preconditioned algorithm requires to solve the linear system at each step.

The Preconditioned Conjugate Gradient algorithm is

1. Compute the initial residual $r^{(0)} = b - Ax^{(0)}$, $p^{(0)} = z^{(0)}$ and $z^{(0)} = M^{-1} r^{(0)}$;
2. **For** j=0,1,..., until convergence **Do**:
3. $\alpha_j = r^{(j)^T} z^{(j)} / q^{(j)^T} p^{(j)}$;
4. $x^{(j+1)} = x^{(j)} + \alpha_j p^{(j)}$;
5. $r^{(j+1)} = r^{(j)} - \alpha_j A p^{(j)}$;
6. solve $M.z^{(j+1)} = r^{(j+1)}$;
7. $\beta_j = r^{(j+1)^T} z^{(j+1)} / r^{(j)^T} z^{(j)}$;
8. $p^{(j+1)} = z^{(j+1)} + \beta_j p^{(j)}$;
9. **End Do**.

In this work, we use a simple diagonal preconditioning matrix, which retains only the inverse of A diagonal elements. Convergence is estimated following two criteria: norm L^2, criterion $||r^{(j)}||/||r^{(0)}|| < \varepsilon$ or norm L^∞, maximum residual value $\max\{r^{(j)}\}/\max\{r^{(0)}\} < \varepsilon$. Values of ε typically range from 10^{-8} to 10^{-3}. We present in appendix an alternative method to the conjugate gradient, which can be used efficiently on uniform grids or in some particular cases.

4.2.4 Implicit scheme on an AMR grid

In the context of star formation, it is necessary to extend our implicit scheme to AMR grids. The difficulty comes from computing the right fluxes and gradients at the interfaces between two cells. We need to consider carefully the energy balance that is done on a given volume. On a regular grid, we do not have to worry about this. Energy balances are thus done on volumes overlapping two cells, that depends on whether the mesh is refined or not. Consider the face of a cell on level ℓ, 3 connecting configurations with other cells are possible (see figure 4.6):

- Configuration 1: the neighboring cell is at the same level ℓ: cells 1 and 3,
- Configuration 2: the neighboring cell is at level $\ell - 1$: cells 1 and i,
- Configuration 3: 2 neighboring cells exist at level $\ell + 1$: cell i with cells 1 and 2.

Our diffusion routine is called only once per coarse step. If finer levels evolve with their own time steps, only their hydrodynamic an gravitational parts will advance in time. Our method scans the full grid, begins with finer cells and then goes to cells on coarser levels and so on... The grid is always scanned from finer to coarser levels. In order to optimize matrix-vectors products, we choose to avoid dealing with configuration 3. Hence, when cells at level $\ell+1$ are monitored, values for cells at level ℓ will be updated. Configurations 2 and 3 are then performed at the same time. Depending on the configuration, gradients and flux estimates are different. In the following, we will focus on cell 1, of size $\Delta x \times \Delta x$.

Figure 4.6: Example of AMR grid configuration

Gradient estimate

Gradients ∇E_r are estimated between the two neighboring cells center:

- Configuration 1: $(\nabla E_r)_{1,3} = \frac{E_{r,1}-E_{r,3}}{\Delta x}$
- Configuration 2: $(\nabla E_r)_{1,i} = \frac{E_{r,1}-E_{r,i}}{3\Delta x/2}$

Flux estimate

Let S^ℓ be the surface of interface of a cell at level ℓ and $F^\ell_{i,j}$ the flux across this surface between two cells i and j. The energy rate $F \times S$ that is exchanged at this interface is:

- Configuration 1: $F^\ell_{1,3} \times S^\ell = \frac{E_{r,1}-E_{r,3}}{\Delta x} \times S^\ell$
- Configuration 2: $F^\ell_{1,i} \times S^\ell = \frac{E_{r,1}-E_{r,3}}{\Delta x} \times S^\ell$
- Configuration 3: $F^\ell_{i,1,2} \times S^{\ell-1} = F^\ell_{i,1} \times S^\ell + F^\ell_{i,2} \times S^\ell$

Since access to neighboring finer cells is not straightforward, we see from configuration 3 all the interest of updating quantities at level $\ell-1$ when scanning grid at level ℓ. The choice of $\Delta x_{i-1/2}$ and $S_{i+1/2}$ in equation (4.46) must then be done carefully in order to conserve energy properly.

4.2.5 Limits of the methods

The first drawback is the use of the FLD approximation that implies isotropy of the radiation field. Anisotropies in transparent regime are not well processed with FLD, contrary to more accurate models like M1 or VETF (Hayes and Norman 2003). A second limitation comes from the grey opacity assumption.

From a technical point of view, our method works only for unique time stepping, i.e. all levels evolve with the same time step. We do not take advantage of the multiple time stepping faculty. As a compromise, we investigate the possibility to evolve finer levels with their own time steps and perform a diffusion-coupling steps every 2, 4 or more finer time step (see §4.4.4). A future development would be to use a multigrid solver or preconditioner for parabolic equations (Howell and Greenough 2003).

Another difficulty comes from the residual norm and scalar α_j, β_j estimates in the CG algorithm. For large grid with a large number of cells, the dot product can be dominated by round-off errors, due to estimates close to machine precision. This becomes even worse in parallel calculations. The usual MPI function MPI_SUM gives strange results, the results of any sum becoming a function of number of processors... This affects dramatically the number of iterations. We implement a new MPI function that performs summation in double-double precision following He and Ding (2000), using the Knuth (1997) trick. In double-double precision arithmetics, each floating point number is represented by two double precision numbers. In fact, the bits in the second double precision number are an extended mantissa of the first double precision number. The dynamic range of the double-double precision number remains the same as the double precision number. One may think the first double precision number as the summation result, and the second double precision number as the estimated rounding error.

Eventually, our method involves only immediate neighboring cells, whatever their refinement level is. This could give rise to loss of accuracy in diffusion problems, since gradient estimates are not second order accurate, when neighboring cells are at finer levels (see configuration 3, Popinet 2003). However, the tests we have been performing, ascertain that the method is nevertheless accurate.

4.3 Radiation solver tests

4.3.1 1D test: linear diffusion

We consider in this test only the radiative energy diffusion equation, without hydrodynamics and coupling with the gas. The equation to integrate is simply

$$\frac{\partial E_{\rm r}}{\partial t} - \nabla \cdot \left(\frac{c}{3\rho\kappa_{\rm R}} \nabla E_{\rm r} \right) = 0. \tag{4.55}$$

Consider a box of length L=1. The initial radiative energy corresponds to a Dirac function, namely it is equal to 1 everywhere in the box, except at the center where it amounts to $E_{\rm r,L/2} = 1 \times 10^5$. To simplify, we choose $\rho\kappa_{\rm R} = 1$ and a constant time step. We apply Von Neumann boundary conditions, i.e. zero-gradient. The analytical solution in a *dim*-dimensional problem is given by

$$E_{\rm r}(x,t) = \frac{E_0}{2^{dim}(\pi\chi t)^{dim/2}} e^{-\left(\frac{x^2}{4\chi t}\right)}. \tag{4.56}$$

Resolution	CPU time (s)	$N_{\rm iter}$ CG	$\rm N_{\Delta t}$	$N_{\rm iter}/N_{\Delta t}$
32	3.5	507	51	9.9
64	7.1	1057	102	10.4
128	14.36	2173	205	10.6
128 (sub)	14.97	2284	205	11.1
256	30.85	4806	409	11.8
256 (sub)	31.8	4922	409	12
256 (pre)	31.	4789	409	11.7

Table 4.1: CPU time, total number of iterations and number of "CFL" time steps for various numbers of cells. Sub-cycling (sub) or preconditioning (pre) are activated or not. Sub-cycling is not efficient in terms of CPU time and number of iterations, but solutions are more accurate.

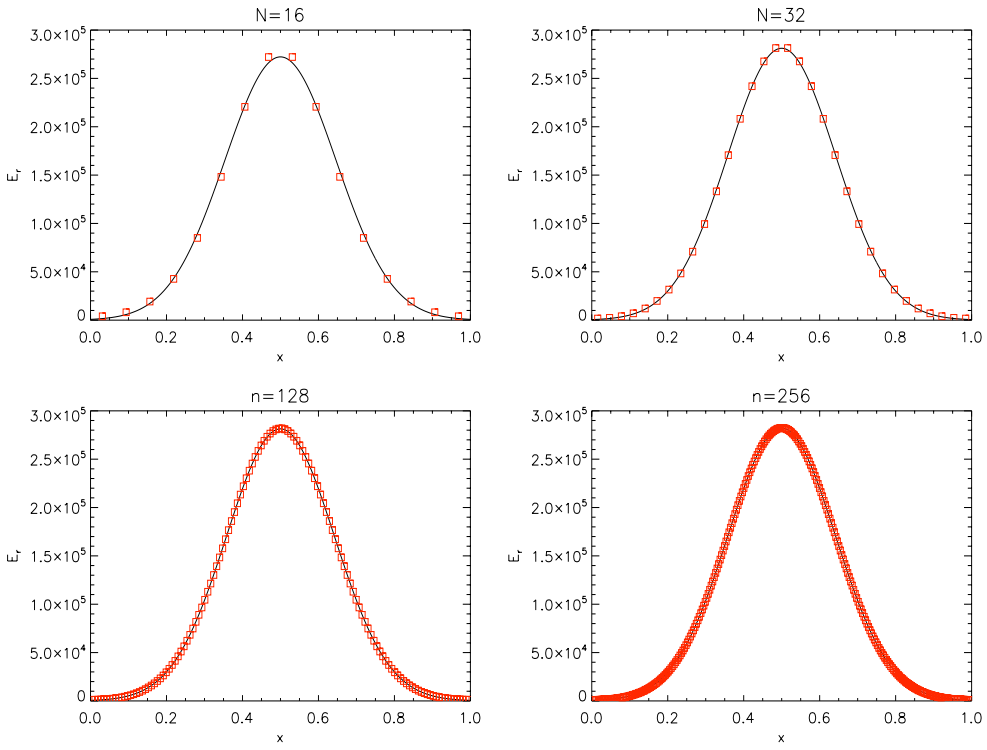

Figure 4.7: Comparison between numerical solution (squares) and analytical solution (line) at time t=1×10^{-12} for calculations with 16, 32, 128 and 256 cells. Subcycling is activated.

Subcycling

Although the implicit scheme for the diffusion equation is unconditionally stable, its accuracy deteriorates when time step becomes too large. It is even worse when the diffusion coefficient, i.e. the opacity, depends on the temperature (non-linear diffusion). In this case, a good way to avoid inaccurate solutions is to limit the time step according to the radiative energy variations (i.e. $||\Delta E_{\rm r}||/||E_{\rm r}|| < \varepsilon$). This can be efficient for steep gradients (e.g. Dirac) and when the time step given by the CFL condition is too large.

Equation (4.44b) can be written in the form

$$\frac{\Delta E_{\rm r}}{\Delta t} = f(E_{\rm r}), \tag{4.57}$$

or

$$\frac{||\Delta E_{\rm r}||}{||E_{\rm r}||} = \Delta t \frac{||f(E_{\rm r})||}{||E_{\rm r}||}. \tag{4.58}$$

Hence, for a given ε

$$\Delta t = \varepsilon \frac{||E_{\rm r}||}{||f(E_{\rm r})||} < \frac{||\Delta E_{\rm r}||}{||E_{\rm r}||} \frac{||E_{\rm r}||}{||f(E_{\rm r})||} \tag{4.59}$$

The first sub-cycling time step is evaluated with the initial values of the radiative energy and of the temperature and is revaluated after convergence for a new CG solving, until the CFL time step is reached. Note that this subcycling method is only used for this test. The accuracy without subcycling appears to be sufficient in most of the next cases.

Figure 4.7 shows results at the same time for different resolutions of the box: 16, 32, 128 and 256 cells. Numerical solution is very close to the analytical one, even with a small number

of cells. In table 4.2, we report the CPU time, the total number of iterations and the number of "CFL" time steps for various numerical resolutions. At low resolution, the number of time steps increases linearly with the number of cells, as well as the CPU time. The number of iterations per time step is constant, i.e. the convergence of CG does not depend on the dimension of the problem, but on the nature on the problem.

4.3.2 1D test: non linear diffusion

Consider a box made of two media with different initial radiative energy states: $E_{\rm r} = 4$ on the left and $E_{\rm r} = 0.5$ on the right. We apply Von Neumann boundary conditions. We integrate the same equation as in the previous test, but with a Rosseland opacity as a nonlinear function of the radiative energy, i.e. $\rho\kappa_{\rm R} = 1 \times 10^{11} E_{\rm r}^{-1.5}$. Last, we allow refinement with a criterion based on radiative energy gradients. In each region where $\nabla E_{\rm r}/E_{\rm r} > 10$ %, the grid is refined.

Figure 4.8(a) shows the radiative energy profiles at different times. Because of the nonlinear opacity, diffusion is more efficient in the high energy region. The mean opacity at cell interface is computed using an arithmetic average, most adapted in case of non-linear opacity. In figure 4.8(b), we report results at time $t = 1.4 \times 10^{-2}$ and AMR level profile (red curve - right axis). Levels are finer in high radiative energy gradient zones. Note that we check that we get similar results in a 2D plane parallel case and in a 2D case with an initial step function making an angle of $\pi/4$ with the computational box axis. This validates our routine in the x and y directions.

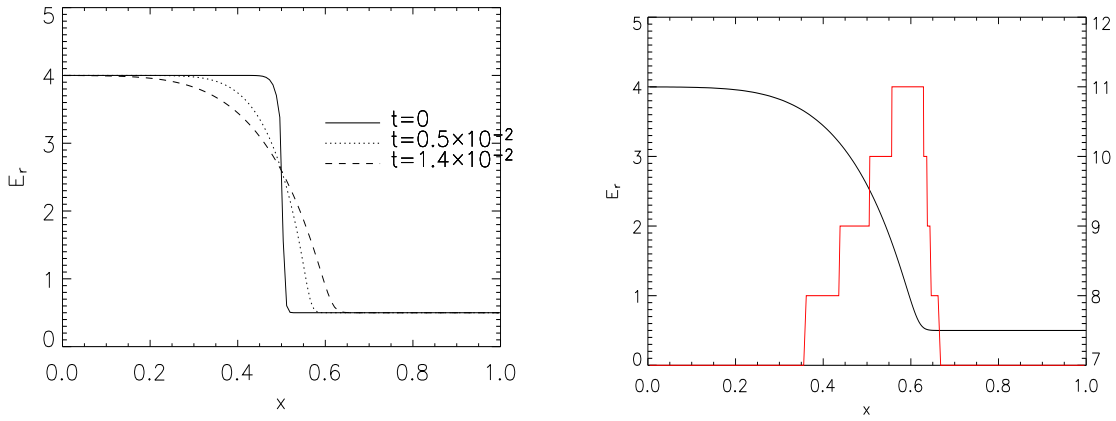

Figure 4.8: Non linear diffusion of an initial step function with AMR plugged in, the refinement criterion based on radiative energy gradients. (a) Radiative energy profiles at 3 different times. The diffusion is more efficient in low opacity regions. (b) AMR levels displayed at time $t = 1.4 \times 10^{-2}$ (red curve - right axis). High resolution zones match with steep gradients of radiative energy.

4.3.3 2D test: linear diffusion

We perform the same test as for the 1D case (§4.3.1), but in a square box with a 2D Dirac function for the radiative energy located at the center. We let the radiative energy diffuse using AMR or not. Figure 4.9 shows results without AMR (left column) and with AMR (right column). Uniform grid calculations have been performed on a 256^2 grid and AMR calculations using a 64^2 coarse grid and 2 levels of refinement, giving an effective resolution of 256^2. In the upper plots, radiative energy profiles (crosses) are in good agreement with the analytic solution

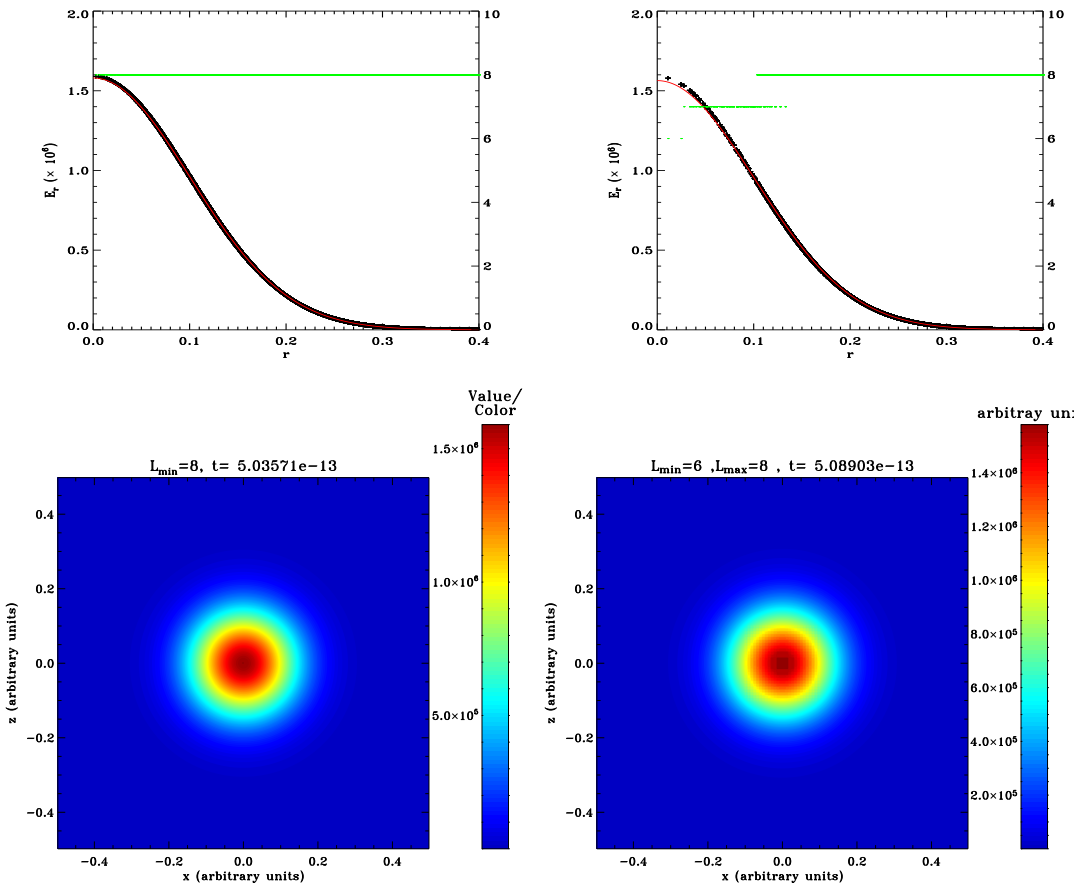

Figure 4.9: 2D linear diffusion test. Top panels give radiative energy profile as a function of the radius. Bottom panels show radiative energy contours with a linear scale for a 256^2 grid. Left column reports calculations done without AMR, and in the right column, AMR is de-refined in cells where radiative energy gradients exceed 10%. The coarse grid is 64^2 and 2 levels of refinement are used.

(red curve). AMR levels are also depicted (right axis - green points). For AMR calculations, the full grid is refined, the criterion on the gradients being too strict (10%). Bottom panels give contours of the radiative energy at similar times. We note that in the AMR calculations, the grid has been unrefined in the center, causing a poor resolution and a loss of accuracy.

Table 4.2 summaries the calculations performed with or without AMR. The CPU time and the total number of iterations are given. The number of iterations is greater when AMR is used, this is due to our unique time step solver for radiation. However, CPU time decreases with AMR, less grids being involved in the calculations. Although a unique time step is used, we recover the benefits of AMR. Note also that the total number of iterations is almost the same, thanks to the new MPI_SUMDD function used to avoid rounding errors (He and Ding 2000).

4.3.4 Sod test without coupling matter/radiation

The next step in our tests cases consists of including hydrodynamics, without coupling between material and radiation and with the flux limiter set to $\lambda = 1/3$. Hence, only the hyperbolic system (4.35) is integrated. We checked in a preliminary test that the radiative energy was

Resolution	$N_{\rm CPUs}$	CPU time (s)	$N_{\rm iter}$
$2^6 - 2^8$	1	191.5	8696
$2^6 - 2^8$	2	117.7	8691
$2^6 - 2^8$	3	95.9	8683
$2^6 - 2^8$	4	81.8	8687
2^8	1	335.3	4159
2^8	2	199.4	4153
2^8	3	145.5	4159
2^8	4	129	4158

Table 4.2: 2D linear diffusion test: CPU time and total number of iterations over 150 coarse time steps for four calculations with (top lines) AMR and four calculations (bottom lines) without AMR, performed using various numbers of processors.

correctly advected. Then, a common test for the accuracy of computational fluid codes is the Sod test (Sod 1978), that reproduces shock tube conditions. The test consists in a one dimensional Riemann problem with given left $\mathbb{U}_{\rm L}$ and right $\mathbb{U}_{\rm R}$ states. The time evolution is described by solving the Euler equations for a radiating fluid, the total pressure being the sum of the thermal and radiative pressures. Initial conditions are: ρ_1=1, $P_1 = 1$, $E_{\rm r,1} = 1 \times 10^{-4}$, ρ_2=0.125, $P_2 = 0.1$ and $E_{\rm r,2} = 1 \times 10^{-5}$. We used the *minmod* slope limiter and the HLL Riemann solver. Refinement was achieved according to density, velocity and thermal pressure gradients (5%).

The results are reported in figure 4.10, where we show the velocity, radiative energy, pressure and density profiles obtained with the numerical simulation (squares) and the analytic solution (red curve). In the density profile, we also display AMR levels (green curve). The analytic solution is convincingly reproduced. Radiative energy and thermal pressure behave like the density, being discontinuous at the entropy wave, since total pressure is the continuous quantity at this contact discontinuity. We do not discern the discontinuity in the thermal pressure profile, because the influence of the radiative pressure is too low.

4.3.5 Matter-Radiation coupling test

A less conventional test is the matter-radiation coupling. Consider a static, uniform, absorbing fluid initially out of thermal balance, in which the radiation energy $E_{\rm r}$ dominates and is constant. An analytic solution can be obtained for the time evolution of the gas energy e, by solving the ordinary differential equation (Turner and Stone 2001)

$$\frac{de}{dt} = c\sigma E_{\rm r} - 4\pi\sigma B(e). \tag{4.60}$$

We performed two tests, with two initial gas energies, $e = 10^{10}$ erg cm^{-3} and $e = 10^2$ erg cm^{-3}. In both tests, the following quantities are taken constant: the radiative energy $E_{\rm r} = 1 \times 10^{12}$ erg cm^{-3}, the opacity $\sigma = 4 \times 10^{-8}$ cm^{-1}, the density $\rho = 10^{-7}$ g cm^{-3}, the mean molecular weight $\mu = 0.6$ and the adiabatic index $\gamma = 5/3$. Figure 4.11 shows the evolution in time of the gas energy for the analytic solution (red line) and the numerical solution (crosses). In the first calculations, where the initial gas temperature is greater than the radiative temperature, we used a variable time step Δt that increases with time, starting from 10^{-20} s. This good sampling gives very good results. In the second case, we use a constant time step $\Delta t = 10^{-12}$ s. Although the sampling is bad at early times and longer than the cooling time, numerical solutions always match the analytic one. This validates our linearization procedure in equation (4.45).

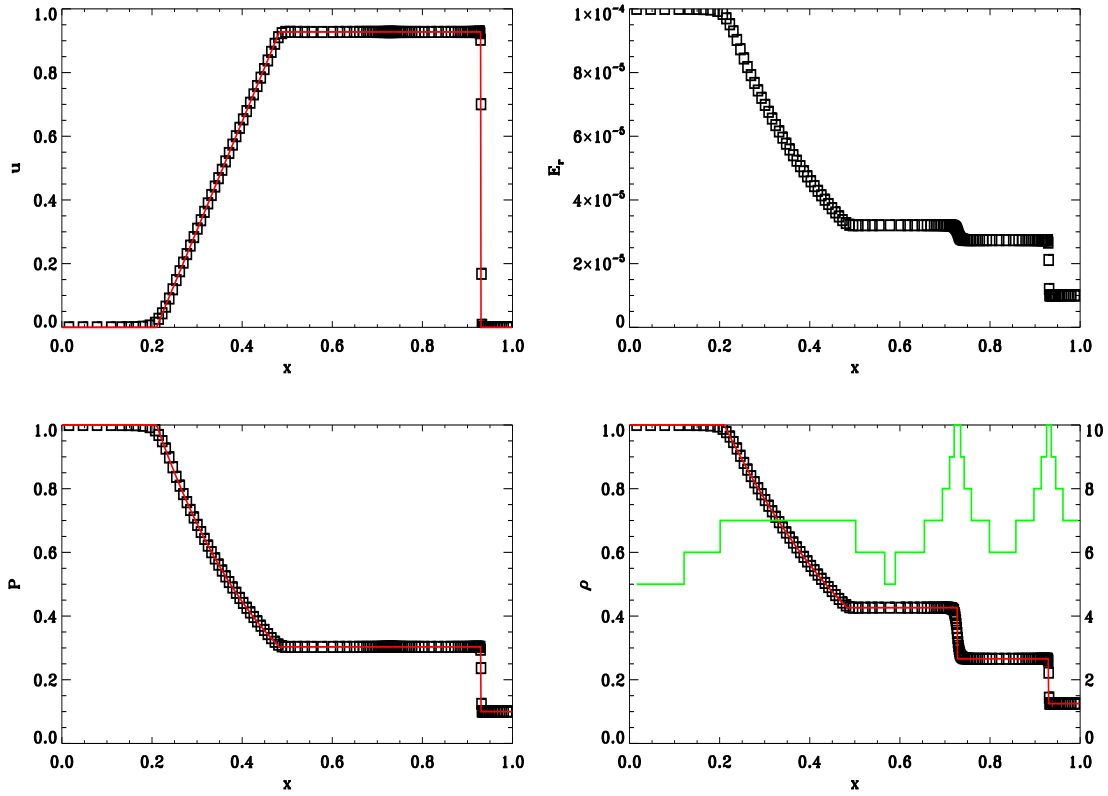

Figure 4.10: Classical Sod shock tube test for a radiating fluid without matter/radiation coupling.

4.3.6 1D full RHD tests: Radiative shocks

Radiative shocks have been introduced in §3.5. Testing our method against radiative shocks calculations is a last important step that every code attempting to integrate RHD equations should pass. Following Ensman (1994) initial conditions, we test our routine for sub- and super-critical radiative shocks. We also compare our solutions with those obtained by the ZEUS code, integrating also the FLD approximation (Hayes et al. 2006).

Initial conditions are as follows: a uniform density $\rho_0 = 7.78 \times 10^{-10}$ g cm^{-3} and temperature T_0=10 K. The box length is L=7 $\times$ 10^{-10}cm, the opacity is constant ($\sigma = 3.1 \times 10^{-10}$ cm^{-1}), $\mu = 1$ and $\gamma = 7/5$. The 1D homogeneous medium moves with a uniform speed (piston speed) from right to left and the left boundary is a wall. The shock is generated at this boundary and travels backwards. The piston velocity varies, producing sub- or super-critical radiative shocks. The refinement criterion is based on density gradients (10%), and the grid has 32 coarse cells and we use five levels of refinement. We use the Minerbo flux limiter. Note that we have implemented both Minerbo and Levermore-Pomraning flux limiters, the differences between both being very small. We do not allow subcycling in the diffusion routine, since it appears to be useless in that case. The time step is given by the hydrodynamics CFL for explicit and implicit schemes, with $C_{\rm CFL} = 0.5$.

Figure 4.12 shows the gas (solid line) and radiative (dashed line) temperatures for sub- and super-critical radiative shocks, as a function of $z = x - vt$, where v is the piston's velocity. In both calculations, AMR is included. The subcritical shock is obtained with a piston's velocity $v = 6$ km s^{-1}, whereas the supercritical shock is obtained with $v = 20$ km s^{-1}. In both tests,

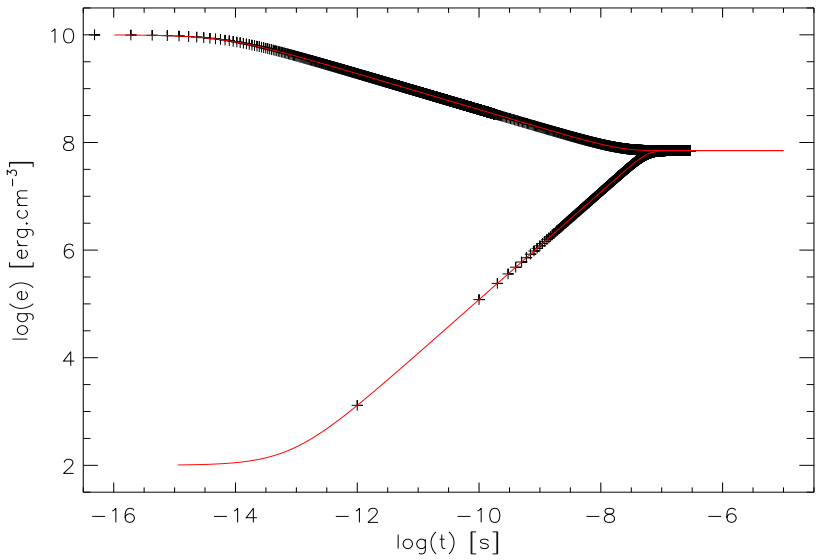

Figure 4.11: Matter/radiation coupling test. The radiative energy is kept constant, $E_r = 1\times10^{12}$ erg cm^{-3}, whereas the initial gas energies are out of thermal balance ($e = 10^2$ erg cm^{-3} and $e = 10^{10}$ erg cm^{-3}). Numerical (crosses) and analytic (red curve) evolutions of gas energy are given as a function of time.

the extended, non-equilibrium, radiative precursor is evident. As expected, in the supercritical case, pre- and post-shock gas temperatures are equal.

For the subcritical case, the postshock gas temperature is given by (Ensman 1994; Mihalas and Mihalas 1984)

$$T_2 \approx \frac{2(\gamma-1)v^2}{\mathcal{R}(\gamma+1)^2}, \tag{4.61}$$

where $\mathcal{R} = k/\mu m_{\rm H}$ is the gas constant. For our initial setup, this analytic estimate gives $T_2 \sim 810$ K. Numerical calculations give T_2 in good agreement with the analytic estimate, comparable to values obtained with more accurate methods (González et al. 2007). The characteristic temperature T_- immediately in front of the shock is in good agreement with the analytic estimate (Mihalas and Mihalas 1984)

$$\frac{\rho v R T_-}{\gamma-1} = \frac{2\sigma_{\rm R} T_2^4}{\sqrt{3}} \sim 276\,{\rm K}. \tag{4.62}$$

This means that, in front of the shock, the gas internal energy flux flowing downstream is equal to the radiative flux flowing upstream. All the radiative energy is absorbed upstream and contribute to heat the gas.

Similarly, the spike temperature, given by

$$T_+ - T_2 = \frac{3-\gamma}{\gamma+1} T_- \sim 980\,{\rm K}, \tag{4.63}$$

is also in good agreement with the analytic estimate of Mihalas and Mihalas (1984).

AMR enables to describe carefully the gas temperature spike at the shock. The medium around the spike is optically thin, and the numerical resolution in this region is therefore of overriding importance. The spike's amplitude varies according to the model used for radiation and to the effective numerical resolution. Thanks to AMR, spike's amplitude is larger in the supercritical case, but not as large as those obtained with M1 or VTEF models (González et al.

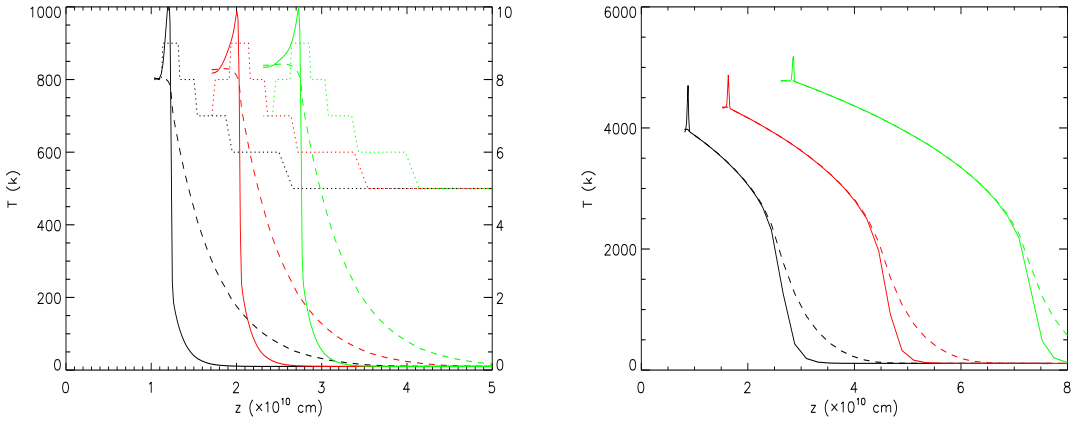

Figure 4.12: *Left*: Temperature profiles for a subcritical shock with piston velocity $v = 6$ km s^{-1}, at times $t = 1.7 \times 10^4$ s (black), 2.8×10^4 s (red) and 3.8×10^4 s (green). AMR levels (dotted line - right axis) are plotted. *Right*: Temperature profiles for a supercritical shock with piston velocity $v = 20$ km s^{-1}, at times $t = 4 \times 10^3$ s (black), 7.5×10^3 s (red) and 1.3×10^4 s (green). In both cases, the gas (solid line) and radiative (dashed line) temperatures are displayed as a function of $z = x - vt$.

2007; Hayes and Norman 2003). However, this last test shows the ability of our time-splitted method to integrate RHD equations.

Comparison with ZEUS code

We compare our results with those obtained with the ZEUS code (Hayes et al. 2006). We use in ZEUS the same initial conditions and the same flux limiter as in RAMSES. Figure 4.13 shows the gas and radiative temperatures profiles (left plot) and the density profiles (right plot) for RAMSES (black line) and ZEUS (red line), at $t = 3.8 \times 10^4$ s, for a subcritical shock. Results are very similar, the radiative precursors have the same extension. A small difference appears in the spike amplitude, which is larger with RAMSES. This could be due to the fact that ZEUS uses artificial viscosity. Last but not least, for a given resolution (512 cells), the same CFL number and convergence criteria, RAMSES appears to be 4 times faster than ZEUS. Indeed, matrix inversion in ZEUS uses Newton-Raphson iterations and is more heavy than the CG algorithm we used.

Assuming that ZEUS has been world-widely tested, this final agreement brings conventional testing of our routine to an end. After a short scalability study, the next step is to apply our method to protostellar collapse.

4.3.7 Scalability test

We present here the scalability performance of our radiative solver. We have performed 3D calculations on 1, 8 and 64 processors with respectively 64^3, 128^3 and 256^3 cells. In figure 4.14, we plot the CPU time per cell as a function of the number of processors. CPU times have been normalized with the value obtained with 1 processor. We see an overhead at large number of processors (13%), but not significant. This is due to the high number of global communications (e.g. MPI_ALLREDUCE function) involved in the Conjugated Gradient algorithm. However, in low mass star formation calculations, only a few processors (8) are needed for a good scalability. The overhead due to our radiative solver will thus not be high.

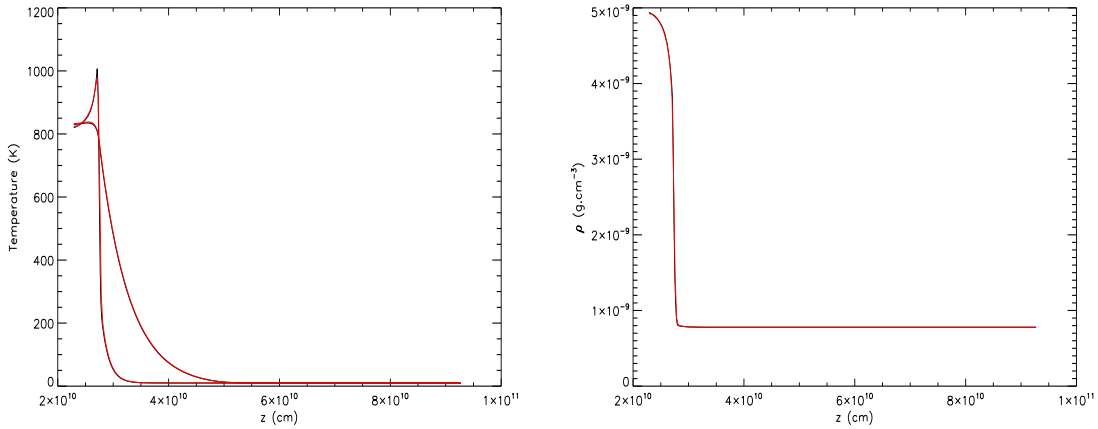

Figure 4.13: Comparison between ZEUS (red line) and RAMSES (black line) calculations for a subcritical shock at time $t = 3.8 \times 10^4$ s. We show gas and radiative temperatures profiles (left plot) and density profiles (right plot) as a function of $z = x - vt$.

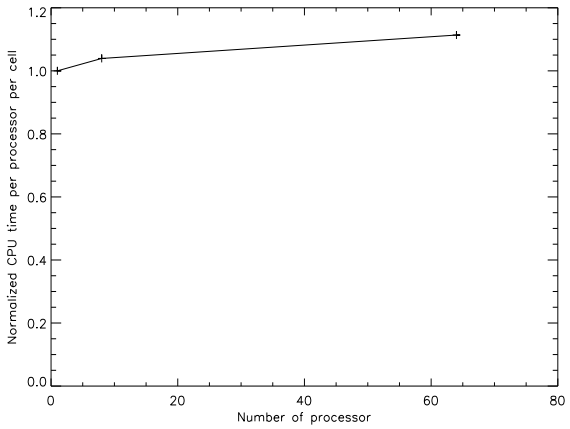

Figure 4.14: Normalized CPU time per processor and per cell for calculations done with 1, 16 and 64 processors. In each case, each processor has 64 cells to monitor.

4.4 Dense core collapse calculations

In this last section, we perform 1 $M_\odot$ dense core collapse calculations with the Flux Limited Diffusion approximation. We first make a comparison with results obtained with the 1D code, for a model without rotation. Then, we quickly look at the effect of the flux limiter on fragmentation. Eventually, we try to speed up calculations using very simply the AMR adaptive time stepping and find that it can strongly alter fragmentation. Note that in this section, we only give a qualitative overall picture of our results. We will consider in more details the effects of the radiative transfer in chapter 6.

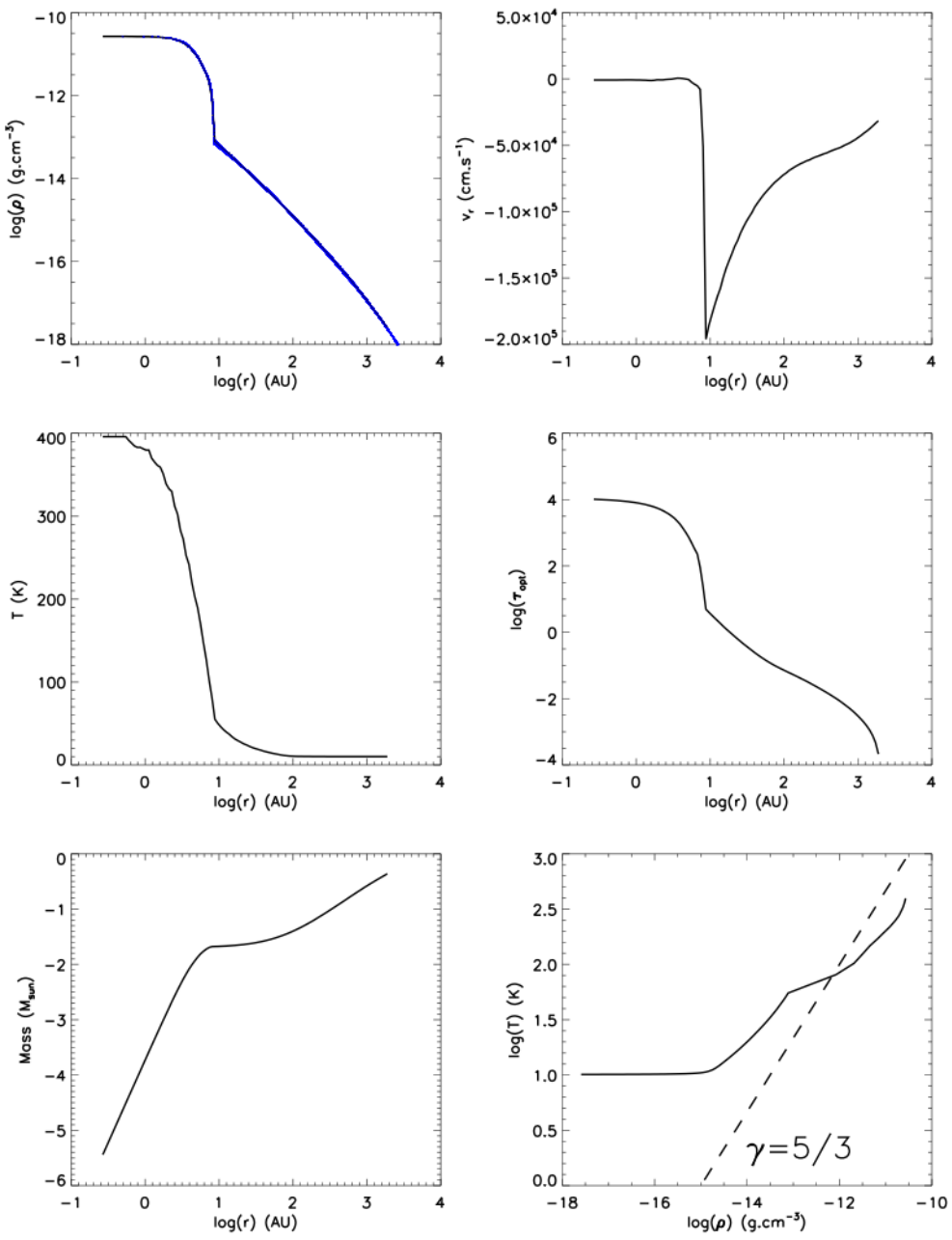

Figure 4.15: Profiles of density, radial velocity, temperature, optical depth and integrated mass as a function of the radius and the temperature as a function of density in the 3D computational domain. All values are computed at time t =1.012 $t_{\rm ff}$.

4.4.1 Initial conditions for RAMSES star formation calculations

One practical limitation of AMR codes is the use of Cartesian grids. RAMSES works with a cubic volume, so that a part of the calculation box is lost when we describe a sphere. The outer region of the sphere is at the same temperature as the core temperature but is 100 times less dense. The outer gas has no effect on the dynamics of the sphere because the two parts are well-separated. The sphere radius is equal to a quarter of the box length in order to minimize border effects.

4.4.2 Collapse without rotation

For this first collapse test, we choose highly gravitationally unstable initial conditions. The initial sphere is isothermal $T_0 = 10$ K and has a uniform density $\rho_0 = 1.38 \times 10^{-18}$ g cm^{-3}. The ratio α between initial thermal energy and gravitational energy is $\alpha \sim 0.50$. The initial radius is $R_0 = 7.07 \times 10^{16}$ cm. The theoretical free-fall time is $t_{\rm ff} = 57$ kyr. To resolve the Jeans length, we use $N_{\rm J} = 10$, i.e. 10 points per Jeans length. Masunaga et al. (1998) showed that, for low mass star formation, the first core properties are independent of the initial conditions. With our setup, we can compare these results with those obtained with the 1D code in chapter 3, even if we use different initial conditions.

$R_{\rm fc}$ (AU)	$M_{\rm fc}$ ($M_\odot$)	$\dot{M}$ ($M_\odot$/yr)	$L_{\rm acc}$ ($L_\odot$)	$T_{\rm c}$ (K)	$T_{\rm fc}$ (K)	$S_{\rm c}$ (erg K^{-1} g^{-1})	α
8	2.1×10^{-2}	3.7×10^{-5}	0.014	396	81	2.11×10^{9}	24

Table 4.3: Summary of first core properties at time t =1.012 $t_{\rm ff}$ and $\rho_c = 2.7 \times 10^{-11}$ g cm^{-3}.

In table 4.3, we summarize the first core properties obtained at time t =1.012 $t_{\rm ff}$ with RAMSES. First core radius and mass are quite similar to results obtained with the 1D code (see table 3.1). There is some difference in the temperature that is greater ($\sim 15\%$) at the first core border in the 3D calculations. However, since the 1D code and RAMSES are conceptually totally different, it is encouraging to get similar results with the multidimensional tools.

In figure 4.15, we show at time t =1.012 $t_{\rm ff}$ the profiles of density, radial velocity, temperature, optical depth and integrated mass as a function of the radius and the temperature as a function of the density in the computational domain. All quantities are mean values in the equatorial plane. In the density profiles, all the cells of the calculations have been displayed. The spread in the density distribution is very small. Thus, the spherical symmetry is well conserved in the 3D case. We compare these profiles with those in figure 3.7. The density jump between the first core border and the center is of the same order of magnitude as the 1D case. The infall velocity at the shock is also comparable ($\sim$ 2 km s^{-1}). The accretion shock takes place around $\tau \sim 5 - 10$, in the optically thick region. We do not see a jump in temperature through the accretion shock, which thus remains supercritical. Eventually, we see from the temperature versus density plot that the thermal behavior of the gas is not perfectly adiabatic in the central core. The slight kink in the curve at T$\sim$ 80 K (log(T)$\sim$ 1.7) corresponds to ice evaporation in the opacity table. The opacity decreases abruptly, this is the reason why the cooling is more efficient in that region.

4.4.3 Influence of the flux limiter

With the Flux Limited Diffusion approximation, we introduced an *ad hoc* flux limiter to preserve causality in the transport regime and especially to deal with the transition between optically thin and thick regimes. In this test, we simply perform two calculations, one with the Minerbo Flux

limiter and one without any limiter ($\lambda = 1/3$) in order to see if the flux limiter has an effective impact on the fragmentation. Our initial spherical dense core has the same ratio of thermal to gravitational energy as previously ($\alpha \sim 0.5$), but we add a $m = 2$ azimuthal perturbation of 10% in the density field and a solid body rotation about the z-axis. The ratio between rotational energy and gravitational energy is $\beta = 0.04$. The combined effects of the azimuthal density perturbation and of the rotation promote spiral arms creation and fragmentation.

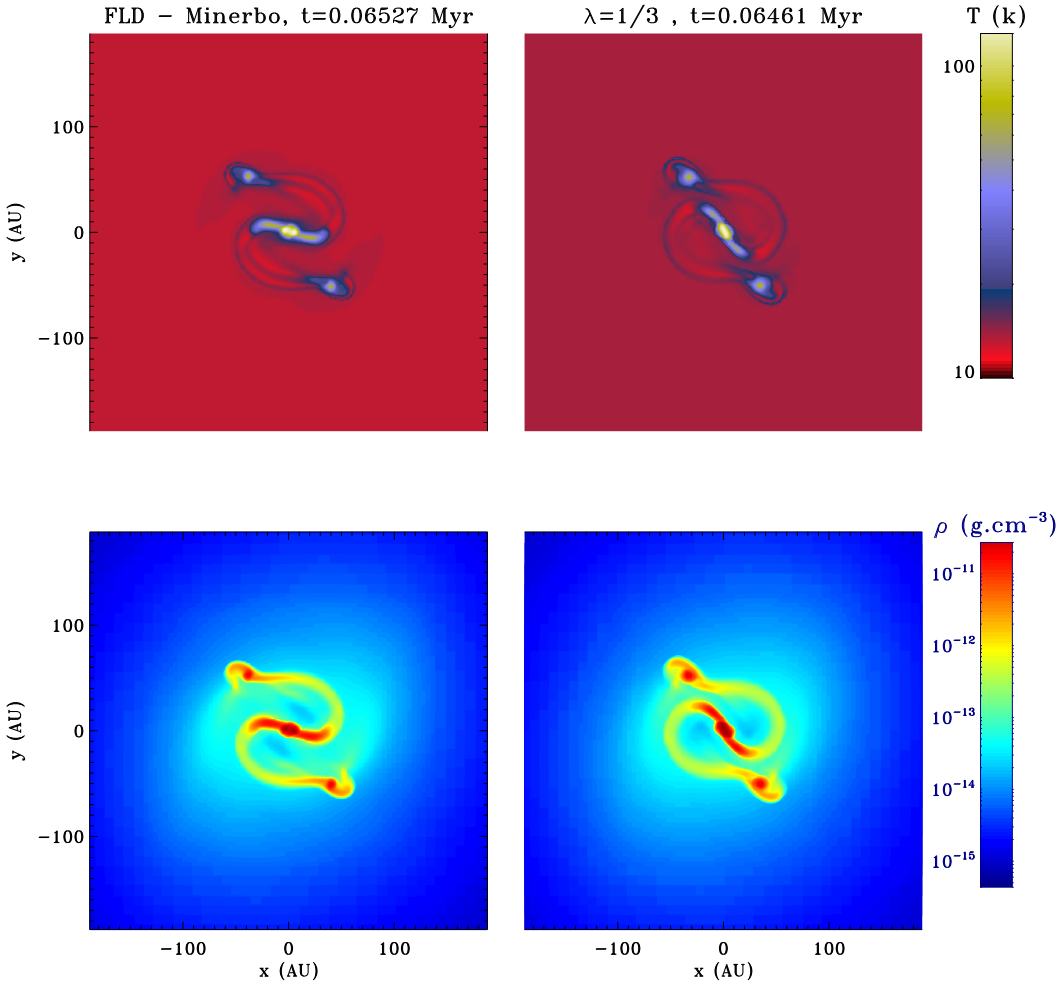

Figure 4.16: Temperature (upper plots) and density (lower plots) maps in the equatorial plane for two calculations, with the Minerbo flux limiter (left column) and without flux limiter (right column). Scales are logarithmic.

Figure 4.16 shows the temperature and density maps in the equatorial plane for the two calculations. The left column shows results obtained with the Minerbo flux limiter and the right column results obtained with $\lambda = 1/3$ everywhere. The first thing we note is that there are almost no difference in the fragmentation mode. However, dynamical timescales are different, the core evolves quickly without flux limiter. Since without flux limiter the cooling is increased, this allows a faster collapse. We also note that the two satellites are closer to the central object since more thermal support has been removed. Eventually, the surrounding temperature is hotter when the flux is not limited in the transition region around $\tau = 1$ and when causality is not preserved.

In figure 4.17, we plot the corresponding mean profiles of the density and gas temperature as a function of the radius in the equatorial plane, using logarithmic scales. Density profiles are close together in the outer part, but differ at the center. The central density in the FLD case is $\sim 1.8 \times 10^{-11}$ g cm^{-3}, and $\sim 2.7 \times 10^{-11}$ g cm^{-3} without flux limiter. Since the cooling is greater without flux limiting, the central core can contract more efficiently. From the temperature profile, we see that temperature is higher in the inner and outer part in the case without flux limiter (123 K against 110 K with FLD). Without flux limiter, the temperature is also higher at the center since the core has contracted slightly further and it is also higher at high radius since heat from contraction and collapse has been evacuated more efficiently.

Figure 4.18, shows the gas temperature as a function of the density for each cell in the computational domain at the same time as in figure 4.16. We first notice that there is a spread in the temperature-density plane that the barotropic EOS cannot reproduce. Moreover, in the two calculations, higher densities with a low temperature are reached. This could have a strong impact on fragmentation. It indicates that a smaller Jeans mass is reached and therefore fragmentation takes place at smaller scales with the FLD. We also note the differences between the calculations: low density gas is hotter without the flux limiter, whereas we get more cold dense gas thanks to flux limiter (around log(T)$\sim$ 1 and log(ρ)$\sim$ -12). We also find that the maximal temperature in the FLD case is higher than in the temperature profile of figure 4.17. This is due to the way we perform the average in the equatorial plane to get the temperature as a function of the radius. However, this smoothing is only effective for a few cells very close to the center. We clearly see that gas with density $10^{-16} < \rho < 10^{-13}$ g cm^{-3} is artificially heated when the radiative flux is artificially too high. These temperature and density ranges correspond to the transition between optically thick and optically thin region. We clearly see from these results that radiative transfer modeling has to be accurate in order to obtain a fragmentation that is of physical origin. In the last part of this work (§6.2.2), we will show that it can have an impact in the outflow launching in the collapse of magnetized dense cores.

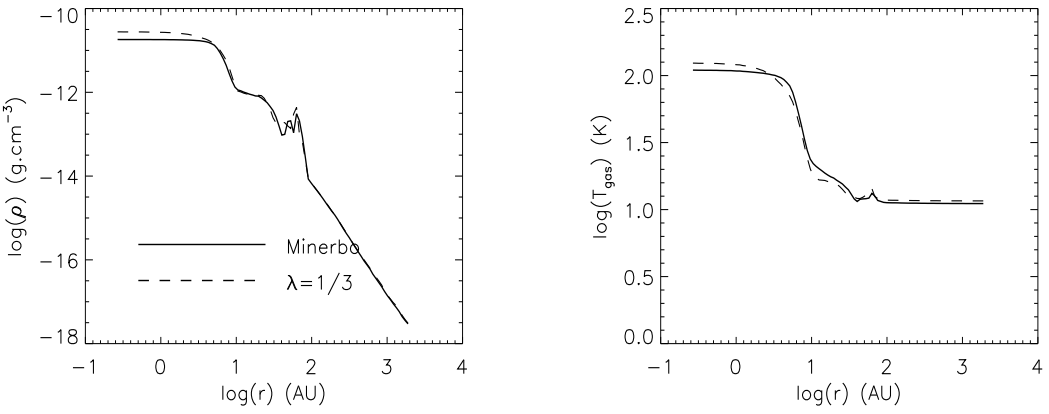

Figure 4.17: Gas temperature and density as a function of the radius in the equatorial plane for calculations made with the Minerbo flux limiter (solid line) and without flux limiter (dashed line).

4.4.4 Subcycling

In this last test, we examine a possible way to speed up calculations CPU time with a limited and controlled impact on the results. Since RAMSES benefits from the adaptive time step

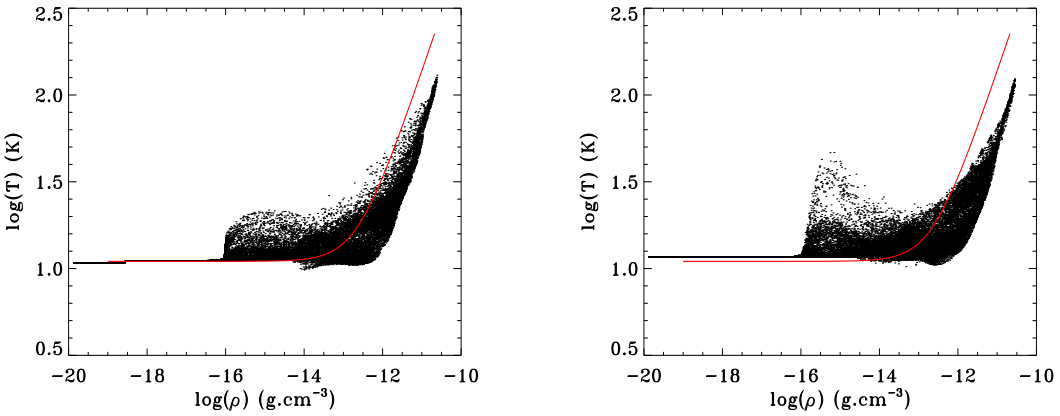

Figure 4.18: Gas temperature as a function of the density for calculations made with the Minerbo flux limiter (left) and without flux limiter (right). Scales are logarithmic. Each point gives temperature and density of a cell of the computational domain. The red curve represents the barotropic law with $\rho_{\rm ad} = 1 \times 10^{-13}$ g cm^{-3}.

scheme for the hydrodynamical part, we couple very simply this scheme to our implicit solver. As we mentioned earlier, the implicit update enforces the time step to be the same for all the AMR levels of the computational domain. However, high resolution regions are concentrated in the center of the core or eventually in the satellites. In these regions, time steps are very short and determined by the contraction of the adiabatic cores. The cooling in these hot and almost adiabatic regions is not efficient during a single time step. Therefore, we let evolve these regions with their own time steps for the hydrodynamical parts and perform a diffusion step every N time steps of the finer levels.

Figure 4.19 shows the run of gas temperature with the density for calculations performed with a diffusion step every 2 (left) and every 64 (right) coarse hydrodynamic time steps, at a later time than in figure 4.18. In the right plot, we see that all the surrounding gas has been heated up significantly since we do not use the flux limiter. Then, when diffusion step is performed too rarely, the gas is spuriously heated up to ~ 300 K (log(T)~ 2.5) at low density. The diffusion has not the resolution in time to propagate at the right speed (see figure A.1 and related comments in appendix A). The total energy is conserved, which is the reason why the gas is hotter in the dense region and cooler in the less dense region compared to the left plot. This effect can also be easily seen in a Barenblatt problem, where the propagation of the diffusion wave, with a non linear diffusion coefficient, is integrated numerically with a time step that exceeds the CFL associated with the diffusion wave speed $v_{\rm th}$ ($\Delta t = \Delta x / v_{\rm th}$).

Figure 4.20 shows density maps in the equatorial plane for four calculations performed with the same initial conditions as in the previous test and with a diffusion step made every 2, 4, 16 and 64 finer time steps. The flux limiter has not been activated. When the diffusion step is performed too rarely, the fragmentation is highly affected. Two satellites have fallen onto the central object whereas they stay in orbit when the diffusion step is performed every 2 or 4 finer time steps. From these results, we admit that fragmentation is not highly affected if the implicit diffusion step is performed more than every 4 finer time steps given by the hydrodynamical CFL condition. However, this empirical criterion depends on the problem and on the numerical resolution. Using a higher numerical resolution in the fragments would allow us to increase this criterion. On the contrary, when resolution is low, subcycling cannot be used.

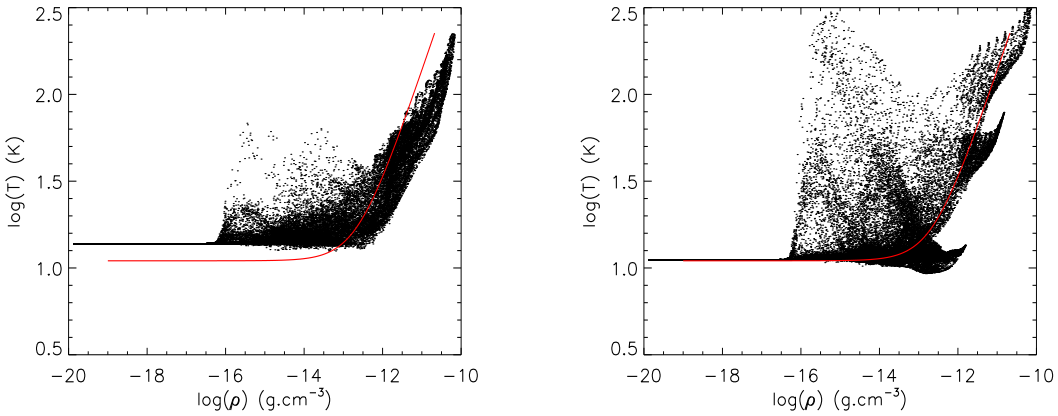

Figure 4.19: Gas temperature as a function of the density for calculations made with a diffusion step every 2 (left) and every 64 (right) coarse hydrodynamic time step. The time is the same as in figure 4.20.

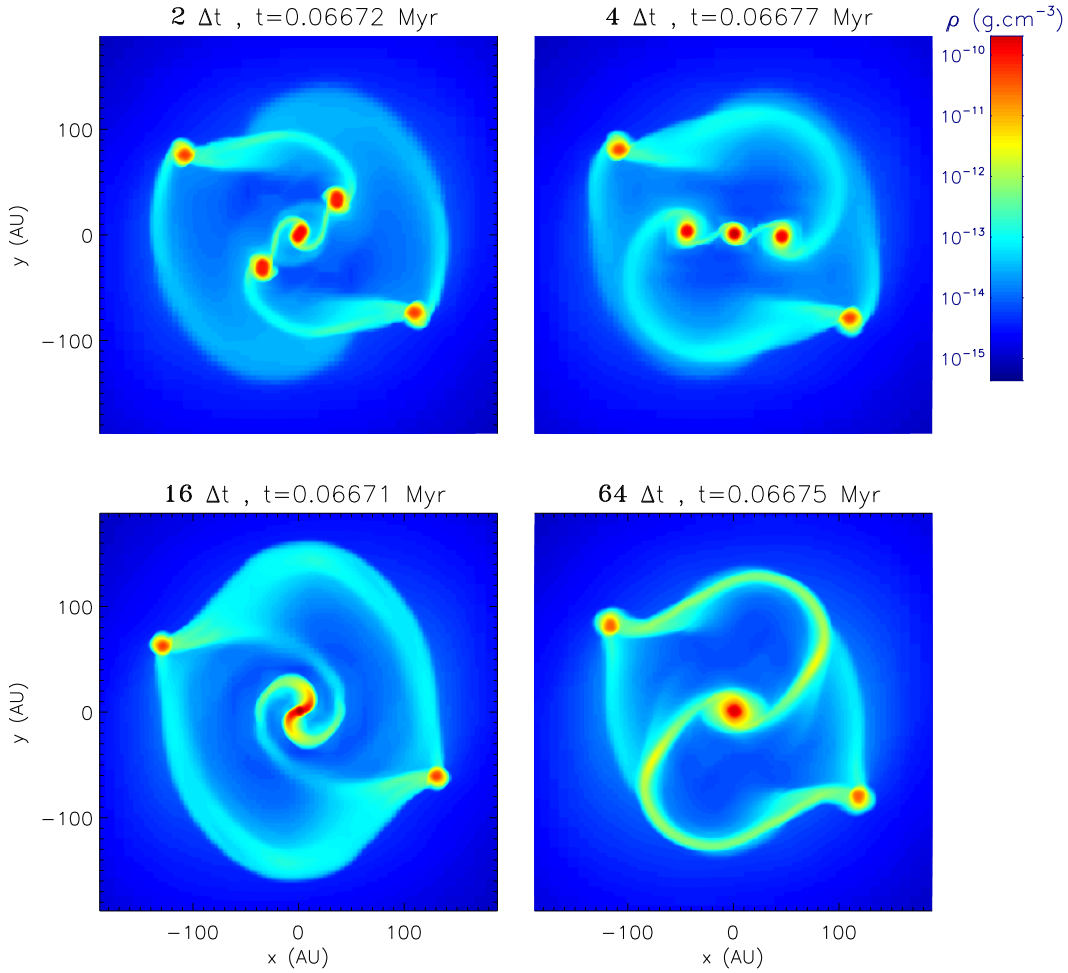

Figure 4.20: Density maps in the equatorial plane for calculations made with an implicit diffusion step performed every 2, 4, 16 and 64 finer hydrodynamical time step.

Chapter 5
Computational star formation today

Contents

The rapid development of parallel supercomputers is enabling the detailed study of the collapse and the fragmentation of prestellar cores with increasingly accurate numerical simulations. Due to the advances also in sub-millimeter observation technology, we are now able to consider many different modes of low-mass star formation using observations of a range of initials conditions. The challenge for the simulations is to reproduce the observational results. Two main numerical methods, namely AMR and SPH, are widely used to simulate the collapse and the fragmentation of prestellar cores. We thoroughly compare these two methods within their standard framework. We use the AMR code RAMSES and the SPH code DRAGON. Our simplified physical model consists of an isothermal sphere rotating about the z-axis. First we study the conservation of angular momentum as a function of the resolution. Then, we explore a wide range of simulation parameters to study the fragmentation of prestellar cores. There appears to be convergence between the two methods, provided numerical resolution in each case is sufficient. We deduced numerical resolution criteria adapted to our physical cases, in terms of resolution per Jeans mass, for an accurate description of the formation of protostellar cores. This

convergence is encouraging for future work in simulations of low-mass star formation, providing the aforementioned criteria are fulfilled.

5.1 Introduction

The study of star formation considers an incredibly wide range of mass and length scales. Although it is established that stars form in dense cores, their non-linear evolution makes it difficult to perform accurate calculations of the collapse and the fragmentation of a prestellar core. The star formation process is the outcome of complex gas dynamics involving non-linear interactions of gravity, turbulence, magnetic field and radiation. The early, pioneering theoretical works of Larson (1969), Penston (1969) or Shu (1977) demonstrated the high complexity of gravitational collapse. Klein et al. (2007) recently stated that developing a theory for low-mass star formation remains one of the most elusive and important goals of theoretical astrophysics. The computational challenge is to consider effectively the extensive ranges of spatial and density scale. Following the gravitational collapse while resolving precisely the Jeans length, which scales as $\lambda_{\rm J} \propto \rho^{-1/2}$ for an isothermal gas, is a major difficulty for numerical simulations.

Different numerical-simulation, techniques are used to study star formation, which have included increasingly more complex physics. One difficulty is always the validation of the numerical methods used to study low-mass star formation. There are two distinct numerical methods that provide sufficient accuracy:

1. **AMR**: Adaptive Mesh Refinement method for Eulerian grids
2. **SPH**: Smoothed Particle Hydrodynamics method for a Lagrangean approach.

No systematic comparison between the two methods has yet been completed for low-mass star formation calculations. Many numerical studies have compiled common test calculations for convergence testing, and intercode comparison. The most famous model was first calculated by Boss and Bodenheimer (1979) and since then, it has been recalculated by several authors with even higher spatial resolution (e.g Arreaga-García et al. 2007; Bate and Burkert 1997; Kitsionas and Whitworth 2002; Truelove et al. 1998). The SPH approach has generated a lot of detailed investigations on the influence of the number of particles and neighbors (Attwood et al. 2007; Lombardi et al. 1999; Rasio 1999), and criteria for numerical convergence have been extracted from these studies. Nelson (2006) performed a large investigation of the influence of these parameters on disk fragmentation, and concluded that the better the resolution the later the fragmentation. Dehnen (2001) investigated the optimal gravitational force softening necessary in three-dimensional N-body codes. Bate and Burkert (1997) provide a minimum-resolution, criterion for SPH calculations with self-gravity to accurately model fragmentation. Fewer studies have been completed for AMR because AMR codes have become available only recently. Truelove et al. (1997) provide an empirical criterion for the Jeans-length resolution in AMR calculations to avoid spurious numerical fragmentation.

There have not been many direct comparison between SPH and AMR calculations. Comparison in the context of cosmological simulations has been completed by the Santa Barbara Cluster Comparison Project (Frenk et al. 1999). Using the AMR method, Fromang et al. (2006) compares quite successfully hydrodynamical collapse calculations with SPH results of Hosking and Whitworth (2004).

In the present chapter, we thoroughly compare the two approaches in the context of low-mass prestellar core formation. The main goal of this study is to investigate whether convergence can be achieved between the two methods. We have conducted calculations over a wide range of numerical @ parameters, in order to study the dependency of angular momentum conservation and

fragmentation on physical and numerical initial conditions. We then determine the resolution criteria required to accurately describe prestellar core formation.

The chapter is organized as follows: in Section 2 we briefly introduce our collapse model. In Section 3, we present the SPH code used in our comparative study, our initial numerical conditions, and the criteria we fulfill to resolve gravitational collapse. The problem of angular momentum conservation is examined in detail in Section 4. In Section 5, we tackle the fragmentation issue and explore the dependency of the results on the numerical parameters. First, we study the numerical convergence of AMR and SPH calculations separately. Then, we compare the converged calculations for each code. This convergence study is completed for different test cases. In section 6, we present our conclusions. For each method, we discuss the numerical criteria required to provide an accurate description of both gravitational collapse and fragmentation.

The convention in this chapter is to call "particles" the SPH particles and "cells" the AMR cells in order to avoid confusion. Note that almost all the work done in this chapter has been published in the **Astronomy & Astrophysics** revue (Commerçon et al. 2008).

5.2 Definitions of the test cases

To make comparison between codes easier, we adopt simple initial conditions, similar to those chosen in previous studies (e.g. Bate and Burkert 1997; Boss and Bodenheimer 1979). We consider a uniform-density sphere of molecular gas of initial radius R_0, rotating about the z-axis with a uniform angular velocity Ω_0, in order to minimize the loss of angular momentum due to friction. We fix the cloud mass at $M_0 = 1$ M$_\odot$ and the temperature at 10 K. For a mixture of molecular hydrogen, helium and heavy elements, this corresponds to an isothermal sound speed of $C_0 \sim 0.19$ km s^{-1}. For the case where fragmentation occurs, we use an m = 2 azimuthal density perturbation.

The initial energy balance of our model is determined by two dimensionless parameters corresponding to the ratio between the thermal energy and the gravitational energy

$$\alpha = \frac{5}{2}\frac{R_0 kT}{GM_0\mu m_{\rm H}}, \tag{5.1}$$

and to the ratio of the rotational and the gravitational energy

$$\beta = \frac{1}{3}\frac{R_0^3\Omega_0^2}{GM_0}. \tag{5.2}$$

Since we use a constant initial mass of 1 M$_\odot$ and a constant temperature, providing the value of the parameter α, gives the sphere radius R_0. The higher α becomes, the larger R_0 is. The angular velocity is given by the parameter β.

In order to mimic the thermal behavior of a star-forming gas, we use a barotropic equation of state (cf. Bonnell 1994). Tohline (1982) and Masunaga and Inutsuka (2000a) showed that the core closely follows a barotropic equation of state, providing a good approximation without resolving radiative transfer. We use

$$\frac{P}{\rho} = C_0^2\left[1 + \left(\frac{\rho}{\rho_c}\right)^{2/3}\right], \tag{5.3}$$

where C_0 is the isothermal sound speed and $\rho_c = 10^{-13}$ g cm^{-3} is the critical density which corresponds to the transition from an isothermal to an adiabatic state (Larson 1969), see fig. 3.1.

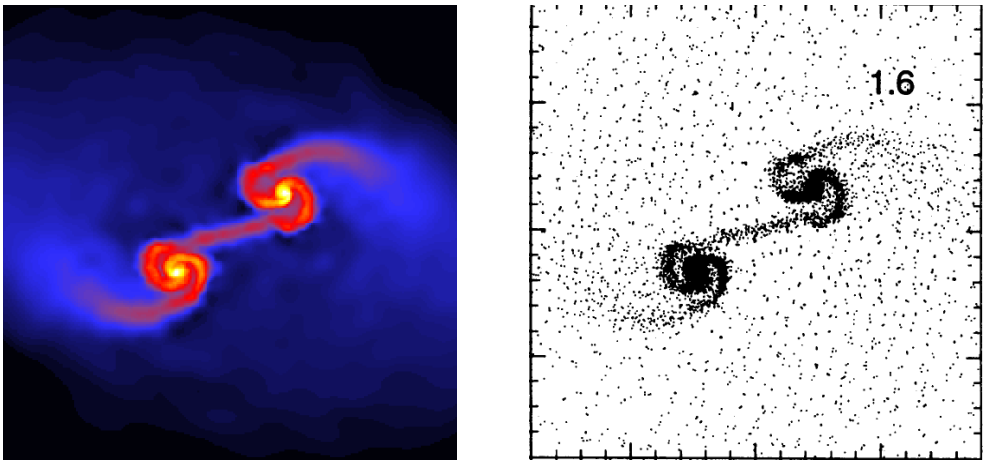

Figure 5.1: *Left plot:* Density map for a collapse SPH calculation with fragmentation. *Right plot:* Corresponding particle distribution, illustrating the Lagrangean nature of SPH (Figures from (Bate et al. 1995) and M. Bate website)

5.3 The SPH method and setup for protostellar collapse

5.3.1 SPH: Smoothed Particles Hydrodynamics

A brief overview

SPH is the most popular fully Lagrangean method used to describe gravitational collapse because of its simplicity for 3D codes and its versatility to incorporate self-gravity. SPH was first designed to simulate nonaxisymmetric phenomena for astrophysical gases (Gingold and Monaghan 1977; Lucy 1977). This method is straightforward to use and develop, and efficiently produces robust results. It can also effectively model hydrodynamical flows in regions of very low mass or particle density. It does not need a grid to calculate spatial derivatives, but consists of a set of discrete particles describing the state of the fluid. The spatial derivatives are found by analytical differentiation of interpolation formulae. SPH particle i should not be perceived as a real fluid element, but as a mathematical entity with coordinates $\mathbf{r}_i$, velocity $\mathbf{v}_i$, mass m_i (i.e. m since all particles have the same mass in the present calculations) and thermal energy e_i. The evolution of the fluid is determined by following the motion of the particles, under the influence of interparticle forces which represent the effects of pressure, viscosity (see below) and self-gravity.

The main advantage of SPH is its strict Galilean-invariant property and its simplicity. Resolution elements are then concentrated in high-density regions in SPH methods. The standard SPH formalism uses artificial viscosity for the hydrodynamics. Some alternative formalism such as Godunov SPH has been proposed (e.g. Inutsuka 1994) in order to avoid the use of artificial viscosity, but these methods have yet to be well developed and tested. SPH has been used by several authors to study fragmentation (Bate and Burkert 1997; Bonnell 1994; Goodwin et al. 2004; Hennebelle et al. 2004).

Hydrodynamical method for DRAGON

We use the standard SPH code DRAGON (Goodwin et al. 2004; Turner et al. 1995), that is in its most simple version. SPH resides in an interpolation method which allows any function to be expressed in terms of its values at a set of disordered points named particles. The integral

interpolant of any variable $A(\mathbf{r})$ is defined by

$$A_I(\mathbf{r}) = \int A(\mathbf{r'})W(|\mathbf{r}-\mathbf{r'}|,h)d^3\mathbf{r'}, \tag{5.4}$$

where W is a normalized kernel function. We use the B2-spline smoothing kernel defined by Monaghan and Lattanzio (1985)

$$W(s) = \frac{\sigma}{h^\nu}\begin{cases} 1-\frac{3}{2}s^2+\frac{3}{4}s^3 & \text{if } 0\le s\le 1,\\ \frac{1}{4}(2-s)^3 & \text{if } 1\le s\le 2,\\ 0 & \text{otherwise,}\end{cases} \tag{5.5}$$

where ν is the number of dimensions and σ a normalization factor depending on the dimensions. σ takes values $\frac{2}{3}$, $\frac{10}{7\pi}$ et $\frac{1}{\pi}$ respectively in 1, 2 and 3 dimensions. Parameter h is the kernel size.

In standard SPH, the integral interpolant for the variable $A(\mathbf{r}_i)$ is approximated by a summation interpolation over the particle's nearest neighbors:

$$A_s(\mathbf{r}_i) = \sum_j m_j \frac{A(\mathbf{r}_j)}{\rho(\mathbf{r}_j)} W(|\mathbf{r}_i-\mathbf{r}_j|,h_{ij}), \tag{5.6}$$

where $A(\mathbf{r}_j)$ is the value associated with particle j, $h_{ij}=(h_i+h_j)/2$, and h_i is the adaptive smoothing length of particle i, defined such that the particle kernel volume contains a constant mass, i.e. a constant number of neighbors N_N. The interpolation mass is then given by mN_N. Thus, density is estimated for particle i by

$$\rho_i = \sum_j m_j W(|\mathbf{r}_i-\mathbf{r}_j|,h_{ij}). \tag{5.7}$$

The momentum equation is written as

$$\frac{\mathrm{d}\mathbf{v}_i}{\mathrm{d}t} = -\sum_j m_j \left(\frac{P_i}{\rho_i^2}+\frac{P_j}{\rho_j^2}+\prod_{ij}\right)\nabla_i W(|\mathbf{r}_i-\mathbf{r}_j|,h_{ij}) - \nabla\Phi, \tag{5.8}$$

where the pressure gradient is symmetric, improving the conservation of linear and angular momentum. Π_{ij} represents the artificial viscosity. We use a standard artificial viscosity scheme (Gingold and Monaghan 1983)

$$\Pi_{ij} = \begin{cases} \left(-a_1 C_{0,ij}\mu_{ij}+a_2\mu_{ij}^2\right)/\rho_{ij} & \text{if } \mathbf{u}_{ij}\cdot\mathbf{r}_{ij}\le 0,\\ 0 & \text{otherwise,}\end{cases} \tag{5.9}$$

with

$$\mu_{ij} = \frac{h_{ij}\mathbf{u}_{ij}\cdot\mathbf{r}_{ij}}{\mathbf{r}_{ij}^2+a_3^2}, \tag{5.10}$$

where $\mathbf{u}_{ij}=\mathbf{u}_i-\mathbf{u}_j$, $\mathbf{r}_{ij}=\mathbf{r}_i-\mathbf{r}_j$, and $C_{0,ij}$ and ρ_{ij} denote arithmetic means of the isothermal sound speed and density of the particles i and j. The free parameters a_1, a_2 and a_3 regulate the strength of viscosity. In our case, we have the combination $a_1=1$, $a_2=2$ and $a_3=0.1h_{ij}$. This artificial viscosity has been the subject of a number of discussions in which authors suggest alternative artificial viscosity. One common improvement is to use a time-dependent viscosity (Morris and Monaghan 1997). We look at the influence of the viscosity scheme in §5.6.2.

The gravitational force between a pair of particles obeys a simple inverse-square law, unless the particles are very closed. Under this circumstance, the gravity force has to be softened to avoid violent two-body interactions. Softening is achieved by invoking Gauss gravitational theorem

$$\nabla\Phi_i = G\sum_{j\neq i}\left\{W^*\left(\frac{|\Delta\mathbf{r}_{ij}|}{h_{ij}}\right)\frac{m_i m_j \Delta\mathbf{r}_{ij}}{|\Delta\mathbf{r}_{ij}|^3}\right\}, with \tag{5.11}$$

$$W^*(s) = \int_{s'=0}^{s'=s} W(s')4\pi s'^2 ds'. \tag{5.12}$$

According to Bate and Burkert (1997), the gravitational softening length should be the same as the hydrodynamic smoothing length. Calculation of the gravitational acceleration of a particle is speeded up using an octal Spatial Tesselation Tree (STT) (Hernquist 1987). It also accounts for the quadrupole moments of the mass distributions. Thus, the term j in (5.11) may represent a particle or a cell of many particles in the tree. The cell j will contribute to the calculation of the gravitational acceleration of particle i if it satisfies the non-opening condition

$$\ell_j < \theta_{\rm crit}|\vec{r}_i - \vec{R}_j|, \tag{5.13}$$

where ℓ_j is the linear size of the cell, $\vec{R}_j$ its center of mass position and $\theta_{\rm crit}$ is the maximum opening angle.

DRAGON benefits from the implementation of "sink particles" creation (Bate et al. 1995), used to continue the calculations without resolving processes on extremely short time-scales. Last but not least, DRAGON uses multiple-particle time steps, so that accelerations of rapidly changing particles are calculated more frequently than the accelerations of slowly changing particles. The maximum possible time-step for each particle is given by

$$\Delta t_i = \gamma \mathrm{MIN}\left[\frac{h_i}{v_{\mathrm{eff},i}}, \frac{h_i}{\sigma_i}, \frac{1}{|\nabla\cdot\mathbf{v}_i|}, \left(\frac{h_i}{|\mathbf{a}_i|}\right)^{1/2}\right], \tag{5.14}$$

where $v_{\mathrm{eff},i} = |\mathbf{v}_i|/c_{\mathrm{s},i}$ and σ_i is the effective particle sound speed including artificial velocity effects.

We allow a variation of the number of neighbors $\Delta N_{\rm N}$ less than 10% of $N_{\rm N}$ in our SPH calculations, i.e $\Delta N_{\rm N} = 5$ when $N_{\rm N} = 50$. Attwood et al. (2007) shows that the smaller $\Delta N_{\rm N}$, the less diffusive is SPH. Ideally, $\Delta N_{\rm N}$ should be set to 0. We report on the influence of setting $\Delta N_{\rm N} = 0$ for local angular momentum conservation in §5.6.2.

Initial conditions for DRAGON

We apply the method as it was originally presented by Whitworth et al. (1995). We derive an initial particle distribution by allowing hydrodynamical forces to act over a few time-steps to randomly settled particles. Another approach sometimes used is to take initial hexagonal-close-paced lattice of SPH particles to generate initial conditions. However, standard SPH calculations start from noisy initial particle distributions at present time (e.g. Arreaga-García et al. 2007). Note that we do not need intercloud and external particles to confine the ones within the sphere since our model is initially far from equilibrium.

5.3.2 The Jeans criterion in numerical codes

Refinement criterion for the AMR method

Our refinement criterion is based on the Jeans length resolution which is necessary to accurately treat gravitational collapse. We impose a minimum number of points $N_{\rm J}$ per Jeans length $\lambda_{\rm J}$.

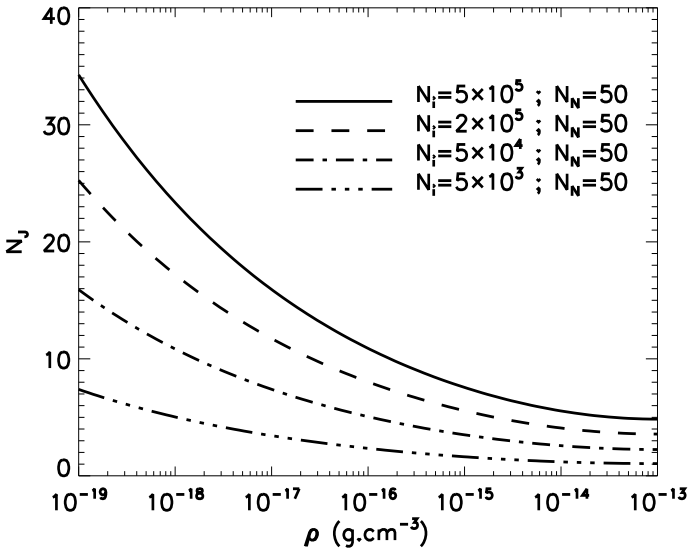

Figure 5.2: AMR-like $N_{\rm J}$ parameter for SPH as a function of the density for different resolutions of a 1 $\mathrm{M}_\odot$ dense core.

The cells' dimensions must be smaller than a constant fraction of the local Jeans length. The dimension of cells belonging to the ℓ_i refinement level is $L_{\rm box}/2^{\ell_i}$, where $L_{\rm box}$ is the physical length of the simulation box. The mesh is locally refined in order to satisfy the local Jeans criterion:

$$\frac{L_{\rm box}}{2^{\ell_i}} < \frac{\lambda_{\rm J}}{N_{\rm J}}. \tag{5.15}$$

Truelove et al. (1997) defined a minimum resolution condition for the validity of grid-based simulations aimed at modeling the collapse of a molecular cloud core, namely $N_{\rm J} > 4$. This condition ensures that the collapse is of physical rather than of numerical origin.

Jeans length description with a SPH code

In standard SPH, the resolution in mass is fixed and thus the Jeans length resolution deteriorates with increasing density for an isothermal gas. The minimum resolvable mass must then be larger than the interpolation mass. Bate and Burkert (1997) showed that the behavior of a Jeans-mass clump of gas with radius $\sim h$ is dominated by the numerical implementation. Bate and Burkert (1997) take the smallest mass that can be resolved in SPH calculations to be equal to the mass of $\sim 2N_{\rm N}$ particles. According to this criterion, we can determine an initial number of SPH particles necessary to solve the Jeans length in the simulations.

The Jeans mass is $M_{\rm J} \sim 6\,G^{-3/2}\rho^{-1/2}C_{\rm s}^3$ and the minimum resolvable mass is $M_{res} = mN_{\rm N}$. Hence, we can define a Jeans condition corresponding to the minimum value of $C_{\rm s}^3\rho^{-1/2}$, given by the barotropic equation of state (3.12), i.e. $2^{3/2}C_0^3\rho_c^{-1/2}$:

$$m < m_{max} \sim \frac{2^{3/2}6\,C_0^3}{2N_{\rm N}G^{3/2}\rho_c^{1/2}} \sim \frac{5.35\times10^{-3}}{N_{\rm N}}\mathrm{M}_\odot. \tag{5.16}$$

Considering an initial spherical mass $M_0 = 1$ $\mathrm{M}_\odot$, the initial number of particles $N_{\rm p}$ has to satisfy $N_{\rm p} > M_0/m_{\rm max} \sim 9300$ if $N_{\rm N} = 50$. This is the critical number of particles used in SPH calculations to study the collapse of a dense core. We have in that case exactly $2N_{\rm N}$ (i.e. two

resolution elements) particles per critical Jeans mass. Hubber et al. (2006) shows that with this numerical resolution, standard SPH will capture fragmentation which is genuine and resolved.

As mentioned before, the mass resolution is fixed in standard SPH. In term of Jeans mass, the resolution is therefore high at the beginning of the simulation and decreases when the density increases up to the critical density. It is nevertheless instructive to have a means of comparing the SPH and AMR resolution. We therefore define for the SPH the parameter $N_{\rm J}$ such that $N_{\rm J}^3 = M_{\rm J}/M_{res}$ is the number of resolution element per Jeans mass. Fig. 5.2 shows the evolution of $N_{\rm J}$ as a function of the density for various resolution masses. At low density, SPH resolution is much better than AMR one, that is kept constant. But at high density, SPH resolution becomes worse because of the high dependency of the Jeans mass on the density. In the next part of this chapter, $N_{\rm J}$ for SPH will be given at the critical density $\rho_{\rm c}$, i.e. the most unfavorable case for the SPH. In the dense core where $\rho > \rho_{\rm c}$, the parameter $N_{\rm J}$ enables us to compare the resolution achieved by SPH and AMR, respectively. Using particle splitting refinement in SPH (e.g. Kitsionas and Whitworth 2002) would improve its resolution. Indeed, particle splitting is an economic way to increase the local resolution and thus to avoid violating the Jeans condition in collapse simulations. However, as mentioned in the introduction, the aim of the present paper is to compare the AMR and the SPH within their standard implementation.

5.4 Free-fall time and angular momentum conservation

We start by comparing the global properties of the collapse in the two codes in the simple case of a uniform-density sphere collapse with no perturbation. We look at the collapse time, the accretion shock and finally the angular momentum conservation.

We completed a first set of simulations using a wide range of resolution parameters. The initial sphere is set up by parameters $\alpha = 0.65$ corresponding to an initial radius $R_0 = 9.2 \times 10^{16}$ cm and a density $\rho_0 \sim 6.02 \times 10^{-19}$ g cm^{-3}. The corresponding free-fall time is $\mathrm{t_{ff}} = (3\pi/32G\rho_0)^{1/2} \sim 86$ kyr.

5.4.1 Free-fall time

The first step is to compare the calculations collapse time when the initial sphere is not rotating (i.e. $\beta = 0$). Note that since α is large and since we use a barotropic equation of state, we expect to find a value larger than the free-fall time. Then, we use as a reference time $\mathrm{t_0} > (\mathrm{t_{ff}})$ for which $\rho_{\rm max} = \rho_c$. Table 5.1 gives collapse times $\mathrm{t_0}$ as a function of resolution parameters for AMR and SPH calculations. AMR calculations were completed for the parameters $N_{\rm J} = 10$ and $\ell_{\rm min} = 5, 6$ and 7. SPH calculations were derived using parameters values $N_{\rm p}$ ranging from 5×10^3 to 2×10^5 and a number of neighbors $N_{\rm N} = 50$. We note that with $N_{\rm p} = 5 \times 10^3$, we do not satisfy the Bate and Burkert (1997) criterion, but the mass of our resolution element, i.e. the sphere containing the $N_{\rm N}$ neighbors, is smaller that the critical Jeans mass.

Table 5.1: Summary of the different simulations for the case with no rotation (left table: SPH; right table: AMR). $N_{\rm i}$ for the AMR calculations gives us the number of cells describing the initial sphere.

$N_{\rm p}$	$N_{\rm N}$	$N_{\rm J}$	$\mathrm{t_0}$ (kyr)
5×10^3	50	1.86	108.6
1×10^4	50	2.33	102
5×10^4	50	4.	94.1
2×10^5	50	6.35	91.5
5×10^5	50	8.61	90.6

$\ell_{\rm min}$	$N_{\rm i}$	$N_{\rm J}$	$\mathrm{t_0}$ (kyr)
5	2 145	10	109
6	17 160	10	98
7	137 260	10	95

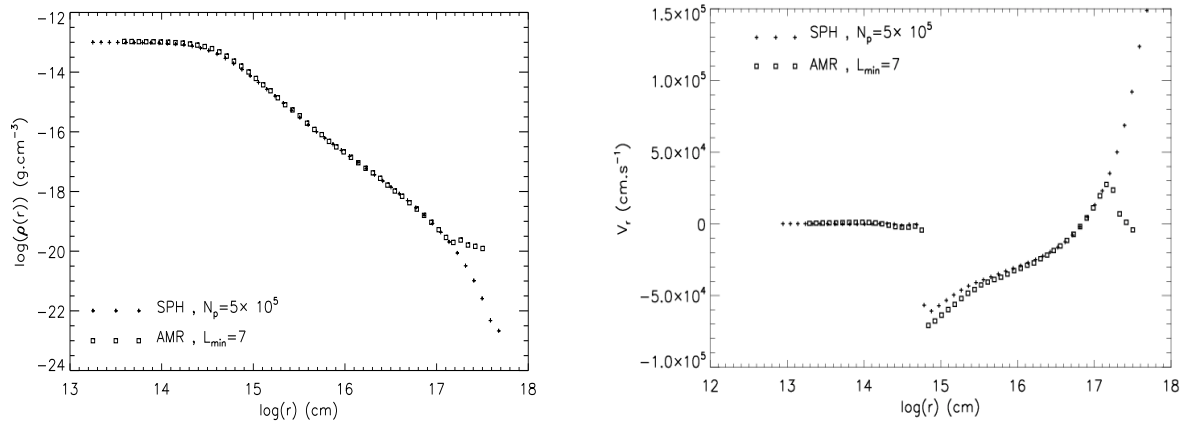

Figure 5.3: (a): Density profiles at t_0 as a function of the radius for the case with $\beta = 0.01$ and for the two most resolved simulations, namely $\ell_{\rm min} = 7$, $N_{\rm J} = 10$ for the AMR (squares) and $N_{\rm p} = 5s10^5$, $N_{\rm N} = 50$ for the SPH (crosses). (b): Illustration of the accretion shock: radial velocity profiles for the two most resolved AMR and SPH simulations in the xy-plane at $t \sim t_0 + 1.2$ kyr.

With increasing numerical resolution, the numerical time t_0 decreases and seems to converge toward a value slightly greater than the free-fall time. Time t_0 changes by less than 5% between AMR calculations with $\ell_{\rm min} = 6$ and 7, and SPH calculations with $N_{\rm p} = 5 \times 10^4$ and 2×10^5. Dynamical times t_0 in SPH calculations are closer to the free-fall time than the AMR ones. This is partly due to the higher initial resolution in SPH.

Collapse and accretion shock with rotation $\beta = 0.01$

The gas sphere is now in solid rotation about the z-axis. We set $\beta = 0.01$, corresponding to an orbital time $t_{\rm rot} = 2.8 \times 10^3$ kyr. Table 5.2 summarizes the different SPH and AMR calculations executed for this case. In order to illustrate the core resolution, we provide the quantity $N_{\rm core}$ representing the number of cells/particles with density $\rho > 1 \times 10^{-15}$ g cm^{-3} at t_0. AMR simulations have been performed with different minimum refinement levels $\ell_{\rm min}$ ranging from 5 to 7 and a refinement criterion $N_{\rm J}$ ranging from 4 to 10. As expected, at a constant $N_{\rm J}$, the various AMR calculations show a convergence. The SPH simulations were performed with a constant number of neighbors $N_{\rm N} = 50$, and a total number of particles $N_{\rm p}$ ranging from 5×10^3 to 5×10^5. For standard SPH, the effects of the decrease in resolution with increasing density are demonstrated by the fact that, for equivalent initial conditions, it is easier to achieve a better core resolution using AMR.

In Fig.5.3(a) we show density profiles as a function of the radius in the equatorial plane for AMR calculations with $\ell_{\rm min} = 7$ and $N_{\rm J} = 10$, and for SPH with $N_{\rm p} = 5 \times 10^5$ and $N_{\rm N} = 50$. The density profiles are very similar, indicating good convergence between the two methods. The behavior differs at relatively high radius because of the external gas in the AMR method. In the present simulations, the dynamical time to reach $\rho_{\rm c}$ is increased by ~ 5 kyr, because of the rotational support. As seen in Table 5.2, when one increases the resolution, one seems to converge toward this time.

When the core becomes adiabatic, the angular momentum conservation induces the formation of an accretion disk around the central object. The centrifugal force becomes comparable to the gravitational one on the equatorial plane, slowing down the collapse. The outer collapsing gas, which has a supersonic infalling speed, suddenly meets the static gas of the core, creating

an accretion shock. This shock can be clearly seen in Fig. 5.3(b) where the radial velocity component averaged over the equatorial plane is displayed. The accretion shock is described slightly more accurately with the AMR method. The SPH curve is smoother before the shock due to the artificial viscosity scheme. The slope before the shock strongly depends on the hydrodynamical solver so the results illustrate the difference between the hydrodynamical methods used in our two codes.

5.4.2 *Theoretical* local angular momentum

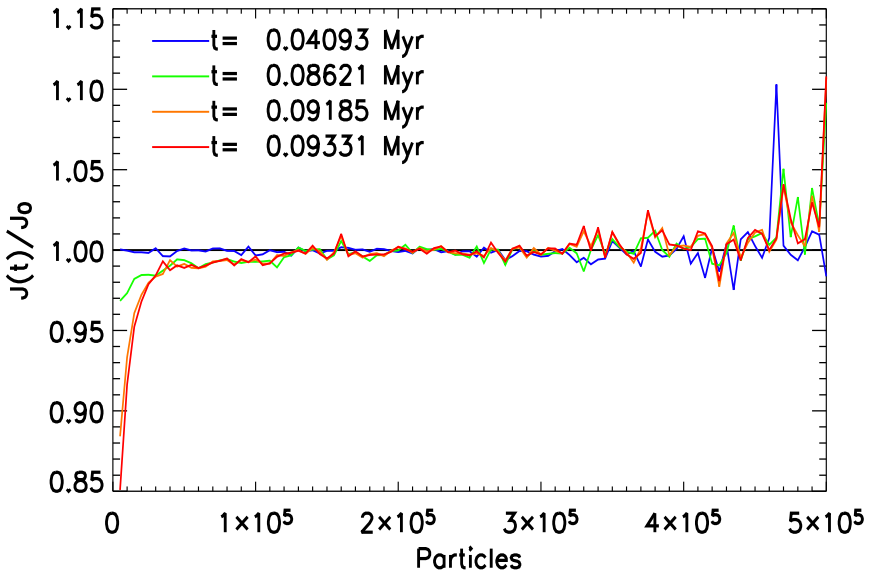

Figure 5.4: Ratio between the angular momentum $\vec{J}(t)$ over the initial angular momentum $\vec{J}_0$ at different times for the SPH simulation with $N_\mathrm{p} = 5 \times 10^5$ and $N_\mathrm{N} = 50$. The ratio is plotted as a function of the number of particles, ordered in decreasing density. The value of the ratio is a mean value over 7 500 particles. The red curve corresponds to results at t_0.

We now investigate the issue of angular momentum conservation. We note that the equations for both SPH and AMR equations imply that linear momentum is conserved. Considering our axisymmetric model, without azimuthal perturbation, we can easily investigate the effect of numerical resolution on angular momentum conservation. The local angular momentum should be well conserved, until azimuthal symmetry is broken. The loss of local angular momentum in our model is only due to unphysical transport inherent to the numerical methods used in the two codes. Due to their Lagrangean properties, the SPH calculations can provide a measure of the initial angular momentum of each particle, that is the angular momentum that the particle should have if angular momentum is perfectly conserved. Having access to the particle initial angular momentum, the loss of angular momentum is easily calculated. The azimuthal velocity component, directly linked to the angular momentum $\vec{J}$, is given by

$$v_\theta = \frac{x v_y - y v_x}{r}, \tag{5.17}$$

where r is the distance from the rotation axis

$$r = \sqrt{x^2 + y^2}, \tag{5.18}$$

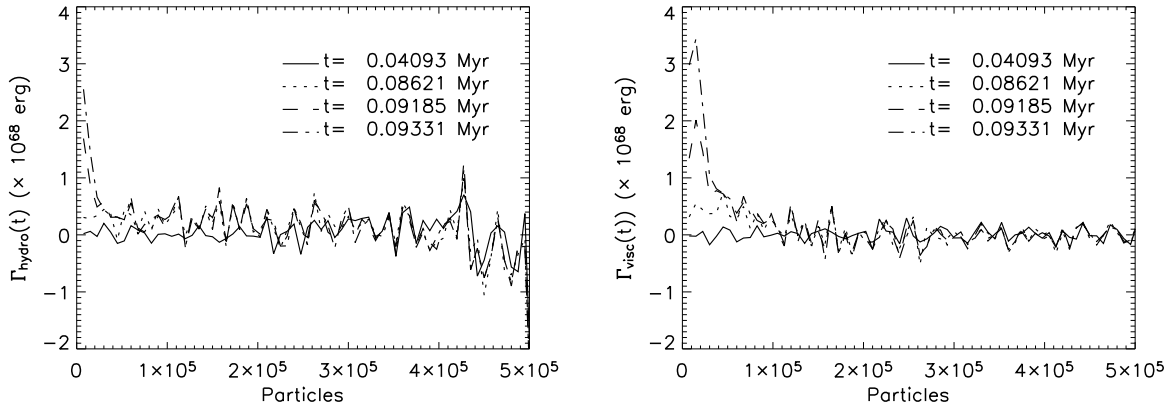

Figure 5.5: *Left plot:* Cumulated hydrodynamical torque on the rotational axis for SPH calculations with $N_\mathrm{p} = 5 \times 10^5$ and $N_\mathrm{N} = 50$ and at the same times as in Fig. 5.4. *Right plot:* Cumulated torque on the rotational axis due to the standard artificial viscosity for the same calculations and times. Particles are ordered in decreasing density and the torques are averaged over 7 500 particles. At t_0 the cumulated torques are significant for the densest particles.

and the angular momentum

$$\vec{J} = xv_y - yv_x. \tag{5.19}$$

The angular momentum conservation along the z-axis allows us to write

$$\vec{J} = xv_y - yv_x = x_0 v_{y,0} - y_0 v_{x,0} = \vec{J_0}. \tag{5.20}$$

Thus, the theoretical angular velocity of a particle at time t is determined by the ratio between its initial angular momentum $\vec{J_0} = (x_0 v_{y,0} - y_0 v_{x,0})$ and its actual radius:

$$v_{\theta,\mathrm{th}} = \frac{\vec{J_0}}{r}. \tag{5.21}$$

Using Eq. (5.21), we compare the theoretical angular velocity component to their numerical values, and in particular with the AMR results for which we do not have access to a theoretical value. Since SPH and AMR density profiles are almost identical at t_0, we suppose that the previous mapping giving $\vec{J_0}(r_0)$ as a function of the radius in the SPH runs is also valid for the AMR calculations. Note also that the method cannot account for the displacement of the particles that would arise by changing the angular momentum.

Azimuthal velocity component

Figure 5.4 presents the ratio of the angular momenta $\vec{J}(t)$ and $\vec{J_0}$ for the SPH simulation with $N_\mathrm{p} = 5 \times 10^5$ and $N_\mathrm{N} = 50$. The particles are arranged in order of decreasing density and the ratio is averaged over 7500 particles. A first interesting result is that denser particles lose more angular momentum. At t_ff, denser particles have lost 3% of their initial angular momentum. In less resolved calculations, i.e. $N_\mathrm{p} = 5 \times 10^3$ particles, the effect is stronger and the densest ones lose more than 10% of their initial angular momentum in a free-fall time t_ff. This percentage slightly decreases when the number of particles is increased. The reason is that the denser the particle the larger the viscous torque (see below) and thus the larger the angular momentum transport. This numerical transport is amplified when the core is close to becoming adiabatic.

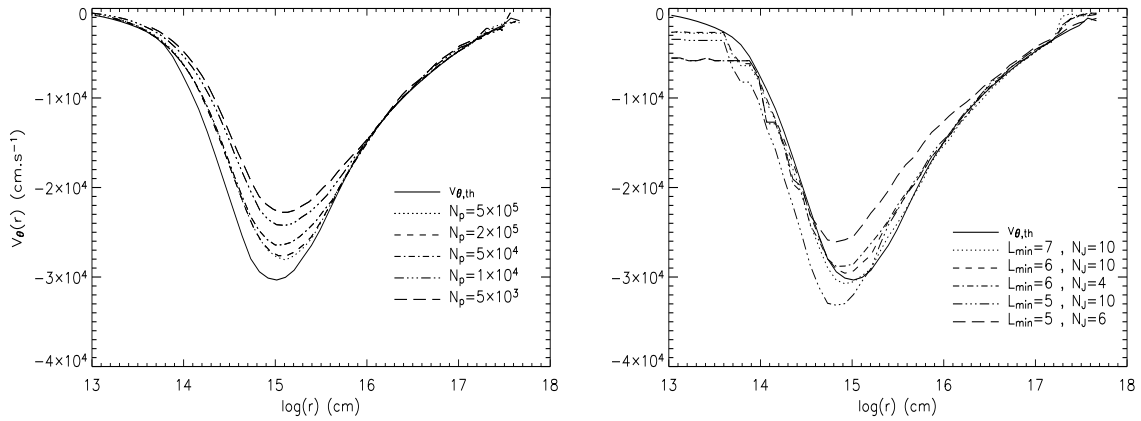

Figure 5.6: Azimuthal velocity at t_0 as a function of the radius on the equatorial plane for SPH (left) and AMR (right) calculations at corresponding t_0. The left-hand plot (Fig. 5.6a) shows SPH results with various N_p and $N_\mathrm{N} = 50$. The solid line represents the theoretical azimuthal velocity interpolated at t_0 and is denoted as $v_{\theta,\mathrm{th}}$. The right-hand plot (Fig. 5.6b) shows AMR results with $N_\mathrm{J} = 10$ and $\ell_\mathrm{min} = 5$, 6 and 7. The theoretical azimuthal velocity is plotted also for easy comparison with the SPH results.

Figure 5.5 shows the cumulated hydrodynamical (left-hand side) and viscous (right-hand side) torques on the rotational axis for the same SPH calculations at the same times as in Fig. 5.4. In principle, there should not be any torque on the rotational axis because of this axisymmetric model. The cumulated torques are computed and summed at each time-step for each particle. The value plotted is an average over 7 500 particles and particles are ordered in decreasing density. Denser particles have the largest cumulated hydrodynamical and viscous torques. The friction forces corresponding to the hydrodynamical torque are stronger for these particles, which is due to the strong differential velocity.

Table 5.2: Summary of the different simulations (upper table: SPH, lower table: AMR) performed to study angular momentum conservation.

N_p	N_N	N_J	N_core	t_0 (kyr)
5×10^3	50	1.86	225	115
1×10^4	50	2.34	422	107
5×10^4	50	4.	1 833	98
2×10^5	50	6.35	7 055	95
5×10^5	50	8.61	17 309	93

ℓ_min	N_i	N_J	N_core	Tot. cells	t_0 (kyr)
5	2 145	6	3 928	$\sim 9.1 \times 10^4$	150
5	2 145	10	30 752	$\sim 1.6 \times 10^5$	116
6	17 160	4	4 016	$\sim 3.1 \times 10^5$	116
6	17 160	10	28 800	$\sim 3.7 \times 10^5$	109
7	137 260	10	29 944	$\sim 2.2 \times 10^6$	96

Figure 5.6a displays the azimuthal velocity component as a function of the radius r on the xy-plane for the SPH simulations. The theoretical azimuthal velocity profile (solid line) is

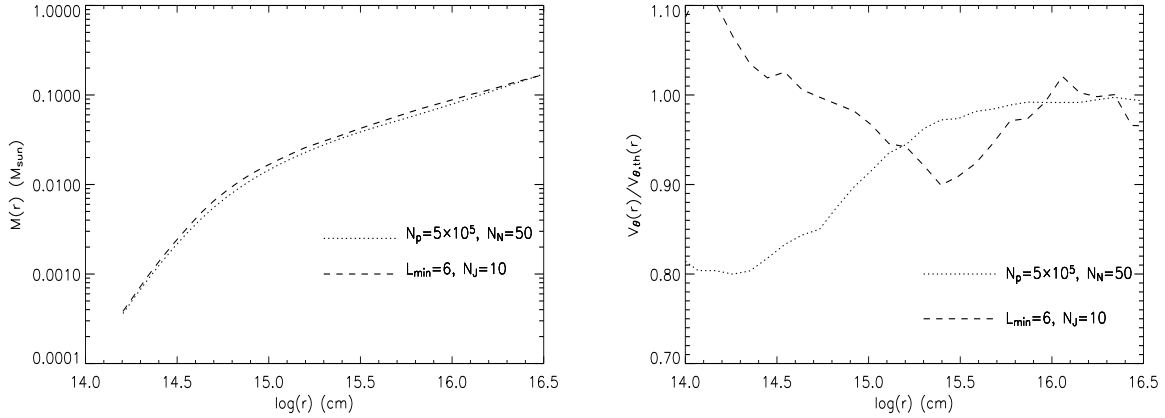

Figure 5.7: (left): Total integrated mass in the equatorial plane at t_0 as a function of the radius for AMR calculations with $\ell_{\rm min} = 6$, $N_{\rm J} = 10$ (dashed-line) and for SPH calculations with $N_{\rm p} = 5 \times 10^5$, $N_{\rm N} = 50$ (dotted line). (Fig.5.7right): Ratio between numerical and theoretical azimuthal velocities at t_0 as a function of the radius in the equatorial plane for the same calculations.

obtained following the previous section. It is obvious that low resolution simulations are not able to conserve properly the angular momentum. With 5×10^3 particles, we obtain counter-rotating particles at the center (not illustrated in Fig. 5.6a because we make the average of the angular velocity in the xy-plane that smoothes the profiles). It appears that a minimum of 5×10^4 particles is required to maintain angular momentum loss within less than 10%, for the case of the present study. The improvement of angular momentum conservation eventually saturates for large numbers of particles. We checked that using a larger number of neighbors does not improve the conservation of local angular momentum.

Figure 5.6b presents results obtained using the RAMSES code. AMR curves are plotted and compared with the theoretical results obtained previously using SPH. The simulations with $\ell_{\rm min} = 6$ and $\ell_{\rm min} = 7$ are close to the theoretical curve. In both AMR simulations with $N_{\rm J} = 10$, dense core resolution is higher than with SPH. For an initial resolution of $\ell_{\rm min}$=5, the AMR scheme does produce some angular momentum lag. This can be due to the fact that with a poor initial resolution, the interpolation of the gravitational potential tends to convert gravitational energy into rotational energy. The outer gas does not alter the angular momentum conservation for AMR calculations because of its tiny density.

In Fig. 5.7, we plot the integrated mass (left) and the ratio of numerical over theoretical angular momentum (right) for AMR calculations with $\ell_{\rm min} = 6$, $N_{\rm J} = 10$ and for SPH calculations with $N_{\rm p} = 5 \times 10^5$, $N_{\rm N} = 50$. In Fig. 5.7a, most of the mass of the forming disk remains within a radius $\sim 1 \times 10^{16}$ cm, for which AMR and SPH have divergent results. In Fig. 5.7b, angular momentum is clearly transported to the outer regions with SPH, but has a trend to be transported to the inner regions with AMR. The overall angular momentum is well conserved in both calculations, but local properties seem to be affected by initial resolution. SPH resolution is much better at the beginning of the calculations, which enables SPH to properly conserve local angular momentum at $r > 1.4 \times 10^{15}$ cm at t_0. In contrast, the smaller initial resolution of the sphere for AMR implies that angular momentum is conserved far less in this region. This effect reverses at lower radius where AMR can reach smaller scales contrary to standard SPH.

The density profiles obtained with the two methods converge towards a similar solution (c.f. Fig.5.3a), but a closer analysis of the velocity profiles shows discrepancies. The angular velocity

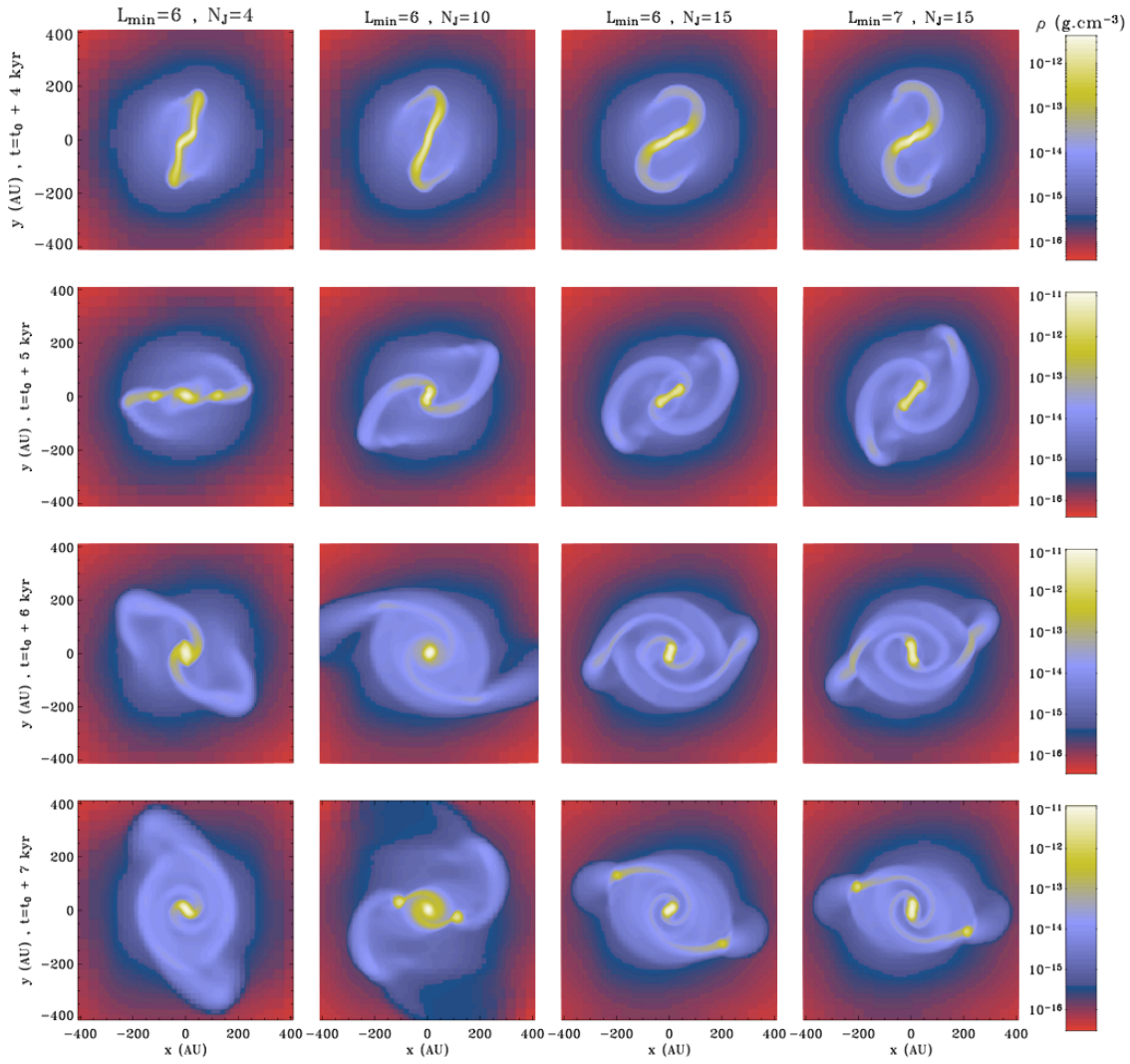

Figure 5.8: AMR calculations density maps on the xy-plane for the case $\alpha = 0.50$, $\beta = 0.04$. From top to bottom, four different times are shown: t=t$_0$ + 4 kyr, t=t$_0$ + 5 kyr, t=t$_0$ + 6 kyr and t=t$_0$ + 7 kyr. The AMR calculations have been performed with, from left to right columns, $\ell_{\rm min} = 6$ and $N_{\rm J} = 4$, $N_{\rm J} = 10$, $N_{\rm J} = 15$ and $\ell_{\rm min} = 7$ and $N_{\rm J} = 15$.

profiles appear to imply that local angular momentum is better conserved by the AMR method than with the SPH method, for the code implementation that we have used. Both can be improved using appropriate methods (see §5.6.2 and 5.6.3).

5.5 Fragmentation

5.5.1 Model

Prestellar core fragmentation is a highly non-linear process. A key issue is to understand the extent to which the fragmentation that occurs in numerical simulations, is influenced by the numerical scheme and resolution.

To study dense core fragmentation, we choose the same previous spherical model and impose a m = 2 azimuthal density perturbation:

$$\rho(\theta) = \rho_0[1 + A\cos(\mathrm{m}\theta)], \tag{5.22}$$

Table 5.3: Summary of the different simulations performed with $\alpha = 0.5$ and $\beta = 0.04$. $N_{\rm core}$ corresponds to particles/cells whose density satisfies $\rho > 1 \times 10^{-15}$ g cm^{-3} at t=t$_0$ + 4 kyr. The upper table (Table 5.3a) gives a summary of the SPH calculations. The lower Table (Table 5.3b) shows a summary of AMR calculations.

$N_{\rm p}$	$N_{\rm N}$	$N_{\rm core}$	t$_0$ (kyr)
5×10^4	50	6 997	64
2×10^5	50	28 516	63
5×10^5	30	72 417	63
5×10^5	50	71 804	62
5×10^5	100	76 390	63
5×10^5	200	71 940	64

$\ell_{\rm min}$	$N_{\rm J}$	$N_{\rm core}$	Tot. cells	t$_0$ (kyr)
6	4	48 680	$\sim 4.4 \times 10^5$	66
6	10	156 588	$\sim 6.2 \times 10^5$	65
6	15	263 304	$\sim 7.9 \times 10^5$	67
7	10	117 108	$\sim 2.4 \times 10^6$	65
7	15	305 896	$\sim 2.7 \times 10^6$	65

where ρ_0 is the mean sphere density, A the perturbation amplitude and θ the azimuthal angle in cylindrical coordinates.

The initial conditions are easy to implement for the AMR calculations. The SPH sinusoidal density perturbation is imposed by adjusting the unperturbed θ-coordinate of each particle to a perturbed value θ^* given by:

$$\theta = \theta^* + \frac{A \sin(\mathrm{m}\theta^*)}{\mathrm{m}}. \tag{5.23}$$

We compare simulations for three different thermal supports, namely $\alpha = 0.35$, 0.5 and 0.65, with a fixed rotational support $\beta = 0.04$. In the following, clumps for which the gas density satisfies $\rho > 1 \times 10^{-12}$ g cm^{-3} are referred to as *fragments*.

5.5.2 Results for a critical case: $\alpha = 0.5, \beta = 0.04$ and A=0.1

We now consider the effects of varying the numerical parameters. First, we study the effect of varying the initial grid resolution $\ell_{\rm min}$ and the number of cells within a Jeans length $N_{\rm J}$ for AMR calculations. Then, we present our SPH calculations with various number of neighbors $N_{\rm N}$ and of particles $N_{\rm p}$. For this set of calculations, the initial parameters are: $\rho_0 = 1.35 \times 10^{-18}$ g cm^{-3}, $R_0 = 7.07 \times 10^{16}$ cm, $\Omega_0 = 2.12 \times 10^{-13}$ rad s^{-1} and t$_{\rm ff}$ = 57 kyr. The initial perturbation amplitude is $A = 0.1$.

Table 5.3 summarizes the calculations we performed for this case. Informations about the core resolution (i.e. $\rho > 1 \times 10^{-15}$ g cm^{-3}) and the total number of cells are given at t=t$_0$+4 kyr. The dynamical times to reach the collapse are quite similar, within less than 2%. Synchronizing calculations at t$_0$ is then well justified. In the following sections, we consider core evolutions over a few thousand years ($\sim$ 10% of t$_0$).

Detailed study of the effect of $N_{\rm J}$ and ℓ_{min} for AMR calculations

In Fig. 5.8, we show density maps on the equatorial plane at four different time-steps for AMR calculations with, from left to right, $\ell_{\rm min} = 6$ and $N_{\rm J} = 4$, 10 and 15 and $\ell_{\rm min} = 7$ (giving 128^3

cells initially) and $N_J = 10$. Maps are given, from top to bottom, at t=t$_0$ + 4 kyr, t=t$_0$ + 5 kyr, t=t$_0$ + 6 kyr, and t=t$_0$ + 7 kyr. As shown in Fig. 5.8, fulfilling the Truelove condition (Truelove et al. 1997), $N_J > 4$, does not guarantee an accurate fragmentation timescale. The calculations with $N_J = 4$ fragments at t$_0$ + 5 kyr while other calculations do not fragment until t=t$_0$ + 7 kyr. This suggests that calculation with $\ell_{min} = 6$ and $N_J = 4$ suffers from inaccurate fragmentation, but this latter is inhibited when fragments fall onto the central object before t$_0$ + 6 kyr. The core will eventually refragment but not at the same time as the other calculations (i.e. t >> t$_0$ + 7 kyr). With increasing N_J, we converge to a fragmented pattern with one central object and two satellites.

Another aspect to be considered quite carefully is the choice of ℓ_{min}, i.e. the initial description of the sphere. The results of the two calculations for $N_J = 15$, with first $\ell_{min} = 6$ and secondly $\ell_{min} = 7$ are very similar, suggesting that numerical convergence has been achieved. We remark that small differences are apparent in the detailed structures. The satellites formed with $\ell_{min} = 7$ are more structured and compact than those formed with the initial resolution $\ell_{min} = 6$. According to these calculations, fragmentation into two identical satellites and a central object should occur around t=t$_0$ + 7 kyr.

Detailed study of the effect of N_p and N_N for SPH calculations

We performed a series of SPH calculations with different N_p, but with a constant $N_N = 50$, and then with a larger N_N for one value of N_p.

Figure 5.9 shows density maps in the equatorial plane for these calculations at four different time-steps, namely, from top to bottom: t=t$_0$ + 4 kyr, t=t$_0$ + 5 kyr, t=t$_0$ + 6 kyr and t=t$_0$ + 7 kyr. The calculations with $N_p = 2 \times 10^5$ and $N_p = 5 \times 10^5$ show good agreement at least until t$_0$ + 6 kyr and differ noticeably from the less resolved calculations ($N_N = 50$, $N_p = 5 \times 10^4$) where fragmentation occurs earlier. The dense core fragments in any case, but its fragmentation is delayed when N_p increases (e.g. Nelson 2006). Early fragmentation is here clearly due to a lack of resolution. As shown in section 5.4.2, the conservation of local angular momentum is bad when N_p is low and leads to very inaccurate collapse and fragmentation timescales of the cloud. Once symmetry is broken, it is useless to continue the simulations, since calculations would obviously diverge. This symmetry-breaking occurs earlier in the SPH calculations, first because of the numerical noise inherent to the relaxed, and random, initial particle distributions, and because of the lower resolution of the Jeans length in the disk.

The other fundamental parameter in SPH calculations is the number of neighbors that determine the kernel size. Increasing the number of SPH particles increases the resolution but also introduces numerical noise on smaller scales. The natural way to reduce this noise is to increase the smoothing kernel length, by increasing N_N. The effects of varying N_N have been investigated by Lombardi et al. (1999) and Rasio (1999). In particular, Rasio (1999) derived the following results:

- higher accuracy is reached when both N_p and N_N are increased, with N_p increasing faster than N_N so that the smoothing length decreases. One possible scaling (Lombardi et al. 1999) is $N_N \propto N_p^q$ with $0.2 \leq q < 1$,
- the SPH scheme is consistent in the limit where $(N_N, N_p) \to \infty$ and $h \to 0$,
- convergence (e.g. the number of timesteps) is accelerated by increasing the smoothness of the kernel.

The usual number of neighbors in previous studies is about 50. However, no study has accurately explored the role played by N_N in the context of star formation. Hence, we performed

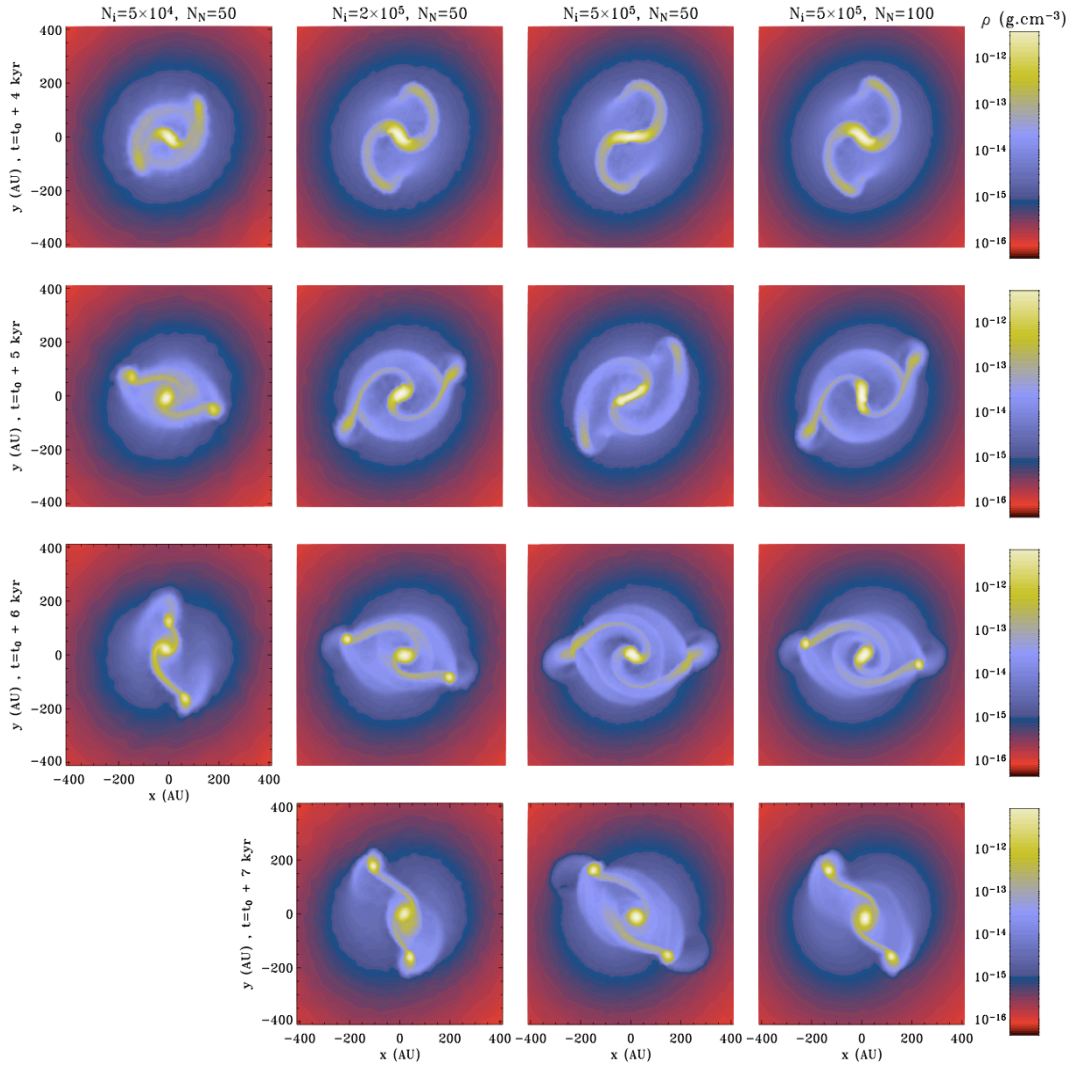

Figure 5.9: SPH calculations density maps in the xy-plane for the case $\alpha = 0.50$, $\beta = 0.04$. From top to bottom, four different times are shown: t=t$_0$ + 4 kyr, t=t$_0$ + 5 kyr, t=t$_0$ + 6 kyr and t=t$_0$ + 7 kyr. The calculations have been performed with, from left to right, $N_{\rm N} = 50$ and $N_{\rm p} = 5 \times 10^4$, $N_{\rm p} = 2 \times 10^5$ and $N_{\rm p} = 5 \times 10^5$ and $N_{\rm N} = 100$ and $N_{\rm p} = 5 \times 10^5$.

calculations with a constant $N_{\rm p}$ and different values of $N_{\rm N}$. This is illustrated in the right column in Fig. 5.9 where we report maps of calculations with $N_{\rm p} = 5 \times 10^5$ and $N_{\rm N} = 100$. The core has already fragmented at t$_0$ + 6 kyr whereas with $N_{\rm N} = 50$ it fragments later. The calculations with parameter set $N_{\rm p} = 2 \times 10^5$ and $N_{\rm N} = 50$ is very similar to the later of similar ratio $N_{\rm p}/N_{\rm N}$. Other calculations with various $N_{\rm N}$ are reported in §5.6.1. It appears clearly that the greater $N_{\rm N}$ the earlier fragmentation occurs, because increasing $N_{\rm N}$ for a fixed $N_{\rm p}$ decreases the spatial resolution (h increases).

Comparison and convergence

In the previous sections, we show that AMR and SPH calculations converged separately. We now compare the converged calculations. Figure 5.10 shows density maps in the equatorial plane for the results of two of the most resolved calculations at three timesteps, namely, from top to bottom, t$_0$+5 kyr, t$_0$+6 kyr and t$_0$+7 kyr. The left column shows maps for AMR calculations with $\ell_{\rm min} = 7$ and $N_{\rm J} = 15$ whereas the right column displays SPH maps for calculations

with $N_{\rm p} = 5 \times 10^5$ and $N_{\rm N} = 50$. We display again the results of Fig.5.8 and Fig.5.9 to illustrate clearly the convergence. Agreement between the two methods for these physical and numerical parameters set is striking for the two first timesteps. The calculations provide the same fragmentation time and pattern, although satellites and the central object are larger for SPH.

Figure 5.11 shows disk density profiles as a function of the radius averaged in the equatorial plane for the same SPH and AMR calculations. This plot complements Fig. 5.10 with the last density maps, where fragments are well-developed. Density profiles show a peak at a radius corresponding to satellite positions in the map. Satellite fragments are denser in the SPH calculations, and the central object is less dense and larger compared with the dense elongated shape obtained with the AMR.

Although there are some obvious differences between the two methods, there seems to be a real convergence between the two types of calculations. For the specific case under study, we find a good agreement between AMR calculations with $\ell_{\rm min} = 7$ or 6, and $N_{\rm J} = 15$ and SPH calculations with $N_{\rm p} = 5 \times 10^5$ and $N_{\rm N} = 50$. However, even for the most resolved simulations, the results between the two methods diverge after some time (i.e. t_0+7 kyr for this specific case). This is not surprising because the dynamics becomes non-linear and chaotic, as the initial and numerical noise become amplified.

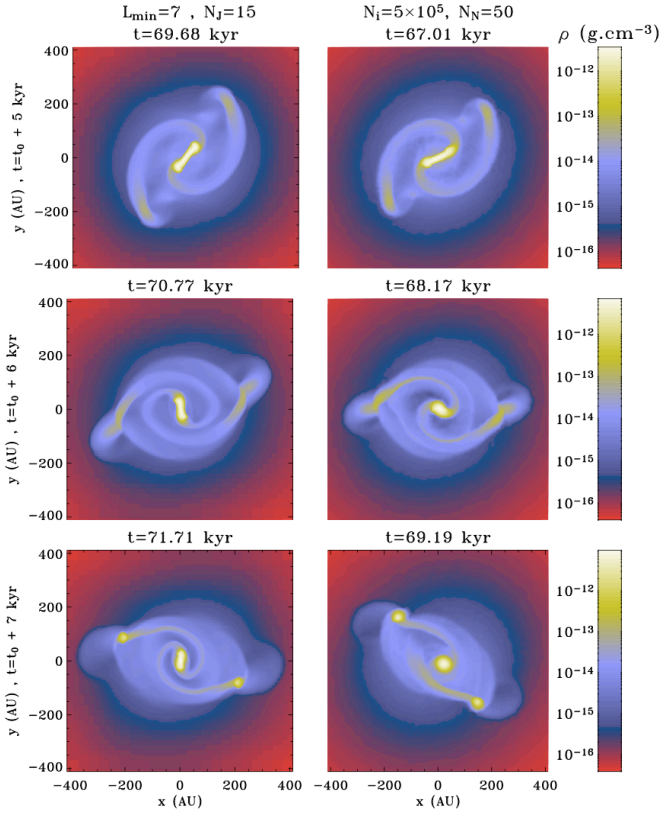

Figure 5.10: AMR and SPH calculations density maps in the xy-plane at three different times for the case $\alpha = 0.50$, $\beta = 0.04$. The times correspond to $t_0 + 5$ kyr, $t_0 + 6$ kyr and $t_0 + 7$ kyr, from to bottom, respectively. The AMR calculations plotted on the left column have been run with $\ell_{\rm min} = 7$ and $N_{\rm J} = 15$. The right column shows the results for the SPH calculations with $N_{\rm p} = 5 \times 10^5$ and $N_{\rm N} = 50$.

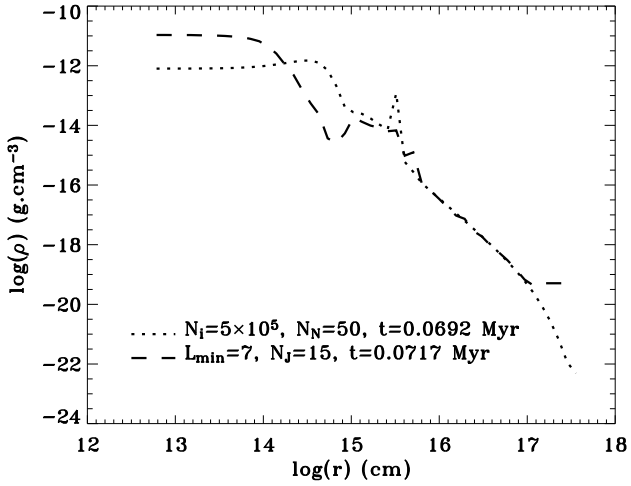

Figure 5.11: Density profiles at t_0+ 7 kyr as a function of the radius, averaged on the equatorial plane, for AMR calculations with $\ell_{\rm min} = 7$ and $N_{\rm J} = 15$ (dashed line), and SPH calculations with $N_{\rm p} = 5 \times 10^5$ and $N_{\rm N} = 50$ (dotted line).

5.5.3 Results for low and high thermal support

Results for a less prone to fragment case: $\alpha = 0.65$**,** $\beta = 0.04$

This second series of calculations is the least prone to fragmentation because of its strong thermal support. We use a perturbation amplitude $A = 0.5$ in order to make fragmentation easier if it should occur.

Figure 5.12 gives density slices on the equatorial plane at t=$t_0 + 10$ kyr. On the left-hand side, we show AMR results for an initial sphere described with $\ell_{min} = 6$ and, from top to bottom, $N_{\rm J} = 4$, 10 and 15. The right-hand column shows slices of SPH calculations with $N_{\rm N} = 50$ and $N_{\rm p} = 5 \times 10^4$, 2×10^5 and 5×10^5, from top to bottom. In the previous cases, the core has already fragmented into three clumps at this time. In this case, the cloud develops spiral arms with no fragmentation. The cloud fragments in some cases after $t_0 + 50$ kyr.

AMR and SPH calculations converge quickly to a pattern with only spiral arms and the formation of a single central object when resolution is sufficient.

Early fragmentation case: $\alpha = 0.35$ **,** $\beta = 0.04$

This last case is the most prone to fragmentation because of its small thermal support against gravitational energy. In this set of calculations, the initial parameters are: $\rho_0 = 3.92 \times 10^{-18}$ g cm^{-3}, $R_0 = 4.95 \times 10^{16}$ cm, $\Omega_0 = 3.63 \times 10^{-13}$ rad s^{-1} and $t_{\rm ff} = 1.06 \times 10^{12}$ s (~ 33.6 kyr). The initial perturbation amplitude is $A = 0.1$. We performed SPH calculations with $N_{\rm p}$ ranging from 5×10^4 to 5×10^5 and $N_{\rm N} = 50$. The AMR calculations were performed with $\ell_{\rm min} = 6$ and 7, and $N_{\rm J}$ varying between 4 and 15. Although all results are very similar at t_0, we find some differences at $t_0 + 1$ kyr. For example, it appears quite clear that AMR calculations with $\ell_{\rm min} = 6$ and $N_{\rm J} = 4$ diverge from the other AMR calculations (tiny spiral arms).

Figure 5.13 shows density maps in the equatorial plane for the most relevant calculations at t=$t_0 + 3$ kyr. On the left column, we provide the AMR results with increasing resolution parameter $N_{\rm J}$ from top to bottom and a constant $\ell_{\rm min} = 6$. According to our previous results, an initial computational domain with $\ell_{\rm min} = 6$ is sufficient to reach convergence for the AMR

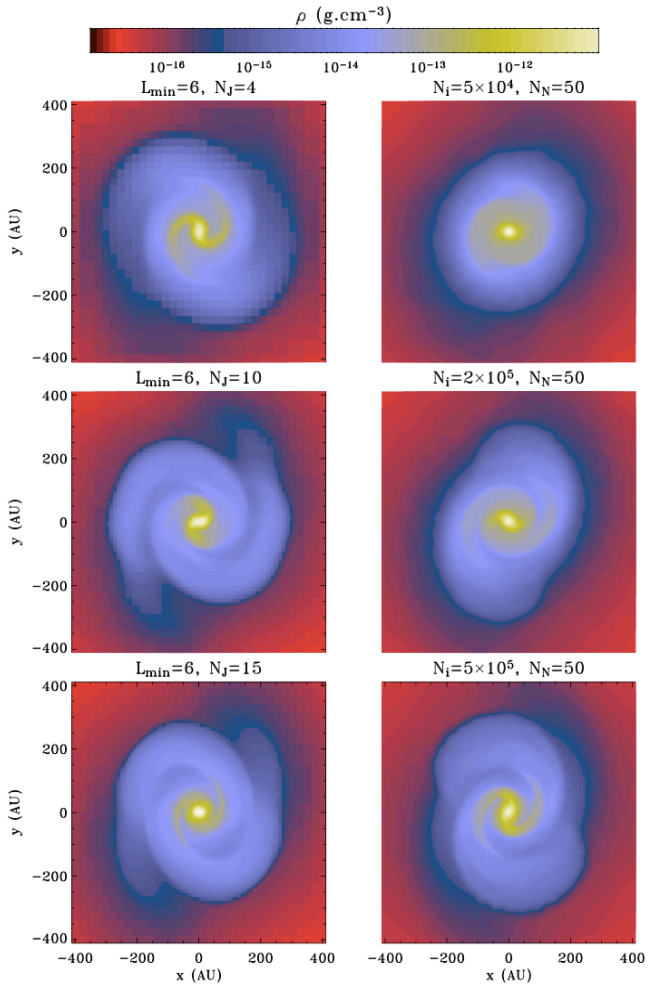

Figure 5.12: Density maps in the equatorial plane at $t_0 + 10$ kyr for $\alpha = 0.65$, $\beta = 0.04$ and $A = 0.5$. On the left-hand side, we show AMR results with $\ell_{\rm min} = 6$ and, from top to bottom, $N_{\rm J} = 4$, 10 and 15. The right-hand side gives slices of SPH calculations with $N_{\rm N} = 50$ and $N_{\rm p} = 5 \times 10^4$, 2×10^5 and 5×10^5, from top to bottom.

calculations. The right column shows SPH calculations, with $N_{\rm p}$ ranging from 5×10^4 to 5×10^5. We seem to reach a convergence between the AMR calculations with $\ell_{\rm min} = 6$ and $N_{\rm J} > 6$. The SPH calculations with $N_{\rm p} = 5 \times 10^4$ diverge quickly compared to two more resolved with $N_{\rm p} = 1 \times 10^2$ and 5×10^5. The most resolved AMR and SPH runs show a convergence towards a similar solution. The patterns have the same size and position. The core fragments into a central clump (of size ~ 30 AU) and two identical outlying clumps (of size ~ 10 AU) for AMR calculations. A similar central object is present in the SPH calculations, but the outlying clumps are larger.

However, as shown in §5.6.3, higher resolution runs show that convergence has not been reached. In that case, one needs either an even better resolution or, alternatively, a more sophisticated numerical scheme.

To conclude our study on core fragmentation, it becomes increasingly difficult to attain convergence in both SPH and AMR simulations as non-linearity increase. Good convergence is found for sufficiently high thermal support. However, for low thermal support (i.e. $\alpha = 0.35$), convergence is more difficult to achieve and the horizon of predictability becomes short.

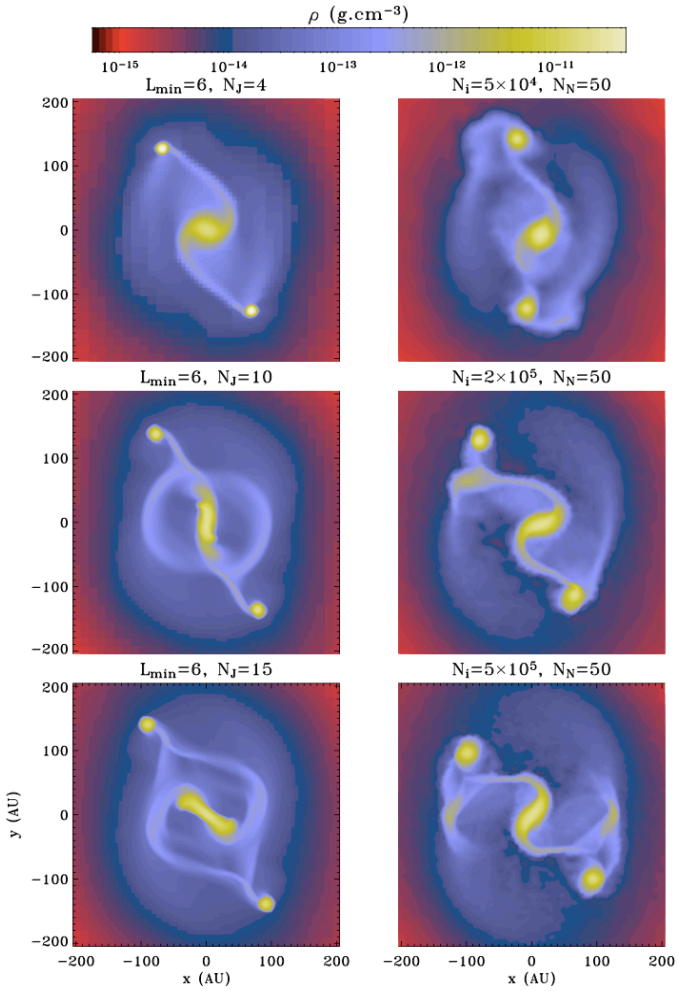

Figure 5.13: Density maps in the equatorial plane at t=t$_0$ + 3 kyr for the case $\alpha = 0.35$, $\beta = 0.04$ and $A = 0.1$. On the left side, we give AMR results with $\ell_{\rm min} = 6$ and, from top to bottom, $N_{\rm J} = 4$, 10 and 15. On the right side, we show SPH maps with calculations with $N_{\rm N} = 50$ and, from top to bottom, $N_{\rm p} = 5 \times 10^4$, $N_{\rm p} = 2 \times 10^5$ and $N_{\rm p} = 5 \times 10^5$.

5.6 Improvements, numerical diffusion and sink particles

5.6.1 Complementary results on the effect of $N_{\rm N}$ for SPH calculations for the case: $\alpha = 0.5, \beta = 0.04$ and A=0.1

Figure 5.14 shows SPH calculations run with a constant $N_{\rm p} = 5 \times 10^5$ and values of $N_{\rm N} = 30$, 50, 100 and 200 from top to bottom for two timesteps (t$_0$+5 kyr on the left column and t$_0$+6 kyr on the right column). These simulations should be compared with simulations presented in Fig. 5.9. The first relevant result is the fact that increasing $N_{\rm N}$ speeds up fragmentation. Moreover, there seems to be a similarity between calculations with low $N_{\rm p}/N_{\rm N}$ ratio, i.e. $N_{\rm N} = 50$, $N_{\rm p} = 2 \times 10^5$ on one side and $N_{\rm N} = 100$ and $N_{\rm p} = 5 \times 10^5$ on the other side. We find the same patterns at different times, postponed when either $N_{\rm p}$ increases or $N_{\rm N}$ decreases, the number of resolution elements being equal. This illustrates the compromise between resolution and convergence that must be respected in SPH calculations (Lombardi et al. 1999; Rasio 1999).

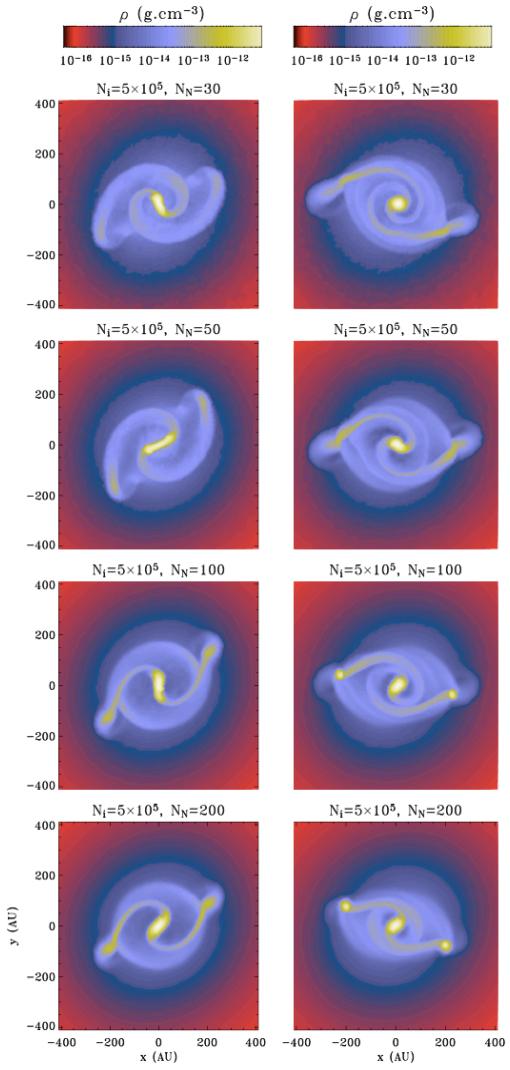

Figure 5.14: Density maps in the equatorial plane at two different times from SPH calculations with $\alpha = 0.50$, $\beta = 0.04$ and $N_{\rm p} = 5 \times 10^5$. The left column shows density maps for calculations with $N_{\rm N} = 30$, 50, 100 and 200 from top to bottom, respectively, at t=t_0 + 5 kyr. The right column represents the same calculations at t=t_0 + 6 kyr.

5.6.2 Artificial viscosity and numerical diffusion in SPH

Diffusivity is a well-known drawback of standard SPH. This issue can be reduced using a constant number neighbors, $\Delta N_{\rm N} = 0$ (Attwood et al. 2007), and an advanced scheme for viscosity such as time-dependent viscosity (Morris and Monaghan 1997). We present here SPH calculations of the collapse of the uniform-density sphere already studied in §5.4, but using another scheme viscosity and/or a constant number of neighbors. This two improvements are straightforward to implement and do not require expensive extra computational costs. Time-dependent viscosity calculations have been completed for $\alpha^\star = 0.1$, and an e-folding constant equal to 0.15.

Figure 5.15a shows the averaged ratio between angular momentum $J(t)$ at time t_0, and initial angular momentum J_0 as a function of particles (ordered in decreasing density) for SPH calculations run with $N_{\rm p} = 5 \times 10^5$ and $N_{\rm N} = 50$. In addition, the improvement on viscosity and number of neighbors above mentioned are either turned on or not. It is clear that time-dependent viscosity can better conserve angular momentum for the denser particles. Hence, less

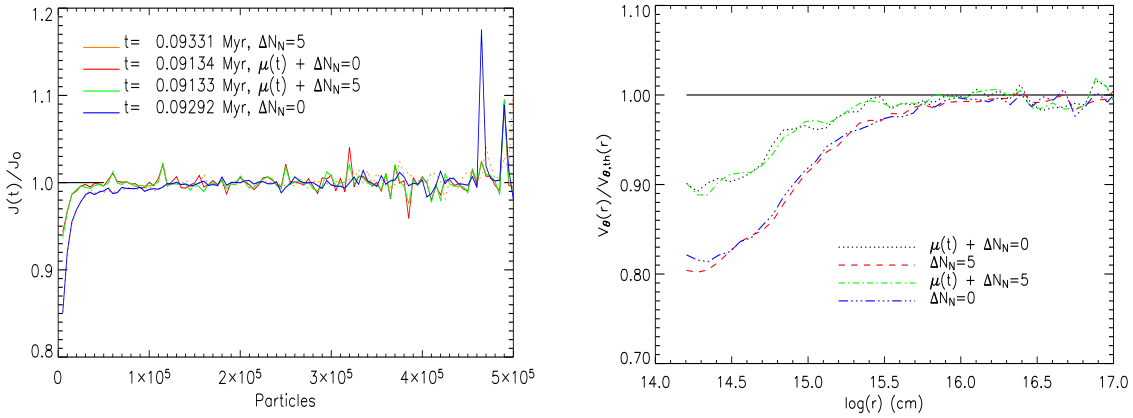

Figure 5.15: *Left polt* (Fig .5.15a): same as Fig. 5.4 with different $\Delta N_{\rm N}$ and artificial viscosity scheme. $\mu(t)$ indicates the use of time-dependent viscosity instead of the standard artificial viscosity scheme in the paper. *Right plot* (Fig .5.15b): same as Fig. 5.7 for the above mentioned SPH calculations.

angular momentum is transported to the outer part of the core. This is confirmed in Fig. 5.15b where we plot the ratio between angular momentum at time t_0 and initial angular momentum, as a function of the radius, for the same calculations. Local angular momentum conservation is increased by 10% in the inner part. However, keeping the number of neighbors constant does not improve local angular momentum conservation because the system evolves only over about one free-fall time, whereas Attwood et al. (2007) shows that dissipation becomes significant after a few free-fall times. All of these improvements of standard SPH will strengthen convergence with the AMR. The particle-splitting appears to be the most promising one.

5.6.3 Diffusion of the numerical schemes in AMR

A key ingredient of the AMR method is the numerical scheme used to compute flux at the grid's interfaces. In this paper, we use a Lax-Friedrich (hereafter LF) Riemann solver designed for MHD calculations (Fromang et al. 2006). However, the LF scheme is known to be a diffusive scheme. In this section, we present AMR calculations carried out with, on one hand, the LF scheme and, on the other hand, a Roe scheme. The Roe scheme is less diffusive than LF, and this could dramatically affect the fragmentation issue.

Case $\alpha = 0.5$, $\beta = 0.04$

Figure 5.16 shows density maps on the equatorial at three different timesteps for two AMR calculations run with the same numerical parameters, i.e. $\ell_{min} = 6$ and $N_{\rm J} = 15$, but with a different solver, i.e. the LF one on the left column and the Roe one on the right column. Results are quite similar, AMR calculations are in good agreement for this critical case with the two solvers. Since less angular momentum has been locally lost or transported with the Roe scheme, the core is smaller and the fragments are closer to the central object. This brings support to the fact that we find good convergence between AMR and SPH calculations for this case.

Case $\alpha = 0.35$, $\beta = 0.04$

Figure 5.17 shows density maps on the equatorial plane at t_0 + 2 kyr (right column) and t_0 + 3 kyr for three simulations of the case $\alpha = 0.35$, $\beta = 0.04$ with numerical parameters $\ell_{\rm min} = 6$ and

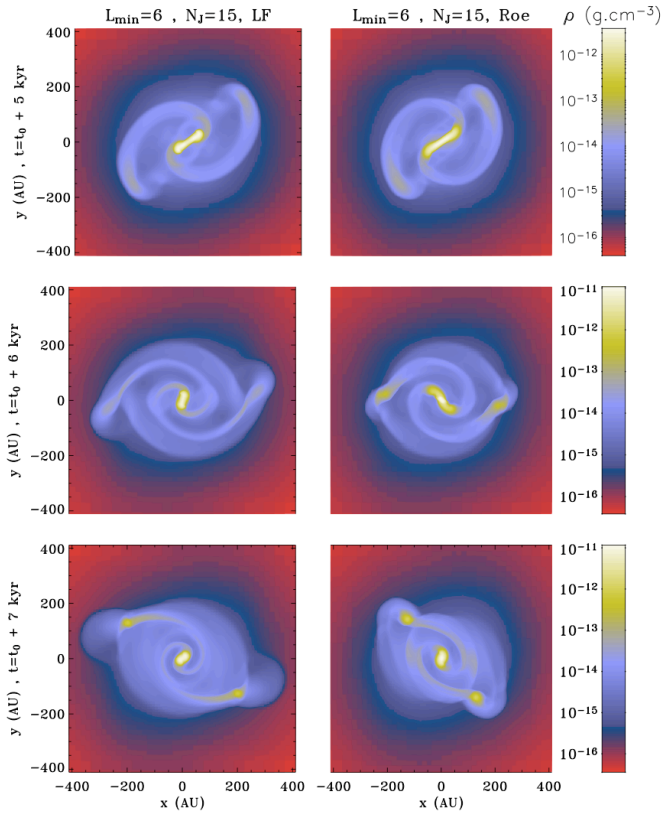

Figure 5.16: Density maps in the equatorial plane for the case $\alpha = 0.5$, $\beta = 0.04$ at, from top to bottom, t=t$_0$ + 5 kyr, t=t$_0$ + 6 kyr and t=t$_0$ + 7 kyr. On the left-hand side, AMR results with Lax-Friedrich solver and $\ell_{min} = 6$, $N_{\rm J} = 15$ are reported and AMR results of calculations with he same parameters but with a Roe solver are given on the right column.

$N_{\rm J} = 12$ (top and bottom maps, LF and Roe schemes) and $\ell_{\rm min} = 7$ and $N_{\rm J} = 15$ (middle row, LF scheme). We remark that in Fig. 5.13, the case $\ell_{\rm min} = 6$ and $N_{\rm J} = 15$ with the LF solver has been displayed. The two calculations with the same numerical parameters differ, according to the numerical scheme used. The fragmentation process changes: one achieves a configuration central object + two satellites with the LF scheme whereas we get a binary system resulting from the fragmentation of the central object with the Roe scheme. If we improve the initial sphere resolution in LF calculations (i.e. $\ell_{\rm min} = 7$, $N_{\rm J} = 15$), we converge to the results obtained with the Roe scheme, i.e. a central binary system, with a value $\ell_{\rm min} < 7$. We know that angular momentum is well conserved using the Roe scheme or the LF scheme with $\ell_{\rm min} = 7$, so it seems that calculations lead to a different core fragmentation because of their less accurate angular momentum conservation. Since we use a small thermal support, it is easy to reach another fragmentation configuration, these processes being highly non-linear.

5.6.4 Sink particles

Sink in SPH

The introduction of sink particles is a widely used method to obtain a compromise between good resolution and acceptable time-step in SPH methods. Creating a sink particle enables the Courant condition on the particle timesteps to be relaxed.

The density level $\rho_{\rm sink}$ at which a sink particle is created has to be chosen with care. In

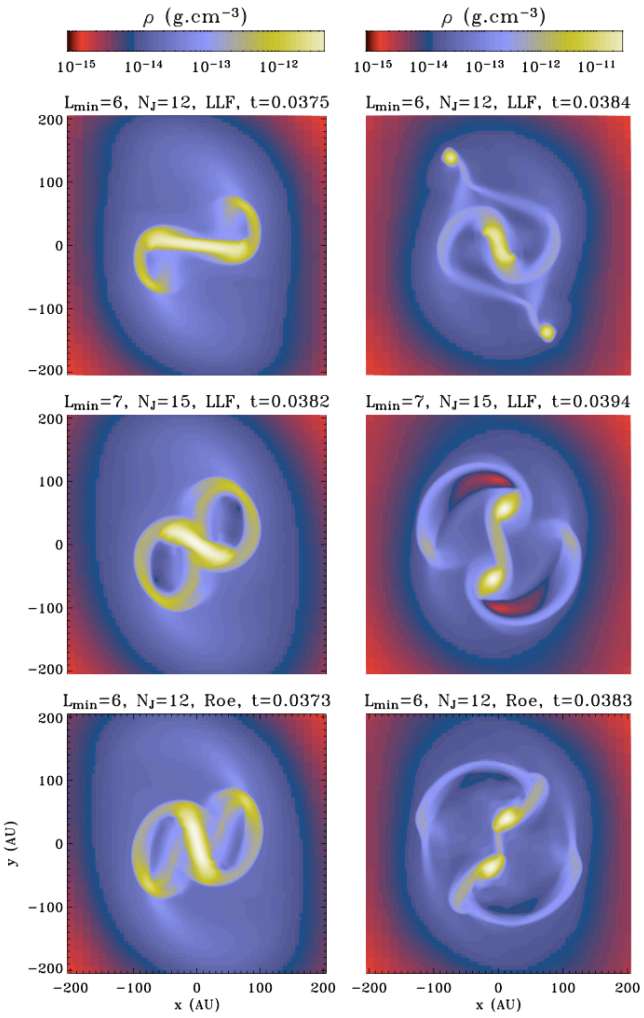

Figure 5.17: Density maps in the equatorial plane for the case $\alpha = 0.35$, $\beta = 0.04$ at t=t$_0$ + 2 kyr on the left-hand side and t=t$_0$ + 3 kyr on the right-hand side. For the two upper rows, we plot results for AMR calculations with ($\ell_{\rm min} = 6$, $N_{\rm J} = 12$), ($\ell_{\rm min} = 7$, $N_{\rm J} = 15$) and our usual Lax-Friedrich scheme. The bottom row gives the results for calculations conducted with ($\ell_{\rm min} = 6$, $N_{\rm J} = 12$) too, but with a Roe solver. Times are given in Myr.

the previous SPH calculations, no sink particles were used. We focus on the highly non-linear fragmentation case, $\alpha = 0.35$, $\beta = 0.04$ and $A = 0.1$ to present SPH calculations carried out with various sink densities.

Figure 5.19 shows calculations carried out with three different densities for the creation of sink particles, $\rho_{\rm sink}$, namely 1×10^{-10} g cm^{-3} (resulting in no sink creation), 1×10^{-11} g cm^{-3} and 3×10^{-12} g cm^{-12}, from top to bottom, and the same number of SPH particles and neighbors, $N_{\rm p} = 5 \times 10^5$ and $N_{\rm N} = 50$. The left-hand side reports results at t$_0$+ 1 kyr and the right-hand column results at t$_0$ + 3 kyr. The CPU time is about 28% smaller for the case $\rho_{\rm sink} = 3 \times 10^{-12}$ g cm^{-3} than for the case $\rho_{\rm sink} = 1 \times 10^{-10}$ g cm^{-3}, but the dense core resulting at t$_0$ + 3 kyr is different. Sink accretion radius has been set at 5 AU. The upper row corresponds to calculations without creation of sink particles, whereas one sink particle has been created with $\rho_{\rm sink} = 1 \times 10^{-11}$ g cm^{-3} and 9 with $\rho_{\rm sink} = 3 \times 10^{-12}$ g cm^{-3}. It is easy to see that, even if only one sink particle is created, the complete dynamic of the flow is affected particularly in the central region.

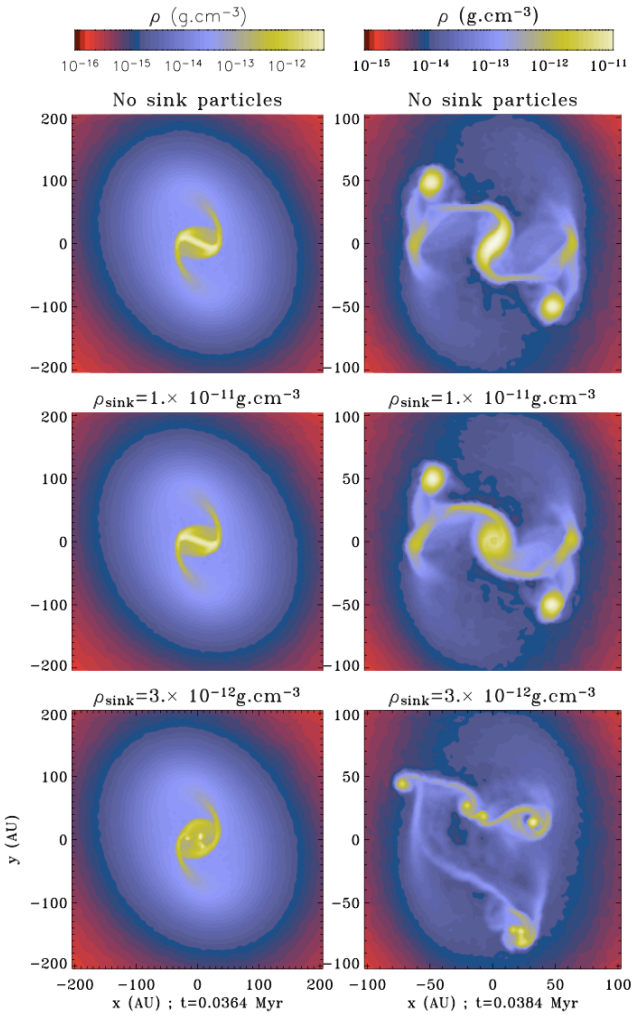

Figure 5.18: Density maps in the equatorial plane for the case $\alpha = 0.35$, $\beta = 0.04$ at t=t_0 + 1 kyr on the left-hand side and t=t_0 + 3 kyr on the right-hand side. 9 sink particles have been created on the bottom figures, affecting the whole dynamic of the dense core.

Sink in AMR

Sink particles in AMR calculations have been introduced for the same purpose as for the SPH case: save CPU time. Krumholz et al. (2004) choose to introduce sinks as star particles in collapse calculations that accretes material following Bondi-Hoyle accretion or sink merger. In that case, sink particles are created when the Jeans length is not resolved at the highest level of refinement. In a following work, Krumholz et al. (2007a) perform massive star calculations, where the accreted mass is converted into luminosity, assuming a prestellar evolution model.

In our case, sinks will be created in the same way as in SPH, i.e. in each cell where density exceeds $\rho_{\rm sink}$, a sink particle is created. To avoid a too large number of sink particles, particles are merged using a friend of friends (FOF) algorithm (Davis et al. 1985). Accretion of the main sink is then only due to merger with other sink.

5.7 Summary and Discussion

We have investigated the effect of changing the numerical resolution in AMR and SPH calculations, on the collapse and the fragmentation of rotating cores.

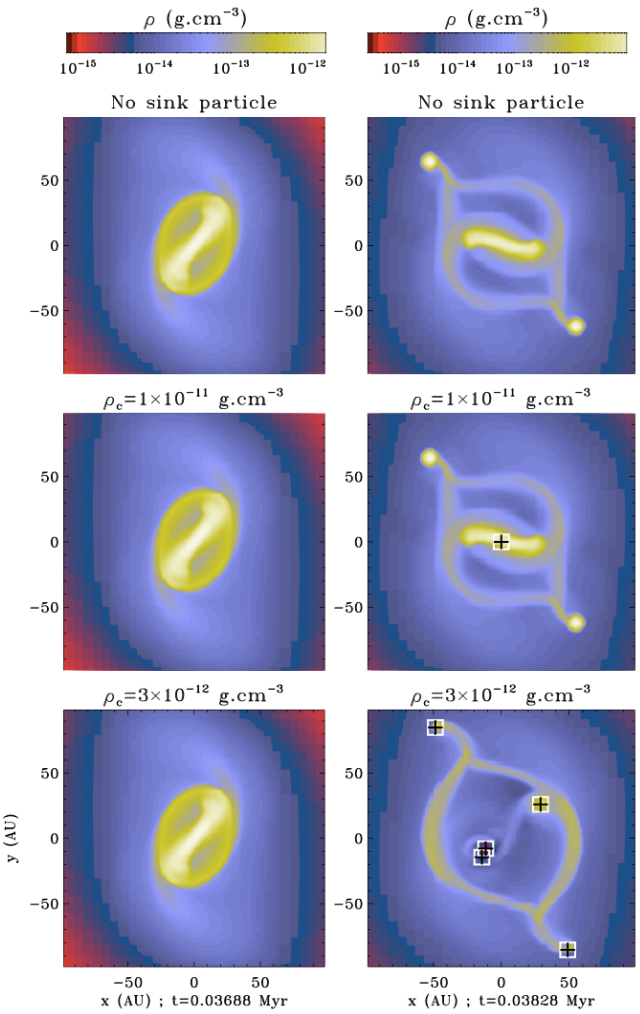

Figure 5.19: Density maps in the equatorial plane for the case $\alpha = 0.35$, $\beta = 0.04$ at t=t$_0$ + 1 kyr on the left-hand side and t=t$_0$ + 3 kyr on the right-hand side. 9 sink particles have been created on the bottom figures, affecting the full dynamic of the dense core.

We show that we reach good convergence between AMR and SPH methods provided one uses sufficient numerical resources. First, we take a simple model to study local angular momentum conservation. The initial study shows that local angular momentum is better conserved with the AMR approach for equivalent computational needs, whereas SPH provides better dynamical times. As shown in Fig. 5.6a, a smaller number of particles in standard SPH calculations leads to poor local angular momentum conservation. Numerical torques on the rotational axis accumulate onto denser particles, whereas our model remains axisymmetric. In AMR calculations, a poor initial computational domain resolution (i.e. $\ell_{\rm min} < 6$) leads to unphysical transfer of gravitational energy to rotational energy (see Fig. 5.6b). A significant loss of angular momentum will affect fragmentation since less rotational support can balance gravitational collapse. The smallest parameter values set for SPH calculations required to be able to simulate gravitational collapse without significant loss of angular momentum corresponds to a number of ~ 530 particles per Jeans mass at the critical density $\rho_{\rm c}$, i.e. 5 particles per Jeans *length*. The equivalent minimum resolution criterion for AMR calculations is $\ell_{\rm min} \geq 6$ and $N_{\rm J} = 4$.

We next investigated fragmentation issues for three different initial condition. For the least prone to fragment case ($\alpha = 0.65$, $\beta = 0.04$), we showed that AMR and SPH methods provide similar results when their respective Jeans resolution criteria are fulfilled. These results

agree with semi-analytical criteria on fragmentation derived by Tsuribe and Inutsuka (1999), for isothermal collapse. We carefully analyzed simulations completed for the initial conditions parameter values $\alpha = 0.5$, $\beta = 0.04$. We reached good agreement between AMR calculations with the parameters $\ell_{\rm min} = 6$ and $N_{\rm J} = 15$ and SPH calculations with $N_{\rm p} = 5 \times 10^5$ and $N_{\rm N} = 50$, i.e. ~ 5370 particles per Jeans mass at critical density $\rho_{\rm c}$. This parameter set appears to correspond to a lower resolution limit for dense core collapse and fragmentation in SPH and AMR calculations. This is required to reach good agreement in both time and space. Using a lower number of particles or number of points per Jeans length will lead to inaccurate early fragmentation due to numerical effects. Initially, we compared the two converged calculations and, for this specific case, we found good agreement between the two methods (see Fig 5.10). For the fragmentation study, the computer time is more expensive for the SPH method due to the lack of use of sink particles. In the case of low thermal support, the dynamic of the flow quickly becomes very non-linear and numerical convergence of the simulation cannot be achieved as easily as for higher thermal support. A statistical analysis over a large number of simulations would be required to assess if convergence can be achieved for fragment masses, sizes and number.

Star formation analyses completed using SPH and AMR simulations provide predictions that, in general, agree. Details are better resolved in AMR calculations thanks to the refinement method based on the local Jeans length, whereas resolution deteriorates with increasing density in standard SPH calculations. Numerical calculations of protostellar collapse should be carefully conducted, with a detailed examination of the effect of numerical resolution. The present work can be used to assess the validity of numerical tools in the study of star formation.

Chapter 6

Radiation-magneto-hydrodynamics collapse calculations

Contents

This last chapter is devoted to original Radiation-magneto-hydrodynamics calculations of dense core collapse. It has been shown in previous studies, that both magnetic field and radiative feedback inhibit the fragmentation (e.g. Krumholz et al. 2007b; Price and Bate 2009). We study in this chapter the combined effect of radiative transfer and magnetic field on the small scales ($R < 100$ AU), using our usual model of the collapse of a rotating, 1 $M_\odot$ dense core. We first perform calculations with radiative transfer using the Flux Limited Diffusion module presented in chapter 4 and compare the results to those obtained with a barotropic EOS. We study the impact of radiative transfer on the cooling and the fragmentation. Then, we add a magnetic field, that is parallel to the rotational axis. We study the influence of radiative transfer on the outflow launching and on fragmentation. Eventually, we present calculations taking into account the radiative feedback of an accreting low mass protostar. We demonstrate that for low mass core, this feedback has no impact on the fragmentation nor on the outflow.

6.1 Hydrodynamical collapse

In this first section, we compare results for calculations performed using a barotropic EOS and the Flux Limited Diffusion approximation. As in the previous chapter, the initial setup consists in a sphere with a uniform density and temperature sphere in solid body rotation. To

foster fragmentation, we add an azimuthal $m = 2$ density perturbation, with an amplitude perturbation A= 0.01. We run two cases with two different thermal and rotational support.

6.1.1 Case $\alpha = 0.5$, $\beta = 0.04$ and $m = 2$ and A= 0.01

Calculations have been run with $\ell_{\rm min} = 6$, $N_{\rm J} = 15$. We use the Lax-Friedrich Riemann solver. In the FLD case, we use the Minerbo flux limiter and the convergence criterion of the conjugate gradient solver has been set to 1×10^{-4}. We do not use subcycling as presented in §4.4.4.

Comparison to the barotropic case

In figure 6.1, we show density and temperature maps in the equatorial plane (2 upper rows) and temperature maps in the xz-plane (bottom), at the same time $t = 1.18\ t_{\rm ff}$. The left column gives results of calculations done with the FLD approximation and the middle and right columns results of calculations performed using a barotropic EOS with respectively $\rho_{\rm ad} = 1{\times}10^{-13}$ g cm^{-3} (middle) and $\rho_{\rm ad} = 2.3 \times 10^{-13}$ g cm^{-3} (right). The black lines give the isocontour of density corresponding to optical depth $\tau_{\rm min} \sim 1$ and $\tau_{\rm min} \sim 10$ (in the next §about the FLD results, we show that the optical depth depends only on the density, see figure 6.4d). First, fragmentation takes place earlier with the FLD. We see that the FLD calculations produce 5 fragments, instead of 3 in the barotropic case (see figure 5.10). For the barotropic case, the higher $\rho_{\rm ad}$, the quicker fragmentation occurs. When $\rho_{\rm ad}$ increases, the critical Jeans mass becomes lower, and it is easier to get fragmentation, at smaller scales. The value of $\rho_{\rm ad} = 2.3 \times 10^{-13}$ g cm^{-3} has been derived in chapter 3 and we clearly see that this value is more appropriate in terms of fragmentation time and size if we take for reference the FLD case. The case with $\rho_{\rm ad} = 1 \times 10^{-13}$ g cm^{-3} fragments later as it is shown in figure 5.10.

From the temperature maps in figure 6.1, we note that the temperature of the disk is greater in the barotropic case compared to FLD. We set the maximum temperature to 20 K in order to put emphasis on the differences between the FLD and the barotropic cases. Temperature differences are quite important, $\sim 4 - 5$K (25%-50%), and big enough to completely alter fragmentation. A difference of 4% in the temperature changes the Toomre parameter Q by $\sim 20\%$ (see equation 6.3). In the FLD case, the temperature is low in most of the disk, which gives a small Toomre parameter. In the xz-plane maps, the disk formed with the two barotropic EOS is clearly hotter than the one produced by FLD. This is due to the fact that radiation escapes in the vertical direction in the FLD case, whereas in the barotropic case, the temperature and thus the cooling are set by the density, and do not depend on the local optical depth (see next part about FLD results). In this particular case, the optical depth depends only on the density, but the spread in temperature at a given optical depth expresses cooling and heating that a barotropic EOS cannot reproduce. Eventually, the gas has been heated up in the optically thin region, whereas radiation should escape and the gas should remain cold!

In figure 6.2, we show the temperature - density distribution for the FLD case and for three barotropic EOS. The first important result is that there is a spread in the density-temperature distribution with the FLD. At high temperature in the FLD case, we distinguish two different adiabatic regions, starting from two different densities. The first adiabatic region, starting from the lower density, corresponds to the central fragments formed earlier. The second adiabatic region corresponds to the orbiting fragments formed later and which have more time to cool down and to reach smaller Jeans mass. The fragments, depending on their location and formation time, do not have the same entropy levels. This can be of prime importance if these fragments survive and produce protostars. Last, we also plot the barotropic law for a material with critical density $\rho_{\rm ad} = 2.3 \times 10^{-13}$ g cm^{-3} and adiabatic exponent 7/5 (blue curve). We have performed

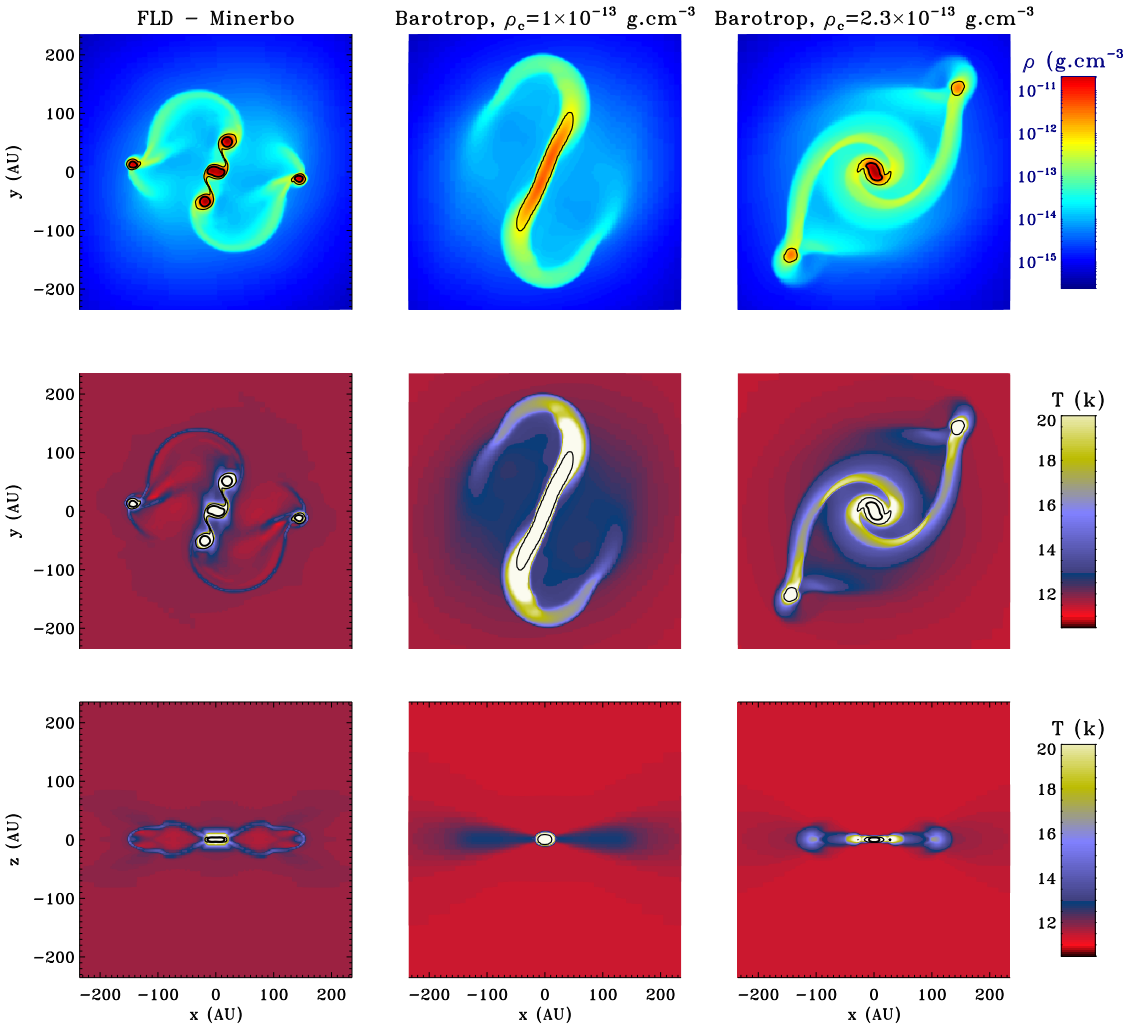

Figure 6.1: Density and temperature maps in the equatorial plane (2 upper lines) and temperature maps in the xz-plane (bottom row), for 3 calculations performed with the FLD approximation (left), and with a barotropic EOS using $\rho_{\rm ad} = 1 \times 10^{-13}$ g cm^{-3} (middle) and $\rho_{\rm ad} = 2.3 \times 10^{-13}$ g cm^{-3} (right).

calculations with this barotropic EOS and found that in that case, fragmentation takes place at smaller scales and the density is greater. With this barotropic EOS, it is easier to get high density in the center and to produce quickly a small and dense fragment in the center.

Figure 6.3 shows the mean profiles in the equatorial plane of the density and the temperature for the calculations performed with the FLD approximation (solid line) and for calculations done with a barotropic EOS with $\rho_{\rm ad} = 1 \times 10^{-13}$ g cm^{-3} (dotted line) and $\rho_{\rm ad} = 2.3 \times 10^{-13}$ g cm^{-3} (dashed line) at the same time $t = 1.18\ t_{\rm ff}$. The density profile obtained with the barotropic EOS using $\rho_{\rm ad} = 2.3 \times 10^{-13}$ g cm^{-3} is in quite good agreement with the FLD results in the central region. At higher radius, fragments formed in the FLD case are closer to the center and much denser than those formed in the barotropic case. The temperature profiles are totally different. The gas temperature is overestimated in the two barotropic cases, for radii included between 10 AU and 100 AU, i.e. in the fragmentation region! At the same density, the material in the FLD case is always cooler and is not fully adiabatic as shown in chapter 3. For $\rho_{\rm ad} = 1 \times 10^{-13}$ g cm^{-3}, we see that both temperature and density are underestimated in the central region.

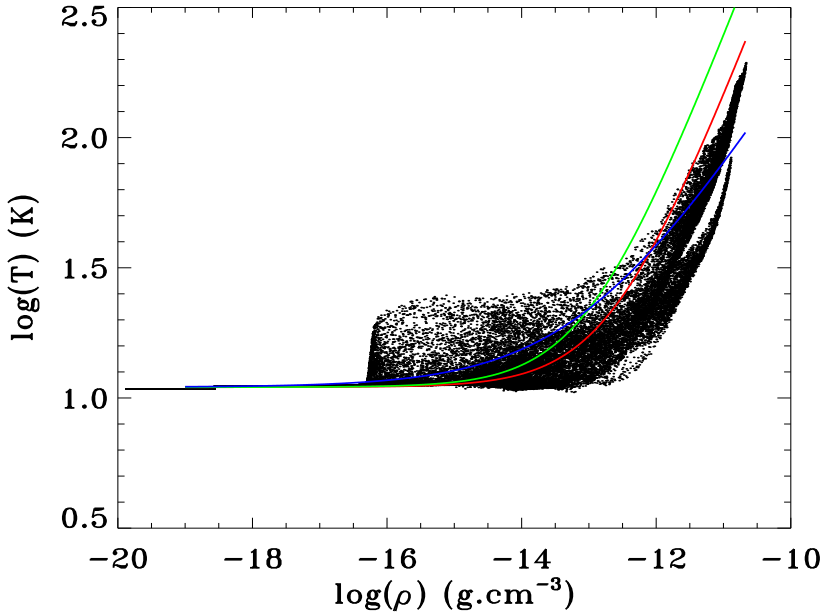

Figure 6.2: Temperature versus density distributions for the FLD case (black) and for the barotropic EOS with $\rho_{\rm ad} = 1 \times 10^{-13}$ g cm^{-3} (green) and $\rho_{\rm ad} = 2.3 \times 10^{-13}$ g cm^{-3} (red). The blue curve gives the temperature density law for a barotropic EOS with $\rho_{\rm ad} = 2.3 \times 10^{-13}$ g cm^{-3} and $\gamma = 7/5$, which is more appropriate for $T > 100$ K.

Results with the FLD

Figure 6.4 shows results at time t=0.06715 Myr (1.18 $t_{\rm ff}$) obtained in the FLD case. Figure 6.4(a) and 6.4(b) show maps of the column density

$$\Sigma(x,y) = \int \rho(x,y,z)dz, \tag{6.1}$$

and of the mass-weighted temperature

$$T(x,y) = \int T(x,y,z)\rho(x,y,z)dz/\Sigma(x,y). \tag{6.2}$$

All quantities have been estimated within a little box in the computational domain, of dimensions $dx = dy \sim 380$ AU and $dz = dx/2 \sim 190$ AU. The black/white lines represent isocontours of $\tau_{\rm min}$= 1 and 10 in the equatorial plane. $\tau_{\rm min}$ represents a simplified optical depth. It is estimated in each cell by taking the minimum of the optical depth computed from the center of the cell to the boundaries of the computational domain along the mesh axis. Note that this minimal value always corresponds to the optical depth computed in the vertical direction. This is the first important result: radiation preferentially escapes in the vertical direction. Contrary to the previous RHD calculations without rotation, which produces an accreting sphere, a disk is formed in the equatorial plane. This disk is relatively thin and accretes free-falling material which is not very dense ($\rho < 10^{-15}$ g cm^{-3}). Fragments are contained within the optically thick region, where $\tau_{\rm min} > 10$.

Figure 6.4(c) shows the Toomre parameter Q map. It expresses the propensity of a thin disk to fragment into dense clumps (Toomre 1964). This parameter represents the balance between thermal energy, rotational energy and gravitational energy. A massive and cold disk, which

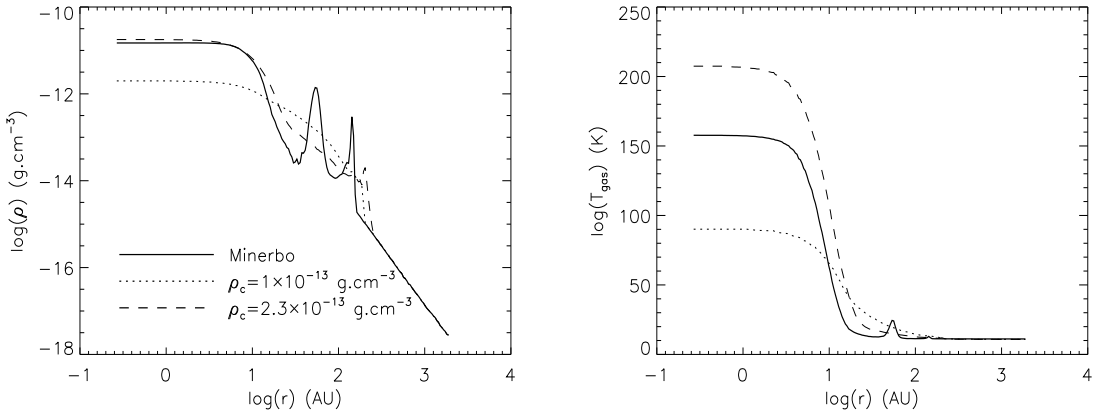

Figure 6.3: Profiles of density and temperature as a function of the radius for calculations run with the FLD approximation (solid line), and a barotropic EOS with $\rho_{\rm ad} = 1 \times 10^{-13}$ g cm^{-3} (dotted line) and $\rho_{\rm ad} = 2.3 \times 10^{-13}$ g cm^{-3} (dashed line). All quantities are averaged in the equatorial plane.

rotates slowly, is then more prone to fragment than a thin and hot disk with a high rotational support. The Toomre parameter is defined as

$$Q = \frac{c_{\rm s}\kappa}{\pi G \Sigma}, \tag{6.3}$$

where $c_{\rm s}$ is the mass-weighted sound speed and κ the mass-weighted epicyclic frequency, evaluated as

$$c_{\rm s}(x,y) = \frac{1}{\Sigma(x,y)} \int \left(\frac{\gamma P(x,y,z)}{\rho(x,y,z)} \right)^{1/2} \rho(x,y,z) dz, \tag{6.4}$$

$$\kappa = \left(4\bar{\Omega}^2 + r \frac{d\bar{\Omega}^2}{dr} \right)^{1/2}, \tag{6.5}$$

and

$$\bar{\Omega}(x,y) = \frac{1}{\Sigma(x,y)} \int \frac{v_\theta(x,y,z)}{r} \rho(x,y,z) dz, \tag{6.6}$$

where $v_\theta = (x v_y - y v_x)/r$ is the azimuthal velocity and $r = (x+y)^{1/2}$ is the distance from the rotational axis. Since our model is axisymmetric, the centre is the centre of the computational box. Note that we use here a simplified estimate of the Toomre parameter, by setting $\kappa = (4\bar{\Omega}^2)^{1/2}$. Therefore, we underestimate the value of Q. A thin disk is unstable when $Q < 1$, because the disk is too cold to be thermally supported against its own gravity. From figure 6.4(c), we clearly see that $Q < 1$ in the fragmentation area. The disk is not hot enough to be thermally supported and it fragments.

Figure 6.4(d) shows the value of $\tau_{\rm min}$ as a function of the density and of the gas temperature for the cells contained in the box used to estimate the Toomre parameter. We can notice that the optical depth only depends on the density, whereas the opacity mostly depends on the temperature. The transition between optically thin and thick regime takes place around $\rho \sim 1 \times 10^{-13}$ g cm^{-3}. The barotropic EOS thus seems to be well-adapted, since it depends only on the density. As mentioned before, and contrary to the barotropic EOS case, there is a spread in the density-temperature distribution with the FLD. One may find warm and diffuse gas or cool and dense gas. Moreover, this spread is even larger when the rotational support is greater.

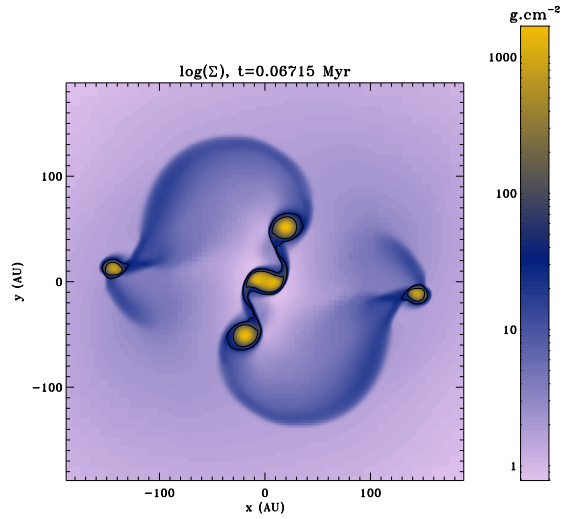

(a) Column density map

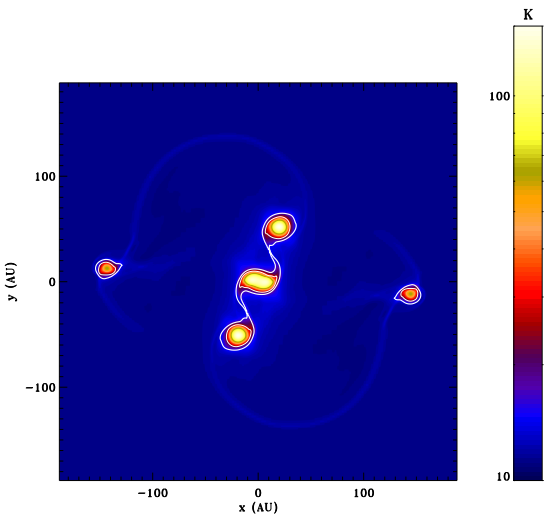

(b) Mass weighted temperature

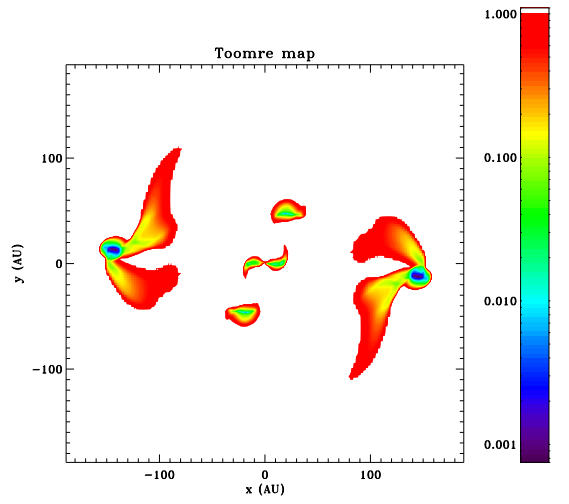

(c) Toomre parameter map

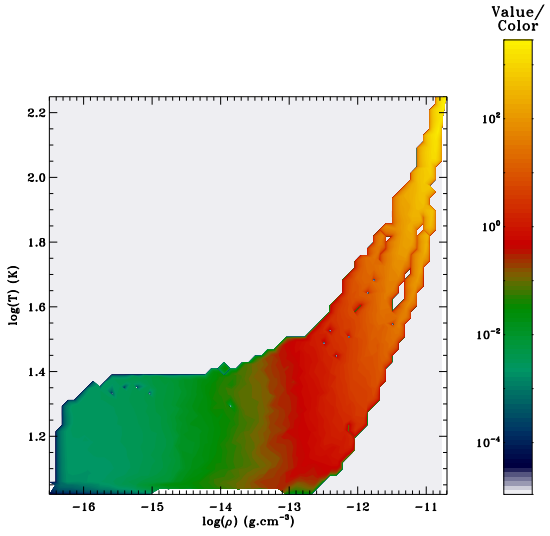

(d) Optical depth as a function of the density and the temperature

Figure 6.4: Results for the case $\alpha = 0.5$, $\beta = 0.04$, $m = 2$ and A= 0.01 at time t= 0.06715 Myr.

Because of the additional centrifugal support due to rotation, the gas has then more time to cool down and thus to reach smaller Jeans masses to fragment. On the other hand, radiation emitted from the dense gas heats up the surrounding region of the fragments.

In figure 6.5(a) and 6.5(b), we show maps of $\tau_{\min}$ in the xy-plane, at the same time as in the previous figures. Figure 6.5(a) displays the minimum value of $\tau_{\min}$ estimated in the x and y directions. Figure 6.5(b) displays the minimum value of $\tau_{\min}$ estimated in the z direction. The optical depth is clearly lower in the vertical plane (*top-right* panel), where radiation can escape more easily. In the spiral arms, the minimum optical depth is close to unity. This illustrates the high complexity of the fragmentation process which takes place between optically thick and thin regions. A barotropic EOS crudely reproduces this transition and cannot handle it accurately.

Figure 6.5(c) shows the local Jeans length computed in the equatorial plane. The black contour represents the isocontour $\tau_{\min} = 10$. The size of the fragments corresponds to the local Jeans length ($\sim$ 10 AU). Contrary to the barotropic case, where the critical Jeans mass is set by the critical density $\rho_{\rm ad}$, the Jeans mass highly depends on the temperature and thus on the microphysics (the opacity) when radiative transfer is accurately modeled.

Figure 6.5(d) shows the ratio between the compression rate $\Gamma_{\rm g} = P\nabla\cdot u$ and the diffusion rate $\Lambda_{\rm diff} = dx^2/(c/3\kappa_{\rm R}\rho)$ computed in the equatorial plane. This ratio expresses the capacity of the gas to cool down thanks to radiation, which evacuates the compression work. In the fragment, $\Gamma_{\rm g} \sim \Lambda_{\rm diff}$, the gas heats up. This corresponds to the results we find in the 1D calculations (see chapter 3), when we look at the evolution of the central compression and diffusion rates. Last, the white regions denote the expanding gas. We see that most of the material is compressed because of gravity.

From these first results, we clearly see the importance of radiative transfer and microphysics, which affect the fragmentation process. Thanks to the radiative transfer, the gas is able to cool down and to reach small Jeans masses, contrary to the barotropic case EOS

6.1.2 Case $\alpha = 0.37$, $\beta = 0.045$ and $m = 2$ and A= 0.01 - Influence of adiabatic exponent γ

For this second case, we choose a highly gravitationally unstable initial dense core. Initial conditions are those of Hennebelle and Fromang (2008) and Hennebelle and Teyssier (2008). The temperature of the sphere is set to 11 K. The initial density is $\rho_0 = 3.97 \times 10^{-18}$ g cm^{-3} and the initial sphere radius is $R_0 = 4.93 \times 10^{16}$ cm ($\sim$ 3300 AU). The corresponding free-fall time is $t_{\rm ff} \sim 33$ kyr. Calculations presented here have been performed using $N_{\rm J} = 10$ and the Lax-Friedrich Riemann solver. We have performed three calculations: one with the barotropic EOS with $\rho_{\rm ad} = 2.3 \times 10^{-13}$ g cm^{-3} and $\gamma = 5/3$, and two with the FLD and a different adiabatic exponent $\gamma = 5/3$ and $\gamma = 7/5$. The value $\gamma = 7/5$ is more appropriate when $T > 100$ K, since the rotational degrees of freedom of H_2 are exited. For instance, barotropic EOS with an adiabatic exponent $\gamma = 7/5$ are often used in star formation calculations (e.g. Bonnell et al. 2008; Machida et al. 2008b). Using $\gamma = 7/5$ gives adiabatic cores, which are cooler than those obtained with $\gamma = 5/3$ at the same density. It is thus easier and faster to reach higher densities and temperatures in the core.

Figure 6.6 shows density and temperature maps in the equatorial plane for the three calculations mentioned above at time $t = 1.15\ t_{\rm ff}$. Temperature ranges from 11.4 K to 20 K. As we pointed out in chapter 5, the horizon of predictability is very short when the initial thermal support is low. As a consequence, calculations do not show a convergence to the same fragmentation pattern. The two calculations using the FLD and two different γ give different fragmentation modes: with $\gamma = 7/5$, we get a central object and two satellites (4 later in time), whereas with $\gamma = 5/3$, we get a ring fragmentation type, with orbiting fragments linked by a bar. We also

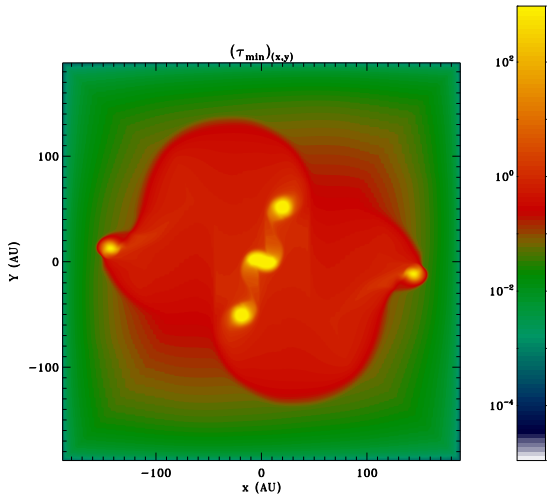

(a) Optical depth $\tau_{\rm min}$ in the xy-plane computed in the x and y directions

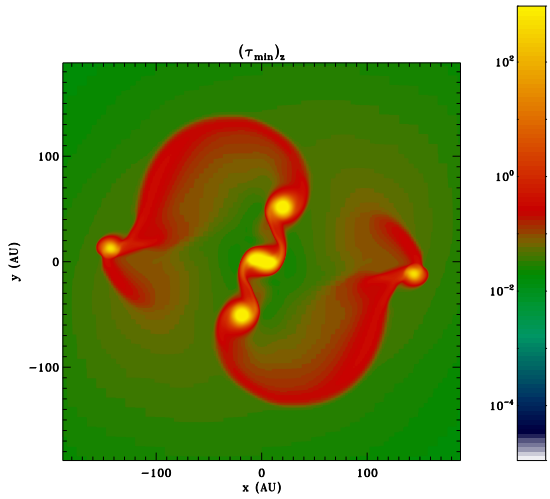

(b) Optical depth $\tau_{\rm min}$ in the xy-plane computed in the z direction

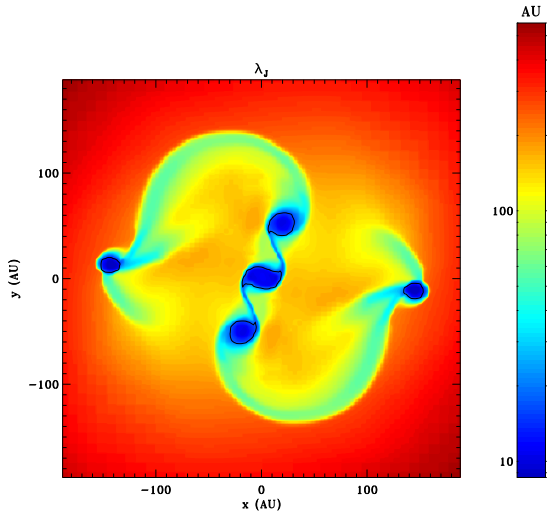

(c) Local Jeans length $\lambda_{\rm J}$ in the xy-plane

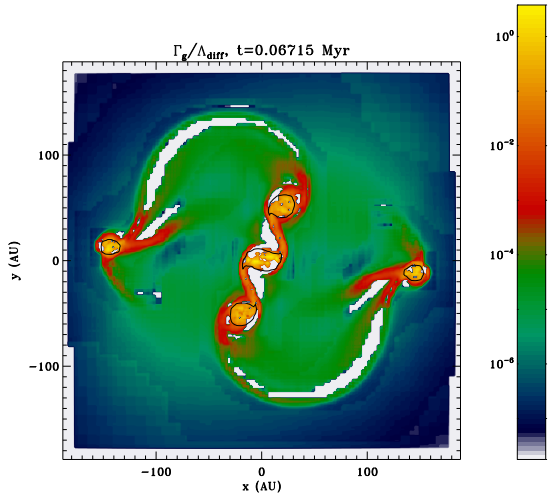

(d) Ratio between compression and diffusion rates.

Figure 6.5: Results for the case $\alpha = 0.5$, $\beta = 0.04$, $m = 2$ and A= 0.01 at time t= 0.06715 Myr.

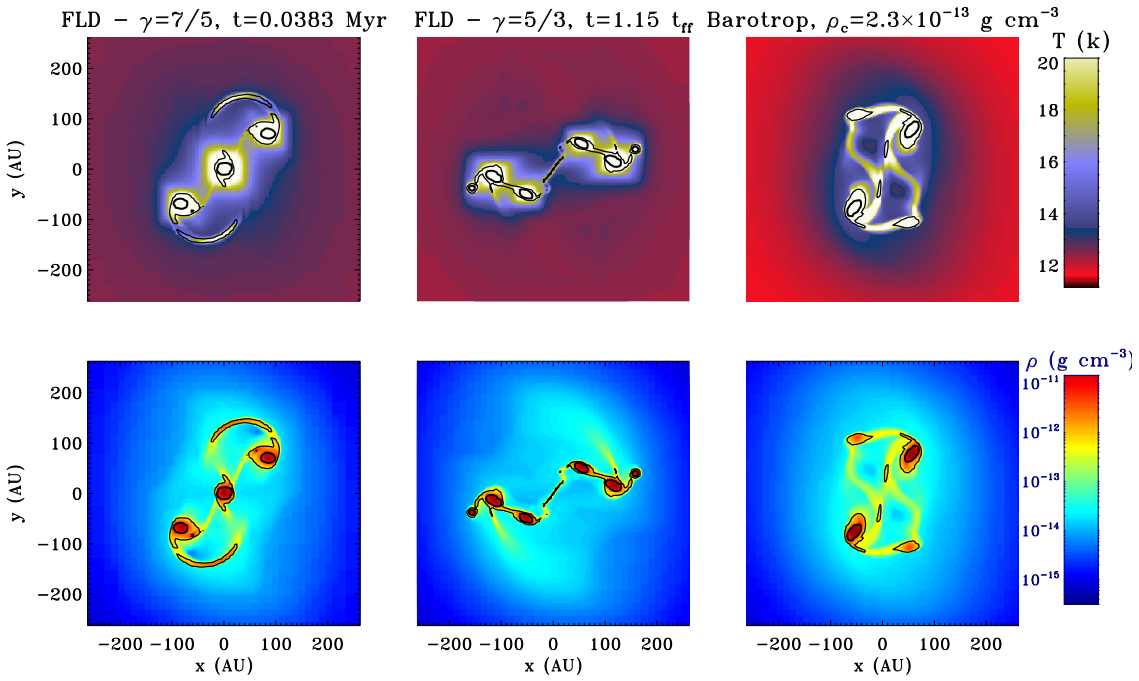

Figure 6.6: Density and temperature maps in the equatorial plane at time t= 38.3 kyr ($1.15t_{\rm ff}$), for three calculations run with the FLD approximation and $\gamma = 7/5$ (*left*), the FLD approximation and $\gamma = 5/3$ (*middle*) and with a barotropic EOS using $\rho_{\rm ad} = 2.3 \times 10^{-13}$ g cm^{-3} and $\gamma = 5/3$ (*right*).

do not get a central object with the barotropic EOS. However, since the first collapse proceeds quickly, we do not find as many differences between the FLD and the barotropic cases as with $\alpha = 0.5$. The gas has less time to cool down and the spread in the density-temperature plane is smaller. From the temperature map of the FLD case with $\gamma = 7/5$, we see that the central region is quite hot. Fragments are more compressed and they radiate more energy. Fragments are also formed faster than the time required for the radiative feedback to become significant (beginning of the second collapse). Eventually, the surrounding gas has been heated up of ~ 1 K in the two FLD calculations, whereas it remains at 11 K in the barotropic case. These differences appear at high radius, > 250 AU, that is out of interest in what concerns fragmentation.

Figure 6.7 shows the density and temperature profiles as a function of the radius for the three calculations at the same time $t = 1.15\ t_{\rm ff}$. Quantities are averaged in the equatorial plane. The density and the temperature in the center are much greater for the FLD case with $\gamma = 7/5$ because of the central fragment. The orbiting fragments have the same distance from the center, ~ 100 AU in the three calculations. The profiles of the barotropic and the FLD calculations using $\gamma = 5/3$ give quite good agreement. The temperature is low at the center and the orbit radius of the fragments are of the same order of magnitude.

In this first section, we have shown that radiative transfer effects are very important for the fragmentation process. The use of a radiative transfer equation allows a significant cooling or heating in different regions of equal densities, whereas with the barotropic EOS, the cooling/heating are set by the density. The microphysics plays here a major role and the use of different Rosseland and Planck opacity tables than the ones of Semenov et al. (2003) may give other results. One must point out that the use of a multi-group method for the radiative transfer

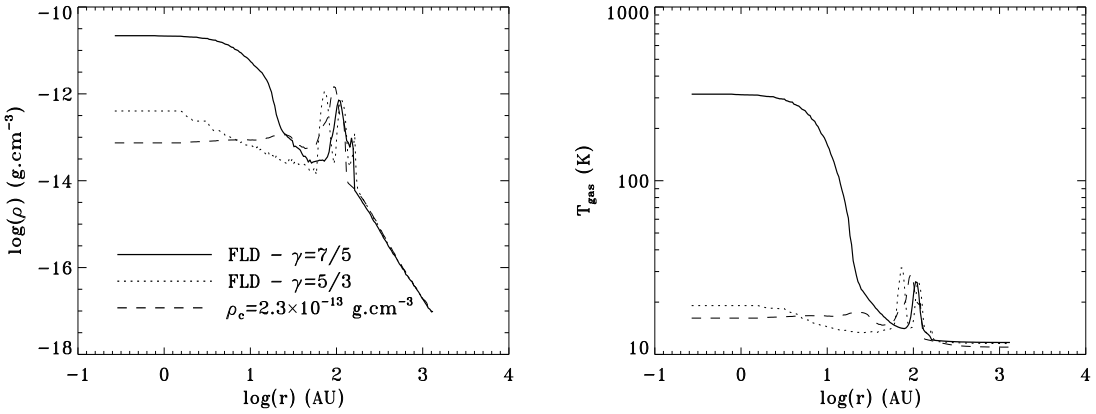

Figure 6.7: Profiles of density and temperature as a function of the radius for calculations performed with the FLD approximation and $\gamma = 7/5$ (solid line), the FLD approximation and $\gamma = 5/3$ (dotted line) and a barotropic EOS with $\rho_{\rm ad} = 2.3 \times 10^{-13}$ g cm^{-3} (dashed line). All quantities are averaged in the equatorial plane.

would also have a great effect (e.g. Yorke and Sonnhalter 2002)

6.2 On the importance of magnetic field

The magnetic field, with rotation and turbulence, is one of the solutions proposed to explain the low observed star formation rate. In this section, we use the ideal MHD solver of RAMSES (Fromang et al. 2006). Because of ideal MHD, magnetic field lines are frozen into the material. During the collapse phase, they are compressed and twisted because of the rotation. Depending on the strength of the magnetic field, the magnetic pressure and tension alter the fragmentation process. As mentioned in the chapter 1, Hennebelle and Teyssier (2008) have shown that fragmentation can be suppressed in presence of magnetic field. This is because angular momentum, which promotes fragmentation, is removed by magnetic effects, such as magnetic breaking and outflows.

6.2.1 Initial setup

In our simple model, the magnetic field is initially uniform and parallel to the rotation axis. The strength of the magnetic field is expressed in terms of the mass-to-flux over critical mass-to-flux ratio

$$\mu = \frac{(M/\Phi)}{(M/\Phi)_{\rm c}}, \tag{6.7}$$

where M is the initial mass of the core, $\Phi = \pi R_0^2 B_0$ is the magnetic flux threading the cloud. $(M/\Phi)_{\rm c}$ is the critical mass-to-flux ratio below which a cloud is supported against gravity by the magnetic field. For a cloud with a uniform density, Mouschovias and Spitzer (1976) derived the critical mass-to-flux ratio

$$\left(\frac{M}{\Phi}\right)_{\rm c} = \frac{\zeta}{3\pi}\left(\frac{5}{G}\right)^{1/2}, \tag{6.8}$$

where $\zeta = 0.53$. For this study, we present here two sets of calculations with a strong magnetic field ($\mu = 5$) and with an intermediate magnetic field strength ($\mu = 20$), the latter being interesting for the fragmentation process. Let us recall that the observations give mostly mass-to-flux ratios $\mu < 10$.

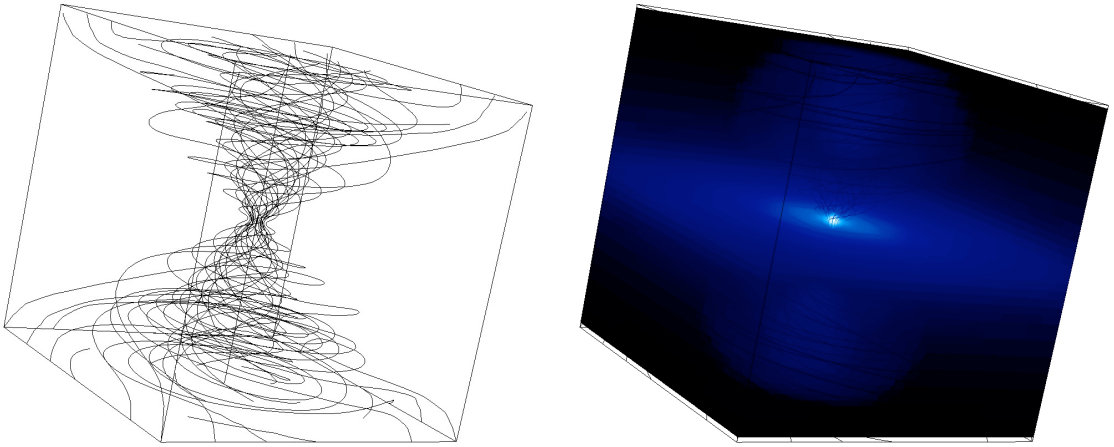

Figure 6.8: Magnetic field lines topology after the formation of the outflow (left plot). Magnetic field lines are twisted and compressed in the equatorial region. The right plot shows a volume rendering of the density which corresponds to the magnetic field line topology.

6.2.2 Outflow launching

The formation and the launch of outflows is a well known process, and is often associated to accretion (Blandford and Payne 1982; Pelletier and Pudritz 1992). Since we consider ideal MHD and only the first collapse phase, we restrict our study to outflows which are made of material moving outward with velocities of a few km s^{-1}. The radiative transfer can here have an influence on the outflow speed. The outflow terminal speed v_∞ can be expressed as (e.g. Pudritz et al. 2007)

$$v_\infty \approx 2^{1/2}\Omega_0 r_\mathrm{A}, \tag{6.9}$$

where Ω_0 is the angular velocity in the mid-plane and r_A is the Alfvén radius, i.e. the radius at which the escape velocity equals the Alfvén speed. The outflow terminal speed depends indirectly on the disk density, since the smaller the launching radius, the faster the outflow (Pelletier and Pudritz 1992). The amount of specific angular momentum which is being extracted from the disk is also a factor of $(r_\mathrm{A}/r_0)^2$ greater than it is for gas in the disk (r_0 is the radius in the equatorial plane). A fast-rotating disk is expected to eject a bigger amount of angular momentum.

6.2.3 Case: $\mu = 5$

To study the effect of radiative transfer on the outflow and the temperature distribution, we have performed four calculations of the collapse of a strongly magnetized dense core, with $\mu = 5$. Calculations have been performed with a barotropic EOS using $\rho_\mathrm{ad} = 1 \times 10^{-13}$ g cm^{-3} and $\rho_\mathrm{ad} = 2.3 \times 10^{-13}$ g cm^{-3}, with the FLD approximation and without Flux limiter ($\lambda = 1/3$). The adiabatic exponent is $\gamma = 5/3$. We use the Lax-Friedrich Riemann solver for hydrodynamics and magnetic field, and $N_\mathrm{J} = 10$. Because of the diffusivity of the Lax-Friedrich Riemann solver for the magnetic field we use, the results should correspond to a lower effective initial mass-to-flux ratio.

In figure 6.8, we display on the left the magnetic field line topology for a collapse simulation done with the FLD which has produced an outflow. The magnetic field lines are twisted because of the rotation, and compressed because of the collapse. The magnetic pressure and tension

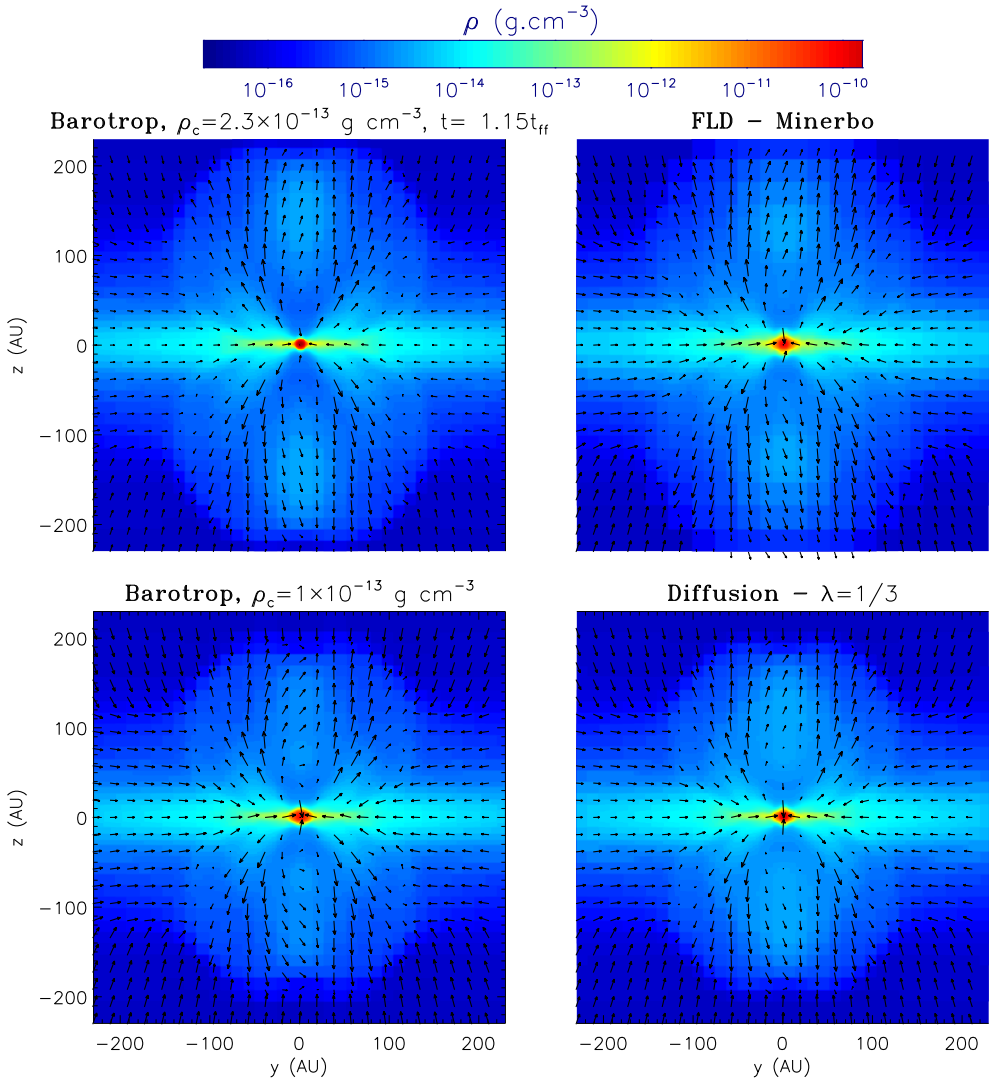

Figure 6.9: Density maps in the yz-plane , for 4 calculations performed with a barotropic EOS using $\rho_{\rm ad} = 2.3 \times 10^{-13}$ g cm^{-3} (top left) and $\rho_{\rm ad} = 1 \times 10^{-13}$ g cm^{-3} (bottom left), with the FLD approximation (top right) and without Flux limiter (bottom right). Results are given at time $t = 1.15 t_{\rm ff}$. Velocity vectors in the yz-plane are also plotted.

increase in the equatorial region. The gas is then accelerated along the field line in the outer part, where the magnetic torque $\mathbf{j} \times \mathbf{B}$ is positive (see Pelletier and Pudritz 1992). The right panel in figure 6.8 shows a volume rendering of the density. We see that the outflow is well collimated in the magnetic tower.

Figure 6.9 shows density maps in the xz-plane for the four calculations, at time $t = 1.15 t_{\rm ff} \sim$ 38 kyr. There are not many differences between the four cases. The central region is more compact in the barotropic case with $\rho_{\rm ad} = 2.3 \times 10^{-13}$ g cm^{-3} than with $\rho_{\rm ad} = 1 \times 10^{-13}$ g cm^{-3}. Therefore, the outflow has propagated a little more. With the FLD, the outflow propagation is about the same and we get the same opening angle of the outflow. The case without flux limiter shows a smaller outflow extent, because of the heating of the gas which prevents the contraction of the core.

In figure 6.10, we show the corresponding temperature maps in the xz-plane. The temper-

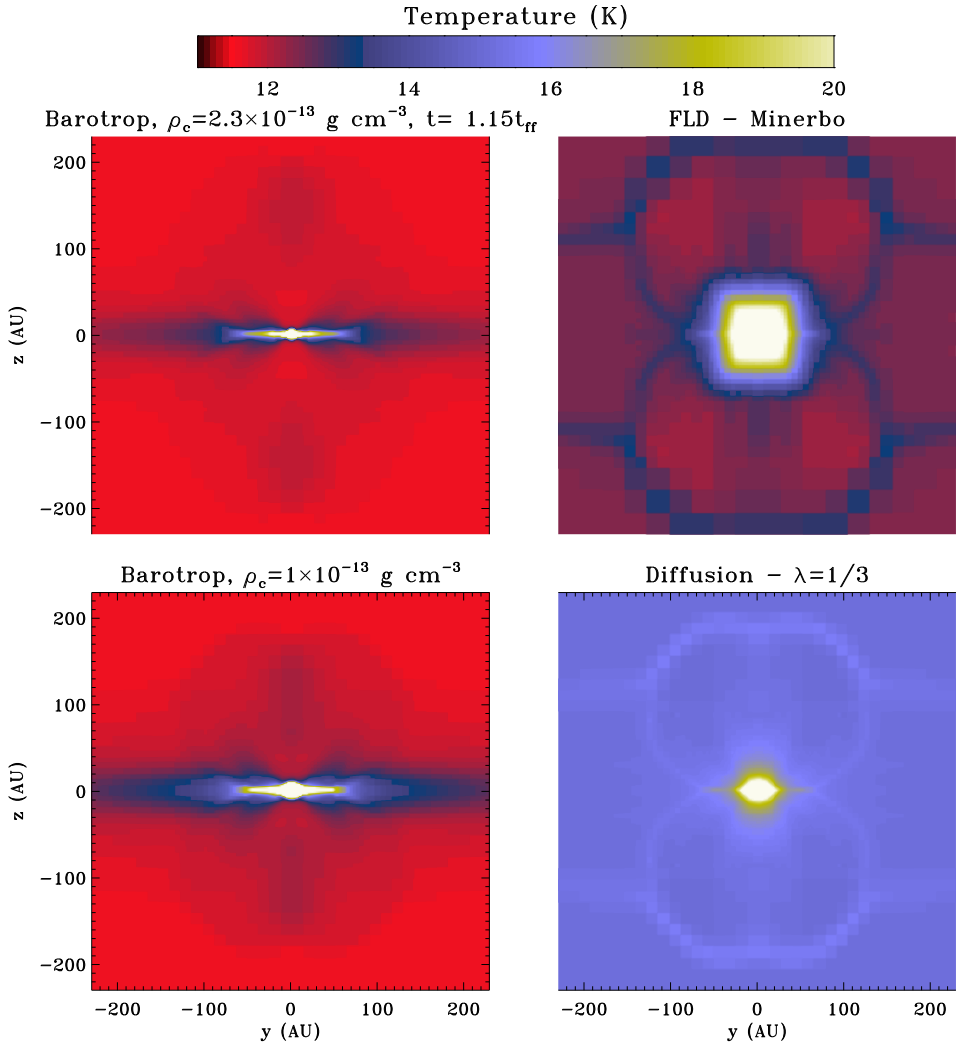

Figure 6.10: Temperature maps in the yz-plane for the same calculations as in figure 6.9.

ature distributions are completely different. As it is shown in Hennebelle and Fromang (2008), a pseudo hot disk is formed in the equatorial plane for the barotropic case. We also do not report any significant heating in the vertical direction. In the FLD case, we clearly see that the gas within the outflow has been heated up, since the radiation escapes preferentially in the vertical direction. The border between the outflow and the infalling gas shows a small spike, since material is shocked and heated up. For a more massive core, this heating of the outflow is expected to be greater, and thus it could affect more strongly its structure. We present in appendix C calculations of the collapse of a 5 $M_\odot$ core. Eventually, without flux limiter, all the gas has been significantly heated up.

Maps of the radial velocity component are shown in figure 6.11, for the same calculations and at the same time as in figure 6.9. The highest velocity, $v_r \sim 1.5$ km s^{-1} is found in the barotropic case with $\rho_{ad} = 2.3 \times 10^{-13}$ g cm^{-3}. In the three other calculations, the outflow velocity is $v_r \sim 1$ km s^{-1}. The radiative transfer with the FLD does not affect the escape velocity. This can be due to the fact that for this highly magnetized model, the magnetic field lines have a strong effect on the dynamic and it is rather the flow which adapts to the magnetic field topology rather than the opposite. The dynamic is dominated by the magnetic field.

In figure 6.12, we display the profiles of the density and temperature in the equatorial plane,

as a function of the radius for the same calculations as in figure 6.9 and at the same time. Contrary to the pure hydrodynamic case of the previous section, the density profiles are in quite good agreement. The central density is the highest in the barotropic case with $\rho_{\rm ad} = 2.3 \times 10^{-13}$ g cm^{-3}, for which we find the highest outflow velocity. For this case, the central temperature is much higher, $\sim$ 1000 K, compared to the three other values $\sim$ 500 K. Within 10 AU, the temperature is the highest for the FLD case, since radiation coming from the center has escaped. Although the barotropic cases form a pseudo hot disk, the differences are significant.

Radial velocity, temperature and toroidal component of the magnetic field profiles in the outflow are plotted in figure 6.13 as a function of the radius. The estimates are averaged in a conic volume contained within an angle with the z-axis ranging from 0 to $\pi/8$. From the radial velocity, we see that there is some infalling gas in the central region, at low radius. The velocity of this infalling gas depends on the central density. This infall is due to the low toroidal magnetic field in this part of the flow (see figure 13 of Hennebelle and Fromang 2008). At higher radius, the gas is ejected with similar velocities $\sim$ 1 km s^{-1}. The radius at which the outflow is stopped by the infalling gas of the envelope is $\sim$ 250 AU.

The thermal structure in the outflow shows some differences. Since the density within the outflow is low, $\rho \sim 5 \times 10^{-15}$ g cm^{-3}, the barotropic EOS gives a low temperature. The temperature falls to 11 K immediately at 10 AU from the center. With the FLD, the radiation which escapes along the z-axis has heated up the gas up to a radius close to 100 AU. This has almost no consequence in our model of a 1 M$_\odot$ core, but we can imagine that for a more massive core with a higher radiative feedback, the heating in the outflow could be more dynamically significant. The toroidal magnetic field component profiles are in good agreement with results of Hennebelle and Fromang (2008). It shows a nearly constant plateau in the outflow.

To conclude this part on the effect of radiative feedback on the outflow, we can say that it has not a strong impact on the outflow launching for low mass dense core. The magnetic field is so strong that it controls by itself the outflow process. In all the cases, even with the FLD, the cores do not fragment. We find some differences in the temperature distribution, $\sim 50\%$ at 50 AU, which could be seen by the observations in the next future. Moreover, the temperature is not uniform and highly depends on the geometry. Eventually, note that even with the very diffusive Riemann solvers that we use, an outflow is produced. At present time, SPH methods fail to reproduce such outflows.

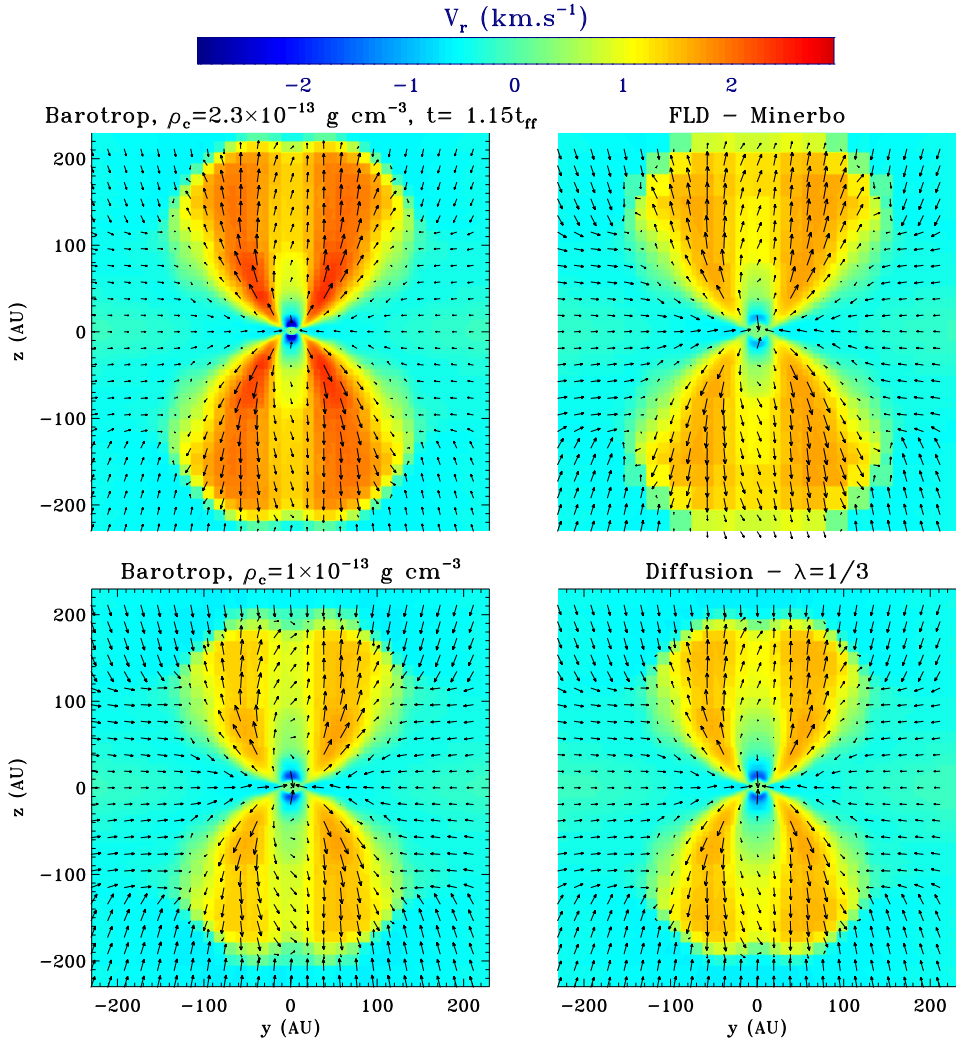

Figure 6.11: Radial velocity maps in the yz-plane for the same calculations as in figure 6.9.

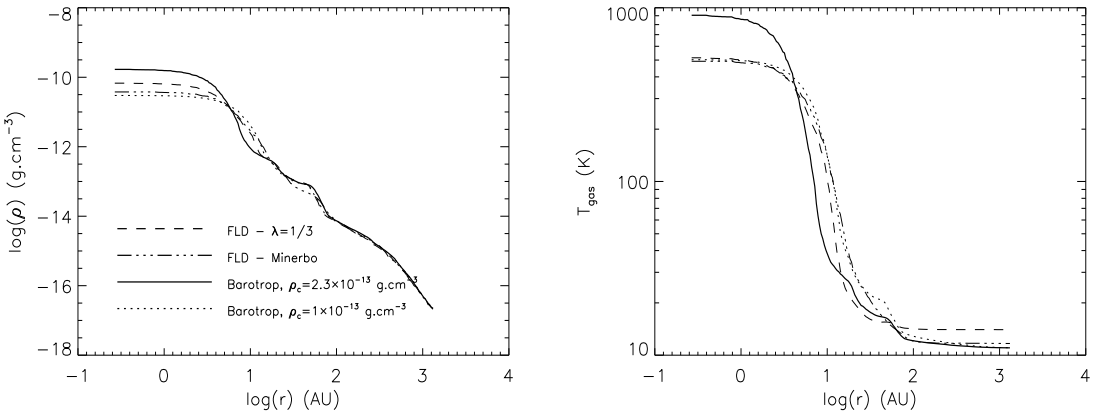

Figure 6.12: Profiles of density and temperature as a function of the radius for the same calculations and at the same time as in figure 6.9. All quantities are averaged in the equatorial plane.

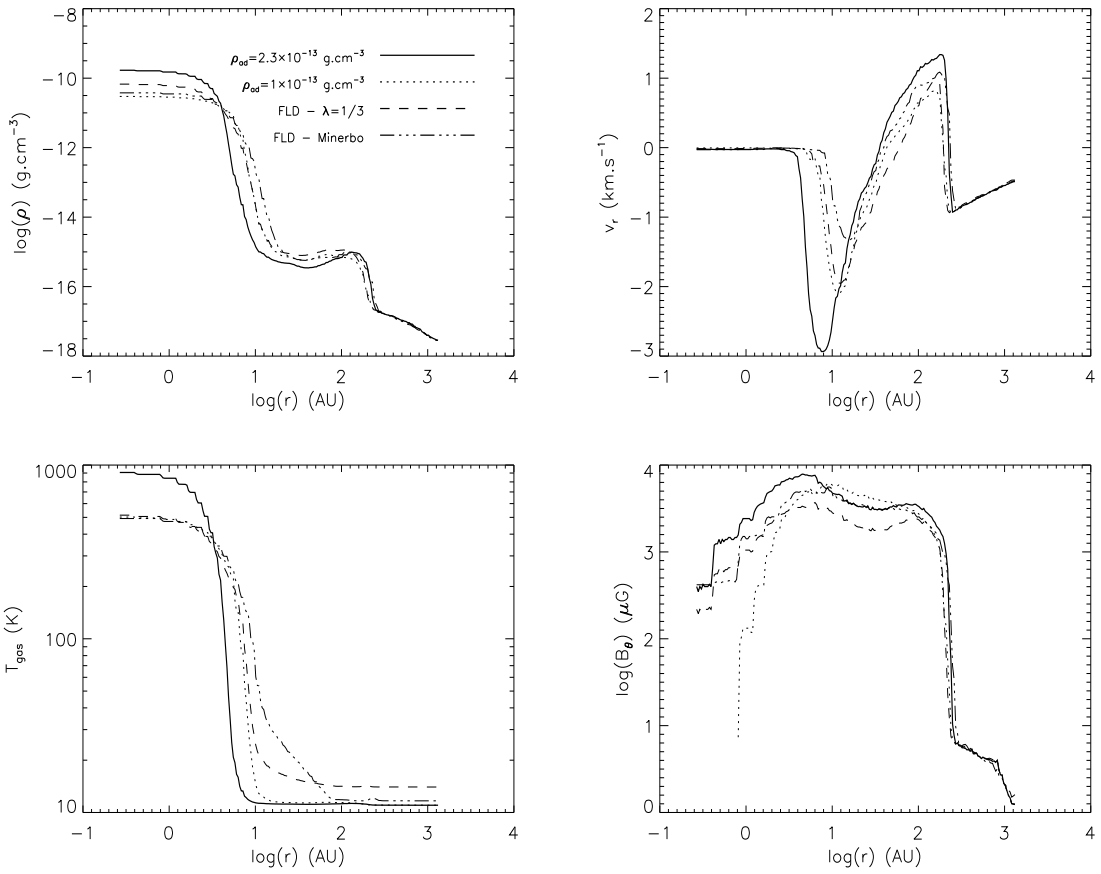

Figure 6.13: Profiles of density, radial velocity, temperature and toroidal magnetic flux component as a function of the radius for calculations for the same calculations and at the same time as in figure 6.9. All quantities are averaged in a conic volume which makes an angle of $\pi/8$ with the z-axis.

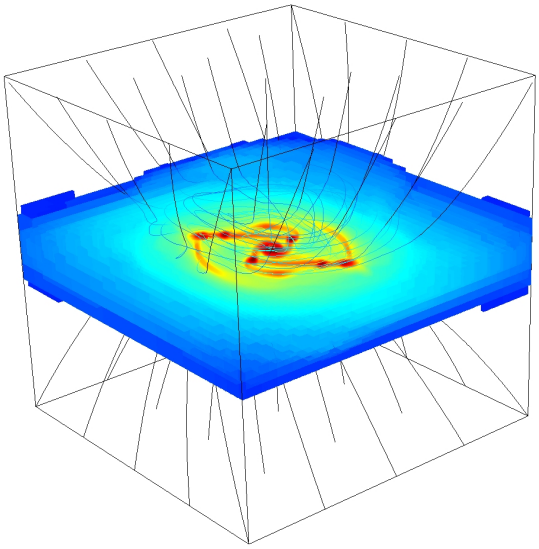

Figure 6.14: Case $\mu = 20$: Volume rendering of the density for calculations done with the FLD model. Magnetic field lines are over-plotted.

6.2.4 Intermediate case: $\mu = 20$

In this test, the strength of the magnetic field is less important. The mass-to-flux ratio is $\mu = 20$. As shown in figure 6.14, a disk is formed and magnetic field lines are less twisted and compressed compared to the case with $\mu = 5$ (see figure 6.8). This time, the magnetic field topology tends to adapt itself to the flow.

We compare FLD calculations performed with the Minerbo flux limiter and barotropic calculations performed with $\rho_{\rm ad} = 2.3 \times 10^{-13}$ g cm^3. The adiabatic index γ has been set to 7/5. Hennebelle and Teyssier (2008) present the same calculations with a barotropic EOS and an adiabatic index $\gamma = 5/3$ and they do not report any fragmentation. Using $\gamma = 7/5$ allows more cooling and then the Jeans mass is smaller compared to the case with $\gamma = 5/3$ with increasing the density in the adiabatic regime. We use the HLL Riemann solver for the hydrodynamics, the Lax-Friedrich Riemann solver for the magnetic field and $N_{\rm J} = 10$. Note that this initial setup does not reflect observational values.

Figure 6.15 shows temperature (*top*) and density (*bottom*) maps in the equatorial plane for the two calculations at the same time $t \sim 38$ kyr. The difference is quite obvious: the FLD case fragments, whereas it does not with the barotropic EOS. At this time, we find 8 orbiting fragments with separations range from ~ 45 AU to ~ 100 AU. The fragments are quite warm and the disk is cold. The disk formed in the barotropic case is hotter and denser. This leads to higher Toomre parameter and Jeans length.

The mean profiles of the density and the temperature as a function of the radius in the equatorial plane are displayed in figure 6.16. Density profiles are in good agreement at high radius (> 100 AU). In the FLD case, the 4 external fragments orbit at a radius ~ 100 AU from the central object and the 4 closer fragments orbit at a radius ~ 45 AU. At small radius (< 10 AU), the density increases in the barotropic case, up to more than 10^{-8} g cm^{-3}. We reach here the limits of our model, since the second collapse phase should start . With an adiabatic exponent $\gamma = 5/3$, the time required to get to this density level is longer. This shows the importance of having a more realistic model for the γ value which ranges from 5/3 at low

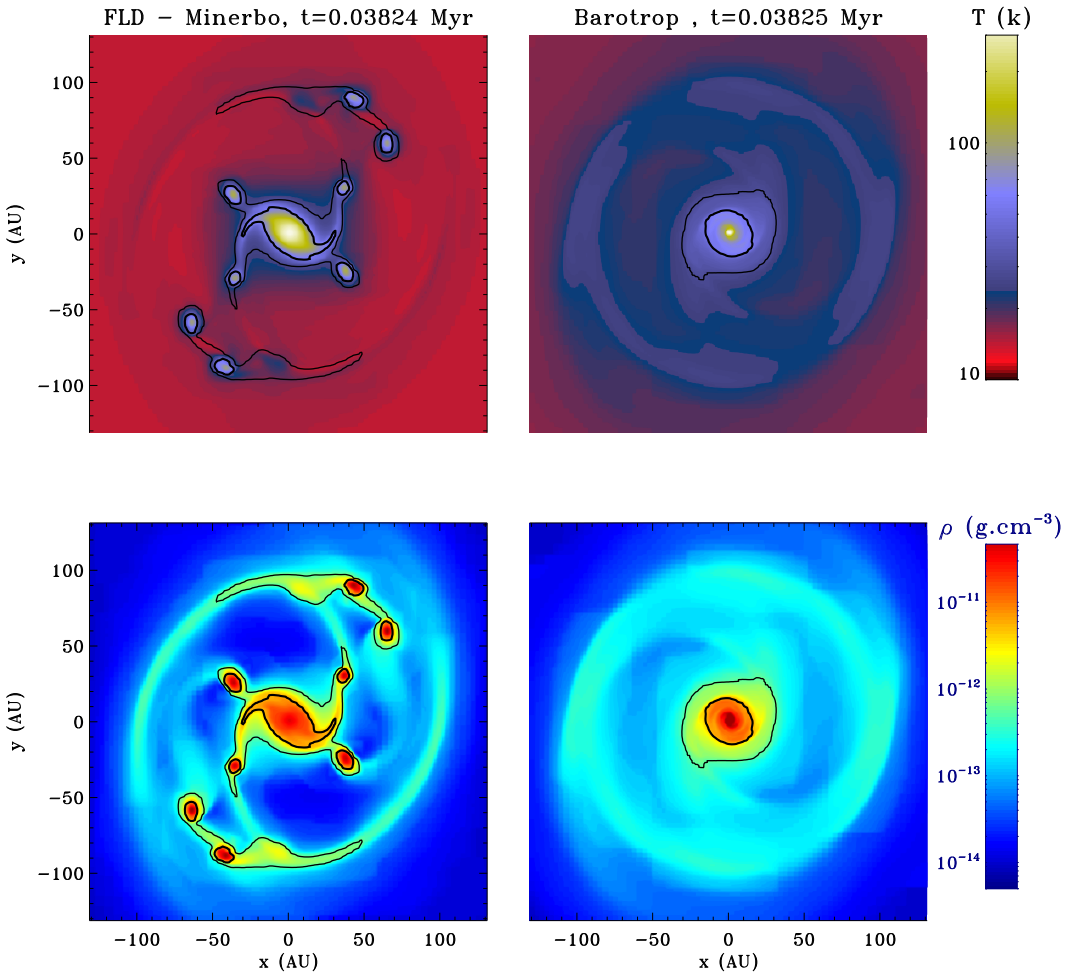

Figure 6.15: Case $\mu = 20$: temperature (*top*) and density *bottom*) maps in the xy-plane for calculations performed with the FLD model (*left*) and a barotropic EOS with $\rho_{\rm ad} = 2.3 \times 10^{-13}$ g cm^{-3} (*right*). Scales are logarithmic.

temperature and then decreases until the second collapse phase (see figure B.1 in appendix B).

Temperature profiles are also completely different. The temperature is higher between 1 AU and 10 AU with the FLD calculations, whereas it is cooler at higher radius. The fragments have temperature which decreases when the distance from the center increases. This confirms our first guess: the external part, because of the rotation and the magnetic supports, has more time to cool down. Fragments can thus reach higher density with a low temperature and a low entropy.

Figure 6.17 shows the temperature and density maps in the yz-plane at the same time and with the same layout as in figure 6.15. The temperature distributions are totally different. In the FLD case, only the central region is hot and radiation has escaped to heat the infalling gas in the vertical direction. This hot region corresponds to density $\sim 10^{-15}$ g cm^{-3}. By definition, the temperature distribution in the barotropic case matches the density: a hot and dense disk has been formed in the equatorial plane, and the gas close to the center has not been heated up in the vertical direction.

These differences are obvious in figure 6.18, which gives the mean density and temperature

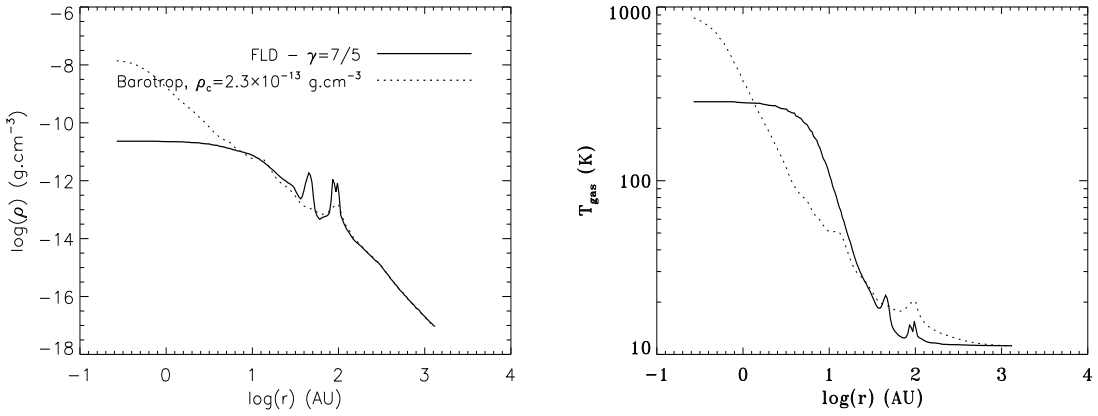

Figure 6.16: Mean profiles of density and temperature in the equatorial plane as a function of the radius for the same calculations and at the same time as in figure 6.15.

profiles in a conic volume which makes an angle of $\pi/8$ with the z-axis. At a radius bigger than 1 AU, the density drops to less than 10^{-14} g cm^{-3} in the barotropic case, whereas the density falls down to this value at a radius $\sim$ 10 AU for the FLD calculations. As a consequence, the temperature is close to the equilibrium temperature of 11 K everywhere in the conic volume in the barotropic case. On the other hand, the radiative feedback from the central object has an influence over a distance of 40 AU. At 10 AU, the gas is three times warmer than in the barotropic case, although the density equals $\sim 10^{-14}$ g cm^{-3}.

In this highly complex case, the barotropic EOS cannot give the correct results. Because of the multidimensionality of the problem, the barotropic approximation cannot account for the cooling of the dense and rotating gas in the equatorial plane and cannot also account for the heating of the less dense gas in the vertical direction, the preferential escaping direction for radiation. Although the initial setup is not realistic in comparison with observations, this case is a good example to illustrate where the barotropic EOS fails. Thanks to the extra magnetic support, the gas has even more time to cool down in comparison to a pure hydrodynamic case. This leads to totally divergent results when we use a more realistic model for the radiative transfer. Last but not least, we must mention that using a less diffusive Riemann solver for the magnetic field (HLLD) does not show any fragmentation in the two cases (Barotropic and FLD). Indeed, with HLLD, the magnetic pressure is higher in the disk and prevents collapse and the gas is spread in a magnetic bubble twice larger in the vertical direction compared to the case using diffusive Lax-Friedrich solver. This illustrates how complex the fragmentation process is and that numerical tools have to be considered with care.

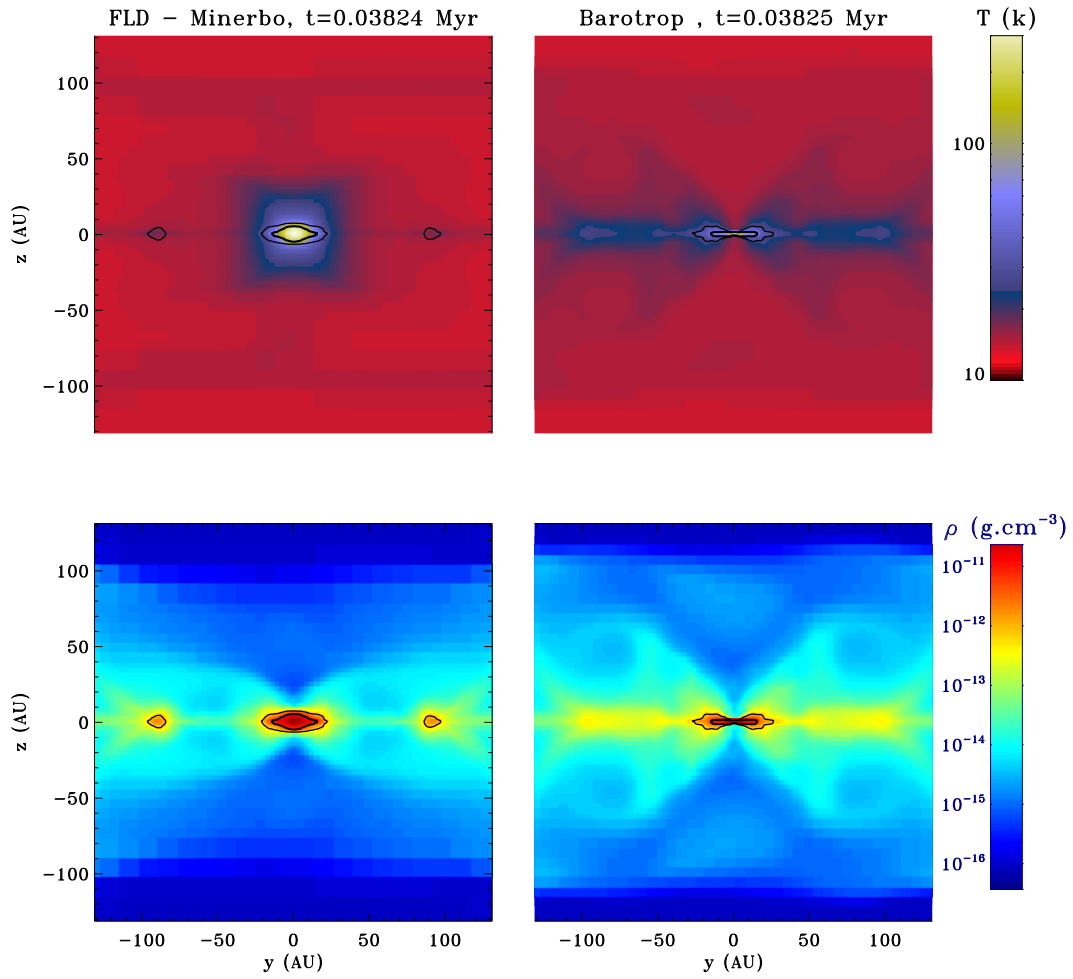

Figure 6.17: Case $\mu = 20$: temperature (*top*) and density *bottom*) maps in the yz-plane for calculations performed with the FLD model (*left*) and a barotropic EOS with $\rho_{\rm ad} = 2.3 \times 10^{-13}$ g cm^{-3} (*right*). Scales are logarithmic.

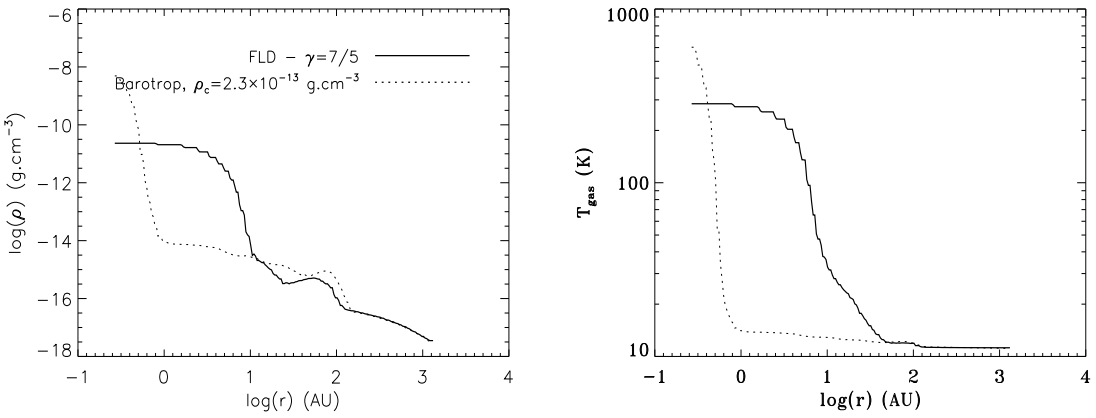

Figure 6.18: Profiles of density (*left*) and temperature (*right*) as a function of the radius for the same calculations and at the same time as in figure 6.15 . All quantities are averaged in a conic volume which makes an angle of $\pi/8$ with the z-axis.

6.3 Influence of the radiative feedback from protostar

In this last part, we attempt to model the radiative feedback from accreting protostars which may form during the collapse. Krumholz et al. (2007a), Bate (2009), Price and Bate (2009) and Offner et al. (2009) have shown that the radiative feedback inhibits fragmentation in high mass star formation and in star cluster formation. Krumholz et al. (2007a) and Offner et al. (2009) use sink particles which accrete according to a Jeans length criterion and to Bondi-Hoyle accretion. Their sink particles are created while the gas is still in free-fall, before the first core formation. Therefore, by creating the sink particles in this supersonic phase, they minimize the impact of the sink particles on the flow. Because of their limited resolution, they are not able to describe scales respectively smaller than 60 AU and 4 AU. Using our less massive model, we accurately resolve these scales. Price and Bate (2009) and Bate (2009) integrate the second collapse physics and create sink particles according to a density threshold just a few days before the formation of the second core. The physics is more accurate than in our case, but the resolution remains limited. In comparison to the criterion we derive in the previous chapter to get convergence between SPH and AMR, i.e. 5×10^5 particles per $M_\odot$, Price and Bate (2009) use 3,5 million particles for a 50 $M_\odot$ core, which gives 7×10^4 particles/$M_\odot$. They also do not report any outflow. Moreover, we do not study the same problem. Price and Bate (2009) and Bate (2009) study the formation of star cluster system, whereas we are interested in the collapse of isolated dense cores.

In our model, the second collapse physics is not integrated, essentially we need an EOS which accounts for H_2 dissociation. We must thus find a subgrid model to deal with this second collapse phase. Sink particles are well adapted for that purpose. Sink particles were originally introduced to save CPU time. The authors generally take benefit of sink particle to add a subgrid model (Krumholz et al. 2004). As shown in part 5.6.4, sink particles should be handled carefully. They can have a huge effect on the results if they are not introduced and modeled correctly. In this section, we present results using two methods for the sink particles. The difficulty resides in the model for the accretion on the sink particles. We use two different models: the first is based on a density threshold and in the other, sink particles are created when the Jeans length is not resolved and they accrete material according to Bondi-Hoyle accretion (see for more details Krumholz et al. 2004, 2007a). In all cases, the sink particles are created on the finest refinement level.

Sink particles have been introduced in RAMSES by Romain Teyssier, following Krumholz et al. (2004). My work has consisted in coupling the sink particles with the RHD solver, by estimating the radiative feedback emerging from the protostars modeled by the sink particles.

In all cases, *all* the matter which is accreted by the sink particles is converted into accretion luminosity emerging from a protostar. The accretion luminosity released by the sink particles is given by

$$L_{\rm sink} = \frac{GM_{\rm sink}\dot{M}}{R_\star}, \tag{6.10}$$

where $M_{\rm sink}$ is the sink particle mass, $\dot{M}$ is the mass accretion rate of the sink particle and $R_\star = 2$ $R_\odot$ is the arbitrary radius of the protostar, which is set constant. This basic model does not account for the formation of a circumstellar disk and for the intrinsic luminosity emerging from the interior of the protostars, which is negligible for low mass protostars. The accretion luminosity is then spread over the sink particle accretion zone, using or not a gaussian weight function $\omega(\mathbf{x}) \propto \exp\left[|\mathbf{r} - \mathbf{r}_{\rm sink}|^2/(2(r_{\rm acc}/n_{\rm acc})^2\right]$, where $r_{\rm acc} = n_{\rm acc}\Delta x_{\rm min}$ is the sink accretion radius, $\Delta x_{\rm min}$ the minimum cell size and $n_{\rm acc}$ the number of finer cells over which accretion takes place. The energy corresponding to the accretion luminosity is then added as a source term in the radiative energy equation.

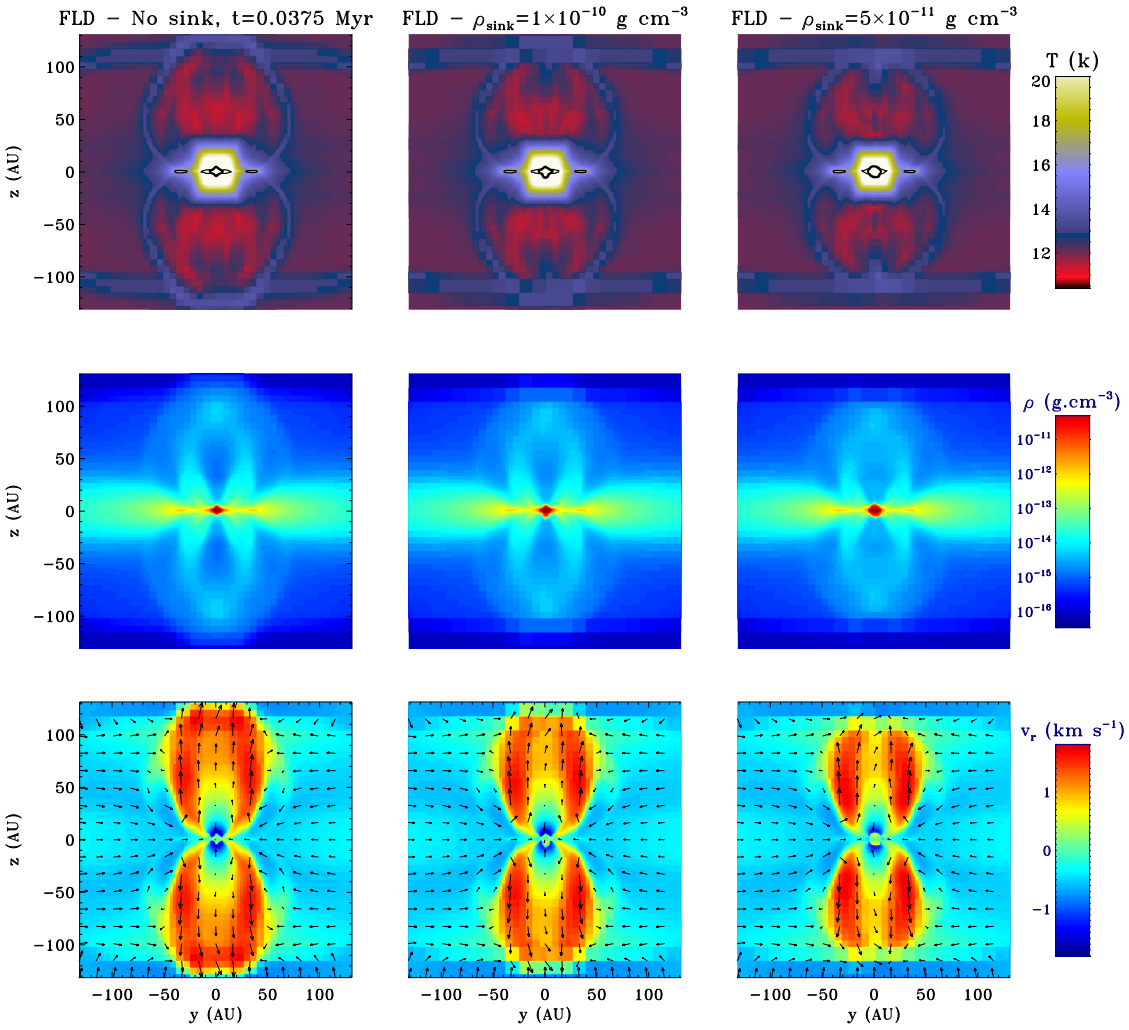

Figure 6.19: Case $\mu = 5$: temperature (*top*), density (*middle*) and radial component of the velocity (*bottom*) maps in the yz-plane for calculations performed with the FLD (*left*), with a sink particle and two density thresholds: $\rho_{\rm sink} = 1 \times 10^{-10}$ g cm^{-3}(*middle*) and $\rho_{\rm sink} = 5 \times 10^{-11}$ g cm^{-3}(*right*). Results are given at time t= $1.12t_{\rm ff}$. We also plot the velocity vectors in the radial velocity maps.

6.3.1 Accretion according to a density threshold

In this case, the sink particles are created according to a density threshold $\rho_{\rm sink}$. This is the most popular model for the sink particles, mostly used by the SPH community. This density threshold has to be chosen carefully in order to induce minimum effects on the dynamics and to avoid spurious accretion. In our calculations, we form only one sink particle in the center. All the matter that will then exceed the density criterion will be accreted by the sink particle. This sets the mass accretion rate used to compute $L_{\rm sink}$. We present here two sets of calculations with initial energy ratios $\alpha = 0.37$ and $\beta = 0.045$ and we use two mass-to-flux ratios: $\mu = 5$ and $\mu = 20$.

Case $\mu = 5$

We present here the results of three calculations using the FLD model, performed with $\ell_{\rm min} = 6$, $N_{\rm J} = 10$. We use 10 levels of refinement and the three finer levels have a nearly constant mass which is set to the minimal Jeans mass. When the density and the temperature and thus the Jeans length increase, the mesh is not de-refined at the center and enables to resolve more accurately the compression work. The contraction of the first core is better resolved than in the case of a refinement criterion only based on the local Jeans length. We use the FLD model, the HLL Riemann solver for the hydrodynamics and the HLLD Riemann solver for the magnetic field. The adiabatic index has been set to $\gamma = 7/5$. In the calculations performed with a sink particle, the latter is created in the center and accretes according to two density thresholds: $\rho_{\rm sink} = 5 \times 10^{-11}$ g cm^{-3} and $\rho_{\rm sink} = 1 \times 10^{-10}$ g cm^{-3}. There is no limitation on the accretion radius and $\Delta x_{\rm min} \sim 0.2$ AU. The use of two different thresholds will tell us what is the impact of the sink particle on the calculations results. We have shown in §6.2.2 that the FLD has a limited impact on the outflow launching. Compared to the barotropic EOS, it only dramatically changes the temperature distribution, but not the density and escape velocity distributions.

Figure 6.19 shows the temperature, density and radial velocity maps in the yz-plane for the three calculations (one without sink particles and two with a sink particle and different $\rho_{\rm sink}$) at time t=37.5 kyr ($\sim 1.12 t_{\rm ff}$). The temperature color map ranges from 10.4 K to 20 K. This shows the first phases of the outflow launching. The sink particle has been created at time $\mathrm{t_{cr}} = 37,244$ yr with $\rho_{\rm sink} = 5 \times 10^{-11}$ g cm^{-3}. Its mass is 6.93×10^{-4} M$_\odot$. The time-averaged accretion rate is about 2.45×10^{-6} M$_\odot$/yr and the maximum accretion radius is ~ 4 AU. This justifies the use of a single sink particle, since the accretion radius is similar to the typical first core radius. The corresponding luminosity is $L_{\rm sink} \sim 0.027$ L$_\odot$. With $\rho_{\rm sink} = 1 \times 10^{-10}$ g cm^{-3}, the sink particle has been created 17 years later. Its mass is 5.44×10^{-4} M$_\odot$. The time-averaged accretion rate is about 2.04×10^{-6} M$_\odot$/yr and the maximum accretion radius is ~ 2.5 AU. The accretion rates are also in good agreement with typical accretion rates in low mass star formation calculations (e.g. Offner et al. 2009). The corresponding luminosity is $L_{\rm sink} \sim 0.017$ L$_\odot$. The accretion rates are different and depend on the density threshold.

In figure 6.19, we see that the outflow extent is smaller in the calculations with the sink particles. This is due to the density thresholds, which set a maximum density which is smaller than in the case without sink particles. As mentioned earlier, the escape velocity grows with the density in the equatorial plane. Hence, the outflow strength is greater when the density is higher. Secondly, the patterns are very similar. The feedback from the sink particle is negligible. For the collapse of a 1 M$_\odot$ dense core, the radiative feedback from the central protostar has no effect on the outflow, contrary to the sink particle which limits the density! For this type of problem, the next step is to model the second collapse, by integrating H_2 dissociation, ambipolar and ohmic diffusions which play an important role (Machida et al. 2008b). Eventually, we note that compared to the case with $\gamma = 5/3$ and the Lax-Friedrich Riemann solver, the opening angle of the outflow is smaller. The temperature distribution is also different. The temperature within the outflow decreases down to ~ 10.4 K and becomes less than the equilibrium temperature of 11 K. The gas expends in the outflow. A barotropic EOS cannot reproduce this feature. We also conclude that the density threshold does not seem to have a dramatic impact, provided it is high enough (typically 10 times the border density of the first Larson core). In appendix C, we study the radiative feedback for the collapse of a strongly magnetized 5 M$_\odot$ dense core.

Case $\mu = 20$

We compare the results obtained in §6.2.4 for the FLD case with those obtained using the sink particle methodology described above. The density threshold for the sink particle creation and

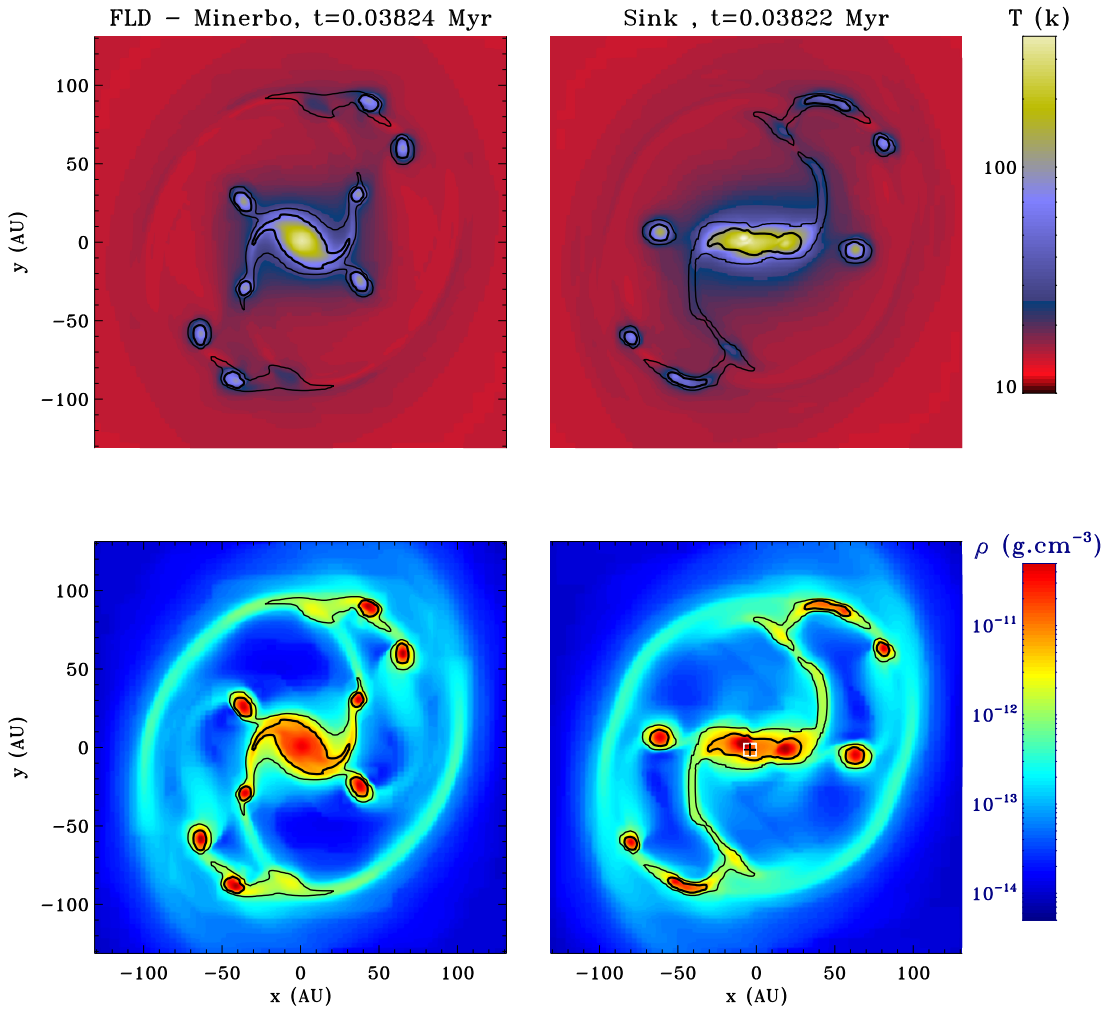

Figure 6.20: Case $\mu = 20$: temperature (*top*) and density (*bottom*) maps in the yz-plane for calculations performed with the FLD, and with a sink particle (*right*). Results are given at the same time as in figure 6.15.

accretion is $\rho_{\rm sink} = 5 \times 10^{-11}$ g cm^{-3}. In the case where a sink particle is created, we use only 8 levels of refinement, contrary to ten in the case without sink particles. This makes the sink creation easier on the finest level and does not alter the fragmentation. The maximum resolution corresponds to 0.8 AU and the refinement is only based on the Jeans length ($N_{\rm J} = 10$), because the criterion presented above on the mass contained within the finer levels cells is too CPU time expensive.

Figure 6.20 shows temperature and density maps in the equatorial plane at time t= 38 kyr. The sink particle has been created at time t= 35.6 kyr, and its mass is $\sim 3.6 \times 10^{-4}$ M$_\odot$. The time-average accretion rate is 1.4×10^{-7} M$_\odot$/yr, which gives an effective mean sink particle luminosity of less than 0.001 L$_\odot$. These values are quite low, but the mass accretion rate remains in the typical range. These low values can be explained by the fact the core has already fragmented and the accretion on the central object is reduced. The overall accretion rate on the first core is higher. Compared to the case without sink particles, we find only seven fragments. The two fragments, closest to the center in the calculations without sink particle,

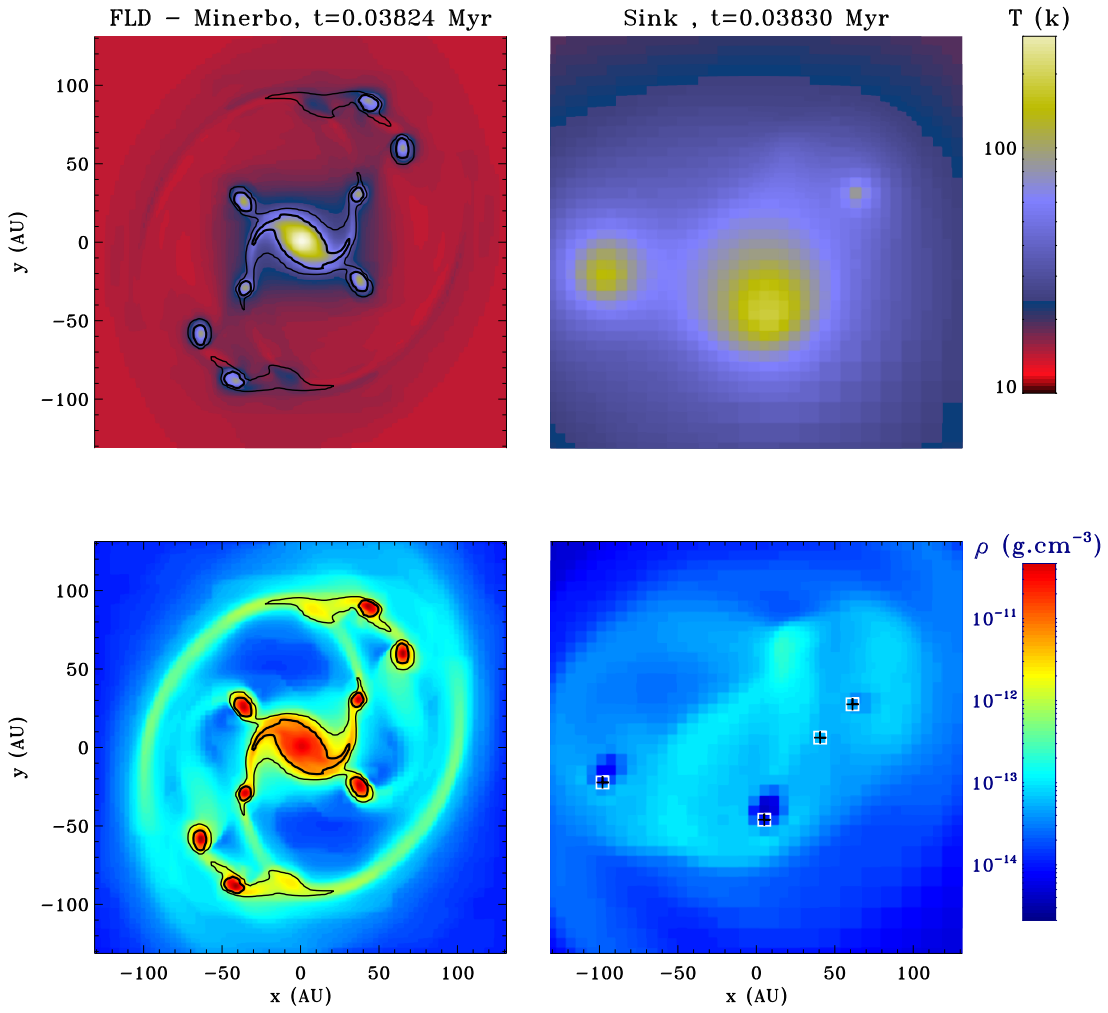

Figure 6.21: Case $\mu = 20$: temperature (*top*) and density (*bottom*) maps in the yz-plane for calculations performed with the FLD, and with sink particles using Krumholz et al. (2004) method (*right*). Results are given at the same time as in figure 6.15.

have disappeared. The sink particle has modified consequently the region within a radius of 40 AU, whereas the maximum accretion radius is ~ 6 AU. As in the case $\mu = 5$, the radiative feedback is negligible and the gas has not been heated up. Here again, the second collapse physics is missing, but the fragments are formed very quickly and in a time shorter than the time required to accumulate 0.05 $M_\odot$ in a fragment, which is the mass required for the second collapse to occur to protostellar densities (Masunaga and Inutsuka 2000b).

6.3.2 Case $\mu = 20$: accretion during the free-fall phase - Bondi-Hoyle accretion

In this last part, we perform calculations using a sink particle methodology similar to the one of Krumholz et al. (2007a) and Offner et al. (2009). We use only 6 levels of refinement, for a highest resolution of 3.2 AU. Sink particles are created when the Jeans length is not resolved any more at level $\ell = 12$ using $N_J = 10$. Using additional levels of refinement would allow to resolve the Jeans length everywhere and the method would not be valid any more. Note that

this criterion is also higher that those used in Krumholz et al. (2007a) and Offner et al. (2009). Once a sink particle is created, it accretes according to Bondi-Hoyle accretion and the accretion is limited to avoid that the sink particles pump out all the gas contained within a cell, following Krumholz et al. (2004). The sink accretion radius is $r_{\rm acc} = 4\Delta x_{\rm min}$.

Figure 6.21 shows temperature and density maps in the equatorial plane at the same time t= 38 kyr. Four sink particles have been created, whose masses are 1.1×10^{-2} $M_\odot$, 5.5×10^{-3} $M_\odot$, 1.33×10^{-3} $M_\odot$ and 2.6×10^{-5} $M_\odot$. The first sink has been created at time t$\sim$ 35.17 kyr ($\sim 1.14 t_{\rm ff}$). The mass accretion rates of the sink particles are very small at this time, since a lot of material has already been accreted by the sink particles. The accretion rate for the more massive sink particle is $\sim 10^{-7}$ $M_\odot$/yr. From the temperature contours, we see that all the gas has been significantly heated up by the accretion luminosity released by the sink particles. The hot spots correspond to the regions where the sink particles accrete. Moreover, the surrounding gas has been accreted by the sink particles. No disk has been formed and the fragmentation is totally suppressed. This illustrates that this method for the sink particle is not adapted to our study, since the small scales and all the related process are not resolved.

6.4 Conclusion and perspectives

This last section summarizes the main results of this chapter. We have performed original high resolution radiation-magnetohydrodynamics calculations of the collapse of a 1 $M_\odot$ dense core. We find that radiative transfer has a significant impact on the fragmentation for models with a small magnetic field. Let us recall our results:

- when the magnetic field is not strong (hydrodynamical and $\mu = 20$ cases), the effects of radiative transfer tend to produce more fragments in comparison with results obtained using a barotropic EOS. The reason is that the magnetic pressure and the dynamic pressure due to rotation provide additional supports against the gravity. The gas in the disk has then more time to cool down and to reach smaller Jeans masses. Because of the disk-type geometry, radiation can escape in the vertical direction. A barotropic EOS cannot deal with this effect;

- in the case of a strong magnetic field, $\mu = 5$, the radiative transfer does not have the same importance. The outflow and the density structure are mainly governed by the magnetic field lines topology. Even if the gas has more time to cool down thanks to the magnetic support, the magnetic pressure and tension totally suppress the fragmentation. Differences between the FLD and the barotropic cases are only found in the temperature distribution. A hot pseudo disk is formed in the barotropic case, whereas this region remains cold with the FLD. The temperature is also cooler in the outflow in the FLD case. The radiation can also escape in the vertical direction. These differences in the temperature distributions can be useful for the processing of observational signals . Last, we do not report any fragmentation for $\mu = 5$;

- we demonstrate that at least in our case, sink particles are not recommended. If sink particles are created and accrete according to a density threshold, the radiative feedback from sink particles is negligible and we recover this artificial feedback in the calculations without sink particles by resolving the gravitational compression scales of the first core. Introducing sink particles during the first free-fall phase is not adapted either. The small scales, at which fragmentation takes place, are not resolved and there is too much radiative feedback. In that case, the sink particles have to be handled with a great care.

We show that our model is well adapted to study the fragmentation during the first adiabatic phase. However, our model is still limited by the lack of physics. The ambipolar and ohmic

diffusions have to be taken into account, as well as H_2 dissociation, in order to monitor the collapse to protostellar densities. This work is under progress...

Chapter 7
Conclusion and Perspectives

This work has been devoted to the study of the low mass star formation process, with a strong numerical component. The original title of this work, given more than three years ago, was: "Numerical study of the collapse and the fragmentation of prestellar dense cores". The second strong component is the radiative transfer that determines the thermal behaviour of the gas during the collapse. All along this work, we show how crucial it is to handle it with care. The philosophy of this work is always to start with simplicity, then to add more detailed physics or numerics and eventually to have a closer look on features of interest. We also focus on the first Larson core formation and evolution, and consider the collapse of a one solar mass dense core with a uniform initial density. In this short conclusion, we give a short summary of this work and highlight its main results.

In chapter 1, we review briefly our current understanding of low mass star formation. We also present a short summary of the state of the art, which has evolved in the past three years... Then, in chapter 2, we consider the basis of radiative transfer and present two moment models, the Flux Limited Diffusion and the M1model, that approximate the radiative transfer equation for dynamical purposes. We insist on the coupling between radiation and hydrodynamics and derive the radiation-hydrodynamics equations in the comoving frame, that we use all along this work.

Chapter 3 presents 1D spherical calculations of protostellar collapse, using a 1D code developed by Edouard Audit and Jean-Pierre Chièze. We develop a FLD module and use the preexisting M1 model. We compare the FLD and the M1 together and with the results obtained using a classical barotropic equation of state. A barotropic equation of state mimics the thermal behaviour of the gas during the star formation process, by setting the temperature as a function of the density. We recover the results of previous studies using 1D tools and demonstrate that the barotropic EOS first fails in setting a proper entropy level for the first core. We show that under the spherical symmetry assumption, the FLD and and the M1 give almost the same results. This validates the FLD for further multidimensional star formation purposes. We study in detail the first core characteristics and find that the accretion shock belongs to the supercritical family of radiative shocks. Last, we develop an original semi-analytical model that describes the first core properties, under the assumption that the accretion shock is supercritical.

The development of a multidimensional numerical tool is presented in chapter 4, where we implement a FLD module in the RAMSES code (Teyssier 2002) and expose the different stages to pass for the implementation. We first present the RAMSES code and its main features. Then we develop a solver that integrates the radiation hydrodynamics equations under the FLD approximation. Then, we test our developments against conventional problems that validate the implementation. In the last section, we perform collapse calculations and recover first core

characteristics without initial rotation. An initial solid body rotation is then added and we study the impact of the flux limiting and of subcycling on the fragmentation. We show that fragmentation is highly sensitive to these *ad-hoc* and numerical aspects.

In Chapter 5, we compare the RAMSES code, with a conceptually different code, the Smoothed Particles Hydrodynamics code DRAGON, designed for star formation calculations. At the beginning of my thesis, there was (and there is still?) a debate on the accuracy of the two methods and each community was wondering about the accuracy of the results of the other community. For instance, Klein et al. (2007) pointed out that a comparison between the two code had to be done in order to clarify the debate. In this study, we carefully study the effect of numerical resolution on the angular momentum conservation and on the fragmentation. We show that the two methods conserve angular momentum and can converge towards a similar fragmentation mode when the problem is not too chaotic, although standard SPH remains more diffusive. We derive numerical resolution parameters necessary to achieve this convergence: we use $N_{\rm J} = 15$, i.e. 15 points per Jeans length, for the AMR code and 5×10^5 particles for a one solar mass dense core in the SPH calculations.

Eventually, in chapter 6, we perform original calculations of prestellar core collapses, using the FLD module we have developed in chapter 4. First, we run calculations with radiative transfer and find that it has a great impact on fragmentation. We also show that a barotropic EOS cannot handle accurately the fragmentation process. In a second part, we add magnetic field using Fromang et al. (2006) ideal MHD module for RAMSES and study the combined effect of radiative transfer and magnetic field on the outflow launching and on the fragmentation. We find that radiative transfer has a limited impact on the outflow dynamic, the magnetic field is too strong. However, radiative transfer changes the temperature distribution compared to the barotropic case, and future observations would perhaps confirm and use this change. For a less magnetized core, we find that radiative transfer calculations can produce fragments where barotropic calculations does not. In a last part, we model the radiative feedback of accreting protostars using two methods for the sink particles and demonstrate that sink particles have to be used with great care. They can have an important impact on the fragmentation and the outflow launching.

Many perspectives for the next or distant future are opened. The next step will be to perform larger scale calculations, starting from a more massive and turbulent core and to study the combined effect of radiative transfer and magnetic field. A second direct application is the massive star formation issue. At present day, no numerical tool is able to tackle massive star formation issue with both radiative transfer and magnetic field. In the distant future and after further developments, we plan to study the second collapse phase with first radiative transfer and then magnetic field with ambipolar diffusion and Ohmic dissipation. What a exciting program for the next years!

Appendix A

The Super-Time Stepping versus the Conjugate Gradient

In this annex, I present the Super-Time-Stepping (STS) method. It is used to solve parabolic equations systems, as the Conjugate Gradient (CG) we use in RAMSES. We implement the STS scheme in RAMSES. In a third part, I compare the CG and the STS methods for the particular case of the 1D linear diffusion test presented in §4.3.1.

A.1 The Super-Time -Stepping

The STS is a very simple and effective way to speed up explicit time-stepping schemes for parabolic problems. The method has been rediscovered recently in Alexiades et al. (1996), but it remains relatively unknown in computational astrophysics (Mignone et al. 2007; O'Sullivan and Downes 2006). The STS frees the explicit scheme from stability restriction on the time-step. It can be very powerful in some cases and is easy to implement compared to implicit methods that involve matrix inversions.

The STS is designed for time dependent problem, such as

$$\frac{dU}{dt}(t) + AU(t) = 0, \tag{A.1}$$

where A is a square, symmetric positive definite matrix. Equation A.1 is rewritten with the corresponding standard explicit scheme

$$U^{n+1} = U^n - \Delta t A U^n, \tag{A.2}$$

The explicit scheme is subject to the restrictive stability condition

$$\rho(\mathbb{I} - \Delta t A) < 1, \tag{A.3}$$

where $\rho(\cdot)$ denotes the spectral radius. The equivalent CFL condition is

$$\Delta t < \Delta t_{\rm expl} = \frac{2}{\lambda_{\max}}, \tag{A.4}$$

where $\lambda_{\max}$ stands for the largest eigenvalue of A. For the case of the 1D heat equation $\partial u/\partial t = \chi \Delta u$, discretized by standard second-order differences on a uniform mesh, we have $\lambda_{\max} = 4\chi\Delta x^2$ ($\Delta t_{\rm expl} = \Delta x^2/2\chi$).

In the STS method, the restrictive stability condition is relaxed by requiring the stability at the end of a cycle of $N_{\rm sts}$ time-steps instead of requiring stability at the end of each time step Δt. It leads to a Runge-Kutta-like method with $N_{\rm sts}$ stages. Following Alexiades et al. (1996),

we introduce a *superstep* $\Delta T = \sum_{j=1}^{N_{\rm sts}} \tau_j$ consisting of $N_{\rm sts}$ *substeps* $\tau_1, \tau_2, \cdots, \tau_{N_{\rm sts}}$. The idea is to ensure stability over the superstep ΔT, while trying to maximize its duration. The inner values, estimated after each τ_j, should only be considered as intermediate calculations. Only the values at the end of the superstep approximate the solution of the problem.

The new algorithm can be written as

$$U^{n+1} = \left(\prod_{j=1}^{N_{\rm sts}} (\mathbb{I} - \tau_j A) \right) U^n, \tag{A.5}$$

and the corresponding stability condition is

$$\rho \left(\prod_{j=1}^{N_{\rm sts}} (\mathbb{I} - \tau_j A) \right) < 1. \tag{A.6}$$

In order to find ΔT as large as possible, the properties of Chebyshev polynomials is exploited, which provides a set of optimal values for the substeps given by

$$\tau_j = \Delta t_{\rm expl} \left[(-1 + \nu_{\rm sts}) \cos \left(\frac{2j-1}{N_{\rm sts}} \frac{\pi}{2} \right) + 1 + \nu_{\rm sts} \right]^{-1}, \tag{A.7}$$

where $\nu_{\rm sts}$ is a damping factor that should verify $0 < \nu_{\rm sts} < \lambda_{\rm min}/\lambda_{\rm max}$. The superstep ΔT is given by

$$\Delta T = \sum_{j=1}^{N_{\rm sts}} \tau_j = \Delta t_{\rm expl} \frac{N_{\rm sts}}{2\nu_{\rm sts}^{1/2}} \left[\frac{(1+\nu_{\rm sts}^{1/2})^{2N_{\rm sts}} - (1-\nu_{\rm sts}^{1/2})^{2N_{\rm sts}}}{(1+\nu_{\rm sts}^{1/2})^{2N} + (1-\nu_{\rm sts}^{1/2})^{2N_{\rm sts}}} \right]. \tag{A.8}$$

Note that $\Delta T \to N_{\rm sts}^2 \Delta t_{\rm expl}$ as $\nu_{\rm sts} \to 0$. The method is unstable in the limit $\nu_{\rm sts} = 0$. The STS method is thus almost $N_{\rm sts}$ times faster than the standard explicit scheme. When ΔT is taken to be the advective (CFL) time step Δt while coupling with the hydrodynamics, the STS requires only approximately $(\Delta t/\Delta t_{\rm expl})^{1/2}$ iterations rather than $\Delta t/\Delta t_{\rm expl}$ with an explicit scheme.

A.2 The STS implementation for the FLD equation

The STS scheme replaces the implicit radiative scheme we present in §4.2.2. Equations of system (4.44) written with an explicit scheme become

$$\left\{ \begin{array}{lcl} \frac{C_v T^{n+1} - C_v T^n}{\Delta t} & = & -\kappa_{\rm P}^n \rho^n {\rm c} (a_{\rm R} (T^n)^4 - E_{\rm r}^n) \\ \frac{E_{\rm r}^{n+1} - E_{\rm r}^n}{\Delta t} & = & \nabla \frac{{\rm c}\lambda^n}{\kappa_{\rm R}^n \rho^n} \nabla E_{\rm r}^n + \kappa_{\rm P}^n \rho^n {\rm c} (a_{\rm R} (T^n)^4 - E_{\rm r}^n) \end{array} \right. . \tag{A.9}$$

The explicit time step $\Delta t_{\rm expl}$ is estimated using values at time n. The next step consist of estimating values of $N_{\rm sts}$ and $\nu_{\rm sts}$, the latter depending on the spectral properties of A. However, as it is mentioned in Alexiades et al. (1996), it is not required to have a precise knowledge of the spectral properties for the method to be robust. $N_{\rm sts}$ and $\nu_{\rm sts}$ are thus arbitrary chosen by the user. Instead of executing one time step of length $\Delta t_{\rm expl}$, one executes supersteps of length ΔT. $N_{\rm sts}$ substeps $\tau_1, \tau_2, \cdots, \tau_{N{\rm sts}}$ are thus performed without outputting until the end of each superstep. When the STS is coupled to the hydrodynamics solver, the cycle is repeated until the time step, given by the hydrodynamical CFL condition, is reached. Superstep ΔT and substeps τ_i are re-estimated at the end of each cycle.

A.3 Comparison with the Conjugate Gradient method

To compare the STS with the Conjugate Gradient algorithm we have used in all this work, we consider the test case presented in part 4.3.1. The equation to integrate is simply

$$\frac{\partial E_{\rm r}}{\partial t} - \nabla \cdot \left(\frac{c}{3\rho\kappa_{\rm R}} \nabla E_{\rm r} \right) = 0. \tag{A.10}$$

The initial setup is identical to those in §4.3.1. It consists of an initial pulse of radiative energy in the middle of the box. We present here calculations made with either the STS method or the CG algorithm. In both cases, CG and STS are applied over an arbitrary time step Δt that the simulates time step that would be given by the hydro CFL. All calculations have been performed on a grid made of 1024 cells. In the STS calculations, for each value of Δt, calculations have been performed using various values of $N_{\rm sts}$ and $\nu_{\rm sts}$. For the CG method, only the convergence criterion $\varepsilon_{\rm conv}$ changes, and the subcycling presented in §4.3.1 is not activated.

Figure A.1 shows the radiative energy profiles at time $t = 1 \times 10^{-13}$ s for all the calculations we have performed. In all panels, the analytic solution is plotted (black line). The two upper plots give results for the CG method. For $\Delta t \geq 10^{-14}$, the accuracy is very limited. We also see that for $\Delta t \geq 10^{-13}$, the diffusion wave does not propagate at the right speed. The total energy is conserved, but the diffusion wave has not the correct extent. This illustrates the problems we encounter in §4.4.4. On the other hand, the STS results are much more accurate, except in the case with $N_{\rm sts} = 20$ and $\nu_{\rm sts} = 1 \times 10^{-6}$. By construction, STS is expected to be more accurate. The stability is not good when $N_{\rm sts} = 20$ and $\nu_{\rm sts} = 1 \times 10^{-6}$ since $\nu_{\rm sts}$ is close to the stability limit (see Alexiades et al. 1996).

In table A.1, we give the CPU time and $N_{\rm iter}$, which corresponds to the number of iterations for the CG and to the number of substeps for the STS. The number of operations per iteration in the CG or per substep in the STS is the same, since it involves the same number of cells (1024). The CPU time spent with the STS is ten times smaller than the one of the CG method. The STS also requires often twice less iterations than the CG. The bottom lines give results for calculations made with a variable time step, which increases with time. The corresponding profiles are plotted in figure A.2. The STS remains in this case more accurate than the CG, which is quite accurate over more than three orders of magnitude. The CG gives good results, because, thanks to the variable time steps, the diffusion wave propagates at a correct speed. Indeed, at $t = 0$, the gradient of radiative energy is steep and the diffusion wave speed is very high. Using an initial short time step $\Delta t = 10^{-16}$ enables to be closer to the CFL condition associated to the diffusion wave speed. Then, radiative energy gradients and the former CFL condition relax and the time step can increase with time. This relaxation on the integration time step enables to maximize the accuracy of implicit methods using a subcycling scheme based on the diffusion wave speed propagation. However, this speed remains quite hard to estimate.

Eventually, we must conclude by pointing out that even if the STS method is well adapted for this problem, it remains very limited for star formation calculations. Indeed, the diffusion time is very short compared to the dynamical time estimated as the free-fall time (see figure A.3) and then, the STS requires a too large number of substeps. The convergence of the CG depends on the nature of the problem and is not affected by strong differences between the diffusion and the dynamical times. Moreover, we never encounter such steep gradients in the radiative energy distribution in star formation calculations. The STS could be efficient only within the fragments, where the diffusion time is very long. This is the reason why we use only the CG method in all this work. An alternative but non-trivial solution would be to couple the CG and the STS methods.

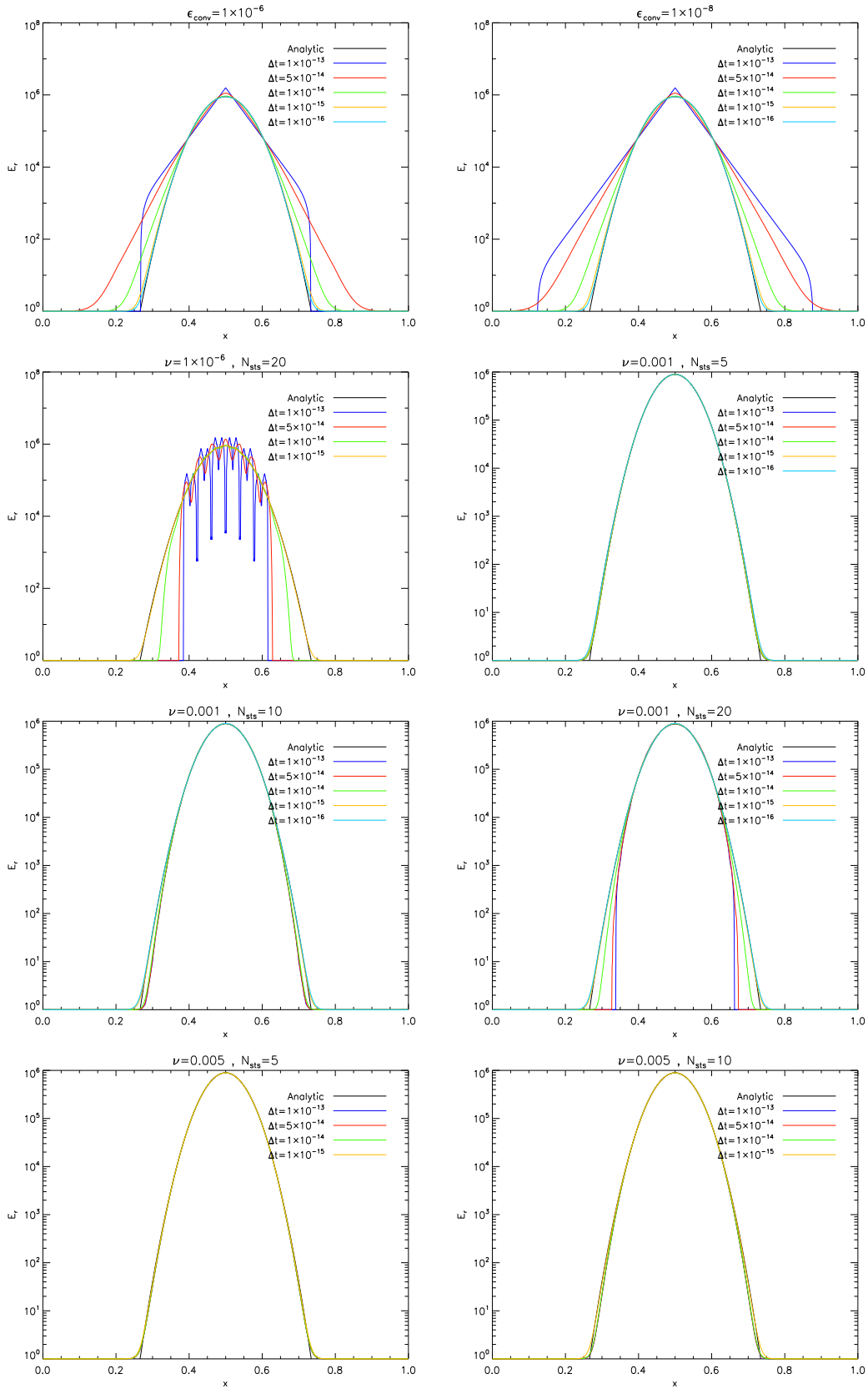

Figure A.1: Comparison of the numerical solutions using STS or CG with the analytic one (black line) at time $t = 1 \times 10^{-13}$ s.

Method	Parameters	Δt	CPU time (s)	N_{iter}
CG	$\varepsilon_{\text{conv}} = 1 \times 10^{-6}$	1×10^{-16}	82.9	10805
CG	$\varepsilon_{\text{conv}} = 1 \times 10^{-8}$	1×10^{-16}	68.5	14623
STS	$\nu_{\text{sts}} = 0.001$, $\text{N}_{\text{sts}} = 10$	1×10^{-16}	20.4	9000
CG	$\varepsilon_{\text{conv}} = 1 \times 10^{-6}$	1×10^{-15}	21.2	4738
CG	$\varepsilon_{\text{conv}} = 1 \times 10^{-8}$	1×10^{-15}	27.8	6456
STS	$\nu_{\text{sts}} = 1 \times 10^{-6}$, $\text{N}_{\text{sts}} = 20$	1×10^{-15}	2.8	2107
STS	$\nu_{\text{sts}} = 0.001$, $\text{N}_{\text{sts}} = 5$	1×10^{-15}	2.9	2408
STS	$\nu_{\text{sts}} = 0.001$, $\text{N}_{\text{sts}} = 20$	1×10^{-15}	2.9	2408
STS	$\nu_{\text{sts}} = 0.001$, $\text{N}_{\text{sts}} = 10$	1×10^{-15}	2.9	2408
STS	$\nu_{\text{sts}} = 0.005$, $\text{N}_{\text{sts}} = 5$	1×10^{-15}	3.1	2709
STS	$\nu_{\text{sts}} = 0.005$, $\text{N}_{\text{sts}} = 10$	1×10^{-15}	3.04	2709
CG	$\varepsilon_{\text{conv}} = 1 \times 10^{-6}$	1×10^{-14}	11.4	2848
CG	$\varepsilon_{\text{conv}} = 1 \times 10^{-8}$	1×10^{-14}	15.4	3892
STS	$\nu_{\text{sts}} = 1 \times 10^{-6}$, $\text{N}_{\text{sts}} = 20$	1×10^{-14}	0.6	600
STS	$\nu_{\text{sts}} = 0.001$, $\text{N}_{\text{sts}} = 5$	1×10^{-14}	0.99	1470
STS	$\nu_{\text{sts}} = 0.001$, $\text{N}_{\text{sts}} = 20$	1×10^{-14}	0.75	900
STS	$\nu_{\text{sts}} = 0.001$, $\text{N}_{\text{sts}} = 10$	1×10^{-14}	0.69	780
STS	$\nu_{\text{sts}} = 0.005$, $\text{N}_{\text{sts}} = 5$	1×10^{-14}	1.1	1620
STS	$\nu_{\text{sts}} = 0.005$, $\text{N}_{\text{sts}} = 10$	1×10^{-14}	0.87	1170
CG	$\varepsilon_{\text{conv}} = 1 \times 10^{-6}$	5×10^{-14}	6.9	1755
CG	$\varepsilon_{\text{conv}} = 1 \times 10^{-8}$	5×10^{-14}	9.3	2365
STS	$\nu_{\text{sts}} = 1 \times 10^{-6}$, $\text{N}_{\text{sts}} = 20$	5×10^{-14}	0.39	390
STS	$\nu_{\text{sts}} = 0.001$, $\text{N}_{\text{sts}} = 5$	5×10^{-14}	0.8	1326
STS	$\nu_{\text{sts}} = 0.001$, $\text{N}_{\text{sts}} = 20$	5×10^{-14}	0.56	756
STS	$\nu_{\text{sts}} = 0.001$, $\text{N}_{\text{sts}} = 10$	5×10^{-14}	0.46	534
STS	$\nu_{\text{sts}} = 0.005$, $\text{N}_{\text{sts}} = 5$	5×10^{-14}	0.87	1476
STS	$\nu_{\text{sts}} = 0.005$, $\text{N}_{\text{sts}} = 10$	5×10^{-14}	0.68	1032
CG	$\varepsilon_{\text{conv}} = 1 \times 10^{-6}$	1×10^{-13}	4.6	1135
CG	$\varepsilon_{\text{conv}} = 1 \times 10^{-8}$	1×10^{-13}	5.6	1399
STS	$\nu_{\text{sts}} = 1 \times 10^{-6}$, $\text{N}_{\text{sts}} = 20$	1×10^{-13}	0.36	351
STS	$\nu_{\text{sts}} = 0.001$, $\text{N}_{\text{sts}} = 5$	1×10^{-13}	0.77	1311
STS	$\nu_{\text{sts}} = 0.001$, $\text{N}_{\text{sts}} = 20$	1×10^{-13}	0.52	729
STS	$\nu_{\text{sts}} = 0.001$, $\text{N}_{\text{sts}} = 10$	1×10^{-13}	0.43	495
STS	$\nu_{\text{sts}} = 0.005$, $\text{N}_{\text{sts}} = 5$	1×10^{-13}	0.83	1467
STS	$\nu_{\text{sts}} = 0.005$, $\text{N}_{\text{sts}} = 10$	1×10^{-13}	0.65	1020
CG	$\varepsilon_{\text{conv}} = 1 \times 10^{-8}$	$1 \times 10^{-16} * 1.05^{\text{istep}}$	19	4680
STS	$\nu_{\text{sts}} = 0.005$, $\text{N}_{\text{sts}} = 10$	$1 \times 10^{-16} * 1.05^{\text{istep}}$	1.7	1782

Table A.1: Summary of calculations plotted in figure A.1. CPU time, the number of iterations in the CG method or the number of substeps in the STS method are given, for various time steps and various values of $\varepsilon_{\text{conv}}$ for the CG, and N_{sts} and ν_{sts} for STS.

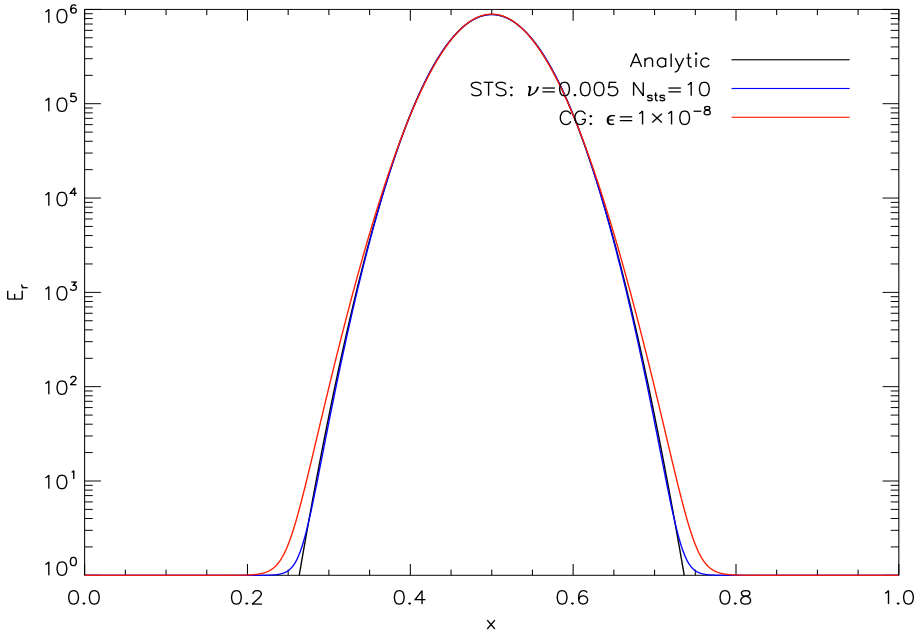

Figure A.2: Comparison of calculations done using STS or CG and a variable time step given by $\Delta t = 1 \times 10^{-16} * 1.05^{\text{istep}}$, where istep is the index of the number of global (hydro) time steps. Results are given at time $t = 1 \times 10^{-13}$s.

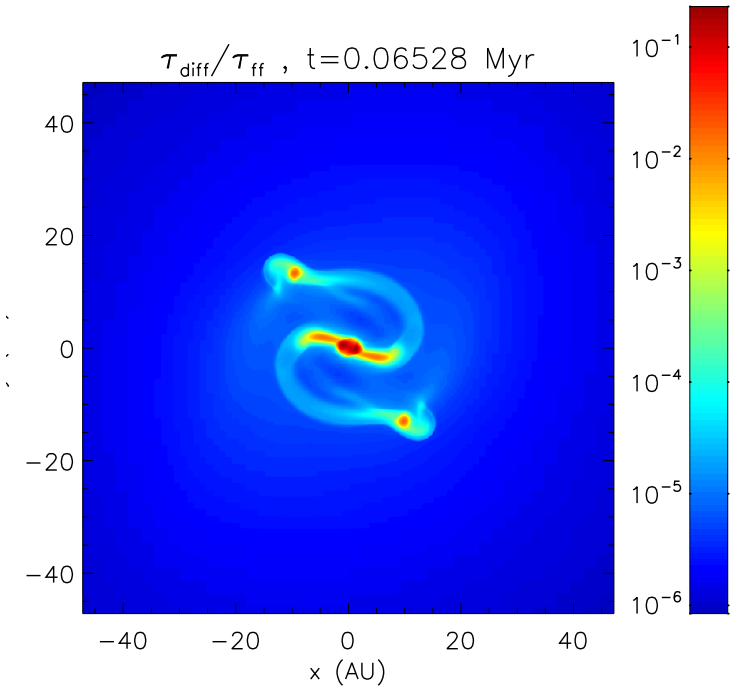

Figure A.3: Contours in the equatorial plane of the ratio between diffusion and free fall times for collapse calculations presented in §4.4.3. The diffusion time is estimated as $\tau_{\text{diff}} = \frac{l^2}{\frac{c}{3\kappa_{\text{R}}\rho}}$, where l is the local Jeans length.

Appendix B
On the specific heat ratio

The specific heats ratio or adiabatic exponent γ is given by the specific heat C_{V}

$$C_{\mathrm{V}} = \frac{1}{\gamma - 1}\frac{k}{\mu m_{\mathrm{H}}}. \tag{B.1}$$

The specific heat at constant volume is described as

$$C_{\mathrm{V}} = \frac{k}{\mu m_{\mathrm{H}}} T \frac{\partial^2}{\partial T^2}(T \ln \mathcal{Z}), \tag{B.2}$$

where $\mathcal{Z}$ is the partition function. The specific heat is divided into three parts: a translational, a vibrational and a rotational part

$$C_{\mathrm{V}} = C_{\mathrm{V,tra}} + C_{\mathrm{V,vib}} + C_{\mathrm{V,rot}}. \tag{B.3}$$

For monoatomic molecules, the specific heat is simply

$$C_{\mathrm{V}} = C_{\mathrm{V,tra}} = \frac{3}{2}\frac{k}{\mu m_{\mathrm{H}}}. \tag{B.4}$$

Thus, the adiabatic exponent is $\gamma = 5/3$. For the H_2 molecule, the vibrational and rotational parts must be taken into account. The translational part is simply given by

$$C_{\mathrm{V,tra}} = \frac{3}{2}\frac{k}{\mu m_{\mathrm{H}}}. \tag{B.5}$$

In the harmonic oscillator approximation, the partition function for the molecular vibration is

$$\mathcal{Z} = \sum_{n=0}^{\infty} \exp\left[-\frac{h\nu}{kT}\left(n + \frac{1}{2}\right)\right]. \tag{B.6}$$

The specific heat for the vibrational part is then given by the analytic solution

$$C_{\mathrm{V,vib}}^{\mathrm{H_2}} = \frac{k}{\mu m_{\mathrm{H}}}\left(\frac{\theta_{\mathrm{vib}}}{T}\right)^2 \frac{\exp\left(\frac{\theta_{\mathrm{vib}}}{\mathrm{T}}\right)}{\left(\exp\left(\frac{\theta_{\mathrm{vib}}}{\mathrm{T}}\right) - 1\right)^2}, \tag{B.7}$$

where $\theta_{\mathrm{vib}} = h\nu/k = 6100$ K.
The rotational part depends on the symmetry of H_2 (*ortho* or *para*). The partition functions for the rotational energy levels are

$$\mathcal{Z}_{\mathrm{o}} = \sum_{j=1,3,5,\ldots}^{\infty} (2j+1)\exp\left[-j(j+1)\frac{\theta_{\mathrm{rot}}}{T}\right], \tag{B.8}$$

for orhto-H_2, and

$$\mathcal{Z}_{\rm o} = \sum_{j=2,4,6,...}^{\infty} (2j+1)\exp\left[j(j+1)\frac{\theta_{\rm rot}}{T}\right], \tag{B.9}$$

for para-H_2. Note that $\theta_{\rm rot} = h^2/8\pi^2 Ik = 85.4$ K, where I is the moment of inertia of the hydrogen molecule. Assuming that ortho-H_2 and para-H_2 are at thermal equilibrium, the ortho:para ratio is close to 3:1. In this case, the rotational part of the specific heat is given by

$$C_{\rm V,rot}^{\rm H_2} = \frac{k}{\mu m_{\rm H}} T \frac{\partial^2}{\partial T^2}\left[T\ln(3\mathcal{Z}_{\rm o} + \mathcal{Z}_{\rm p})\right]. \tag{B.10}$$

The total adiabatic exponent is then given by

$$\gamma = 1 + \frac{\sum_{i=1}^{n} y_i}{\sum_{i=1}^{n} \frac{y_i}{\gamma_i - 1}}, \tag{B.11}$$

where the summation is over all chemical species. y_i denotes the concentration of the ith species. In our case, we consider molecular clouds made of 70% of H_2 and 30% of monoatomic elements, mainly He. The evolution of γ as a function of the temperature is given in figure B.1. The black curve shows the adiabatic exponent of the molecular gas and the red curve shows the evolution of the adiabatic exponent for the H_2 molecule. Below $T = \theta_{\rm vib}$, the rotational and the vibrational energy levels are not excited. Then, γ drops to 7/5 at higher temperature, because the increase in temperature excites the rotational levels of H_2. The adiabatic exponent for the molecular gas is higher, ~ 1.45. When $T > 100$ K, the vibrational levels are excited, but our estimate is not valid any more, since we do not account for H_2 dissociation. A next step to describe more accurately the microphysics during the collapse is to account for the variations of γ as a function function of the gas temperature in our calculations.

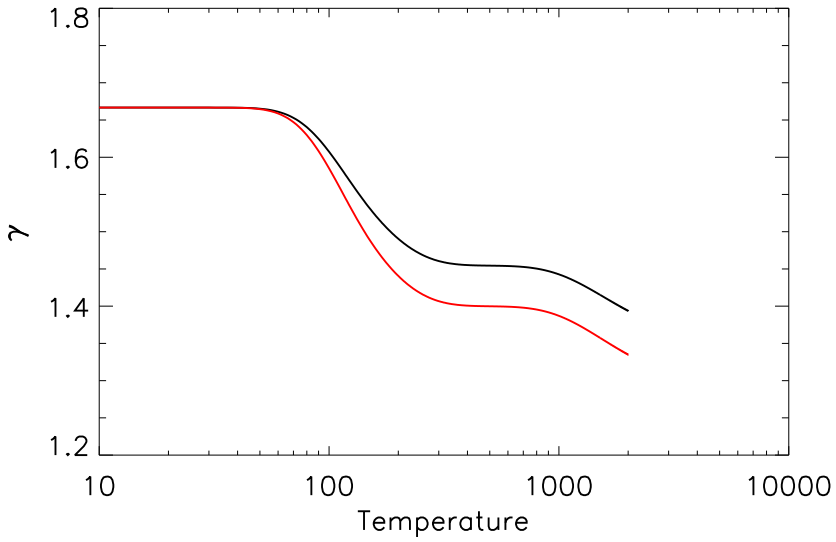

Figure B.1: Evolution of the adiabatic index γ with the temperature for a with an hydrogen fraction of 0.7, the remaining species behave as monoatomic molecule with $\gamma_i = 5/3$ (black curve). The red curve displays the adiabatic index of H_2.

Appendix C
Collapse of an initial 5 $M_\odot$ core

In this appendix, we present calculations of the collapse of a 5 $M_\odot$ dense core, with initial conditions given by $\alpha = 0.37$, $\beta = 0.045$ and $\mu = 5$. The initial density is $\rho_0 = 3.1 \times 10^{-20}$ g cm^{-3} and the initial radius is $R_0 = 5.3 \times 10^{17}$ cm (~ 0.17 pc). We have performed two calculations using the FLD module of RAMSES: the first without sink particles and the second with a sink particle using the method of the density threshold presented in section 6.3. In this case, the density threshold has been set to $\rho_{\rm sink} = 2 \times 10^{-12}$ g cm^{-3} (relatively low value chosen to save CPU time...). The refinement criterion is $N_{\rm J} = 10$ and the coarse grid is established at level $\ell_{\rm min} = 6$. We use the Lax-Friedrich Riemann solver for the hydrodynamics and the HLLD Riemann solver for the magnetic field. The adiabatic index is $\gamma = 7/5$. We use 8 levels of refinement, for a maximum resolution of 8.6 AU.

In figure C.1, temperature and density maps are displayed in the yz-plane at time t= $1.19 t_{\rm ff}$ for the two calculations. The outflow extent, ~ 3000 AU, is much larger than in the case of a 1 $M_\odot$ core. In the two calculations, the density patterns are in very good agreement. The temperatures are different at radii < 1000 AU. The radiative feedback due to accretion on the sink becomes somewhat significant, and the gas has been heated up of a few degrees. However, this heating does not affect the outflow. The sink particle mass at time t=1.19 $t_{\rm ff}$ (49 kyr) is 8.2×10^{-3} $M_\odot$, its accretion rate is $\dot{M} = 2.55 \times 10^{-6}$ $M_\odot$/yr and the luminosity released by the sink particle is $L_{\rm sink} = 0.33$ $L_\odot$. The sink has been created 2990 years earlier. The time-averaged accretion rate since its creation is $\bar{\dot{M}} \sim 2.74 \times 10^{-6}$ $M_\odot$/yr and the corresponding luminosity is $\bar{L}_{\rm sink} = 0.33$ $L_\odot$.

In figure C.2, the mean density and temperature profiles in the equatorial plane, as a function of the radius, are plotted. The density profiles obtained in the two cases are in good agreement, as for the case of a 1 $M_\odot$ core. The temperature profiles are different for radii < 1000 AU. When the radiative feedback of the sink particle is plugged in, this gives a temperature higher than in the case without sink particles.

The density, radial velocity, temperature and toroidal magnetic field component profiles, averaged in a conic volume that makes an angle of $\pi/8$ with the z-axis, are plotted in figure C.3. In this region that corresponds to the outflow, the differences between the cases without and with a sink particle are smaller. The temperature is still warmer in the case with the radiative feedback from the sink particle, but the heating is not as significant as in the equatorial plane, since the gas is optically thin. In comparison with results obtained in chapter 6, the outflow velocity is much higher, with a maximum close to 4 km s^{-1}. In the region where the in-falling gas is stopped by the outflow ($R > 1000$ AU), an over-density is produced.

These results show that the radiative feedback from a central protostar increases when the mass of the initial core increases. The star formation process is more drastic than in the case of a less massive dense core. However, the question is to estimate to what extent the subgrid model we introduce with the sink particle is realistic, especially in what concerns the different

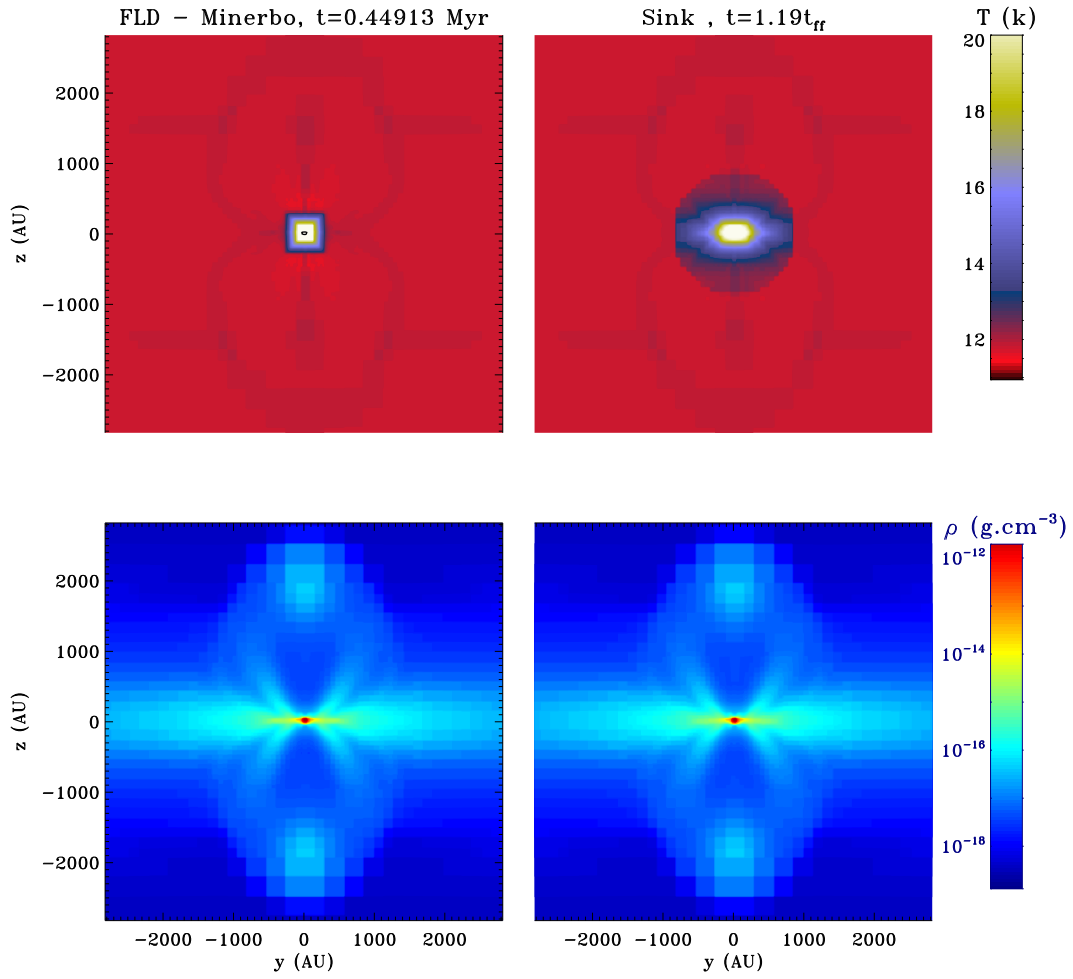

Figure C.1: Case $\mu = 5$: temperature (*top*) and density (*bottom*) maps in the yz-plane for calculations performed with the FLD (*left*), without sink particles (*left*) and with a sink particle using the density threshold $\rho_{\rm sink} = 2\times10^{-12}$ g cm^{-3} (*right*). Results are given at time t= 1.19$t_{\rm ff}$.

time scales. For this reason, it is compulsory to perform the same calculations, but with the physics of the second collapse.

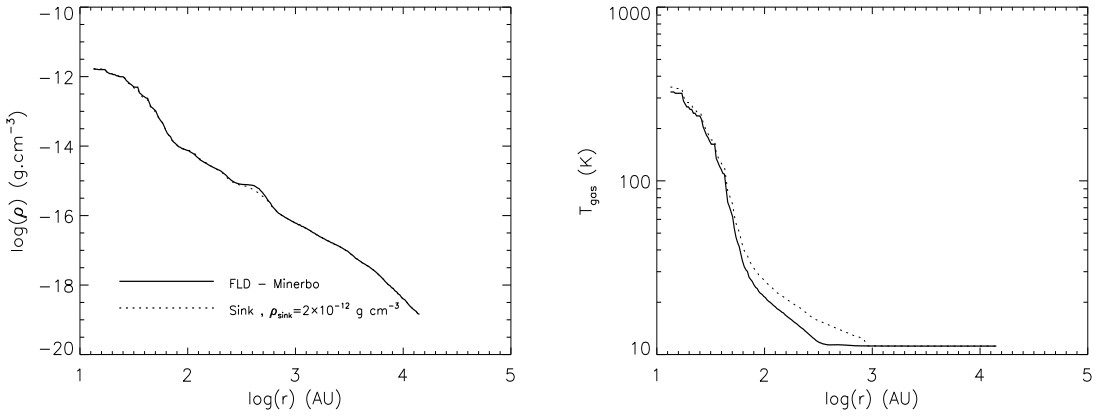

Figure C.2: Profiles of density and temperature as a function of the radius for the same calculations and at the same time as in figure C.1. All quantities are averaged in the equatorial plane.

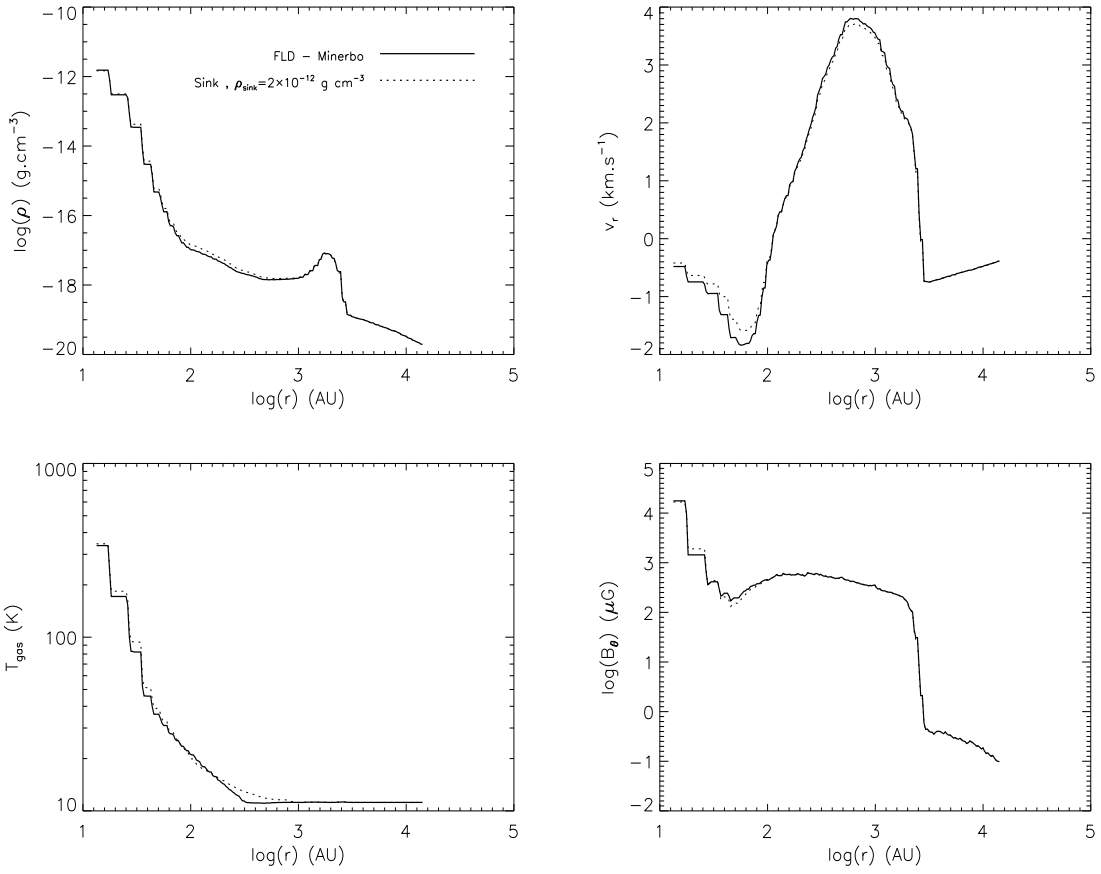

Figure C.3: Profiles of density, radial velocity, temperature and toroidal magnetic flux component as a function of the radius for the same calculations and at the same time as in figure C.1. All quantities are averaged in a conic volume that makes an angle of $\pi/8$ with the z-axis.

Bibliography

Vasilios Alexiades, Geneviéve Amiez, and Pierre-Alain Gremaud. Super-time-stepping acceleration of explicit schemes for parabolic problems. *Com. Num. Meth. Eng*, 12:12–31, 1996. 143, 144, 145

H. Alfvén. On the Existence of Electromagnetic-Hydrodynamic Waves. *Arkiv for Astronomi*, 29:1–7, 1943. 61

J. F. Alves, C. J. Lada, and E. A. Lada. Internal structure of a cold dark molecular cloud inferred from the extinction of background starlight. *Nature*, 409:159–161, January 2001. xv, 6

P. André. The Initial Conditions for Protostellar Collapse: Observational Constraints. 3:1–38, 2002. xv, 4, 5

P. André, D. Ward-Thompson, and M. Barsony. Submillimeter continuum observations of Rho Ophiuchi A - The candidate protostar VLA 1623 and prestellar clumps. *ApJ*, 406:122–141, March 1993. doi: 10.1086/172425. 4

P. André, D. Ward-Thompson, and F. Motte. Probing the initial conditions of star formation: the structure of the prestellar core L 1689B. *A&A*, 314:625–635, October 1996. 6

P. André, D. Ward-Thompson, and M. Barsony. From Prestellar Cores to Protostars: the Initial Conditions of Star Formation. *Protostars and Planets IV*, pages 59–+, May 2000. 2, 4

P. André, A. Belloche, F. Motte, and N. Peretto. The initial conditions of star formation in the Ophiuchus main cloud: Kinematics of the protocluster condensations. *A&A*, 472:519–535, September 2007. doi: 10.1051/0004-6361:20077422. 6

P. André, S. Basu, and S.-i. Inutsuka. The Formation and Evolution of Prestellar Cores. *ArXiv e-prints*, January 2008. xv, 3, 7

G. Arreaga-García, J. Klapp, L. D. G. Sigalotti, and R. Gabbasov. Gravitational Collapse and Fragmentation of Molecular Cloud Cores with GADGET-2. *ApJ*, 666:290–308, September 2007. doi: 10.1086/520492. 86, 90

R. E. Attwood, S. P. Goodwin, and A. P. Whitworth. Adaptive smoothing lengths in SPH. *A&A*, 464:447–450, March 2007. doi: 10.1051/0004-6361:20066606. 86, 90, 106, 107

R. E. Attwood, S. P. Goodwin, D. Stamatellos, and A. P. Whitworth. Simulating star formation in molecular cloud cores. IV. The role of turbulence and thermodynamics. *A&A*, 495:201–215, February 2009. doi: 10.1051/0004-6361:200810806. 9

E. Audit and P. Hennebelle. Thermal condensation in a turbulent atomic hydrogen flow. *A&A*, 433:1–13, April 2005. doi: 10.1051/0004-6361:20041474. 2

E. Audit, P. Charrier, J. . Chièze, and B. Dubroca. A radiation-hydrodynamics scheme valid from the transport to the diffusion limit. *ArXiv Astrophysics e-prints*, June 2002. 29

R. Bachiller. Bipolar Molecular Outflows from Young Stars and Protostars. *ARA&A*, 34:111–154, 1996. doi: 10.1146/annurev.astro.34.1.111. 3

J. Ballesteros-Paredes, R. S. Klessen, M.-M. Mac Low, and E. Vazquez-Semadeni. Molecular Cloud Turbulence and Star Formation. In B. Reipurth, D. Jewitt, and K. Keil, editors, *Protostars and Planets V*, pages 63–80, 2007. 2

R. Banerjee and R. E. Pudritz. Outflows and Jets from Collapsing Magnetized Cloud Cores. *ApJ*, 641:949–960, April 2006. doi: 10.1086/500496. 3, 9

I. Baraffe, G. Chabrier, and J. Gallardo. Episodic Accretion at Early Stages of Evolution of Low-Mass Stars and Brown Dwarfs: A Solution for the Observed Luminosity Spread in H-R Diagrams? *ApJ*, 702:L27–L31, September 2009. doi: 10.1088/0004-637X/702/1/L27.

S. Basu, G. E. Ciolek, W. B. Dapp, and J. Wurster. Magnetically-regulated fragmentation induced by nonlinear flows and ambipolar diffusion. *New Astronomy*, 14:483–495, July 2009. doi: 10.1016/j.newast.2009.01.004. 2

M. R. Bate. The importance of radiative feedback for the stellar initial mass function. *MNRAS*, 392:1363–1380, February 2009. doi: 10.1111/j.1365-2966.2008.14165.x. 133

M. R. Bate and I. A. Bonnell. The origin of the initial mass function and its dependence on the mean Jeans mass in molecular clouds. *MNRAS*, 356:1201–1221, February 2005. doi: 10.1111/j.1365-2966.2004.08593.x. 9

M. R. Bate and A. Burkert. Resolution requirements for smoothed particle hydrodynamics calculations with self-gravity. *MNRAS*, 288:1060–1072, July 1997. 86, 87, 88, 90, 91, 92

M. R. Bate, I. A. Bonnell, and N. M. Price. Modelling accretion in protobinary systems. *MNRAS*, 277:362–376, November 1995. xvii, 88, 90

A. Belloche, P. André, D. Despois, and S. Blinder. Molecular line study of the very young protostar IRAM 04191 in Taurus: infall, rotation, and outflow. *A&A*, 393:927–947, October 2002. doi: 10.1051/0004-6361:20021054. 6

M. J. Berger and J. Oliger. *J. Chem. Phys*, 53:484, 1984. 54

D. C. Black and P. Bodenheimer. Evolution of rotating interstellar clouds. I - Numerical techniques. *ApJ*, 199:619–632, August 1975. doi: 10.1086/153729. 8

R. D. Blandford and D. G. Payne. Hydromagnetic flows from accretion discs and the production of radio jets. *MNRAS*, 199:883–903, June 1982. 123

P. Bodenheimer, A. Burkert, R. I. Klein, and A. P. Boss. Multiple Fragmentation of Protostars. *Protostars and Planets IV*, pages 675–+, May 2000. 8

I. Bonnell, H. Martel, P. Bastien, J.-P. Arcoragi, and W. Benz. Fragmentation of elongated cylindrical clouds. III - Formation of binary and multiple systems. *ApJ*, 377:553–558, August 1991. doi: 10.1086/170384. 8

I. A. Bonnell. A New Binary Formation Mechanism. *MNRAS*, 269:837–848, August 1994. 8, 87, 88

I. A. Bonnell, M. R. Bate, C. J. Clarke, and J. E. Pringle. Accretion and the stellar mass spectrum in small clusters. *MNRAS*, 285:201–208, February 1997. 2

I. A. Bonnell, M. R. Bate, and H. Zinnecker. On the formation of massive stars. *MNRAS*, 298: 93–102, July 1998. doi: 10.1046/j.1365-8711.1998.01590.x. 9

I. A. Bonnell, P. Clark, and M. R. Bate. Gravitational fragmentation and the formation of brown dwarfs in stellar clusters. *MNRAS*, 389:1556–1562, October 2008. doi: 10.1111/j.1365-2966.2008.13679.x. 119

W. B. Bonnor. Boyle's Law and gravitational instability. *MNRAS*, 116:351–+, 1956. 6

A. P. Boss and P. Bodenheimer. Fragmentation in a rotating protostar - A comparison of two three-dimensional computer codes. *ApJ*, 234:289–295, November 1979. doi: 10.1086/157497. 8, 86, 87

A. Burkert and J. Alves. The Inevitable Future of the Starless Core Barnard 68. *ApJ*, 695: 1308–1314, April 2009. doi: 10.1088/0004-637X/695/2/1308. xv, 6

J. I. Castor. Radiative Transfer in Spherically Symmetric Flows. *ApJ*, 178:779–792, December 1972. doi: 10.1086/151834. 26

J. I. Castor. *Radiation Hydrodynamics*. November 2004. 24

G. Chabrier and I. Baraffe. Theory of Low-Mass Stars and Substellar Objects. *ARA&A*, 38: 337–377, 2000. doi: 10.1146/annurev.astro.38.1.337. 3

J. P. Chieze. The fragmentation of molecular clouds. I - The mass-radius-velocity dispersion relations. *A&A*, 171:225–232, January 1987. 8

B. Commerçon, P. Hennebelle, E. Audit, G. Chabrier, and R. Teyssier. Protostellar collapse: a comparison between smoothed particle hydrodynamics and adaptative mesh refinement calculations. *A&A*, 482:371–385, April 2008. doi: 10.1051/0004-6361:20078591. 87

R. Courant, K. Friedrichs, and H. Lewy. ber die partiellen Differenzengleichungen der mathematischen Physik. *Mathematische Annalen*, 100:32–74, 1928. 58

M. Davis, G. Efstathiou, C. S. Frenk, and S. D. M. White. The evolution of large-scale structure in a universe dominated by cold dark matter. *ApJ*, 292:371–394, May 1985. doi: 10.1086/163168. 110

W. Dehnen. Towards optimal softening in three-dimensional N-body codes - I. Minimizing the force error. *MNRAS*, 324:273–291, June 2001. 86

B. Dubroca and J. N. Feugeas. Etude théorique et numérique d'une hiérarchie de modèles aux moments pour le transfert radiatif. *Comptes Rendus de l'Académie des Sciences*, 329:915–920, 1999. 22, 23

R. Ebert. Über die Verdichtung von H I-Gebieten. Mit 5 Textabbildungen. *Zeitschrift fur Astrophysik*, 37:217–+, 1955. 6

L. Ensman. Test problems for radiation and radiation-hydrodynamics codes. *ApJ*, 424:275–291, March 1994. doi: 10.1086/173889. 74, 75

C. R. Evans and J. F. Hawley. Simulation of magnetohydrodynamic flows - A constrained transport method. *ApJ*, 332:659–677, September 1988. doi: 10.1086/166684. 62

N. J. Evans, II. Physical Conditions in Regions of Star Formation. *ARA&A*, 37:311–362, 1999. doi: 10.1146/annurev.astro.37.1.311. 6

J. W. Ferguson, D. R. Alexander, F. Allard, T. Barman, J. G. Bodnarik, P. H. Hauschildt, A. Heffner-Wong, and A. Tamanai. Low-Temperature Opacities. *ApJ*, 623:585–596, April 2005. doi: 10.1086/428642. xv, 31, 32

P. N. Foster and R. A. Chevalier. Gravitational Collapse of an Isothermal Sphere. *ApJ*, 416: 303–+, October 1993. doi: 10.1086/173236. 2

C. S. Frenk, S. D. M. White, P. Bode, J. R. Bond, G. L. Bryan, R. Cen, H. M. P. Couchman, A. E. Evrard, N. Gnedin, A. Jenkins, A. M. Khokhlov, A. Klypin, J. F. Navarro, M. L. Norman, J. P. Ostriker, J. M. Owen, F. R. Pearce, U.-L. Pen, M. Steinmetz, P. A. Thomas, J. V. Villumsen, J. W. Wadsley, M. S. Warren, G. Xu, and G. Yepes. The Santa Barbara Cluster Comparison Project: A Comparison of Cosmological Hydrodynamics Solutions. *ApJ*, 525:554–582, November 1999. doi: 10.1086/307908. 86

S. Fromang, P. Hennebelle, and R. Teyssier. A high order Godunov scheme with constrained transport and adaptive mesh refinement for astrophysical magnetohydrodynamics. *A&A*, 457: 371–384, October 2006. doi: 10.1051/0004-6361:20065371. 54, 61, 62, 86, 107, 122, 142

R. A. Gingold and J. J. Monaghan. Smoothed particle hydrodynamics - Theory and application to non-spherical stars. *MNRAS*, 181:375–389, November 1977. 88

R. A. Gingold and J. J. Monaghan. On the fragmentation of differentially rotating clouds. *MNRAS*, 204:715–733, August 1983. 89

S. K. Godunov. A Finite Difference Method for the Computation of Discontinuous Solutions of the Equations of Fluid Dynamic. *Matematicheskii Sbornik*, 47:271–306, 1959. 55

P. F. Goldsmith. Molecular Depletion and Thermal Balance in Dark Cloud Cores. *ApJ*, 557: 736–746, August 2001. doi: 10.1086/322255. 6

M. Gonzáles. *Contribution à l'étude numérique de l'hydrodynamique radiative : des expériences de chocs radiatifs aux jets astrophysiques*. PhD thesis, 2006. xvi, 19, 47

M. González, E. Audit, and P. Huynh. HERACLES: a three-dimensional radiation hydrodynamics code. *A&A*, 464:429–435, March 2007. doi: 10.1051/0004-6361:20065486. 75

A. A. Goodman, P. J. Benson, G. A. Fuller, and P. C. Myers. Dense cores in dark clouds. VIII - Velocity gradients. *ApJ*, 406:528–547, April 1993. doi: 10.1086/172465. 6

S. P. Goodwin, A. P. Whitworth, and D. Ward-Thompson. Simulating star formation in molecular cloud cores. I. The influence of low levels of turbulence on fragmentation and multiplicity. *A&A*, 414:633–650, February 2004. doi: 10.1051/0004-6361:20031594. 88

A. Harten. High resolution schemes for hyperbolic conservation laws. *Journal of Computational Physics*, 49:357–393, 1983. doi: 10.1006/jcph.1997.5713. 56

J. C. Hayes and M. L. Norman. Beyond Flux-limited Diffusion: Parallel Algorithms for Multidimensional Radiation Hydrodynamics. *ApJS*, 147:197–220, July 2003. doi: 10.1086/374658. 68, 76

J. C. Hayes, M. L. Norman, R. A. Fiedler, J. O. Bordner, P. S. Li, S. E. Clark, A. ud-Doula, and M.-M. Mac Low. Simulating Radiating and Magnetized Flows in Multiple Dimensions with ZEUS-MP. *ApJS*, 165:188–228, July 2006. doi: 10.1086/504594. 54, 74, 76

Yun He and Chris H. Q. Ding. Using accurate arithmetics to improve numerical reproducibility and stability in parallel applications. In *ICS '00: Proceedings of the 14th international conference on Supercomputing*, pages 225–234, New York, NY, USA, 2000. ACM. ISBN 1-58113-270-0. doi: http://doi.acm.org/10.1145/335231.335253. 69, 72

C. Heiles and R. Crutcher. Magnetic Fields in Diffuse HI and Molecular Clouds. 664:137–+, 2005. doi: 10.1007/11369875_7. xv, 7

P. Hennebelle and G. Chabrier. Analytical Theory for the Initial Mass Function: CO Clumps and Prestellar Cores. *ApJ*, 684:395–410, September 2008. doi: 10.1086/589916. 9

P. Hennebelle and G. Chabrier. Analytical Theory for the Initial Mass Function. II. Properties of the Flow. *ApJ*, 702:1428–1442, September 2009. doi: 10.1088/0004-637X/702/2/1428. 9

P. Hennebelle and S. Fromang. Magnetic processes in a collapsing dense core. I. Accretion and ejection. *A&A*, 477:9–24, January 2008. doi: 10.1051/0004-6361:20078309. 3, 9, 119, 125, 126

P. Hennebelle and R. Teyssier. Magnetic processes in a collapsing dense core. II. Fragmentation. Is there a fragmentation crisis? *A&A*, 477:25–34, January 2008. doi: 10.1051/0004-6361:20078310. 9, 119, 122, 129

P. Hennebelle, A. P. Whitworth, P. P. Gladwin, and P. André. Protostellar collapse induced by compression. *MNRAS*, 340:870–882, April 2003. doi: 10.1046/j.1365-8711.2003.05584.x. 2

P. Hennebelle, A. P. Whitworth, S.-H. Cha, and S. P. Goodwin. Protostellar collapse induced by compression - II. Rotation and fragmentation. *MNRAS*, 348:687–701, February 2004. doi: 10.1111/j.1365-2966.2004.07378.x. 88

L. Hernquist. Performance characteristics of tree codes. *ApJS*, 64:715–734, August 1987. doi: 10.1086/191215. 90

J. G. Hosking and A. P. Whitworth. Fragmentation of magnetized cloud cores. *MNRAS*, 347: 1001–1010, January 2004. doi: 10.1111/j.1365-2966.2004.07274.x. 86

L. H. Howell and J. A. Greenough. Radiation diffusion for multi-fluid Eulerian hydrodynamics with adaptive mesh refinement. *Journal of Computational Physics*, 184:53–78, January 2003. doi: 10.1016/S0021-9991(02)00015-3. 68

D. A. Hubber, S. P. Goodwin, and A. P. Whitworth. Resolution requirements for simulating gravitational fragmentation using SPH. *A&A*, 450:881–886, May 2006. doi: 10.1051/0004-6361:20054100. 92

S. Inutsuka. Godunov-type SPH. *Memorie della Societa Astronomica Italiana*, 65:1027–+, 1994. 88

J. H. Jeans. The Stability of a Spherical Nebula. *Philosophical Transactions of the Royal Society of London*, 199:1–53, 1902. 11

A. M. Khokolov. *J. Chem. Phys*, 143:519, 1998. 54, 59

S. Kitsionas and A. P. Whitworth. Smoothed Particle Hydrodynamics with particle splitting, applied to self-gravitating collapse. *MNRAS*, 330:129–136, February 2002. doi: 10.1046/j.1365-8711.2002.05115.x. 86, 92

R. I. Klein. Star formation with 3-D adaptive mesh refinement: the collapse and fragmentation of molecular clouds. *Journal of Computational and Applied Mathematics*, 109:123–152, September 1999. 8

R. I. Klein, S.-I. Inutsuka, P. Padoan, and K. Tomisaka. Current Advances in the Methodology and Computational Simulation of the Formation of Low-Mass Stars. In B. Reipurth, D. Jewitt, and K. Keil, editors, *Protostars and Planets V*, pages 99–116, 2007. 7, 86, 142

R. S. Klessen, A. Burkert, and M. R. Bate. Fragmentation of Molecular Clouds: The Initial Phase of a Stellar Cluster. *ApJ*, 501:L205+, July 1998. doi: 10.1086/311471. 9

R. S. Klessen, M. R. Krumholz, and F. Heitsch. Numerical Star-Formation Studies – A Status Report. *ArXiv e-prints*, June 2009. 7

Donald E. Knuth. *The art of computer programming, volume 2 (3rd ed.): seminumerical algorithms*. Addison-Wesley Longman Publishing Co., Inc., Boston, MA, USA, 1997. ISBN 0-201-89684-2. 69

A. V. Kravtsov, A. A. Klypin, and A. M. Khokhlov. Adaptive Refinement Tree: A New High-Resolution N-Body Code for Cosmological Simulations. *ApJS*, 111:73–+, July 1997. doi: 10.1086/313015. 60

M. R. Krumholz, C. F. McKee, and R. I. Klein. Embedding Lagrangian Sink Particles in Eulerian Grids. *ApJ*, 611:399–412, August 2004. doi: 10.1086/421935. xxi, 60, 110, 133, 137, 138

M. R. Krumholz, R. I. Klein, and C. F. McKee. Radiation-Hydrodynamic Simulations of Collapse and Fragmentation in Massive Protostellar Cores. *ApJ*, 656:959–979, February 2007a. doi: 10.1086/510664. 110, 133, 137, 138

M. R. Krumholz, R. I. Klein, C. F. McKee, and J. Bolstad. Equations and Algorithms for Mixed-frame Flux-limited Diffusion Radiation Hydrodynamics. *ApJ*, 667:626–643, September 2007b. doi: 10.1086/520791. 9, 10, 26, 113

M. R. Krumholz, R. I. Klein, C. F. McKee, S. S. R. Offner, and A. J. Cunningham. The Formation of Massive Star Systems by Accretion. *Science*, 323:754–, February 2009. doi: 10.1126/science.1165857. xv, 8, 9, 10

R. B. Larson. Numerical calculations of the dynamics of collapsing proto-star. *MNRAS*, 145: 271–+, 1969. 2, 7, 35, 86, 87

R. B. Larson. The Collapse of a Rotating Cloud. *MNRAS*, 156:437–+, 1972. 8

R. B. Larson. The physics of star formation. *Reports on Progress in Physics*, 66:1651–1697, October 2003. doi: 10.1088/0034-4885/66/10/R03. 7

R. B. Larson. KEY ISSUES REVIEW: Insights from simulations of star formation. *Reports on Progress in Physics*, 70:337–356, March 2007. doi: 10.1088/0034-4885/70/3/R01. 7

C. D. Levermore. Relating Eddington factors to flux limiters. *Journal of Quantitative Spectroscopy and Radiative Transfer*, 31:149–160, 1984. xv, 21, 22, 23

C. D. Levermore and G. C. Pomraning. A flux-limited diffusion theory. *ApJ*, 248:321–334, August 1981. doi: 10.1086/159157. 21

J. C. Lombardi, A. Sills, F. A. Rasio, and S. L. Shapiro. Tests of Spurious Transport in Smoothed Particle Hydrodynamics. *Journal of Computational Physics*, 152:687–735, July 1999. 86, 100, 105

R. B. Lowrie, D. Mihalas, and J. E. Morel. Comoving-frame radiation transport for nonrelativistic fluid velocities. *Journal of Quantitative Spectroscopy and Radiative Transfer*, 69:291–304, May 2001. doi: 10.1016/S0022-4073(00)00085-6. 23

L. B. Lucy. A numerical approach to the testing of the fission hypothesis. *AJ*, 82:1013–1024, December 1977. 88

M. N. Machida, S.-i. Inutsuka, and T. Matsumoto. Magnetic Fields and Rotations of Protostars. *ApJ*, 670:1198–1213, December 2007. doi: 10.1086/521779. 3, 9

M. N. Machida, S.-i. Inutsuka, and T. Matsumoto. High- and Low-Velocity Magnetized Outflows in the Star Formation Process in a Gravitationally Collapsing Cloud. *ApJ*, 676:1088–1108, April 2008a. doi: 10.1086/528364. xv, 8, 9

M. N. Machida, K. Tomisaka, T. Matsumoto, and S.-i. Inutsuka. Formation Scenario for Wide and Close Binary Systems. *ApJ*, 677:327–347, April 2008b. doi: 10.1086/529133. 9, 119, 135

H. Masunaga and S.-I. Inutsuka. Does "tau˜1" Terminate the Isothermal Evolution of Collapsing Clouds? *ApJ*, 510:822–827, January 1999. doi: 10.1086/306608. 36

H. Masunaga and S.-i. Inutsuka. A Radiation Hydrodynamic Model for Protostellar Collapse. II. The Second Collapse and the Birth of a Protostar. *ApJ*, 531:350–365, March 2000a. doi: 10.1086/308439. 31, 87

H. Masunaga and S.-i. Inutsuka. A Radiation Hydrodynamic Model for Protostellar Collapse. II. The Second Collapse and the Birth of a Protostar. *ApJ*, 531:350–365, March 2000b. doi: 10.1086/308439. xv, 2, 3, 28, 137

H. Masunaga, S. M. Miyama, and S.-I. Inutsuka. A Radiation Hydrodynamic Model for Protostellar Collapse. I. The First Collapse. *ApJ*, 495:346–+, March 1998. doi: 10.1086/305281. 28, 30, 31, 51, 79

T. Matsumoto and T. Hanawa. Fragmentation of a Molecular Cloud Core versus Fragmentation of the Massive Protoplanetary Disk in the Main Accretion Phase. *ApJ*, 595:913–934, October 2003. doi: 10.1086/377367. 54

C. F. McKee and E. C. Ostriker. Theory of Star Formation. *ARA&A*, 45:565–687, September 2007. doi: 10.1146/annurev.astro.45.051806.110602. 2, 7

R. R. Mellon and Z.-Y. Li. Magnetic Braking and Protostellar Disk Formation: Ambipolar Diffusion. *ApJ*, 698:922–927, June 2009. doi: 10.1088/0004-637X/698/1/922. 3

A. Mignone, G. Bodo, S. Massaglia, T. Matsakos, O. Tesileanu, C. Zanni, and A. Ferrari. PLUTO: A Numerical Code for Computational Astrophysics. *ApJS*, 170:228–242, May 2007. doi: 10.1086/513316. 143

D. Mihalas and L. H. Auer. On laboratory-frame radiation hydrodynamics. *Journal of Quantitative Spectroscopy and Radiative Transfer*, 71:61–97, 2001. doi: doi:10.1016/S0022-4073(01)00013-9. 23

D. Mihalas and R. I. Klein. On the solution of the time-dependent inertial-frame equation of radiative transfer in moving media to O(v/c). *Journal of Computational Physics*, 46:97–137, April 1982. doi: 10.1016/0021-9991(82)90007-9. 26

D. Mihalas and B. W. Mihalas. *Foundations of radiation hydrodynamics*. 1984. 17, 20, 25, 41, 44, 45, 46, 47, 50, 75

G. N. Minerbo. Maximum entropy Eddington factors. *Journal of Quantitative Spectroscopy and Radiative Transfer*, 20:541–545, 1978. 21

S. M. Miyama. Criteria for the collapse and fragmentation of rotating clouds. *PASJ*, 44:193–202, June 1992. 8

T. Miyoshi and K. Kusano. A multi-state HLL approximate Riemann solver for ideal magnetohydrodynamics. *Journal of Computational Physics*, 208:315–344, September 2005. doi: 10.1016/j.jcp.2005.02.017. 62

J. J. Monaghan and J. C. Lattanzio. A refined particle method for astrophysical problems. *A&A*, 149:135–143, August 1985. 89

J. P. Morris and J. J. Monaghan. A switch to reduce sph viscosity. *J. Comput. Phys.*, 136(1): 41–50, 1997. ISSN 0021-9991. doi: http://dx.doi.org/10.1006/jcph.1997.5690. 89, 106

T. C. Mouschovias. Magnetic braking, ambipolar diffusion, cloud cores, and star formation - Natural length scales and protostellar masses. *ApJ*, 373:169–186, May 1991. doi: 10.1086/170035. 2

T. C. Mouschovias and L. Spitzer, Jr. Note on the collapse of magnetic interstellar clouds. *ApJ*, 210:326–+, December 1976. doi: 10.1086/154835. 122

T. Nakano. Star Formation in Magnetic Clouds. *ApJ*, 494:587–+, February 1998. doi: 10.1086/305230. 2

A. F. Nelson. Numerical requirements for simulations of self-gravitating and non-self-gravitating discs. *MNRAS*, 373:1039–1073, December 2006. doi: 10.1111/j.1365-2966.2006.11119.x. 86, 100

S. S. R. Offner, R. I. Klein, C. F. McKee, and M. R. Krumholz. The Effects of Radiative Transfer on Low-Mass Star Formation. *ArXiv e-prints*, April 2009. 9, 10, 133, 135, 137, 138

K. Omukai. Observational Characteristics of the First Protostellar Cores. *PASJ*, 59:589–606, June 2007. 50

S. O'Sullivan and T. P. Downes. An explicit scheme for multifluid magnetohydrodynamics. *MNRAS*, 366:1329–1336, March 2006. doi: 10.1111/j.1365-2966.2005.09898.x. 143

P. Padoan and Å. Nordlund. The "Mysterious" Origin of Brown Dwarfs. *ApJ*, 617:559–564, December 2004. doi: 10.1086/345413. 9

G. Pelletier and R. E. Pudritz. Hydromagnetic disk winds in young stellar objects and active galactic nuclei. *ApJ*, 394:117–138, July 1992. doi: 10.1086/171565. 123, 124

M. V. Penston. Dynamics of self-gravitating gaseous spheres-III. Analytical results in the free-fall of isothermal cases. *MNRAS*, 144:425–+, 1969. 7, 86

S. Popinet. Gerris: A tree-based adaptive solver for the incompressible euler equations in complex geometries. *Journal of Computational Physics*, 190:572–600, 2003. 69

D. J. Price and M. R. Bate. The impact of magnetic fields on single and binary star formation. *MNRAS*, 377:77–90, May 2007. doi: 10.1111/j.1365-2966.2007.11621.x. 9

D. J. Price and M. R. Bate. Inefficient star formation: The combined effects of magnetic fields and radiative feedback. *ArXiv e-prints*, April 2009. 9, 113, 133

R. E. Pudritz, R. Ouyed, C. Fendt, and A. Brandenburg. Disk Winds, Jets, and Outflows: Theoretical and Computational Foundations. In B. Reipurth, D. Jewitt, and K. Keil, editors, *Protostars and Planets V*, pages 277–294, 2007. 123

Frederic A. Rasio. Particle methods in astrophysical fluid dynamics, 1999. URL `http://www.citebase.org/abstract?id=oai:arXiv.org:astro-ph/9911360`. 86, 100, 105

D. Semenov, T. Henning, C. Helling, M. Ilgner, and E. Sedlmayr. Rosseland and Planck mean opacities for protoplanetary discs. *A&A*, 410:611–621, November 2003. doi: 10.1051/0004-6361:20031279. xv, 31, 32, 37, 121

F. H. Shu. Self-similar collapse of isothermal spheres and star formation. *ApJ*, 214:488–497, June 1977. 3, 7, 29, 86

F. H. Shu, F. C. Adams, and S. Lizano. Star formation in molecular clouds - Observation and theory. *ARA&A*, 25:23–81, 1987. doi: 10.1146/annurev.aa.25.090187.000323. 2

Gary A. Sod. A survey of several finite difference methods for systems of nonlinear hyperbolic conservation laws. *Journal of Computational Physics*, 27(1):1–31, April 1978. doi: 10.1016/0021-9991(78)90023-2. URL `http://dx.doi.org/10.1016/0021-9991(78)90023-2`. 73

L. Spitzer. *Physical processes in the interstellar medium*. 1978. 12

S. W. Stahler. Deuterium and the stellar birthline. *ApJ*, 332:804–825, September 1988. doi: 10.1086/166694. 3

S. W. Stahler, F. H. Shu, and R. E. Taam. The evolution of protostars. I - Global formulation and results. *ApJ*, 241:637–654, October 1980. doi: 10.1086/158377. 29, 44, 51

D. Stamatellos, A. P. Whitworth, T. Bisbas, and S. Goodwin. Radiative transfer and the energy equation in SPH simulations of star formation. *A&A*, 475:37–49, November 2007. doi: 10.1051/0004-6361:20077373. 9

J. M. Stone and M. L. Norman. ZEUS-2D: A radiation magnetohydrodynamics code for astrophysical flows in two space dimensions. I - The hydrodynamic algorithms and tests. *ApJS*, 80:753–790, June 1992. doi: 10.1086/191680. 54

J. M. Stone, D. Mihalas, and M. L. Norman. ZEUS-2D: A radiation magnetohydrodynamics code for astrophysical flows in two space dimensions. III - The radiation hydrodynamic algorithms and tests. *ApJS*, 80:819–845, June 1992. doi: 10.1086/191682. 28

R. Teyssier. Cosmological hydrodynamics with adaptive mesh refinement. A new high resolution code called RAMSES. *A&A*, 385:337–364, April 2002. doi: 10.1051/0004-6361:20011817. 9, 25, 53, 54, 60, 141

R. Teyssier, S. Fromang, and E. Dormy. Kinematic dynamos using constrained transport with high order Godunov schemes and adaptive mesh refinement. *Journal of Computational Physics*, 218:44–67, October 2006. doi: 10.1016/j.jcp.2006.01.042. 61, 62

J. E. Tohline. Hydrodynamic collapse. *Fundamentals of Cosmic Physics*, 8:1–81, 1982. 8, 87

A. Toomre. On the gravitational stability of a disk of stars. *ApJ*, 139:1217–1238, May 1964. doi: 10.1086/147861. 116

E. Toro. Riemann Solvers and Numerical Methods for Fluid Dynamics (Springer). 1999. 55, 56

J. K. Truelove, R. I. Klein, C. F. McKee, J. H. Holliman, II, L. H. Howell, and J. A. Greenough. The Jeans Condition: A New Constraint on Spatial Resolution in Simulations of Isothermal Self-gravitational Hydrodynamics. *ApJ*, 489:L179+, November 1997. doi: 10.1086/316779. 8, 60, 86, 91, 100

J. K. Truelove, R. I. Klein, C. F. McKee, J. H. Holliman, II, L. H. Howell, J. A. Greenough, and D. T. Woods. Self-gravitational Hydrodynamics with Three-dimensional Adaptive Mesh Refinement: Methodology and Applications to Molecular Cloud Collapse and Fragmentation. *ApJ*, 495:821–+, March 1998. doi: 10.1086/305329. 86

W. Tscharnuter. On the Collapse of Rotating Protostars. *A&A*, 39:207–+, March 1975. 8

T. Tsuribe and S.-I. Inutsuka. Criteria for Fragmentation of Rotating Isothermal Clouds. I. Semianalytic Approach. *ApJ*, 526:307–313, November 1999. doi: 10.1086/307983. 9, 112

J. A. Turner, S. J. Chapman, A. S. Bhattal, M. J. Disney, H. Pongracic, and A. P. Whitworth. Binary star formation: gravitational fragmentation followed by capture. *MNRAS*, 277:705–726, November 1995. 88

N. J. Turner and J. M. Stone. A Module for Radiation Hydrodynamic Calculations with ZEUS-2D Using Flux-limited Diffusion. *ApJS*, 135:95–107, July 2001. doi: 10.1086/321779. 73

B. van Leer. Towards the Ultimate Conservative Difference Scheme, V. A Second-Order Sequel to Godunov's Method. *Journal of Computational Physics*, 32:101–136, 1979. 56

D. Ward-Thompson, F. Motte, and P. Andre. The initial conditions of isolated star formation - III. Millimetre continuum mapping of pre-stellar cores. *MNRAS*, 305:143–150, May 1999. doi: 10.1046/j.1365-8711.1999.02412.x. 6

D. Ward-Thompson, P. André, and J. M. Kirk. The initial conditions of isolated star formation - V. ISOPHOT imaging and the temperature and energy balance of pre-stellar cores. *MNRAS*, 329:257–276, January 2002. doi: 10.1046/j.1365-8711.2002.04969.x. 6

S. C. Whitehouse and M. R. Bate. The thermodynamics of collapsing molecular cloud cores using smoothed particle hydrodynamics with radiative transfer. *MNRAS*, 367:32–38, March 2006. doi: 10.1111/j.1365-2966.2005.09950.x. 9

A. Whitworth and D. Summers. Self-similar condensation of spherically symmetric self-gravitating isothermal gas clouds. *MNRAS*, 214:1–25, May 1985. 8

A. P. Whitworth and C. J. Clarke. Cooling behind mildly supersonic shocks in molecular clouds. *MNRAS*, 291:578–+, November 1997. 31

A. P. Whitworth, A. S. Bhattal, J. A. Turner, and S. J. Watkins. Estimating density in smoothed particle hydrodynamics. *A&A*, 301:929–+, September 1995. 90

H. W. Yorke and C. Sonnhalter. On the Formation of Massive Stars. *ApJ*, 569:846–862, April 2002. doi: 10.1086/339264. 122

Y. B. Zel'Dovich and Y. P. Raizer. *Physics of shock waves and high-temperature hydrodynamic phenomena*. 1967. xvi, 44, 45

U. Ziegler. Self-gravitational adaptive mesh magnetohydrodynamics with the NIRVANA code. *A&A*, 435:385–395, May 2005. doi: 10.1051/0004-6361:20042451. 54

La compréhension des processus conduisant à la formation des étoiles est l'un des enjeux majeurs de l'astrophysique contemporaine. Au sein des nuages conduisant à la formation d'étoiles, les conditions de température, pression, etc... sont telles qu'il est impossible de les reproduire par l'expérience. C'est pourquoi la simulation numérique reste le seul moyen d'étudier les phénomènes physiques intervenant dans le processus de formation des étoiles et ainsi de vérifier la théorie. Ma thèse est axée autour des méthodes numériques utilisées dans le contexte de la formation d'étoiles, phénomène multi-échelles et hautement non-linéaire, nécessitant l'utilisation d'outils bien adaptés.

Dans cette thèse autour de l'étude des premières phases de l'effondrement de coeurs denses préstellaires, mon travail s'est divisé en 4 parties liées. Dans une première étude, j'ai utilisé un code lagrangien 1D à symétrie sphérique (Audit et al. 2002) pour comparer plusieurs modèles traitant plus ou moins précisément le transfert radiatif et l'interaction matière-rayonnement. Cette comparaison est basée sur des calculs simples d'effondrement gravitationnel conduisant à la formation du premier coeur de Larson. J'ai aussi tiré bénéfice de ce premier travail pour étudier les propriétés du choc d'accrétion sur le premier coeur de Larson. Nous avons développé un modèle semi-analytique permettant de reproduire les propriétés de saut au choc en partant d'hypothèses bien connues. Ayant validé les méthodes utilisées précédemment, nous avons retenu l'approche de diffusion à flux limité que j'ai ensuite intégrée avec les équations de l'hydrodynamique radiative dans le code AMR RAMSES (Teyssier 2002). Après validation des schémas implémentés, nous avons utilisé RAMSES pour réaliser des effondrements multidimensionnels avec champ magnétique et transfert radiatif. Nous avons ainsi réalisé les premières simulations combinant les effets du champ magnétique et du transfert radiatif aux petites échelles avec une grande précision. Nos résultats montrent que le transfert radiatif à un impact significatif sur la fragmentation au cours de l'effondrement des coeurs denses préstellaires. Enfin, j'ai réalisé une comparaison du code RAMSES (approche eulérienne) et du code SPH DRAGON (Goodwin 2004, approche lagrangienne). Nous avons étudié l'impact de la résolution numérique sur la conservation du moment angulaire et la fragmentation. Nous avons montré qu'en utilisant des critères de résolution forts et bien supérieurs aux critères usuels de la littérature, les deux outils convergent et semblent donc bien adaptés à la formation d'étoiles.